quantum beam science

Special Issue Reprint

Laser Assisted Manufacturing

Edited by
Swee Leong Sing and Wai Yee Yeong

mdpi.com/journal/qubs

MDPI

Laser Assisted Manufacturing

Laser Assisted Manufacturing

Guest Editors

Swee Leong Sing
Wai Yee Yeong

MDPI

Basel • Beijing • Wuhan • Barcelona • Belgrade • Novi Sad • Cluj • Manchester

Guest Editors

Swee Leong Sing Department of Mechanical Engineering National University of Singapore Singapore	Wai Yee Yeong Singapore Centre for 3D Printing School of Mechanical and Aerospace Engineering Nanyang Technological University Singapore

Editorial Office
MDPI AG
Grosspeteranlage 5
4052 Basel, Switzerland

This is a reprint of the Special Issue, published open access by the journal *Quantum Beam Science* (ISSN 2412-382X), freely accessible at: https://www.mdpi.com/journal/qubs/special_issues/laser_assisted.

For citation purposes, cite each article independently as indicated on the article page online and as indicated below:

Lastname, A.A.; Lastname, B.B. Article Title. *Journal Name* **Year**, *Volume Number*, Page Range.

ISBN 978-3-7258-4267-4 (Hbk)
ISBN 978-3-7258-4268-1 (PDF)
https://doi.org/10.3390/books978-3-7258-4268-1

© 2025 by the authors. Articles in this book are Open Access and distributed under the Creative Commons Attribution (CC BY) license. The book as a whole is distributed by MDPI under the terms and conditions of the Creative Commons Attribution-NonCommercial-NoDerivs (CC BY-NC-ND) license (https://creativecommons.org/licenses/by-nc-nd/4.0/).

Contents

About the Editors

Swee Leong Sing

Swee Leong Sing is an Assistant Professor at the Department of Mechanical Engineering, National University of Singapore (NUS). Prior to joining NUS in August 2021, he was a Presidential Postdoctoral Fellow at the Singapore Centre for 3D Printing (SC3DP) and School of Mechanical and Aerospace Engineering (MAE), Nanyang Technological University (NTU), Singapore, after being awarded the prestigious fellowship in 2020.

Swee Leong has been active in the 3D printing field. He obtained his BEng (Hons) in Aerospace Engineering and PhD in Mechanical Engineering with a topic in additive manufacturing (AM) in 2012 and 2016, respectively. Swee Leong's research focuses on using advanced manufacturing techniques as enablers for materials development and to create strategic values for the industries. He is also active in inter-disciplinary research and translational work. Swee Leong has worked on numerous 3D printing projects with government agencies, universities, research institutes, and industrial collaborators. Swee Leong has filed five patents pertaining to 3D printing processes and materials. He has published more than 90 peer reviewed journal and conference articles. Swee Leong currently has an h-index of 39 with more than 9000 citations (Web of Science, 30 April 2025).

Wai Yee Yeong

Professor Wai Yee Yeong is the winner of the TCT Women in 3D Printing Innovator Award 2019 and features on the Singapore 100 Women in Tech List 2021. Her work is well-recognized, with an H-index of 73 and more than 23,000 citations on Google Scholar. She has filed multiple patents and knowhows, with a keen interest in Bioprinting and the 3D printing of new materials. On academic fronts, she is the Associate Editor for two international journals and has authored three textbooks on 3D printing. Prof Yeong serves as Program Director in the Singapore Centre for 3D Printing and HP-NTU Digital Manufacturing Corp Lab. Prof Yeong was awarded the NRF Investigatorship (Class of 2022) in her pursuit for groundbreaking and high-risk research. She is also the Chair of the School of Mechanical and Aerospace Engineering at Nanyang Technological University, Singapore.

quantum beam science

Article

Blue Diode Laser Welding of Commercially Pure Titanium Foils

Tim Pasang [1,*], Pai-Chen Lin [2], Wojciech Z. Misiolek [3], Jia-Yuan Wei [2], Shinichiro Masuno [4], Masahiro Tsukamoto [4], Eiji Hori [4], Yuji Sato [4], Yuan Tao [5], Danang Yudhistiro [6] and Salahuddin Yunus [6]

[1] Department of Mechanical and Manufacturing Engineering and Technology, Oregon Institute of Technology, Klamath Falls, OR 97601, USA
[2] AIM-HI, National Chung Cheng University, No. 168, Section 1, Daxue Rd, Minxiong Township Chiayi County 62102, Taiwan; imepcl@ccu.edu.tw (P.-C.L.); k6816512@gmail.com (J.-Y.W.)
[3] Loewy Institute, Department of Materials Science and Engineering, Lehigh University, Bethlehem, PA 18015, USA; wzm2@lehigh.edu
[4] Joining and Welding Research Institute (JWRI), Osaka University, Osaka 567-0047, Japan; masuno.snicr@gmail.com (S.M.); tukamoto@jwri.osaka-u.ac.jp (M.T.); hori@jwri.osaka-u.ac.jp (E.H.); sato@jwri.osaka-u.ac.jp (Y.S.)
[5] Department of Mechanical Engineering, Auckland University of Technology, Auckland 1010, New Zealand; yuan.tao@aut.ac.nz
[6] Department of Mechanical Engineering, Universitas Jember, Jember 68121, Jawa Timur, Indonesia; danang.ft@unej.ac.id (D.Y.); salahudin.teknik@unej.ac.id (S.Y.)
* Correspondence: tim.pasang@oit.edu; Tel.: +1-541-851-5262

Abstract: The need for thin foil welding is increasing significantly, particularly in the electronic industries. The technologies that are currently available limit the joining processes in terms of materials and their geometries. In this paper, a series of trials of fusion welding (bead-on- plate) of commercially pure titanium (CPTi) foils were conducted using a blue diode laser (BDL) welding method. The power used was 50 W and 100 W for 0.1 mm and 0.2 mm thick foils, respectively. Following welding, various samples were prepared to examine the weld profiles, microstructures, hardness, tensile strength, and fracture surface characteristics. The results showed that the base metal (BM) had an annealed microstructure with equiaxed grains, while the weld zones contained martensite (α') with large grains. The hardness increased in both regions, from around 123 HV to around 250 HV, in the heat-affected zone (HAZ) and fusion zone (FZ) areas. The tensile tests revealed that the strengths of the welded samples were slightly lower than the unwelded samples, i.e., UTS = 300–350 MPa compared with 325–390 MPa for the unwelded samples. Fracture took place within the BM area. All of the samples, welded and unwelded, showed identical fracture mechanisms, i.e., microvoid coalescence or ductile fracture. The weld zone experienced very small strains (elongation) at fracture, which indicates a good weld quality.

Keywords: blue diode laser (BDL) welding; digital image correlation (DIC); commercially pure titanium (CP Ti); bead-on-plate; mechanical properties; fracture surface

1. Introduction

The blue diode laser (BDL) is one of the laser technologies that is commonly used in applications such as lights for projectors and general lighting. However, many more potential applications are possible in the near future if the laser's power and brightness can be increased [1,2]. A new generation of blue diode laser (BDL) has recently been developed at the Joining and Welding Research Institute (JWRI), Osaka University, in collaboration with Shimadzu Corporation, Japan. The welding machine has a power of up to 100 W and an energy density of 1.3×106 W/cm^2 at the end of the output fiber. This new device uses a GaN-based diode [1] and is expected to be used as a light source for various applications, including welding of the so-called difficult-to-weld metals such as gold, copper, and other reflective metals as well as in 3D printing of such metals because blue light can be efficiently absorbed by these metals [1,2]. Given its very small spot beam size, BDL technology can also be applied extensively to thin foil manufacturing, such as in cutting and/or welding processes. Joining (welding) of thin foils has always been required, for example, in battery cell applications [3]. In addition, with a very small spot size, the heat distortion is also minimized, which means post-weld heat treatment to remove residual stresses may not be required [1]. Furthermore, it is also expected to contribute to reducing the processing time and electrical power consumption in these applications, which is not possible with conventional modules. More details about the BDL machine developed at the JWRI can be found in the paper by Tojo et al. [1].

The need for thin foil welding is increasing significantly, particularly in electronic industries. The technologies that are currently available are limiting the joining processes in terms of materials and their geometries. Several welding experiments on thin foils have been reported where the infra-red or direct laser was utilized, but none have reported on titanium foils. Ventrella and co-authors [4] used infra-red laser technology to weld 0.1 mm thick stainless steel 316 L foils. Following the experimental work and analyses, they concluded that the quality of the thin foil weld was good in terms of the mechanical properties. Abe et al. [5] utilized a direct diode laser to weld 0.05 mm SS304 stainless steel without any spatter and reported a nearly equal strength as the un-welded samples. Kim [6] reported their findings following welding of a 0.05 mm thick AM350 stainless steel foil onto SS304 stainless steel with a thickness of 1 mm. They concluded that the beam diameter played a significant role in thin foil welding, and further recommended that a smaller beam diameter would be preferred. Pakmanesh et al. [7] performed a lap joint of a 316 L stainless steel foil using a pulsed Nd:YAG laser to optimize the process parameters. It was concluded that the underfill and undercut increased with the increased power. On the one hand, the underfill increased with a reduced frequency; however, on the other hand, the undercut increased with an increased high frequency. The authors managed to overcome the presence of these defects by superimposing different responses. The above-mentioned welding methods are, however, not suitable for bright and reflective metals such as copper, and gold; therefore, the development of new technology is still needed.

Limited articles have been published on blue laser or blue diode lasers related to welding, cladding, and materials processing, and they are summarized in the following. Das et al. [3] performed welding of multi-layered stainless steel (SS316L) by stacking 20 layers of micro-foils with a thickness of 0.025 mm onto a 0.2 mm thick SS316L foil sandwich and welded them together. They suggested that this welding technique is suitable for industrial needs, especially for electrical micro joining, as it results in free cracks, low porosity, and low spatter. Zediker et al., conducted welding on copper using a blue laser with a power of 500 W and a spot size of 215 μm. They were able to perform welding at an angle of 90°. The authors reported that neither porosity nor spatter was found [8]. In addition, Zediker et al., performed a full penetration bead-on-plate welding on copper with a power of 600 W and a spot size diameter of 200 μm. They concluded that the shorter wavelength, such as that of the blue laser, is well absorbed by copper [9]. Wang et al., used a blue diode laser of 250 W for material processing for successful laser irradiation on a steel sample [10]. Suwa et al., developed a blue laser for processing copper foils and melting copper powder, with a power of 100 W and a core diameter of 100 μm. The blue laser is called BLUE IMPACT, and they stated this new laser technology can improve the manufacturing quality of copper for electronic and automotive applications [11]. Another blue laser that was recently developed was reported by Konning et al., at Coherent DILAS. The authors reported two types of modules, both with a wavelength of 450 nm—one module with 500 W power and a 200 μm core diameter, and the second with 550 W power with a 400 μm core fiber. The intention of this newly developed laser technology was for material processing [12]. The BDL technology at JWRI has been successfully used for cladding pure copper on a stainless steel (SS304) substrate [13,14]. Hummel et al. [15] conducted a feasibility study by conducting micro-welding of copper using a diode laser with a wavelength of 450 nm (no other detail was provided, but presumably a BDL) and 150 W of power. The thickness of the copper samples ranged from 150 μm to 1 mm. It was concluded that the butt and lap joints could be satisfactorily achieved up to a thickness of 500 μm with a speed of up to 10 mm/s. Xu et al. [16] compared the cladding characteristics of copper on martensitic stainless steels using TIG and diode laser methods. They found out the laser cladding had fine microstructures, a narrow heat-affected zone, and excellent wear resistance compared with the TIG method. Separately, Boese et al. [17] reviewed blue laser technology with added power and brightness, and suggested that this technology allowed for welding copper samples and that it also improved the ability to weld dissimilar metals, for example, copper to stainless steels or copper to aluminum alloys.

In this paper, the results from the recent investigation on the welding of CP Ti foils using the BDL welding method are presented. The purpose of this work was to establish if BDL could be applied to the welding of thinner metallic foils and higher welding speeds. At this stage, the focus of the work was on relatively less-bright metals such as titanium to identify the possible parameters for the subsequent welding of the thin copper or gold foils. The microstructure and the strength of the welds were examined. In addition to the hardness and tensile testing results, a digital image correlation (DIC)—a post-processing feature following the tensile testing—was also conducted to gain a better understanding of the weld response to tensile stresses. The fracture surfaces from the tensile testing were also examined with the scanning electron microscope (SEM) and are reported in this paper.

2. Experimental Procedures

2.1. Materials

The material used in this investigation was commercially pure titanium (CP Ti) Grade 2 foil with a thickness of 100 μm and 200 μm. The nominal composition of the material is given in Table 1.

Table 1. Chemical composition of commercially pure titanium (CP Ti) in wt.%.

Material	Ti	Fe	H	N	O	C
CP Ti	Balance	<0.3	<0.015	<0.03	<0.25	<0.1

2.2. Welding Procedures

Bead-on-plate using a blue diode laser welding technique was performed at the Joining and Welding Research Institute (JWRI), Osaka University, Japan. Prior to welding, the foils were cleaned thoroughly with ethanol to ensure they were free from dirt, grease, and other surface contaminations. The system employed up to six diode laser modules with a single module power of around 20 W. The focal spot of the laser light had a top-hat profile of 100 μm diameter. The welding was performed without any filler metal (autogenous) with the following parameters: 50 and 100 W of power and a welding speed of 20 and 30 mm/s for the 100 μm and 200 μm thick foils, respectively, and a wavelength of 450 nm. Note that the speed used in this investigation was 2–3 times higher than what was reported previously [9]. Pure argon gas (purity of up to 99.9%) was used as shielding with a flow of 25 L/min. The welding heat input was estimated to be between 1 and 5 J/mm.

The schematic diagram of the BDL welding used in this investigation is given in Figure 1. More details about the BDL system at JWRI have been provided by Sato et al. [13] and Asano et al. [14].

2.3. Metallography

For the microstructural and microhardness examinations, metallographic samples were prepared from the welded specimens. The samples were cut in the normal to the welding direction. They were mounted in a conductive bakelite resin. The mounted samples were ground using SiC paper up to 2400 grit size and were polished down to 0.05 μm using colloidal silica on polishing cloths. The polished samples were etched with

Kroll's reagent (100 mL H_2O + 2 mL HF + 5 mL HNO_3) and were examined using an Olympus BX51M optical microscope to characterize the microstructures.

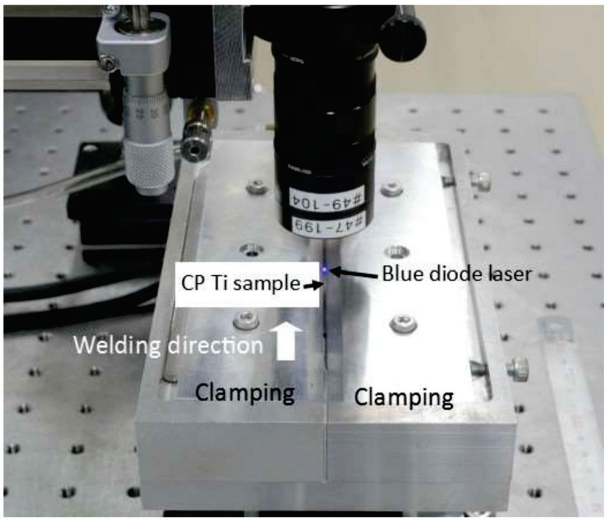

Figure 1. Blue diode laser (BDL) welding set up.

2.4. Mechanical Testing

2.4.1. Microhardness

To produce the hardness profiles, micro-hardness tests were conducted on the polished and etched samples using a Vickers machine (Leco AMH 55, St. Joseph, MI, USA) with a load of 50 g and a dwell time of 10 s. Indentations were made on the base metal (BM), heat-affected zone (HAZ), and the fusion zone (FZ). The results were then plotted to determine the hardness profiles.

2.4.2. Tensile Testing

Tensile testing was conducted on dog bone-shaped samples using the Shimadzu Universal Testing Machine model AG-IS (Shimadzu, Kyoto, Japan) with a crosshead speed of 0.07 mm/s. Three samples were tested for each welding condition. The dimensions of the samples are shown in Figure 2. The tensile testing machine used was equipped with a digital image correlation (DIC) system with a couple of 5.0 Megapixel CCD cameras. This non-contact technique was employed to measure the overall strain, its distribution, and the local strain gradients at the fracture locations. The post-processing of the DIC was performed and analyzed using the VIC-3D system (Correlated Solutions, Irmo, SC 29063, USA).

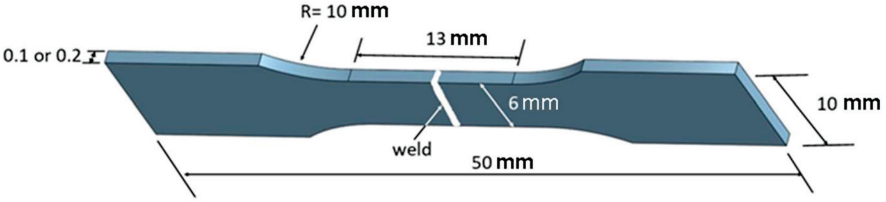

Figure 2. Schematic diagram of the dog-bone sample with dimensions (in mm).

2.4.3. Fracture Surface Examination

A scanning electron microscope (SEM), Hitachi SU70 (Hitachi High-Technologies Corporation, Minato-ku, Tokyo, Japan), was employed to study the fracture surfaces following tensile testing. The samples were prepared using ultrasonic cleaning for 10 min using ethanol prior to the SEM examinations.

3. Results and Discussions

The general appearance of the CP Ti foils with weldments are shown in Figure 3.

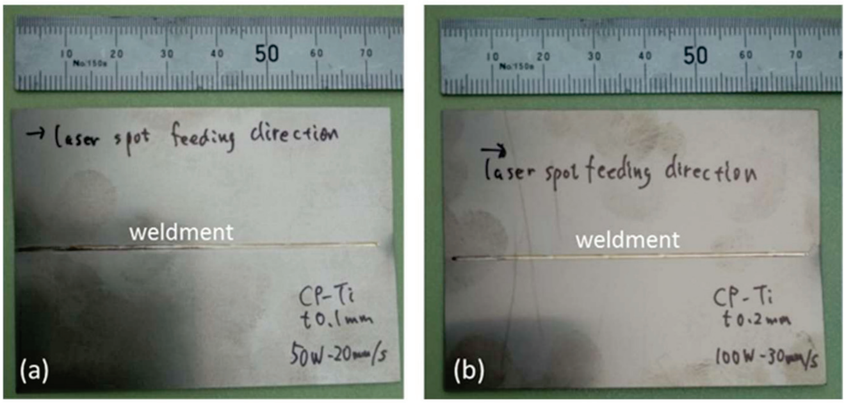

Figure 3. Welded CP Ti foils: (**a**) 100 µm thick and (**b**) 200 µm thick.

A full penetration bead-on-plate was achieved for both foils (Figures 3 and 4) with the parameters indicated in Section 2.2. The weldments showed a V-shaped configuration for the FZ and HAZ zones (Figure 4). The width of the weldments was up to 450 µm and 200 µm on the face and the root surfaces for the 100 µm thick foil, and up to 700 µm and 250 µm for the 200 µm thick foil for the face and root surfaces, respectively. It is also worth mentioning that there was very little distortion during metallography handling of the weldments. The slight bend of the 0.1 mm sample (Figure 4a) might be due to the handling of the sample after welding or during the metallography sample preparation.

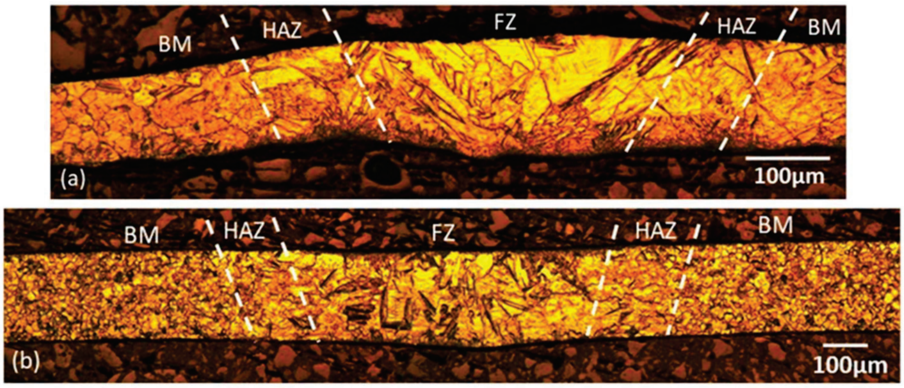

Figure 4. Optical micrographs showing weld profiles: (**a**) 100 µm thick welded with 50 W of power and at a speed of 20 mm/s, and (**b**) 200 µm thick welded with 100 W of power and at a speed of 30 mm/s.

The microstructure of the base metal showed an annealed structure with equiaxed grains (Figure 4). They were approximately between 5 and 10 µm in diameter. In the FZ area, the grains were fairly large, i.e., up to 20 µm in width and 100 µm in length. The grain size in the HAZ was smaller than for the grains in the FZ, but larger than in the BM area. A few cases of twin grains were also observed within the base metal and the weld zones. It was also noted that the weld zones, particularly in FZ (Figure 5), contained the α' structure (martensite), which is the main strengthening element in titanium alloys, including the high-grade CP Ti used in this investigation [18–25]. In addition, lamellar α phases were also present in the weld zone, especially in the FZ area [18,23,24]. More detailed information regarding the microstructures of CP Ti welds can be found in Danielson et al. [18] and Lathabai et al. [22].

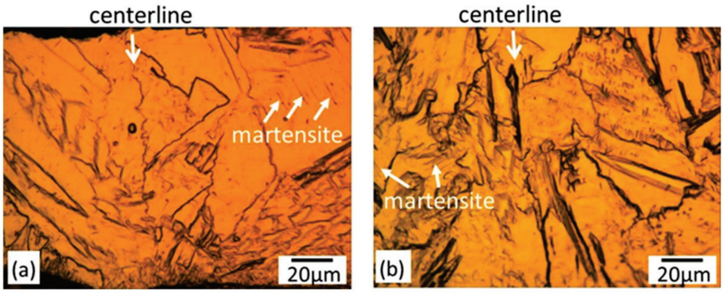

Figure 5. High magnification optical micrographs showing the weld centerlines and martensite (α′) phase on the (**a**) 100 µm thick foil welded with 50 W of power and at a speed 20 mm/s, and the (**b**) 200 µm thick foil welded with 100 W of power and at a speed of 30 mm/s.

The results from the microhardness testing showed that HAZ and FZ had higher hardness compared with the base metal (Figures 6 and 7). This probably is due to the presence of α′ (martensite) in WZ. The presence of α′ is associated with a fast cooling rate because both samples were fairly thin. Danielson et at. reported an increase in the weld zone area due to a high oxygen content [18]. In addition, the hardness of the 100 µm thick foil on the HAZ area increased earlier than that of the 200 µm thick foil due to its thinner size; hence, it had arguably faster cooling rates and more martensite (α′) compared with the later foil.

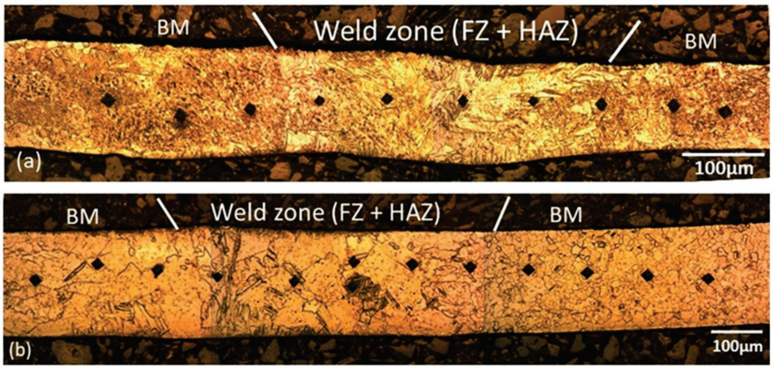

Figure 6. Hardness indentations on metallographically prepared samples: (**a**) 100 µm and (**b**) 200 µm thick foil samples.

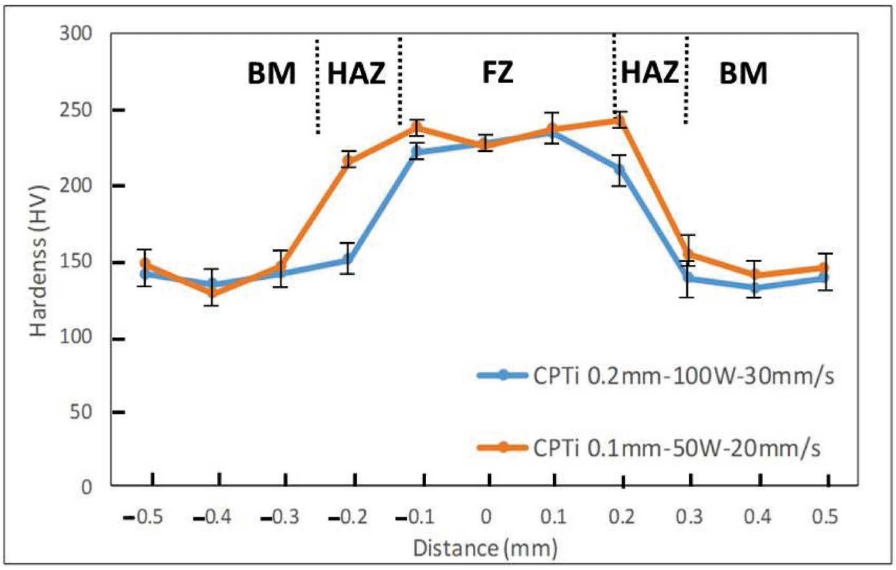

Figure 7. Hardness profiles of the welded samples for two different foils.

The tensile testing results are presented in Table 2. The results from the DIC analysis are presented in Figures 8–11.

Table 2. Tensile data of both the welded (BOP) and unwelded samples.

Material	Thickness (µm)	Power (Watt)	Welding Speed (mm/s)	Yield Strength (MPa)	Tensile Strength (MPa)	Elongation (%)	Fracture Location
CP Ti (BOP)	100	50	20	140	300	20	BM
				145	306	20	BM
				148	305	22	BM
CP Ti (BOP)	200	100	30	310	355	23	BM
				300	350	25	BM
				301	350	25	BM
CP Ti unwelded	100	N/A	N/A	170	325	24	N/A
	200	N/A	N/A	320	390	28	N/A

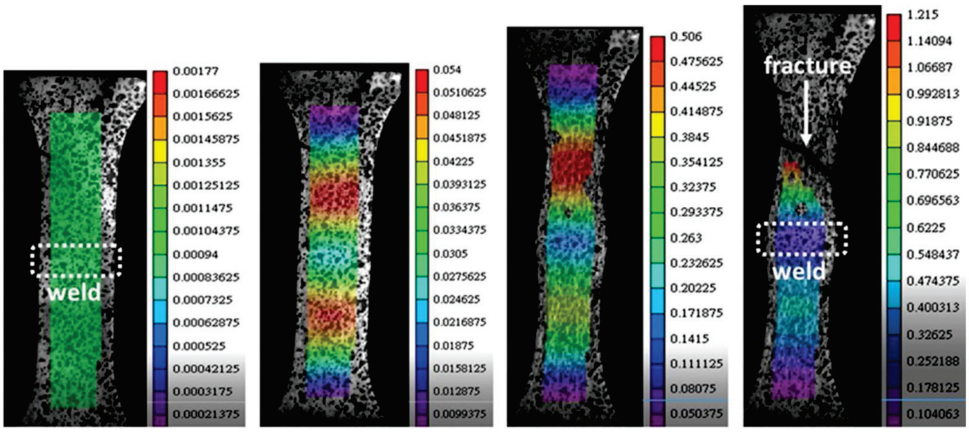

(a) 0% (b) 5% (c) 15% (d) 22%

Figure 8. Pictures from digital image correlation (DIC) of CP Ti, 100 µm, 50 W, and 20 mm/s during tensile testing showing sample conditions at various percentages of strain (**a**) at 0%, (**b**) 5%, (**c**) 15%, and (**d**) 22%, which correspond to fracture. Note: the numbers associated with the images are local strains × 100%.

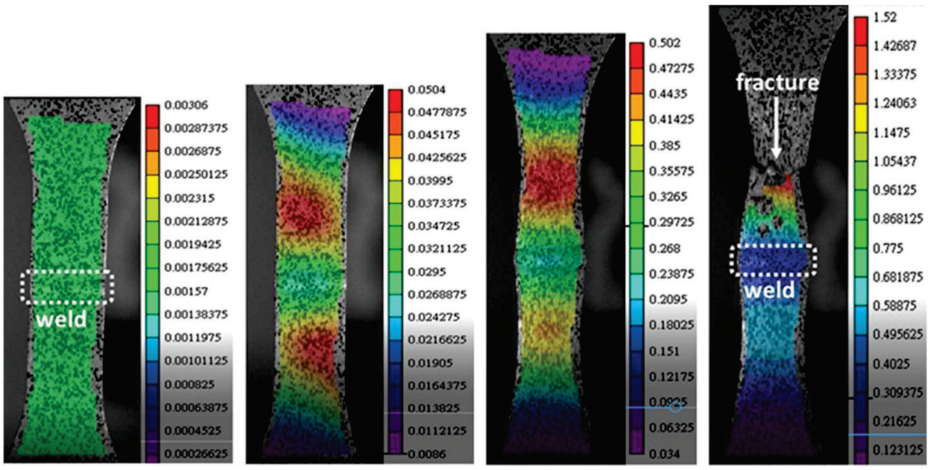

(a) 0% (b) 5% (c) 15% (d) 25%

Figure 9. Images from the digital image correlation (DIC) of CP Ti, 200 µm, 100 W, and 30 mm/s during tensile testing showing sample conditions at various percentages of strain (**a**) at 0%, (**b**) 5%, (**c**) 15%, and (**d**) 25%, which correspond to fracture. Note: the numbers associated with the images are local strains × 100%.

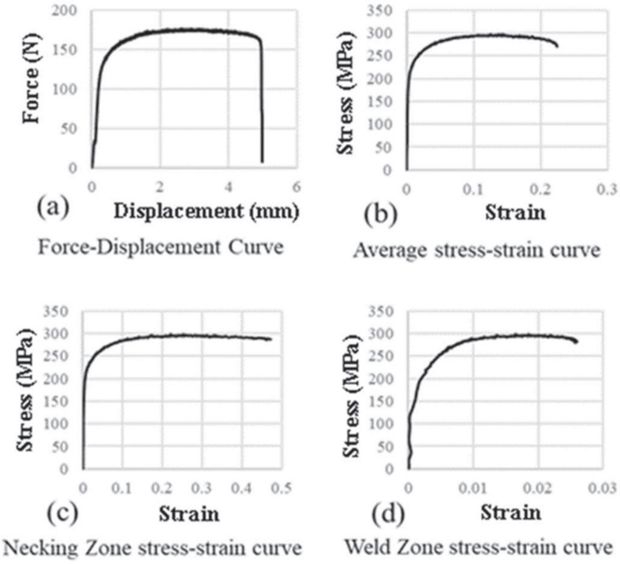

Figure 10. Diagrams showing (**a**) force−displacement curves and (**b**–**d**) stress−strain curves representing various stages/places during tensile testing on the 100 μm thick foil, with 50 W of power and at a speed of 20 mm/s.

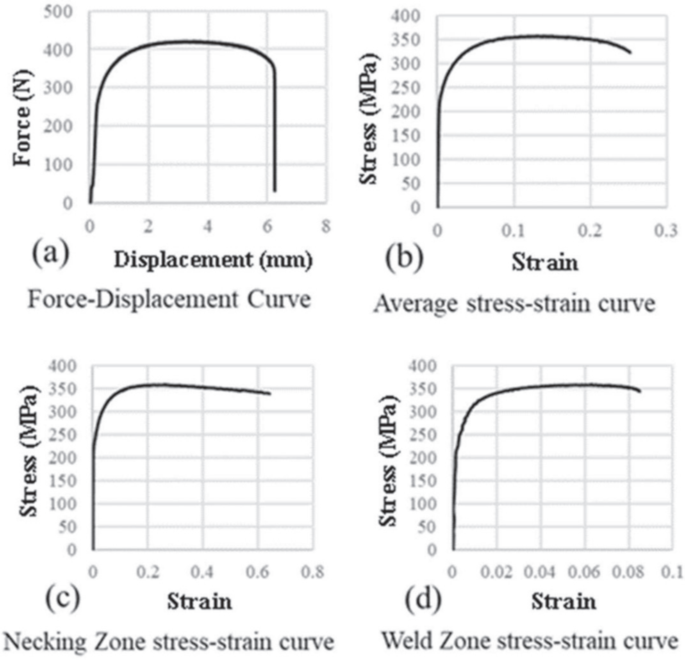

Figure 11. Diagrams showing (**a**) force−displacement curves and (**b**–**d**) stress−strain curves representing various stages/places during tensile testing on the 200 μm thick foil, with 100 W of power and at a speed of 30 mm/s.

Figures 8 and 9 show the strains within the samples at various location along the gauge length for the 100 μm and 200 μm thick foils, respectively. At an early stage, e.g., roughly less than 5% strain (Figures 8b and 9b), it is obvious that localized strains (necking) started to take place on each side (outside) of the weld zone, as indicated by the red color. Necking continued within these areas until the strains reached around 15 to 17% before a localized necking at a “single” location prior to fracture (Figures 8d and 9d). Figures 8d and 9d present the strain experienced by the samples upon fracture, i.e., around 22% and 25% for the 100 μm and 200 μm thick samples, respectively. The reason for the slightly higher percentage of strain (i.e., higher elongation) on the 200 μm thick samples could be due to their thicker sizes, which may delay the localized strain taking place. All of the tested samples fractured outside the weldments, which indicated a good weld quality and strong joints (also shown and confirmed by the high hardness in the weld zones).

Following the tensile testing, the DIC results were post-processed, and various relationships were derived including force vs. displacement, stress vs. strain, stress vs. strain at the necking zone, and stress vs. strain at the weld zone (Figures 10 and 11). These diagrams provide detailed information about the loads, displacements, stresses, and strains across the gauge lengths, weld zones, and fracture locations. The maximum forces recorded during the tensile testing were around 180 N for the 100 μm thick foil and around 420 N for the 200 μm thick foil. The displacements of the samples were found to be around 5 mm and 6.2 mm for the 100 μm and 200 μm thick foils, respectively. The unwelded foil samples had higher strengths (UTS) and elongations than the welded samples, which was, arguably, due to the uniform stress and strain distribution along the entire sample's gauge length. Additionally, the unwelded foil samples presented uniform strength distribution within the entire gauge, resulting in one localized deformation site (necking). For the welded samples, the presence of weldment (shown by the fine weld line) in the middle of the gauge length limited the stress and strain distribution to a much more limited volume in the test sample. In other words, the much smaller actual gauge size is found on each side of the weldment. Hence, relatively the early fracture resulted in slightly lower strengths and elongations compared with the unwelded samples. More detailed information about the strengths (both the yield and ultimate tensile strengths) can be seen in Table 2.

The strains deduced from the DIC system are presented in Figures 10b–d and 11b–d. The average strains (measured on the whole gauge length) showed 0.22 (22%) and 0.25 (25%) for the 100 μm and 200 μm thick samples, respectively. Within the necking zone, the 100 μm thick samples experienced a 0.46 (46%) strain compared with the 0.61 (61%) strain on the 200 μm thick samples. The DIC may also provide strains specifically in the weld zone area. The strain within the 100 μm thick samples was around 0.026 (2.6%), while the 200 μm thick sample had a strain of around 0.085 (8.5%). The weld zones area clearly did not experience significant strains compared with the other areas of the samples, which indicates a good weld quality (weld defects, if any, were not detected) and strong joints.

As indicated in Table 2, fractures for all of the welded samples occurred at the base metal (BM) locations. The examination of the fracture surfaces using scanning electron microscopy (SEM) showed a relatively highly ductile behavior with the presence of dimples throughout the surfaces (Figure 12). No indication of weld defects, such as porosity, gas bubbles, or lack of penetration, was observed. The presence of dimples on the fracture surface indicated a micro-void coalescence mechanism present for both specimen thicknesses.

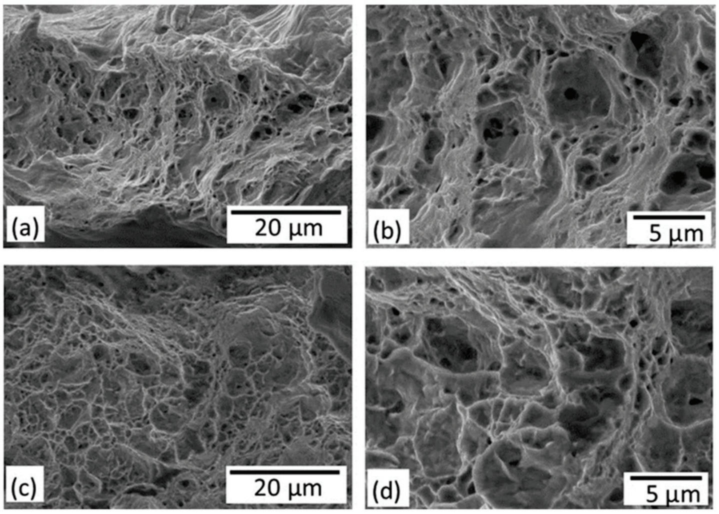

Figure 12. SEM micrographs showing fracture surfaces of (**a**,**b**) 100 μm, 50 W, and 20 mm/s, and (**c**,**d**) 200 μm, 100 W, and 30 mm/s.

4. Summary

Based on the performed investigation, the following can be concluded:

1. The blue diode laser (BDL) can be successfully used to perform welding on thin metallic foils such as CP Ti with thicknesses of 100 µm and 200 µm, and with a speed of up to 30 mm/s.
2. Although the samples were fairly thin, there was no distortion observed on the welded samples associated with the BDL process.
3. The weld zone (FZ and HAZ) displayed a high hardness (strengths) compared with the base metal (BM). This is due to the formation of α' (martensite) within the HAZ and FZ.
4. Based on the DIC results, the strains observed were concentrated within the BM where the fracture eventually took place. The samples fractured with a microvoid coalescence (ductile) mechanism where dimples can be observed throughout the fracture surfaces. This implies good weld quality and strong weld joints.

Author Contributions: Conceptualization, T.P.; methodology, experiments, writing—draft preparation, and editing, P.-C.L.; experiments and analysis, W.Z.M.; analysis and editing, J.-Y.W.; experiments and visualization, S.M.; experiments, M.T., supervision and funding acquisition, E.H.; experiments and investigation, Y.S.; investigation and supervision, Y.T.; experiments and analysis, D.Y., experiments and data curation, S.Y., experiments and data analysis. All authors have read and agreed to the published version of the manuscript.

Funding: This research was funded by JWRI, Osaka University, UNDER, JIJRec, 2019.

Acknowledgments: The work on the blue diode laser (BDL) has been promoted by the New Energy and Industrial Technology Development Organization (NEDO) project under "Development of advanced laser processing with intelligence based on high-brightness and high-efficiency laser technologies (2016–2020)" project. One of the authors (T.P.) would like to thank JWRI for its generous support under the JIJRec scheme in order to be able to carry out the experiments at JWRI, Osaka University. In addition, two co-authors (T.P. and W.Z.M.) would also like to thank the Lowey Institute at Lehigh for their continued support up until the completion of this manuscript.

Conflicts of Interest: The authors declare no conflict of interest.

References

1. Tojo, K.; Masuno, S.; Higashino, R.; Tsukamoto, M. Project Works towards Goal of Next-Generation Laser Processing System with High-Power Blue Diode Lasers. Available online: https://www.industrial-lasers.com/cutting/article/16485172/japan-develops-blue-laser-for-advanced-materials-processing (accessed on 1 September 2018).
2. Nakamura, S.; Pearton, S.; Fasol, G. *The Blue Laser Diode: The Complete Story*, 2nd ed.; Springer Science and Business Media: New York, NY, USA, 2000.
3. Das, A.; Fritz, R.; Finuf, M.; Masters, I. Blue laser welding of multi-layered AISI 316L stainless steel micro-foils. *Opt. Laser Technol.* **2020**, *132*, 106498. [CrossRef]
4. Ventrella, V.A.; Berretta, J.R.; de Rossi, W. Pulsed Nd: YAG laser seam welding of AISI 316L stainless steel thin foils. *J. Mater. Process. Technol.* **2010**, *210*, 1838–1843. [CrossRef]
5. Abe, N.; Funada, Y.; Imanaka, T.; Tsukamoto, M. Micro welding of thin stainless steel foil with a direct diode laser. *Trans. JWRI* **2005**, *34*, 19–23.
6. Kim, J.; Kim, S.; Kim, K.; Jung, W.; Youn, D.; Lee, J.; Ki, H. Effect of beam size in laser welding of ultra-thin stainless steel foils. *J. Mater. Process. Technol.* **2016**, *233*, 125–134. [CrossRef]
7. Pakmanesh, M.R.; Shamanian, M. Optimization of pulsed laser welding process parameters in order to attain minimum underfill and undercut defects in thin 316L stainless steel foils. *Opt. Laser Technol.* **2018**, *99*, 30–38. [CrossRef]
8. Zediker, M.; Fritz, R.; Finuf, M.; Pelaprat, J. Laser welding components for electric vehicles with a high-power blue laser system. *J. Laser Appl.* **2020**, *32*, 022038. [CrossRef]
9. Zediker, M.S.; Fritz, R.D.; Finuf, M.J.; Pelaprat, J.M. Stable keyhole welding of 1 mm thick copper with a 600 W blue laser system. *J. Laser Appl.* **2019**, *31*, 022404. [CrossRef]
10. Wang, H.; Kawahito, Y.; Yoshida, R.; Nakashima, Y.; Shiokawa, K. Development of a high-power blue laser (445 nm) for material processing. *Opt. Lett.* **2017**, *42*, 2251–2254. [CrossRef] [PubMed]

11. Suwa, M.; Wakabayashi, N.; Hiroki, T.; Tojo, K.; Masuno, S.-I.; Higashino, R.; Tsukamoto, M. Development of BLUE IMPACT, a 450nm-wavelength light source for laser processing. In Proceedings of the High-Power Diode Laser Technology XVII, Proc. SPIE 10900, San Francisco, CA, USA, 3–5 February 2019. [CrossRef]
12. Könning, T.; Drovs, S.; Stoiber, M.; König, P.; Kissel, H.; Harth, F.; Köhler, B.; Biesenbach, J.; König, H.; Lell, A.; et al. High brightness fiber coupled diode lasers at 450 nm. In Proceedings of the High-Power Diode Laser Technology XVII, Proc. SPIE 10900, San Francisco, CA, USA, 3–5 February 2019. [CrossRef]
13. Sato, Y.; Tsukamoto, M.; Shobu, T.; Funada, Y.; Yamashita, Y.; Hara, T.; Sengoku, M.; Sakon, Y.; Ohkubo, T.; Yoshida, M.; et al. In situ X-ray observations of pure-copper layer formation with blue direct diode lasers. *Appl. Surf. Sci.* **2019**, *480*, 861–867. [CrossRef]
14. Asano, K.; Tsukamoto, M.; Sechi, Y.; Sato, Y.; Masuno, S.-I.; Higashino, R.; Hara, T.; Sengoku, M.; Yoshida, M. Laser metal deposition of pure copper on stainless steel with blue and IR diode lasers. *Opt. Laser Technol.* **2018**, *107*, 291–296. [CrossRef]
15. Hummel, M.; Schöler, C.; Häusler, A.; Gillner, A.; Poprawe, R. New approaches on laser micro welding of copper by using a laser beam source with a wavelength of 450 nm. *J. Adv. Join. Process.* **2020**, *1*, 100012. [CrossRef]
16. Xu, G.; Kutsuna, M.; Liu, Z.; Yamada, K. Comparison between diode laser and TIG cladding of Co-based alloys on the SUS403 stainless steel. *Surf. Coat. Technol.* **2006**, *201*, 1138–1144. [CrossRef]
17. Boese, E.; Finuf, M.; Zediker, M.; Pelaprat, J.M. Blue Lasers Add Power and Brightness. Available online: https://www.industrial-lasers.com/welding/article/14173138/blue-lasers-add-power-and-brightness (accessed on 20 May 2020).
18. Danielson, P.; Wilson, R.; Alman, D. Microstructure of Titanium Welds. *Adv. Mater. Process.* **2003**, *161*, 39–42.
19. Karpagaraj, A.; Shanmugam, N.S.; Sankaranarayanasamy, K. Some studies on mechanical properties and microstructural characterization of automated TIG welding of thin commercially pure titanium sheets. *Mater. Sci. Eng. A* **2015**, *640*, 180–189. [CrossRef]
20. Choi, B.H.; Choi, B.K. The effect of welding conditions according to mechanical properties of pure titanium. *J. Mater. Process. Technol.* **2008**, *201*, 526–530. [CrossRef]
21. Li, C.; Muneharua, K.; Takao, S.; Kouji, H. Fiber laser-GMA hybrid welding of commercially pure titanium. *Mater. Des.* **2009**, *30*, 109–114. [CrossRef]
22. Lathabai, S.; Jarvis, B.L.; Barton, K.J. Comparison of keyhole and conventional gas tungsten arc welds in commercially pure titanium. *Mater. Sci. Eng. A* **2001**, *299*, 81–93. [CrossRef]
23. Liu, H.; Nakata, K.; Zhang, J.X.; Yamamoto, N.; Liao, J. Microstructural evolution of fusion zone in laser beam welds of pure titanium. *Mater. Charact.* **2012**, *65*, 1–7. [CrossRef]
24. Pasang, T.; Tao, Y.; Azizi, M.; Kamiya, O.; Mizutani, M.; Misiolek, W.Z. Welding of Titanium alloys. *MATEC Web Conf.* **2017**, *123*, 1–6. [CrossRef]
25. Lütjering, G.; Williams, J.C. *Titanium*; Springer: Berlin, Germany, 2007.

quantum beam science

MDPI

Article

Laser Cleaning as Novel Approach to Preservation of Historical Books and Documents on a Paper Basis

Vadim Parfenov [1,*], Alexander Galushkin [2], Tatiana Tkachenko [2] and Vladimir Aseev [3]

[1] Department of Photonics, St. Petersburg Electrotechnical University, 197376 St. Petersburg, Russia
[2] St. Petersburg Branch of the Archive of the Russian Academy of Sciences, 199034 St. Petersburg, Russia; lkrd@rambler.ru (A.G.); restlaser@gmail.com (T.T.)
[3] Faculty of Photonics, National Research University ITMO, 197101 St. Petersburg, Russia; aseev@oi.ifmo.ru
* Correspondence: vaparfenov@etu.ru

Abstract: The purpose of this work is the study of laser cleaning of historical paper. The effect of laser exposure of the paper reflectance, fracture resistance and acidity was investigated. The paper surface roughness before and after laser treatment was analyzed by optical and scanning electron microscopy. It was shown that use of multi-pulse micromachining in combination with high-speed scanning of laser beams provides high safety for paper cleaning. The optimal parameters of laser radiation for effective and safe cleaning are a power density of about 2 × 105 W/cm^2 at a wavelength of 1.06 μm, pulse repetition rate is 20 kHz; and a beam scanning speed of 200 mm/s–500 mm/s. The selective laser cleaning method for books and documents was proposed. Selective cleaning is achieved by means of high-precision control of the trajectory of movement of laser beams.

Keywords: laser cleaning; paper; books; documents; contaminants; cultural heritage; restoration

---

1. Introduction

The use of laser technology in the field of preservation of cultural heritage (CH) is a new but rapidly developing scientific and technical direction. Most often, lasers are used to determine the chemical composition, structural diagnostics, and documentation of works of art. These applications are based on the use of laser spectroscopy, interferometry, holography, and 3D scanning [1–3]. The restoration exploits laser cleaning technology, which allows solving the problems of removing natural layers and anthropogenic pollution from the surface of CH objects. However, despite the fact that lasers were first used in restoration almost 50 years ago, to date, only the technology of cleaning the stone has been developed. Laser restoration of other, primarily organic materials is still in the process of conducting exploratory research [3–19]. This is due to the fact that in the process of laser treatment, damage to their surface may occur, which is unacceptable according to the canons of restoration.

This article is devoted to the development of technology of cleaning of books and documents in the paper base. Cleaning paper sheets of dirt is a necessary and very time-consuming operation in the restoration of books and documents. Wax stains, soot and dust pollution, biological lesions, the so-called "fly ash", etc., are subject to removal. However, traditional methods of restoration cleaning do not always give satisfactory results. Thus, mechanical cleaning (based on the use of an eraser, rubber crumb or abrasive sandpaper with fine grain) violates the integrity of the surface structure of the paper, and reduces the thickness of the sheets, which ultimately negatively affects their mechanical strength. In addition, some of the removed dirt remains in the upper layer of the damaged paper surface in the form of dust. It should also be noted that there are often cases when the physical condition of books, especially the dilapidation of the lower corners of the book block sheets, in principle does not allow the use of mechanical cleaning. As an alternative to mechanical cleaning, water washing and chemical treatment with organic solvents and enzymes are sometimes used. Although such methods may be effective, they cannot be used to clean handwritten documents, as well as books with unstable printing ink.

For these reasons, the search for alternative methods of restoration of books and documents is currently relevant. One possible approach to solving this problem may be the use of laser cleaning. The first experimental works on the use of lasers for this purpose was carried out in the late 1990s [4,5], but is still being carried out by a few scientific groups in Europe [6–18]. These works show the possibility of using a laser for cleaning, but the method is not yet widely used. For this, it is necessary to develop appropriate technologies and specialized laser systems suitable for a wide range of contaminants.

Therefore, the purpose of this work is to develop a method for laser cleaning of documents and books with different types of paper.

2. Experimental

Model samples of paper that differed by chemical composition as well as fragments of historical documents and books of XVI-XIX centuries were used in experiments (Table 1).

Table 1. List of samples.

Label	Paper Composition	Dating
	Model samples	
B-2	100% sulphate cellulose	XX century
B-5	100% sulphate cellulose, kaolin filler, ash content–5.2%	XX century
B-6	100% Linen half-mass	XX century
B-19	100% sulphate cellulose, kaolin filler, ash content–4.6%	XX century
B-25	100% cotton half-mass, kaolin filler, ash content–9.3%	XX century
Pag paper	100% flax fiber, sizing-starch	XX century
	Historical paper	
Russian typographic book		beginning of the XIX century
Russian handwritten book		XVII century
Arabic manuscript		Late of 19th century
Arabic manuscript		Medieval

A pulsed ytterbium fiber laser generating at the wavelength of 1.06 μm was used for paper cleaning.

For all paper samples, reflection spectra were measured, whiteness of the paper, its acidity (pH) and fracture resistance were determined. Measurements were taken before and after laser cleaning. Reflection spectra were measured on a LAMBDA 900 spectrophotometer (manufactured by PerkinElmer LLC, Santa Clara, CA, USA) in the wavelength range of 300–2500 nm with a scanning step of 1 nm. The whiteness of the paper was measured on an FMSh-56 M ball photometer. An electron scanning microscope JSM-35 (JEOL Ltd., Tokyo, Japan) was used for surface study.

3. Results and Discussion

3.1. Choosing a Laser for Paper Cleaning

Laser cleaning of paper is based on the use of physical effects, which is called photoablation. Photoablation is the contaminant particles' ejection by photons as a result of their absorption by dirt material to be removed in the process of cleaning. The concept of the use of laser radiation for selective removal from the surface of an optically absorbing different substance, for instance, a secondary encrustation, was first demonstrated in 1965 by Arthur Schawlow, one of the laser inventors, who evaporated selectively absorbing black pigments of printing ink from a strongly reflecting white sheet of paper [20]. Later, in 1972 John Asmus first demonstrated the laser cleaning of Cultural Heritage objects [21]. Nowadays, basic physical principles of laser cleaning are well known and described in the scientific literature (see, for instance [2,22,23]).

The first step towards the development of laser technology for paper restoration is the choice of such laser radiation parameters that allow for high efficiency in cleaning books and documents. However, laser output parameters must be so they do not cause any negative consequences (including carbonization as well as changes in color, acidity, porosity and other physical and chemical properties of the paper). When choosing the type of laser and its output characteristics, it is necessary to keep in mind that paper is a very fragile, easily damaged material. It is a porous-capillary body in the form of a "carcass" formed by cellulose fibers connected to each other by chemical hydrogen bonds. Under the influence of heat, mechanical stresses and chemical reagents, the paper fibers are easy to damage.

It is known from the scientific literature that various types of lasers were used for paper cleaning, including excimer lasers (in particular, the XeCl laser with a radiation wavelength of 308 nm and the KrF laser with wavelength of 248 nm), as well as a solid-state Nd: YAG laser operating either at the main wavelength or at the wavelengths of the second, third and fourth harmonics (with wavelength of 1064 nm, 532 nm, 355 nm and 266 nm, respectively) [2,4–13]. In all cases, pulsed laser radiation was used. In particular, when working with a solid-state Nd:YAG laser, a Q-switched generation regime with a pulse duration of 10 ns–30 ns is usually used. As for the pulse repetition rate, it is usually in the range 1 Hz–100 Hz (maximum—1 kHz).

In order to choose the optimal laser wavelength for efficient and safe cleaning of books and documents, the spectral characteristics of the paper measured at the initial stage of our work. Measurements of the reflectance spectra give information on the spectral bandwidth where paper has maximum absorption. Since paper is a scattering medium, we used an integrating sphere. Results of these measurements are shown in Figure 1.

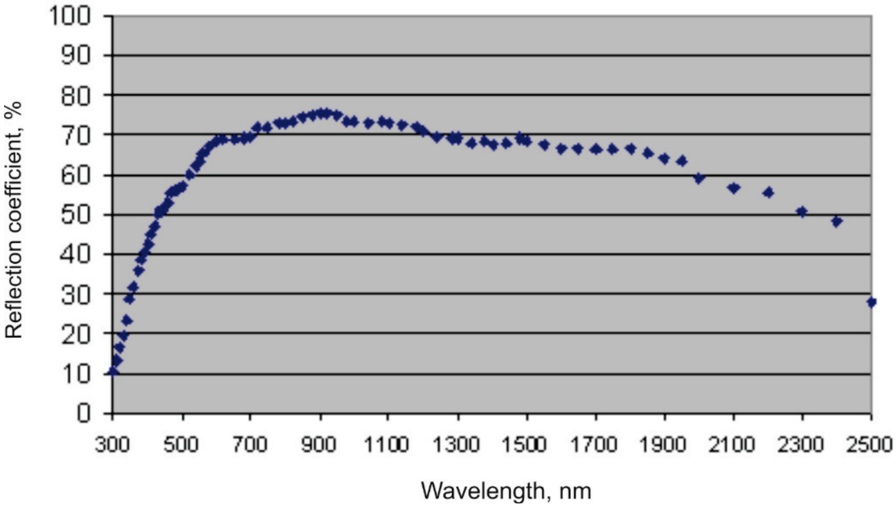

Figure 1. Reflection coefficient of paper versus laser radiation wavelength (for sheet of a Russian typographic book of the beginning of the XIX century made of wood pulp).

Then, we measured the reflectance of paper sheets of historical books and documents These measurements were conducted using a LAMBDA 900 spectrophotometer (manufacturer—PerkinElmer LLC, Santa Clara, CA, USA). A diaphragm with a diameter of 10 mm was used to select the measurement area. The area included typical paper contaminations: traces of silicate glue and rust, dust and dirt stains, grease stains, moisture traces, etc. Obtained spectra are presented in Figure 2.

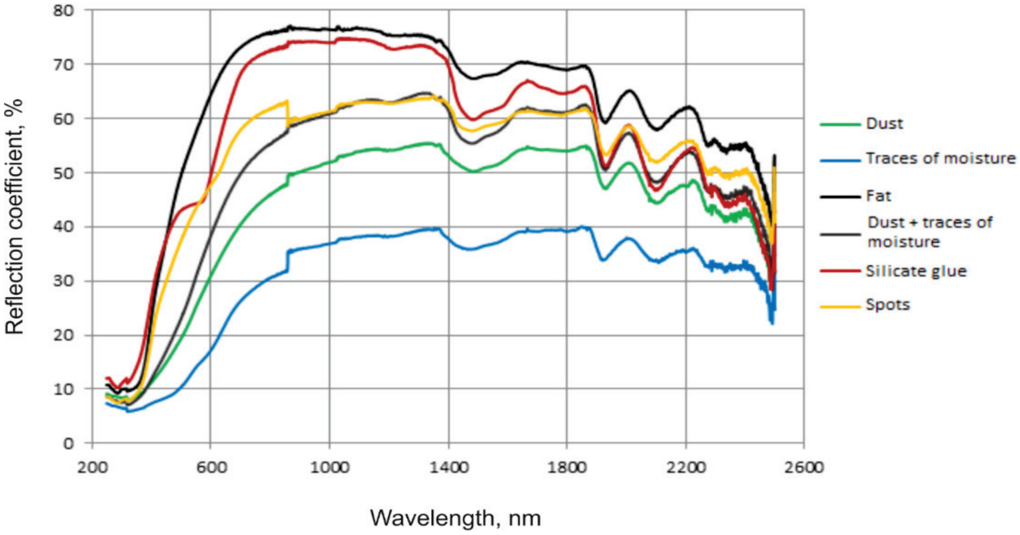

Figure 2. Reflection coefficient of paper with contaminants versus laser radiation wavelength.

From Figures 1 and 2, one can see that all the recorded spectra are identical to each other, and the differences are only in the absolute values of the reflection coefficient, which depend on the specific type of surface contamination. The most important finding is that the paper has the lowest reflectance values in the UV region of the spectrum. Consequently, the use of short-wave lasers for cleaning books and documents can be dangerous for their state of preservation due to the significant absorption of radiation energy by the paper. Indeed, the authors of some works (see, for example, [5]) reported damage to paper during its cleaning by an excimer laser with a radiation wavelength of 308 nm. From the graph in Figure 1 it is also clear that the maximum value of the reflection coefficient of the paper is in the range of 900 nm–1100 nm. Therefore, it is advisable to use lasers with a wavelength of radiation in this spectral region, and the best “candidates” for this role are solid-state neodymium lasers, as well as fiber ytterbium lasers with wavelength of about 1 micrometer. It is obvious that when using such lasers, the effect of their radiation on the surface of the paper cleaned of impurities will be insignificant, which ensures its safety during laser processing.

As for paper with contaminants on the surface from Figure 2, one can see that in the wavelength range of 900 nm–1100 nm, samples with dust contamination and under the lobes have lower reflection coefficients (about 35–60%) than samples with grease, silicate glue and stains of unknown origin (about 60–70%). In this case, the maximum value of the reflection coefficient (about 80%) has a sample with fat spots. It is clear that using lasers with a wavelength of about 1 micrometer with enough one can remove contaminants if the intensity of radiation will be enough high.

Another important parameter of laser radiation in the treatment of materials is the pulse repetition rate. Since at a fixed level of the average laser output power, an increase in the frequency leads to a decrease in the energy density of a single pulse, it is obvious that this allows for a higher “delicacy” of paper processing by reducing the thermal energy generated as a result of its absorption of laser radiation. It is for this reason that, unlike other scientific groups involved in study of laser paper cleaning, the authors of this work decided to check the possibility of using very high values of the repetition rate of laser pulses (at the level of tens of kilohertz). With all the above parameters, the effect of the laser on the paper becomes similar to the so-called multi-pulse laser micro-processing, which is widely used in industrial processing of materials. For the first time, the idea of using this approach in the restoration of paper was expressed by one of the authors of this article in 2007 [24].

However, it should be noted that to ensure maximum safety of paper processing, it is important not only to reduce the pulse energy density, but also to eliminate the cumulative effect of the thermal effect of laser radiation. Local temperature increase, which can occur during prolonged exposure to the same area of the surface, may cause negative effects—color change and even charring of the paper. To avoid this, it is necessary to ensure a very fast and uniform movement of the laser beam on the surface of the paper sheet. This problem can be solved by using high-speed laser beam scanning systems. For this purpose, you can use, for example, 2-coordinate scanners based on galvanometric mirrors, which are used in lasers for marking and engraving. In this case, each time the laser beam passes over the surface of the paper sheet, very thin layers of dirt will be removed. If the cleaning level is insufficient, the processing can be continued by re-scanning the entire sheet or its individual sections.

Based on the above considerations, in the experiments on paper cleaning, a pulsed solid–state fiber ytterbium laser was used. It has the following output characteristics: radiation wavelength—1.06 µm; maximum average power—10 W; pulse duration—10 ns; maximum pulse repetition rate—100 kHz.

3.2. Characterization of Paper before and after Laser Cleaning

The scheme of the experimental setup is shown in Figure 3a. The laser beam was focused onto the surface of paper and the sample was scanned (the spot diameter of focused laser beam was about 50 µm). The general view of the experimental setup in the process of laser cleaning of paper is shown in Figure 3b.

Laser processing parameters have been determined to ensure the safe and efficient removal of contaminants from the paper surface. Safe cleaning does mean the absence of such negative side effects as charring (carbonization), discoloration and roughness change of the paper surface. The maximum removal efficiency without paper damage was obtained at an average power of 4 W, while the pulse repetition rate was 20 kHz. Thus, the power density in the spot was about 2 × 105 W/cm^2. The beam scanning speed was varied in the range of 200 mm/s–500 mm/s, and the laser processing area was 4 × 6 cm^2.

At the first stage, there was a study of the effect of laser processing on the physical, mechanical and chemical properties of paper and its wear resistance. The following parameters of paper properties were determined: fracture strength, pH value of aqueous extraction and whiteness. In the field of book restoration, exactly these parameters characterize the safety of any restoration treatment. Accelerated thermal aging of the studied samples (105 °C, 72 h) was carried out to study the effect of laser processing on the durability of paper. To reduce the thermal effect of the laser on the paper, high-speed scanning in two mutually perpendicular directions was used. The paper samples were lasered on both sides of the sheet. The values of the index of resistance to destruction of paper samples of various compositions after laser processing of its surface (on both sides) are presented in Table 2.

The maximum effect of laser cleaning on the mechanical strength of paper was in samples B-2 (from 100% sulfate pulp) and B-6 (from 100% half-mass of flax). For these samples, the average value of the number of double kinks (ndk) decreased by 12–20%, and the decrease in fracture resistance occurs only in the longitudinal direction. For other types of paper (B-5, B-19, B-25 and Pag paper), the fracture resistance index does not decrease after laser processing.

A slight increase in the ndk in the transverse direction was also observed. The nature of fracture resistance in mutually perpendicular directions is different, in the longitudinal direction it is determined by the strength and elasticity of the fiber, and in the transverse direction it depends on the strength of the interfiber bonds. Heating to a temperature of 220 °C leads to dehydration, which reduces the elasticity of the paper and leads to a decrease in the tear resistance of the paper. This is proved by a small weight loss associated with the dehydration of cellulose fiber, which was observed during DSC analysis in [25]. At the same time, the removal of hygroscopic water should lead to strengthening of hydrogen bonds, which make the main contribution to the energy of interfiber bonds in paper. Laser exposure leads to heating of the paper and similar processes can be observed in this case.

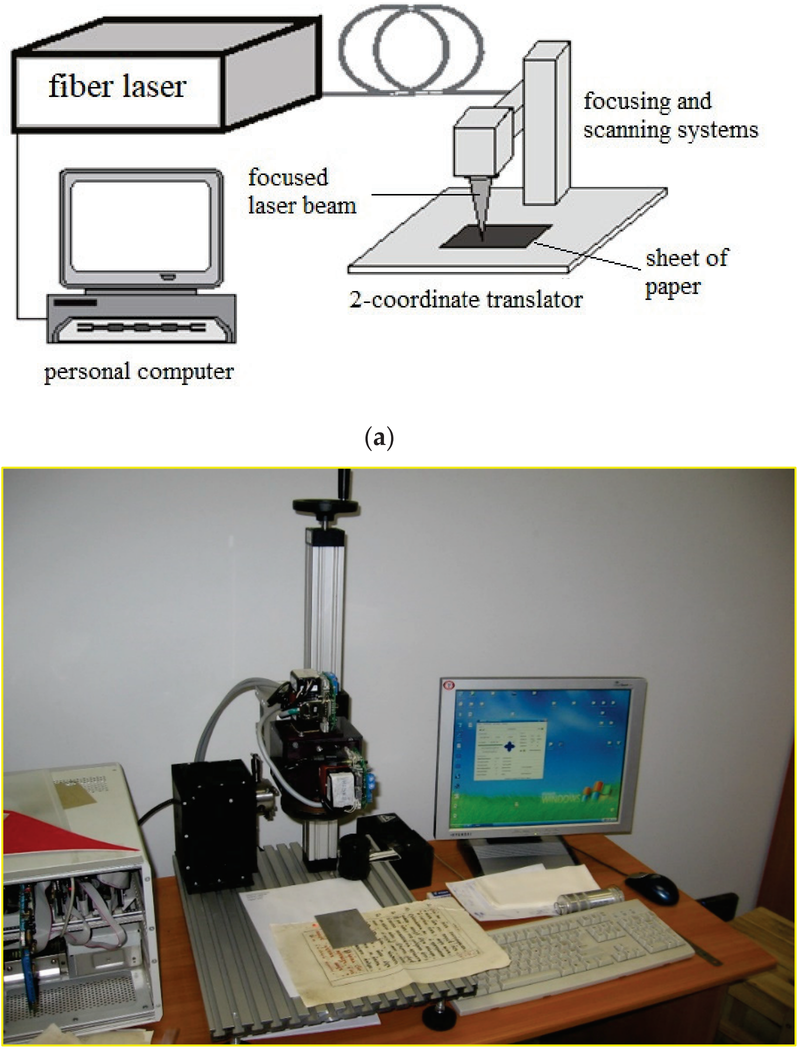

(**a**)

(**b**)

Figure 3. Experimental setup for laser treatment of paper: (**a**)—diagram of experimental setup; (**b**)—general view.

Table 2. The effect of laser processing on the physical and mechanical properties of paper (index-fracture resistance).

	Paper Composition	Fracture Resistance (Number of Permissible Double Kinks)					
		Control			After Laser Treatment		
		Longitudinal Direction	Transverse Direction	Average Value	Longitudinal Direction	Transverse Direction	Average Value
B-2	100% sulphate cellulose	208	160	184	150	174	162
B-5	100% sulphate cellulose, kaolin filler, ash content–5.2%	14	31	22	13	36	24

Table 2. *Cont.*

	Paper Composition	Fracture Resistance (Number of Permissible Double Kinks)					
		Control			After Laser Treatment		
		Longitudinal Direction	Transverse Direction	Average Value	Longitudinal Direction	Transverse Direction	Average Value
B-6	100% Linen half-mass	630	274	452	469	284	376
B-19	100% sulphate cellulose, kaolin filler, ash content-4.6%	134	92	113	170	97	134
B-25	100% cotton half-mass, kaolin filler, ash content-9.3%	10	7	8	10	8	9
Pag paper	100% flax fiber, sizing-starch	9	9	9	9	9	9

The whiteness and acidity index values of paper samples before and after laser treatment (Table 3) show that paper properties (related to whiteness and pH) do not change.

Table 3. The effect of laser treatment on the whiteness of the paper and the value of the acidity index (pH).

Cipher of Sample	Control		After laser Treatment	
	Whiteness,%	pH	Whiteness,%	pH
B-5	73.0	5.1	72.0	4.8
B-19	72.0	7.2	72.0	7.0
B-25	83.0	7.3	82.0	7.6
Rag paper	58.0	4.9	58.0	4.9

Analyzing the data of accelerated thermal aging of the samples, it can be concluded that laser processing did not affect the durability of the paper. Changes in fracture resistance, brightness, and pH values of the laser-treated and control samples were identical (see Table 4).

Table 4. Changes in the physical, mechanical, optical, and chemical properties of control paper samples and laser-treated paper samples after thermal aging (100 °C, 72 h).

Cipher of Sample	Thermal Aging									
	Control					After Laser Treatment				
	Fracture Resistance (n.p.k.)			White, %	pH	Fracture Resistance (n.p.k.)			White, %	pH
	Longitudinal Direction.	Transverse Direction	Average Value			Longitudinal Direction.	Transverse Direction	Average Value		
B-5	9	20	14	69.0	4.9	7	22	14	69.0	4.8
B-19	168	116	142	70.0	6.9	192	113	152	69.0	7.0
B-25	10	8	9	82.0	7.6	10	7	8	81.0	7.4
Rag paper	4	5	4	55.0	4.5	4	6	5	55.0	4.5

Visual inspection of the cleaning areas (using an optical stereomicroscope) showed that as a result of a single laser treatment, a significant part of the contamination is removed without disturbing the microrelief of the paper surface and its color characteristics. After completing a series of test tests on model images that demonstrated the safety of the selected laser and its output characteristics on the properties of paper, experiments were conducted on laser cleaning of original historical documents—a sheet of a handwritten book of the XVII century, as well as a page of a Russian typographic book of the early XIX century with typical types of contamination. As a result of laser treatment, the main surface contamination was removed in both cases. The condition of the paper before and after laser cleaning, as well as when working with model samples, was monitored using an optical microscope. Additionally, an scanning electronic microscope (SEM) JSM-35 was also used. Optical microscopic and SEM images shown in Figures 4–6 allow us to conclude that laser processing does not lead to a violation of the surface morphology and structure of the cellulose fibers of the paper. In addition, there are no changes in its color. It was confirmed by means of colorimetric measurements including the original measuring technique described in one of our recent publications [17].

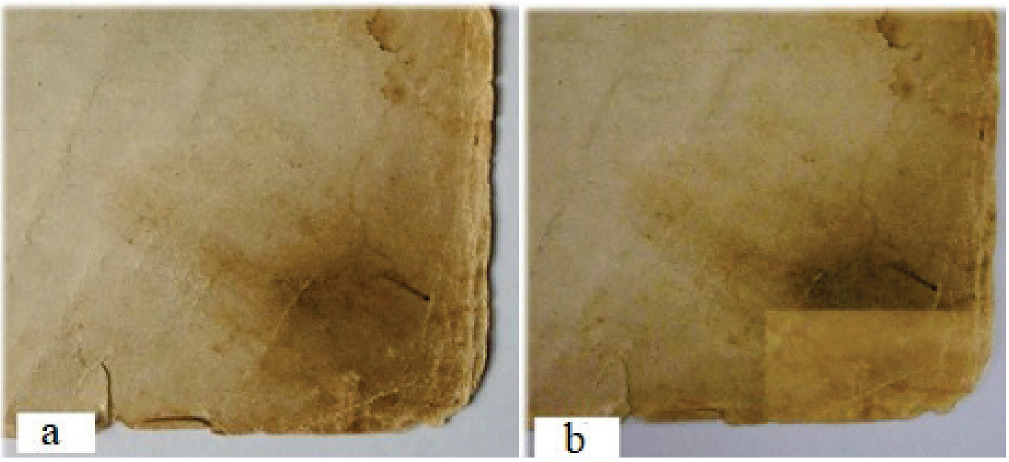

Figure 4. Flyleaf of a Russian typographic book (the beginning of the XIX century) with characteristic surface contamination: (**a**)—before laser cleaning; (**b**)—after laser treatment (light yellow rectangle in the lower right part of the sheet).

Figure 5. Page of a Russian handwritten book of the XVII century with characteristic surface contamination: (**a**)—the initial state; (**b**)—the lower right corner marked with a pencil—the experimental area for clearing with a laser; (**c**)—the same section of the page after laser processing.

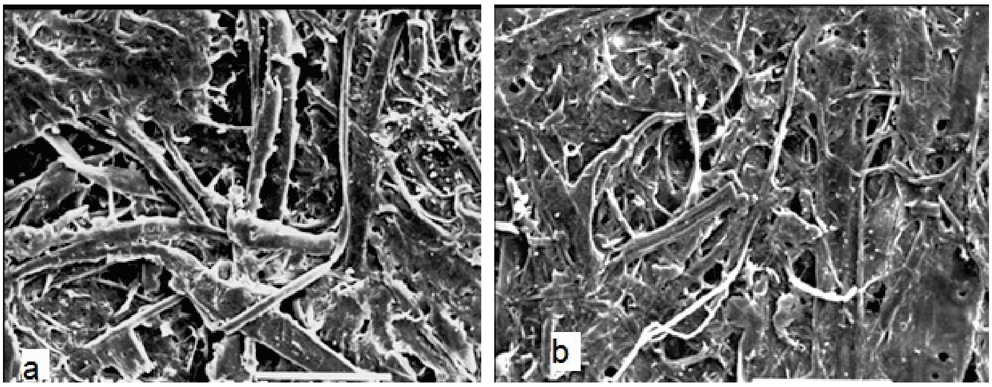

Figure 6. Images of the surface of a sheet of handwritten paper book obtained on an electronic scanning microscope: (**a**)—the initial state, (**b**)—after cleaning with a laser.

It should be noted that Fourier Transform Infrared spectroscopy makes it possible to control the chemical changes of paper after laser treatment at the molecular level, but in our work such measurements have not been conducted since from scientific literature it is known (see, for instance [11]) that with the right choice of laser exposure, such a negative side effect can be prevented.

Therefore, our experiments confirmed high efficiency and safety of laser cleaning of paper.

3.3. Selective Laser Cleaning

Consider the security of such processing for the entire page, which may include text and pictures. Since the absorption of carcasses and ink differs from the absorption of paper, it is necessary to study the effect of laser cleaning on such objects.

The preliminary experiments were carried out on a sheet of modern Russian strong paper "type 1000" on which typewritten text was printed in black ink. Laser cleaning removed the text from the paper, along with the dirt.

Then, a fragment of a sheet of a medieval Arabic handwritten book with text written in multi-colored ink (red and black) was cleaned. The text in red ink has not changed. Removal of surface dirt from the paper also led to partial removal of black ink (Figure 7).

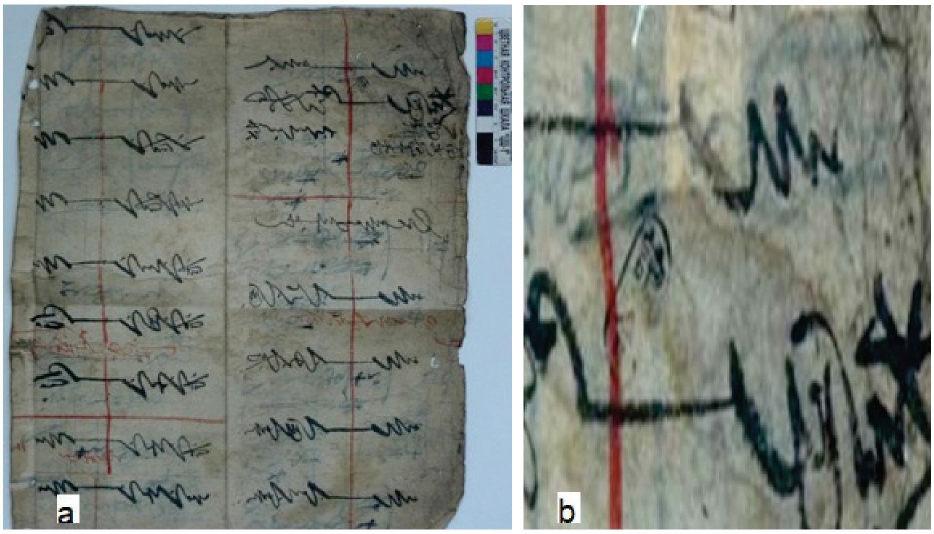

Figure 7. Images of a sheet of medieval Arabic manuscript: (**a**)—a general view, (**b**)—a fragment (a light rectangle in the middle at the top) cleaned by a laser.

From a later Arabic manuscript (19th century), both black and red ink were partially removed by laser treatment (see Figure 8). That is, if a pencil, iron gall and soot ink were used to write books, then special protection measures must be taken during their laser cleaning. Aniline ink does not require any special protection procedures.

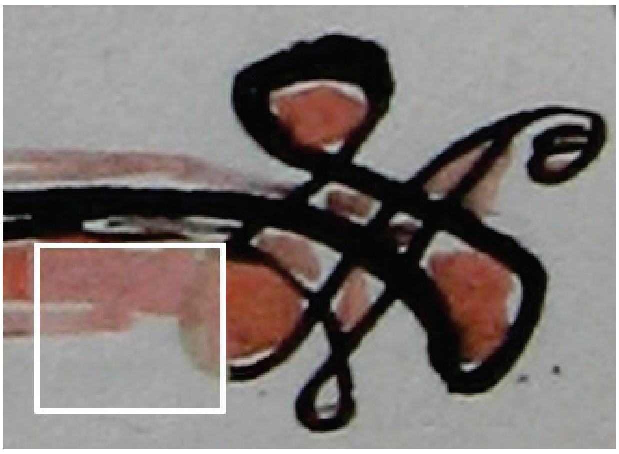

Figure 8. A fragment of an Arabic manuscript page after laser processing (the white square shows the area processed by the laser).

To ensure the safety of paper documents, it is necessary to exclude the effect of laser radiation on text and drawings applied by handwriting and printing. Thus, for the restoration of books and documents, it is necessary to use selective laser cleaning.

It should be noted that the idea of selective purification has already been described in [26]. Laser cleaning the BAM (Federal Institute for Materials Research and Testing, Berlin, Germany) prototype (designed by W. Kautek) was based on the use of a Nd:YAG laser (generating at 1064 nm or 532 nm) with a maximum repetition rate of up to 1 kHz and an energy density of ~10 J/cm^2. Increasing the repetition rate to 35 kHz while maintaining a power density of 10 J/cm^2 allowed us to reduce the energy of a single pulse, which is safer for paper heating.

The method of selective cleaning by zones was developed on model samples, which were sheets of modern office paper with laser-printed text. Coal dust was applied to the surface of the paper to simulate contamination. To remove from the processing area areas containing text, their inverted vector image (mask image) was sent to the scanning system operation control program. The mask image was created by cropping the original sheet image with text and converting it using CorelDRAW X7 (designed by Corel Inc., Ottawa, ON, Canada).

With laser cleaning, it is necessary to ensure a very precise alignment of the processed area of the paper sheet with the scanning field in order to avoid the risk of damaging text and graphic information. For this, a combination of special fiducial marks (previously applied to the processed area of paper) and the so-called overall frame was made. Reference marks are applied to the treated surface to align it with the working area of the laser.

During the experiments, an artificially polluted sheet of paper was treated with a focused laser beam. The results of laser processing of the model sample sheet are shown in Figure 9. As one can see from these photos (on the left—a sheet of paper in its original state, on the right—after laser cleaning), the contamination was successfully removed, but the typographic text remained unchanged. This confirms the effectiveness of the proposed technical solution.

At the final stage of the work, experiments were carried out on the selective cleaning of authentic historical documents. In particular, a page of an early 20th-century Arabic book was used for this purpose. A small area of the text sheet was selected for cleaning. After completing all the preparatory technological stages (it is described in details in [17]), it was necessary to accurately position the processing area selected on the book sheet relative to the laser working area. The processing area was a rectangle drawn in pencil (see Figure 10).

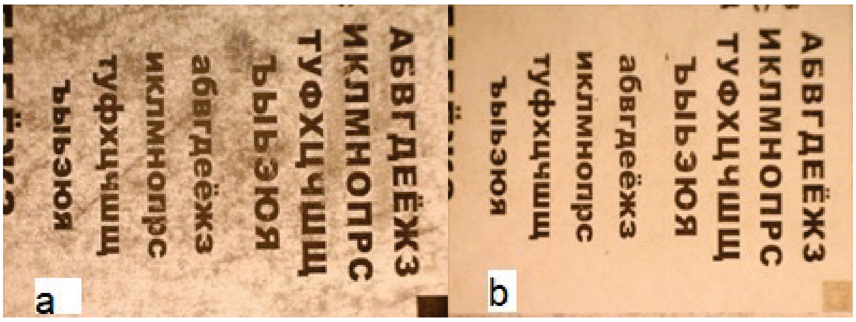

Figure 9. A model sample of paper with simulation of contaminants on the surface: (**a**)—before cleaning, (**b**)—after laser treatment.

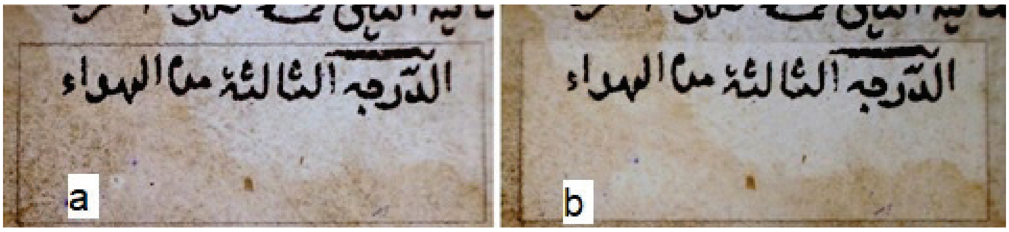

Figure 10. A fragment of antique Arabic manuscript: (**a**)—before cleaning, (**b**)—after laser treatment.

As can be seen from Figure 10, during the experiment it was possible to successfully perform selective cleaning—the book sheet was cleared of surface contamination, but the original text was saved in the laser processing zone.

The analysis of the cleaning was evaluated visually. Figure 11 shows a photo of a small fragment of a book sheet with typographic text before and after cleaning. It clearly shows that the integrity and readability of the letters of the typographic text is well preserved during the laser processing.

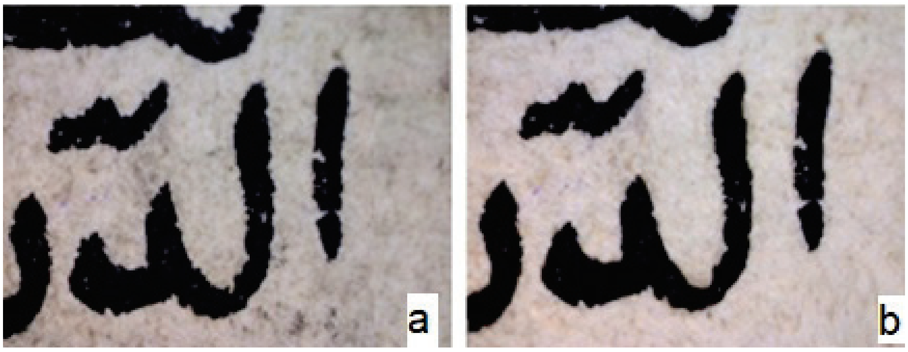

Figure 11. A small fragment of antique Arabic manuscript: (**a**)—before cleaning, (**b**)—after laser treatment.

4. Conclusions

Based on the experimental results obtained, the following main conclusions can be drawn:

1. Laser cleaning of paper using a pulsed IR laser with wavelength of about 1 μm provides high efficiency and safety of divestment of historical books and documents.
2. The use of multi-pulse micromachining in combination with high-speed scanning of laser beam provides high safety for paper cleaning. The optimal parameters of

laser cleaning of paper are: pulse duration—about 10 ns; average power—of about 4 W (power density of about 2 × 105 W/cm^2); pulse repetition rate—about 20 kHz; scanning speed—200 mm/s–500 mm/s.

3. To ensure the safety of books and documents during laser cleaning, it is necessary to exclude the impact of laser radiation on the text and drawings to avoid their damage. It can be achieved using a high-precision laser beam scanning system that allows you to display typographic text and graphic information from the laser processing area.

Author Contributions: Conceptualization, V.P.; methodology, V.P. and A.G.; validation, V.P., T.T., A.G., and V.A., investigation, V.P., T.T. and A.G.; resources, V.P. and V.A.; data curation, V.P. and A.G.; writing— V.P.; writing—review and editing, V.P., V.A. and A.G.; supervision, V.P.; project administration, V.P. All authors have read and agreed to the published version of the manuscript.

Funding: This research received no external funding.

Data Availability Statement: Not applicable.

Acknowledgments: The authors would like to acknowledge L.G. Levashova, S.V. Titov, A.N. Gerashchenko (present name—A.Adelberg) and A.A. Efimov, who took part in the experiments, for their contribution to the obtained results.

Conflicts of Interest: The authors declare no conflict of interest.

References

1. Fotakis, C.; Anglos, D.; Zafiropulos, V.; Georgiou, S.; Tornari, V. Lasers in the Preservation of Cultural Heritage. In *Principles and Applications*; CRC Press, Taylor & Francis Group: Boca Rayton, FL, USA, 2007.
2. Cooper, M. *Laser Cleaning in Conservation: An Introduction*; Butterworth-Heinemann: Oxford, UK, 1998.
3. Markov, V.B.; Mironyuk, G.I. Holography in museums of the Ukraine. In *Three-Dimensional Holography: Science, Culture, Education*; SPIE: Bellingham, WA, USA, 1991; Volume 123, pp. 340–347.
4. Friberg, T.R.; Zafiropulos, V.; Petrakis, Y.; Fotakis, C. Removal of fungi and stains from paper substrates using laser cleaning strategies. In *Lasers in the Conservation of Artworks (LACONA I)*; Restauratorenblatter (Special Isuue); Kautek, W., Konig, E., Eds.; Mayer & Comp: Vienna, Austria, 1997; pp. 79–82.
5. Kolar, J.; Strlic, M.; Pentzien, S.; Kautek, W. Near-UV, visible and IR pulsed laser light interaction with cellulose. *Appl. Phys. A* **2000**, *71*, 87–90. [CrossRef]
6. Kolar, J.; Strlic, M.; Müller-Hess, D.; Gruber, A.; Troschke, K.; Pentzien, S.; Kautek, W. Laser cleaning of paper using Nd:YAG laser running at 532 nm. *J. Cult. Herit.* **2003**, *4*, 185–187. [CrossRef]
7. Pilch, E.; Pentzien, S.; Madebach, H.; Kautek, W. Anti-Fungal Laser Treatment of Paper: A Model Study with a Laser Wavelength of 532 nm. Lasers in the Conservation of Artworks. *Springer Proc. Phys.* **2005**, *100*, 19–27. [CrossRef]
8. Kautek, W.; Pentzien, S. Laser Cleaning System for Automated Paper and Parchment Cleaning. *Springer Proc. Phys.* **2005**, *100*, 403–410.
9. Strlic, M.; Selih, V.; Kolar, J.; Kocar, D. Optimisation and on-line acoustic monitoring of laser cleaning of soiled paper. *Appl. Phys.* **2005**, *81*, 943–951. [CrossRef]
10. Bilmes, G.M.; Freisztav, C.M.; Cap, N. Laser cleaning of 19th century papers and manuscripts assisted by digital image processing. In *Lasers in the Conservation of Artworks*; Castillejo, M., Moreno, P., Oujja, M., Radvan, R., Ruiz, J., Eds.; Taylor & Francis Group: London, UK, 2008. [CrossRef]
11. Brandt, N.N.; Chikishev, A.Y.; Itoh, K.; Rebrikova, N.L. ATR-FTIR and FT Raman spectroscopy and laser cleaning of old paper samples with foxings. *Laser Phys.* **2009**, *19*, 483–492. [CrossRef]
12. Arif, S.; Kautek, W. Laser cleaning of paper: Cleaning efficiency and irradiation dose. *Stud. Conserv.* **2015**, *60*, S97–S105. [CrossRef]
13. Ciofini, D.; Osticioli, I.; Micheli, S.; Montalbano, L.; Siano, S. Laser Removal of Mold and Foxing Stains from Paper Artifacts: Preliminary Investigation. In *Fundamentals of Laser-Assisted Micro- and Nanotechnologies 2013*; SPIE Proceedings: Bellingham, WA, USA, 2013. [CrossRef]
14. Zekou, E.; Tsilikas, I.; Chatzitheodoridis, E.; Serafetinides, A. Laser paper cleaning: The method of cleaning historical books. In Proceedings of the 19th International Conference and School on Quantum Electronics: Laser Physics and Applications, Sozopol, Bulgaria, 5 January 2017; SPIE Proceedings: Bellingham, DC, USA, 2017; Volume 10226. [CrossRef]
15. Rosati, C.; Ciofini, D.; Osticioli, I.; Giorgi, R.; Tegli, S.; Siano, S. Laser removal of mold growth from paper. *Appl. Phys. A Mater. Sci. Process.* **2014**, *117*, 253–259. [CrossRef]
16. Balakhnina, I.A.; Brandt, N.N.; Chikishev, A.Y.; Shpachenko, I.G. Single-pulse two-threshold laser ablation of historical paper. *Laser Phys. Lett.* **2018**, *15*, 065605. [CrossRef]

17. Parfenov, V.A.; Titov, S.V. Technical and Technological Aspects of Laser Cleaning for Books and Documents. In Proceedings of the 2019 IEEE Conference of Russian Young Researchers in Electrical and Electronic Engineering (EIConRus), St. Petersburg, Russia, 28–30 January 2019; pp. 903–906. [CrossRef]
18. Atanassova, V.; Yankov, G.; Zahariev, P.; Grozeva, M. Laser treatment of contaminations on paper: A preliminary study. In Proceedings of the Conference "Applicazioni Laser nel Restauro (APLAR), Venezia, Italy, 7–8 November 2019; pp. 433–445.
19. Abdel-Maksouda, G.; Emamb, H.; Ragab, N.M. From Traditional to Laser Cleaning Techniques of Parchment Manuscripts: A ReviewAdvanced Research in Conservation Science. *Adv. Res. Conserv. Sci.* **2020**, *1*, 52–76.
20. Schawlow, A.L. Lasers. *Science* **1965**, *149*, 13–22. [CrossRef] [PubMed]
21. Lazzarini, L.; Asmus, J.; Marchesini, M.L. Laser for cleaning of statuary, initial results and potentialities. In Proceedings of the 1st Int. Symp. on the Deterioration of Building Stone, La Rochelle, France, 11–16 September 1972; pp. 89–94.
22. Luk'yanchuk, B.S. *Laser Cleaning*; World Scientific Publishing Company, Inc.: Singapore, 2002.
23. Kovalenko, V.S. Laser micro-and nanoprocessing. *Int. J. Nano.* **2006**, *1*, 173–180. [CrossRef]
24. Mokrushin Yu., M.; Parfenov, V.A. Use of copper-vapor laser for restoration of artworks. *J. Opt. Technol.* **2008**, *75*, 476–477. [CrossRef]
25. Vilesova, M.S.; Lazareva, C.Y.; Saprykina, N.P.; Tkachev, B.I.; Levashova, L.G.; Khalizova, E.M. Study of thermal transformations of paper. In Proceedings of the International Conference "Library of Academy of Sciences: Ten Years after Fire", St.Petersburg, Russia, 16–18 February 1997; pp. 135–139.
26. Kautek, W. Laser Cleaning of Paper and Other Organic Materials. Available online: http://www.science4heritage.org/COSTG7/booklet/chapters/org.htm (accessed on 27 June 2022).

quantum beam science

Article

Effect of Process Parameters on Laser Powder Bed Fusion of Al-Sn Miscibility Gap Alloy

Chiara Confalonieri *, Riccardo Casati and Elisabetta Gariboldi *

Department of Mechanical Engineering, Politecnico di Milano, Via La Masa 1, 20156 Milan, Italy; riccardo.casati@polimi.it
* Correspondence: chiara.confalonieri@polimi.it (C.C.); elisabetta.gariboldi@polimi.it (E.G.)

Abstract: Al-Sn binary system is a miscibility gap alloy consisting of an Al-rich phase and a Sn-rich phase. This system is traditionally applied in bearings and more recently found application as form-stable phase change material (PCM) exploiting solid-liquid phase transition of Sn. A careful choice of production process is required to avoid macro-segregation of the two phases, which have different densities and melting temperatures. In the present study, the additive manufacturing process known as laser powder bed fusion (LPBF) was applied to an Al-Sn alloy with 20% volume of Sn, as a rapid solidification process. The effect of process parameters on microstructure and hardness was evaluated. Moreover, feasibility and stability with thermal cycles of a lattice structure of the same alloy were experimentally investigated. An Al-Sn lattice structure could be used as container for a lower melting organic PCM (e.g., a paraffin or a fatty acid), providing high thermal diffusivity thanks to the metallic network and a "safety system" reducing thermal diffusivity if the system temperature overcomes Sn melting temperature. Even if focused on Al-Sn to be applied in thermal management systems, the study offers a contribution in view of the optimization of manufacturing processes locally involving high solidification rates and reheat cycles in other miscibility gap alloys (e.g., Fe-Cu) with similar thermal or structural applications.

Keywords: phase change materials; Al-Sn; miscibility gap alloys; selective laser melting; powder bed laser fusion

1. Introduction

Al-Sn binary systems are miscibility gap alloys (MGAs), i.e., they consist of two phases which are immiscible in solid state. In more detail, the two phases are almost pure Al and pure Sn. Thanks to their anti-wear performance, these alloys have been widely used in bearings [1]. More recently, they were studied as form-stable phase change materials (PCMs), specifically composite materials in which the Sn-rich active phase undergoing a solid/liquid transition is mixed to a high-melting Al-rich phase [2,3]. The latter can provide structural properties as well as modify thermal and other characteristics of the material. PCMs can be used in thermal energy applications since they can store the latent heat associated to an endothermic transition (e.g., melting) and release it when the transition is reversed (e.g., solidification). Furthermore, the material can be used to limit the maximum temperature of the system, at least within certain heat input limits.

Simple casting of molten MGAs results in both micro-segregation of the lower melting phase at grain boundaries of the high-melting one, and in macro-segregation of the low-melting phase in the last solidifying regions [4]. Contrarily, powder metallurgy and rapid solidification processes can result in a more homogeneous and finer phase distribution. Powder metallurgy has been applied either for Al-Sn based bearing materials by Zhu et al. [1,5–7] and for metallic Al-Sn based PCMs by Confalonieri et al. [3,8,9] and Sugo et al. [2]. With these kind of techniques, the homogeneous and fine phase distribution is provided through compaction and sintering of homogeneous powder blends, which are not, or only partially, melted, thus preventing macro-segregation of low-melting phase. On the other hand, rapid solidification methods involve complete melting of base material in form of powders or homogeneous ingots. The following solidification with high cooling rate entraps low-melting phase in the network created by primary nucleation of high-melting one. Several techniques are reported in literature to obtain fast solidification of Al-Sn based alloys, like laser alloying (Zhai et al. [4], Makhatha et al. [10]), high-velocity oxyfuel (Marrocco et al. [11]), and melt spinning (Lucchetta et al. [12], Kim and Cantor [13], Zhang W. et al. [14], and Zhang Z. et al. [15]). Confalonieri and Gariboldi [16] studied the possibility of using laser powder bed fusion (LPBF) as rapid solidification process in which a blend of Al and Sn powders is locally melted through a pulse laser. In laser-based powder bed systems, a powder layer is first applied on a building platform, then a laser melts it locally according to the input 3D model, and finally the platform is lowered; the cycle is repeated until the part is fully built, embedded in the powder bed [17]. Confalonieri and Gariboldi [16] observed that the extremely fine microstructure obtained for Al-Sn alloy with LPBF was similar to the finest microstructures obtained from compressed ball-milled powders [8,9]. This microstructure can provide high hardness and wear resistance [1], as well as interesting thermal properties. In more detail, a fine distribution of Al-Sn phases results in a relatively fast thermal storage followed by a more gradual heat release in a wide range of temperatures, thus reducing thermal stresses during cooling [3,9]. The advantage of using LPBF is, therefore, the possibility to couple a suitable microstructure for conventional Al-Sn based MGA applications in bearings or as PCMs, with the design freedom typical of an additive manufacturing technique compared to the limitations of powder metallurgy involving compression and sintering.

The present paper aims to study the effect of LPBF process parameters on the properties of Al-Sn alloy with Al/Sn ratio equal to 80/20, in view of its application in thermal storage and thermal management devices. Differently from typical LPBF applications, the classical target of reducing discontinuities like pores and cracks is flanked by the need to control phase distribution and to have a microstructurally stable material over several thermal cycles. Once the relationship between parameters and microstructure is established, the material designer can select the proper parameters according to the features required by the specific application. The results of this study can also be helpful to produce other MGAs through LPBF. For example, Fe-Cu based MGAs are investigated for their higher thermal conductivity with respect to steels and high strength [18,19], as well as for the possibility of using them as PCMs [2].

In addition to simple parallelepiped samples, a 3D lattice structure was produced to prove the feasibility to print a complex structure. The microstructure of the materials was investigated by electron microscopy. Material hardness was measured by Vickers tests. The thermal stability was evaluated by experimenting possible operating conditions for PCMs.

Lattice structures could be used as a container for a low-melting PCM [20,21]. This kind of hybrid system contains two PCM systems: a low-melting one, such as paraffin (melting temperature range: 6–108 °C [22]) or fatty acids (with melting temperature in a slightly narrow melting range), which stores latent heat in the temperature range of interest; and a high-melting one (e.g., Al-Sn), which enhances thermal diffusivity to the overall system thanks to the metallic network [23] and also can act as "safety system" by reducing thermal diffusivity upon its phase transition if the system temperature increases too much. The presence of the low-melting PCM, with high wettability on Al alloys could also avoid the formation of Sn particles at the material surface.

2. Materials and Methods

Commercially pure Al (ECKA Granules Germany GmbH, Fürth, Germany) and pure Sn (STAGNO 106, Metalpolveri S.r.l., Gussago (BS), Italy) powders were mixed to obtain a blend with 20% volume of Sn, corresponding to about 40% in mass. Both powders had high purity (>99.7% mass). Al powder had grain size lower than 45 μm, while Sn powder contained also coarser particles (>106 μm: 0.1%, >45 μm: 15–45%, <45 μm: 55–85%). SEM micrographs of powders are shown in Figure 1. Before the mixing processes, powders were sieved separately with a −63 µm mesh, to remove coarse particles and agglomerates. Then, they were blended in a tumbler mixer (Adler T-0) with about 1/3 of empty space in the jar, for 1 h at 20 rpm at room temperature.

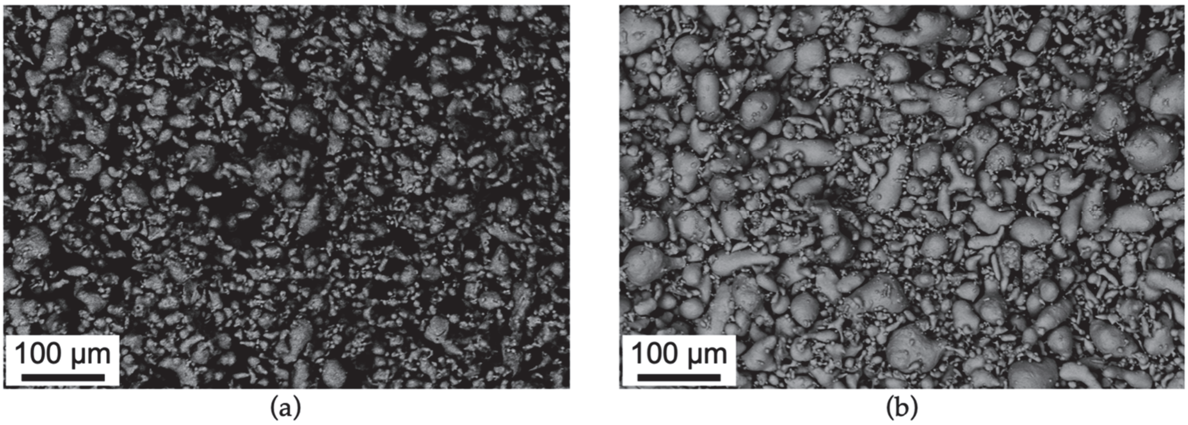

Figure 1. SEM micrographs of Al (**a**) and Sn (**b**) powders.

LPBF process was carried out using a pulsed laser Renishaw (Wotton-under-Edge, United Kingdom) AM 250 system equipped with a Reduced Build Volume apparatus (powder bed 90 mm × 90 mm). Using a pulsed laser, powders are melted by discrete and partially overlapped laser spots, which are exposed to the radiation for a given time (exposure time) [24]. The process was carried out in protective Ar atmosphere to reduce contamination from oxygen (oxygen content < 1000 ppm). A meander scanning strategy was applied and the scanning direction was rotated by 67° after each layer completion. The selected process parameters were in the range of typical values for Al alloys [24]. Layer thickness (25 µm), laser power (200 W), and exposure time (160 µs) were the same for all the samples. On the other hand, different values for hatch distances (d_h), i.e., the distance between the parallel adjacent scanned tracks, and point distance (d_p), i.e., distance between two neighbor points exposed to the pulsed laser, were selected, as reported in Table 1.

Table 1. Sample names and VED calculated accordingly to Equation (1).

		Point Distance, d_p [µm]			
		60	80	100	120
Hatch distance, d_h [µm]	60	A 356 J/mm^3	B 267 J/mm^3	C 213 J/mm^3	
	80	D 267 J/mm^3	E 200 J/mm^3	F 160 J/mm^3	
	100	G 213 J/mm^3	H 160 J/mm^3	I 128 J/mm^3	L 107 J/mm^3
	120			M 107 J/mm^3	N 89 J/mm^3

Volumetric energy density (also referred as specific energy, and expressed in J/mm^3) can be evaluated according to Equation (1), by approximating the scanning speed (v) as the ratio between point distance (d_p) and exposure time (t_{exp}):

$$\underline{E} = \frac{P}{d_h \cdot v \cdot l} \approx \frac{P \cdot t_{exp}}{d_h \cdot d_p \cdot l} \tag{1}$$

where P is the laser power, d_h is the hatch distance, and l is the layer thickness. Calculated values for each set of parameters are in Table 1. Two batches of samples were produced (A-I1, L-N); powders for the second batch were dried in a desiccator with silica for about 24 h before LPBF.

Specimens are parallelepipeds, with size $8 \times 8 \times 4$ mm^3 for batch 1 (A-I1) and $10 \times 8 \times 4$ mm^3 for batch 2 (L-N). Furthermore, a longer sample ($40 \times 9 \times 5$ mm^3), called I2, that was cut in smaller pieces for testing, and two lattice structures (with geometry shown in Figure 2 and produced with combination of parameters I) were added to the specimens of batch 2.

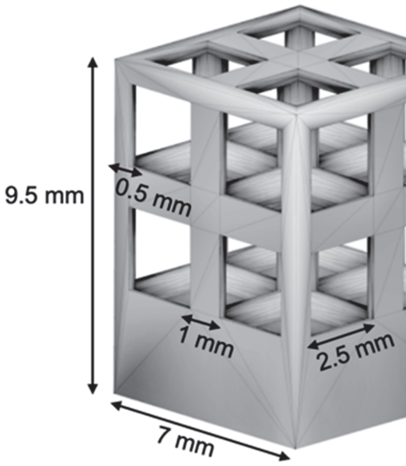

Figure 2. Three-dimensional model of lattice structure.

Characterization of parallelepiped samples consisted of the analysis of microstructure and hardness. Samples were sectioned, mounted, and ground with abrasive papers followed by polishing with diamond suspensions down to 1 µm. For microstructural characterization, both Optical Microscopy (OM, Eclipse LV150NL, Nikon, Tokyo, Japan) and Scanning Electron Microscopy (SEM, EVO 50, Zeiss, Jena, Germany) were used to evaluate materials features at different scale levels. Micrographs were analyzed using ImageJ software [25], measuring area fraction of pores, pore features, and crack density. In more detail, analyzed pore features are [26–28]:

- Equivalent diameter ($\varnothing_{eq}$), i.e., calculated diameter of a circle with the same area as the pore;
- Circularity, i.e., $4{\cdot}\pi{\cdot}$area/perimeter^2, which tends to 1 if the particle is round and smooth, and tends to 0 if it has irregular surface and/or elongated shape;
- Solidity, i.e., ratio between pore area and the minimum convex area that can cover the pore, which tends towards 1 if the pore has a convex shape, and tends towards zero if the boundary is irregular.

Crack density (d_{cracks}) is the average distance between cracks measured on a section parallel to building direction at low magnification.

Vickers microhardness tests were done on samples built on the diagonal of process parameter matrix shown in Table 1 (A, E, I, N). HV was measured along the sample direction parallel to the building direction, using a Future-tech FM-700 microhardness tester with a load of 4.91 N and a dwell time of 15 s. The test was repeated at least five times per sample choosing indentation points randomly on the sample surface to obtain an average value of hardness.

Analysis of lattice structures focused on evaluation of their behavior during thermal cycling reproducing operative conditions. Therefore, one of the lattice structures underwent 100 thermal cycles between 180 °C and 280 °C at a heating/cooling rate of ~27 °C/min, in protective Ar atmosphere to avoid oxidation of molten Sn. Photographs were taken before and after thermal cycles to observe possible changes.

3. Results

3.1. Low Magnification Analysis

Specimens printed with the two jobs are shown in Figure 3. The upper surface can have accumulated material at corners of the parallelepipeds, as pointed out by arrows for sample A in Figure 3. The accumulated material form peaks that are taller and wider as the VED increases, especially in samples from A to E. On the other hand, the samples with the lowest VED have an almost flat upper surface.

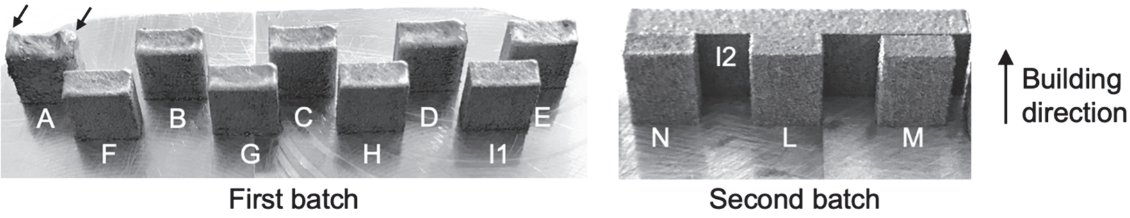

Figure 3. Photographs of parallelepiped samples before removal from support; arrows indicate accumulated material at corners of upper surface in sample A.

Optical micrographs of samples with the related process parameters are shown in Figure 4. At this relatively low magnification, Al and Sn phases are too fine to be distinguished; thus, specimens appear as consisting of a homogeneous grey metallic matrix with black areas corresponding to discontinuities, i.e., pores or cracks.

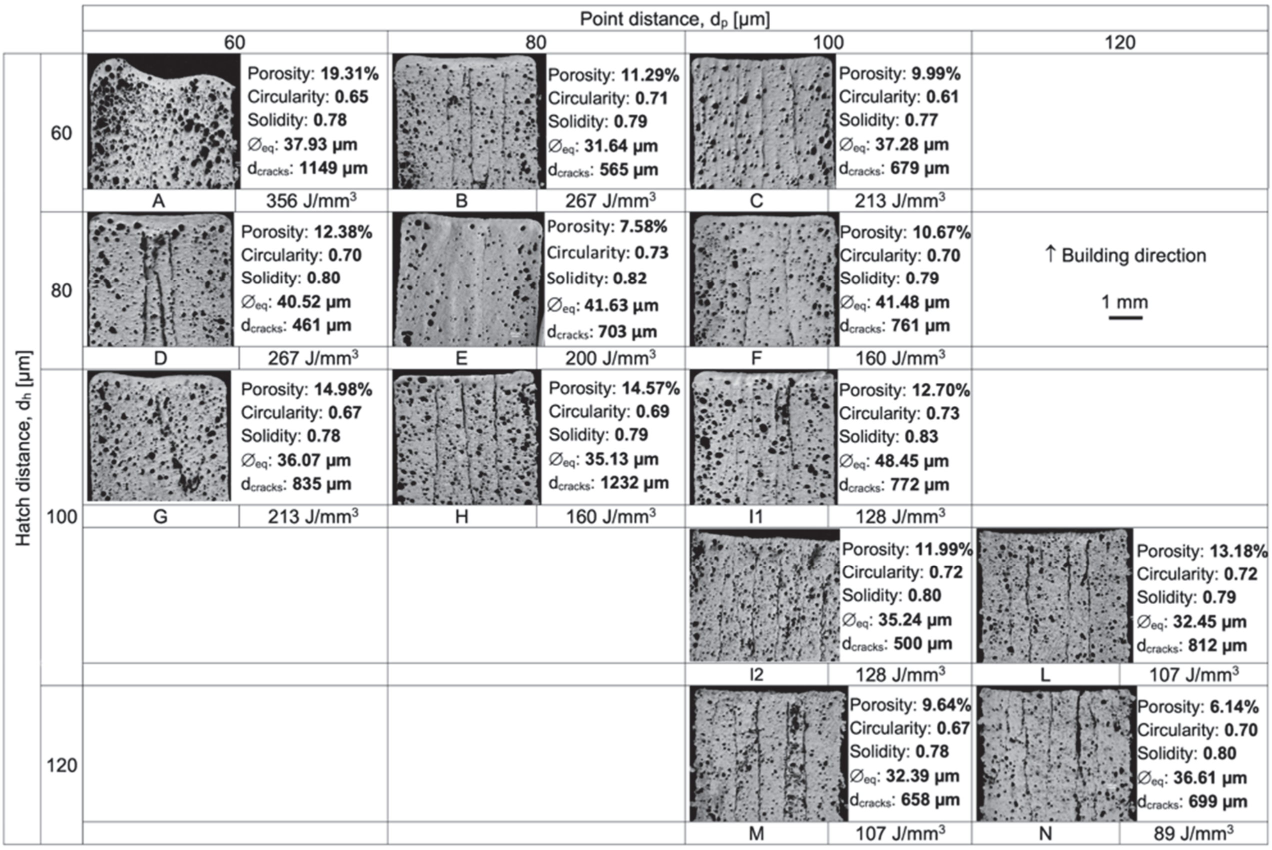

Figure 4. Optical micrographs, process parameters (hatch distance and point distance) and features of samples (porosity, circularity, solidity, equivalent diameter $\varnothing_{eq}$, and crack density d_{cracks}). Shown sections are parallel to building direction (vertical).

The average area fraction of pores (later on simply referred as porosity) as measured on OM micrographs ranges between 6% and 19%, with the highest value for the highest calculated VED (A) and the lowest ones for the lowest VED (N) and the central condition (E) (Figures 4 and 5). The other specimens have porosity between 9% and 15%, but, as shown in Figure 5, there is not a clear trend, neither considering the calculated VED variation nor single parameter (hatch or point distance) variation. Average values of circularity and solidity equal to about 0.7 and 0.8, respectively (Figure 4), show that pores tend to have a spherical shape with smooth surface. Considering pore size, the average equivalent diameter is between 30 µm and 50 µm for all samples (Figure 4).

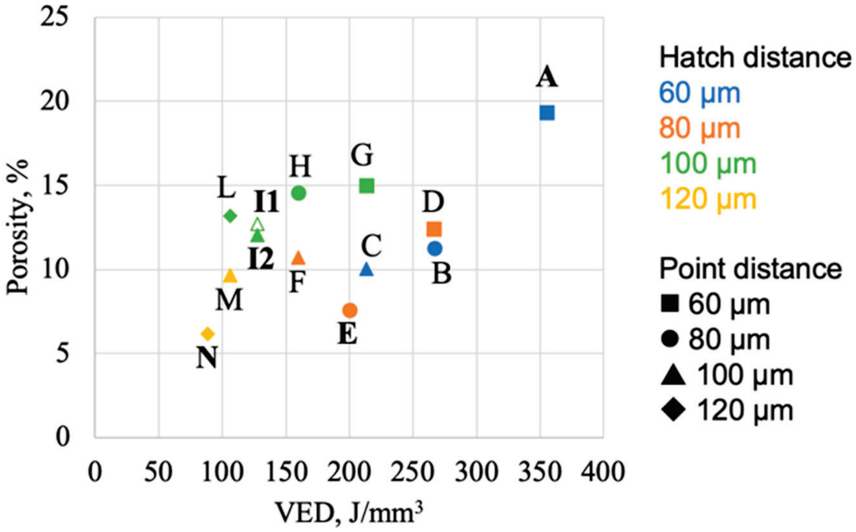

Figure 5. Porosity for each sample as function of VED.

The most significant differences between specimens can be found in pore size distribution (Figure 6) and pore location in the plane parallel to build direction (Figure 4). In all the samples, most of pores (40–50%) have equivalent diameter lower than 50 µm and the percentage of pores per size decreases as equivalent diameter reduces (Figure 6a). As shown in Figure 6b, the standard deviation of equivalent diameter generally reduces with VED. The high standard deviation of specimen I1, here represented with open symbol, is related to the presence of interconnected big pores, considered as a single one by ImageJ software during particles analysis. Figure 6b suggests that high energy samples have a wider pore size range, between ~10 µm and ~100 µm, with respect to low energy ones, generally with bigger pores concentrated near the external surface and in correspondence with the upper surface peaks mentioned above (Figure 4). By reducing the VED, the standard deviation of equivalent diameter reduces as well, i.e., pore size distribution becomes narrower, and the arrangement of pores in the sample tends to be more homogeneous. Such features, that were observed on longitudinal sections of the specimens, have also been confirmed by analyses of transversal sections of samples. For sake of comparison, see OM image of samples A, E, I1, and N in Figure 7.

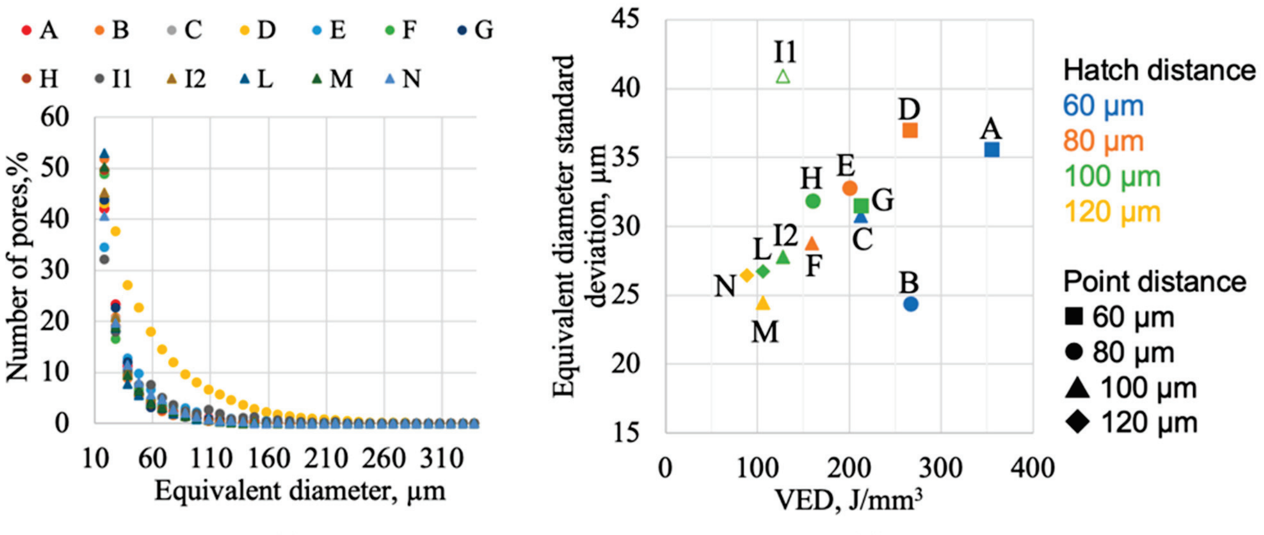

(a) (b)

Figure 6. Pore size distribution described through: (**a**) percentage of pores per equivalent diameter (each point corresponds to an equivalent diameter range ± 5 μm), and (**b**) standard deviation of equivalent diameter as function of VED.

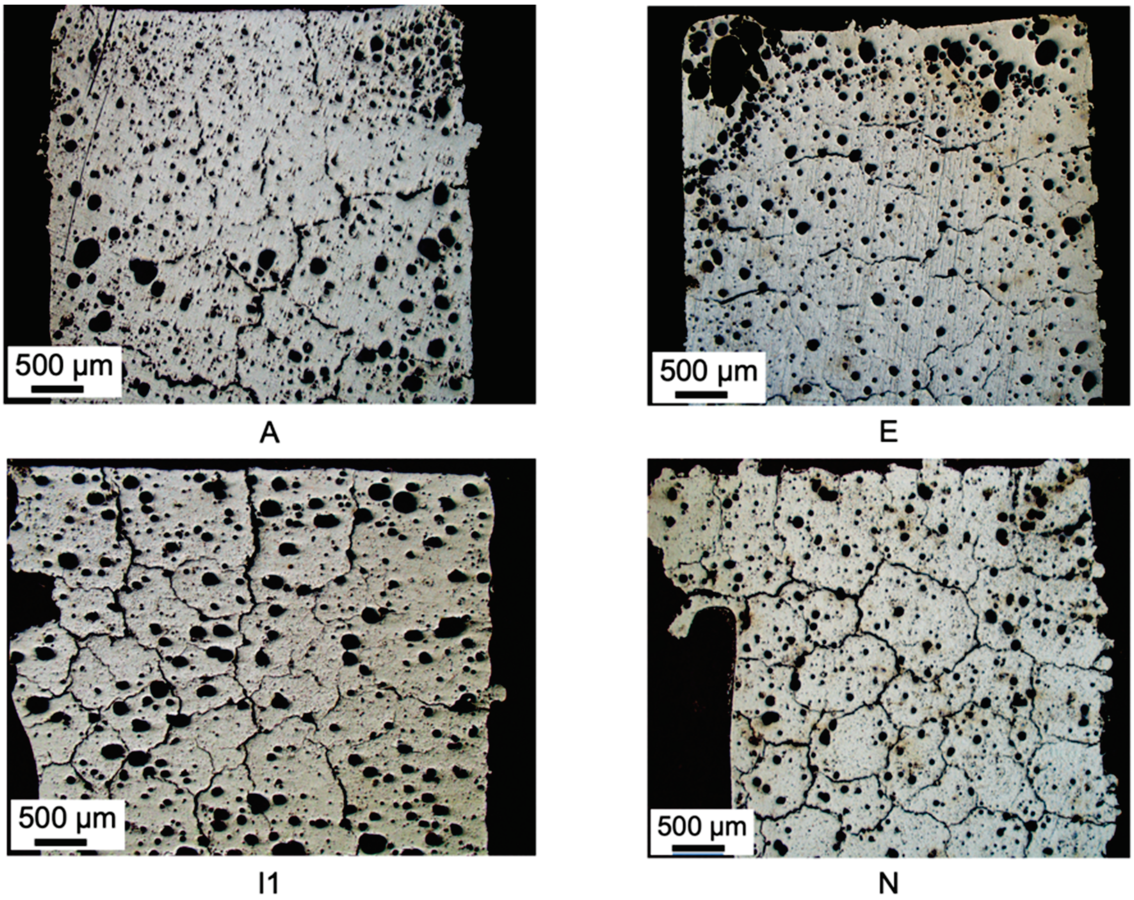

A E I1 N

Figure 7. OM micrograph of samples A, E, I1, and N: section perpendicular to the building direction.

Vertical cracks (Figure 4) are generally parallel to the building direction, while cracks in sections perpendicular to building direction (Figure 7) tend to form a continuous network. In both sections, sample A (i.e., the one produced with the highest VED) displays few small cracks, concentrated especially in the region close to the building platform. On the other hand, the number of cracks increases as VED reduces. Considering crack position, they tend to concentrate in the middle of the sample at high energies, while they are more spread within the sample and interconnected in transverse direction at low energies. The minimum average distances between vertical cracks are 461 µm for sample D, while for the other samples this value ranges between 565 µm and 1232 µm or even higher. The range is compatible with the crack network distribution observed on transversal sections.

3.2. SEM Analysis

SEM micrographs of samples on diagonal of parameter matrix are shown in Figure 8, with increasing VED from A to N sample. Sn (bright contrast) and Al phases (dark contrast) can be distinguished in the SEM micrographs. The horizontal bands are formed by the grains grown between consequent layers in the production process; at low energies, Sn-rich zones are observed in these bands, highlighting the shape of molten pools. By decreasing energy, a finer structure is observed. The size of the Sn particles dispersed in Al phase is between ~2 µm and ~100 nm in sample A. In sample N, fine Sn films are formed along with Sn particles. The film is ~100 nm thick and the small particles are ~100 nm in size.

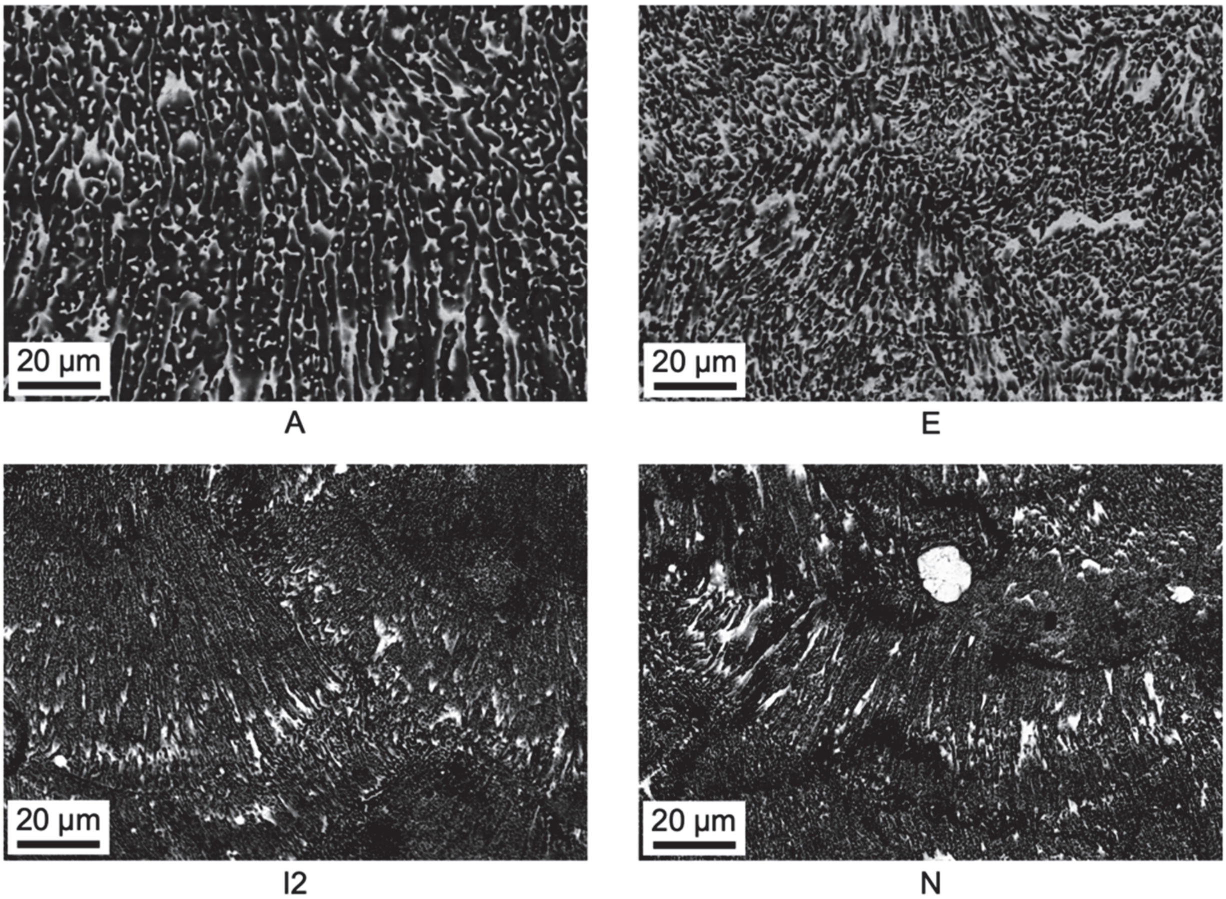

Figure 8. SEM micrographs (BSE) of samples A, E, I2, and N at 3000× magnification.

In all the samples, round-shape Sn particles with diameter of ~15 µm are observed (e.g., see sample N in Figure 8 and samples I and E in Figure 9). These particles seldomly show inner porosities (Figure 9b). Focusing on cracks (Figure 9), it is possible to notice that they can be partially or fully filled with Sn.

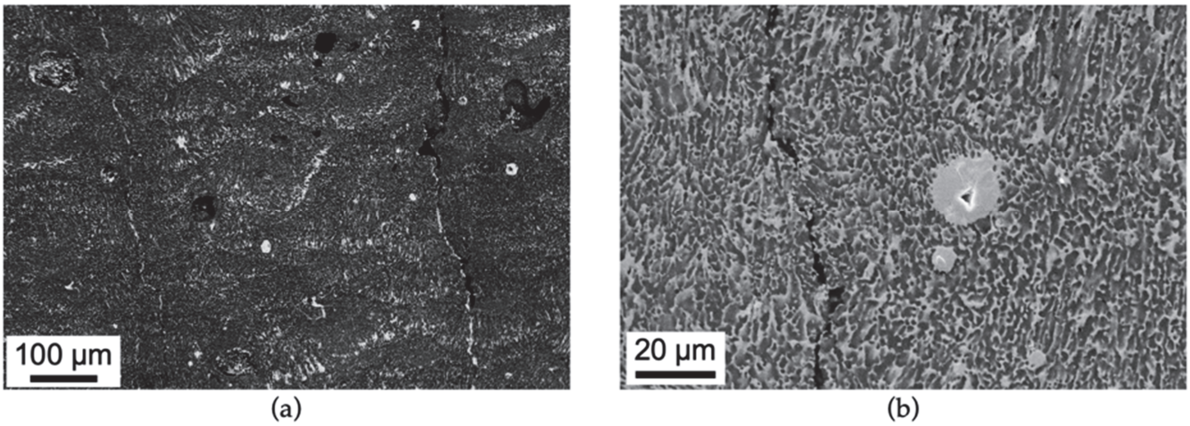

Figure 9. SEM micrographs (BSE) of sample I (**a**) and sample E (**b**) showing cracks at different orders of magnitude.

3.3. Vickers Microhardness

Results of Vickers microhardness measurements for samples on diagonal of parameters matrix are shown in Figure 10. Samples from the first batch (A, E, and I1) have hardness values of about 30 HV, while values for second-batch samples (I2 and N) are slightly above 40 HV.

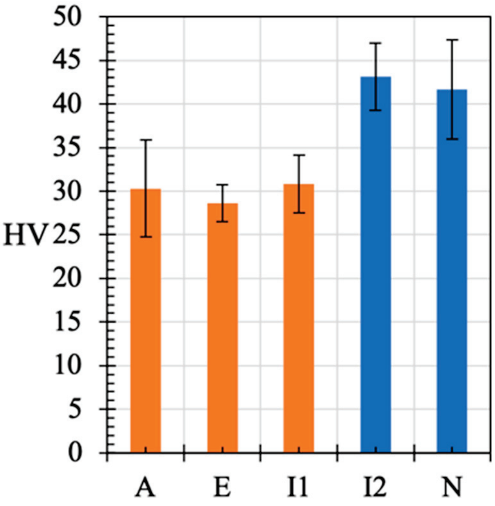

Figure 10. Vickers microhardness numbers for samples on the diagonal of parameter matrix (i.e., those with same hatch distance and point distance). Orange series and blue series indicate samples belonging to the first batch and to the second batch, respectively.

3.4. Lattice Structures

Lattice structures were produced using parameters I, i.e., hatch distance and point distance of 100 μm, correspondingly to those of sample I2. In as-built conditions (Figure 11a), the obtained structure does not show evident deformations or discrepancies with the CAD model. Poor surface quality is observed in the down-skin of horizontal trusses. After 100 thermal cycles between 180 °C and 280 °C, only a minimal deformation is observed in one of the upper corners (dashed ellipse in Figure 11b). Furthermore, Sn droplets (pointed out with arrows in Figure 11b) appear seldomly on surfaces.


(a) (b)

Figure 11. Photographs of lattice structures in as-produced conditions (**a**) and after 100 cycles across Sn melting temperature (**b**). In image (**b**), the dashed ellipse highlights a deformed region of the lattice, and the arrows point out Sn droplets.

SEM micrographs of the as-built lattice surface (Figure 12a) show the absence of surface cracks in vertical trusses, which are 0.5 mm or 1 mm wide. On the other hand, vertical cracks appear on horizontal trusses, which are 7 mm long. The distance between cracks ranges from 250 μm to 700 μm, with an average value of ~400 μm. The lowest average distances between longitudinal cracks can be found in the most highly constrained regions, i.e., at lattice nodes where 1 mm thick trusses converge, and at the bottom part of the lattice, in direct contact with the bulk Al substrate. After thermal cycling, lattice surface shows relatively coarse Sn droplets with diameter of hundreds of microns (Figure 12b), as well as small droplets with diameter below 50 μm and thread-like Sn whiskers (Figure 12c).

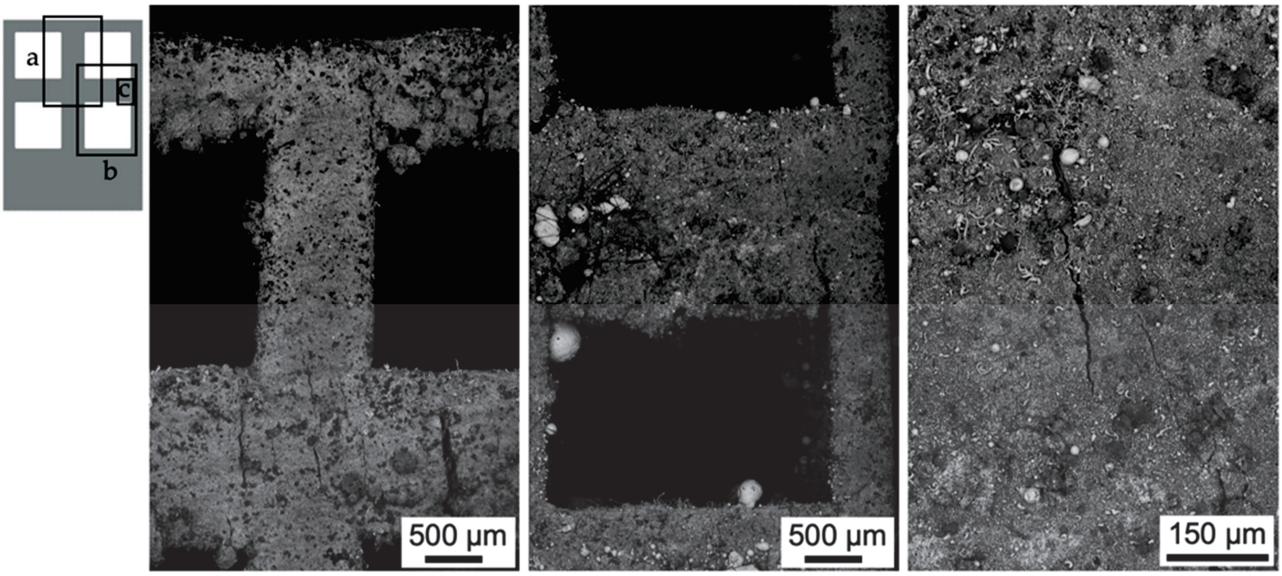

(a) (b) (c)

Figure 12. SEM micrographs (SE) of lattice structure surface before (**a**) and after (**b**,**c**) thermal cycling. The schema shows micrographs position.

4. Discussion

4.1. Effect of Process Parameters on Microstructure

Various process parameters affected microstructural features, as phase distribution, discontinuities (pores and cracks) and topology of the upper surface. The main physical principle that lies behind them is that the energy input (here considered in terms of VED) during LPBF affects the local thermal history of the material. The laser scanning induces fast melting and solidification of the material and the formation of steep thermal gradients affecting also the already printed material, with a complex set of consequences on the microstructure of MGA. As observed in a previous work by Confalonieri and Gariboldi [16], Al-20%vol Sn alloy produced through LPBF has an extremely fine microstructure thanks to the high cooling rate of the molten pool. This small size of microstructural features is comparable with those observed for the same alloy produced through ball milling, compression and sintering [3,8,9]. In addition, a similar microstructure was obtained with LPBF by Zafari and Xia [19] for MGA Fe-20%vol Cu. During cooling, due to the immiscibility of the two phases, Al grains solidify first, while Sn is segregated at grain boundaries reducing primary grain growth [19]. If, due to high energy input, the cooling rate is relatively slow and extensive remelting occurs during deposition of upper layers, Al cells are relatively coarse and the structure appears generally homogeneous, see samples A and E in Figure 8. As VED decreases, the microstructure becomes finer with Al cells elongated in vertical cooling direction with Sn at boundaries; at the same, Sn agglomerates form especially at the bottom of the melting pool, “trapped” during the fast solidification, as previously discussed by the authors in [16]. Thus, low VED results in less homogeneous microstructure. With this phase distribution, which was not significantly modified by the upper layer deposition, the former molten pools can be more easily appreciated. These various types of microstructures can affect thermal diffusivity of the system, leading to an isotropic or anisotropic behavior accordingly [16].

Porosity changes significantly in each sample in terms of quantity, size, and location. The investigated values of hatch distance and point distance do not have a clear effect on porosity, which, in any case, seems to be more affected by the overall VED. To further analyze the correlation between process parameters and porosity, an alternative description of energy density values suggested by Ferro et al. [29] was applied (Equation (2)).

$$\underline{E} = \frac{C(P, t_{exp}, \alpha, \beta, \phi)}{d_h\sqrt{d_p}} \Longrightarrow \underline{E} \propto \frac{1}{d_h\sqrt{d_p}} \tag{2}$$

This expression includes thermal transport phenomena (α = powder thermal diffusivity, β = absorption coefficient, ϕ = spot size diameter). It relates the VED to the inverse of the product between hatch distance and the square root of point distance, while in Equation (1) the inverse proportionality of VED is with the product between hatch distance and the point distance. Accordingly, considering that C parameter is the same for all the samples, porosity and standard deviation of equivalent diameter are plot as function of $(d_h \times d_p{}^{0.5})^{-1}$ in Figure 13. Despite the change in VED dependency on hatch and point distance, the plots show the same trends observed in Figures 5 and 6b, i.e., the point series does not follow a clear law. The complexity in relating process parameters to microstructural features can be ascribed to the peculiar features that characterize an MGA. In more detail, it should be considered that heat transfer phenomena, especially at low temperature, are significantly affected by the phase transition of low-melting phase and thermal properties cannot be considered constant with temperature, thus heat transport cannot be easily modelled.

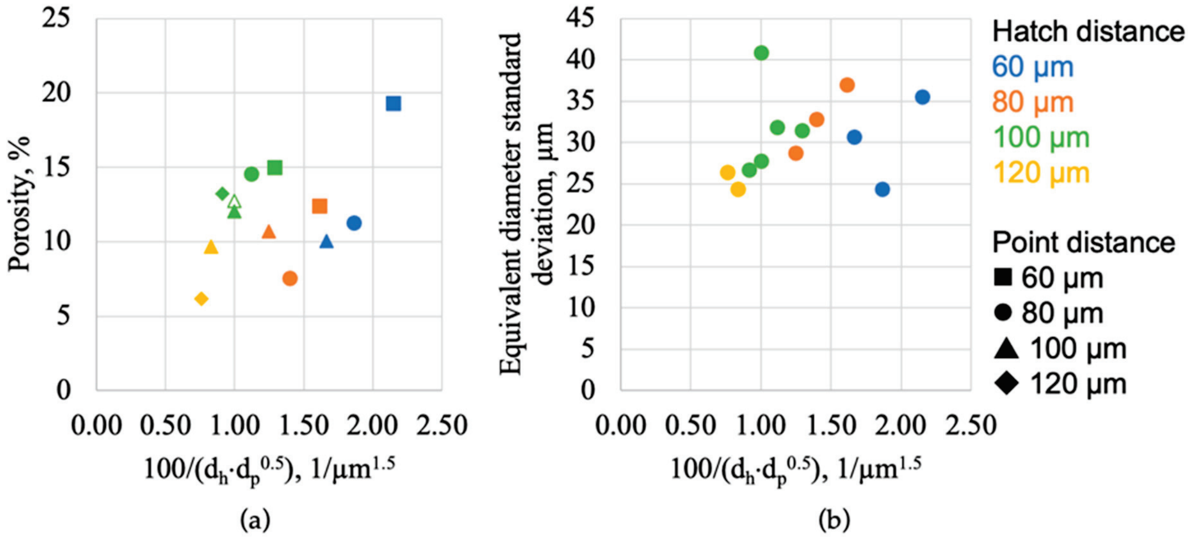

Figure 13. Porosity for each sample (**a**) and standard deviation of equivalent diameter (**b**) as function of $(d_h \times d_p^{0.5})^{-1}$, representing the alternative description of VED according to [29].

In the investigated MGAs the formation of pores can be ascribed to two main causes: presence of gases in the molten pool and Sn particles detachment during specimen preparation (artifact). The presence of gas in the molten pool, which gives rise to spherical-shape pores, can be related to several causes [30]. First, shielding gas (Ar in the present case) can be trapped in the molten pool due to turbulence, which is more likely to occur at high VED. At the same time, turbulence in the molten pool is known to concurrently lead to the formation of peaks on upper surface of specimens [30]. In addition, moisture initially adsorbed by the powders can also be responsible for porosity [31]. Comparing samples I1 and I2, produced with the same parameters in the two batches, it is possible to observe that the one produced with dried powders (I2) smaller average pore size has a slightly lower amount of porosity (almost 1% less). The last gas-related cause for porosity is the evaporation of Sn due to the higher absorptivity of Sn with respect to Al and the high energies involved to melt Al, since it is necessary to break the Al oxide layer and to compensate the high laser reflectivity [32,33]. Despite the specific cause for pore formation, pore size tends to reduce with VED, since gas expansion is lower as temperature decreases and turbulence of molten pool is lower as well.

Gas pores tend to form closer to the external regions of the sample and to be bigger as VED increases. In facts, the outer regions of the samples are the hottest, because (i) they are affected by slower cooling rates, due to the fact that the surrounding unmolten powder has lower thermal diffusivity than the compacted material, and (ii) the laser direction is inverted following the meander scanning strategy, resulting in close consecutive laser pulses. This phenomenon is clearly more emphasized as VED increases together with more turbulence in the molten pool. On the other hand, lower VED values result in lower temperatures and, consequently, lower porosity, that is spread more homogeneously throughout the analyzed sections.

Vertical cracks are mainly caused by thermal stresses related to solidification shrinkage [18]. Sn has a solidification temperature much lower than Al, which means that solid and liquid coexist in a wide temperature range, thus promoting hot cracking. High VED, causing slower cooling rates and less severe thermal gradients, reduces cracks, especially in the inner part of samples that is more constrained. Moreover, as previously mentioned, the outer areas of high-VED specimens are hotter than the core, so cracks tend to concentrate in the middle of the sample, whereas cracks are distributed throughout the section in low-VED samples.

Hardness of the alloy can be considered as constant for samples produced in the same job. The difference between the hardness of samples of the two batches (+25% in batch

2 samples), can be reasonably ascribed to the effect of moisture. Dried powder (batch 2) shows less and smaller pores and higher hardness. Within samples of the same batch, considering that coarse discontinuities (e.g., cracks and big pores) were avoided during HV measurements, microstructural differences are probably too small to affect significantly hardness. Comparing the obtained values with earlier studies, hardness values obtained for the first batch (~30 HV) are close to values for cast and press-and-sintered Al-Sn alloys with the same nominal composition [1,34]. Hardness of samples from the second batch (~40 HV) are close to those of samples produced by ball-milled powder that are pressed-and-sintered [3,9].

Summarizing, according to microstructural analysis, the effects of process parameters are the following:

1. Excessively high energy density increases pore size and results in accumulation of materials on the top surface corners;
2. Most of the parameter sets lead to coarse porosity located at the outer surface, especially in high VED conditions. As energy decreases porosity is more homogeneously distributed in the sample;
3. High energy results in coarse and homogeneous phase distribution;
4. Low VED samples are more affected by hot-cracking.

Therefore, the best conditions, i.e., minimum number of pores and cracks are in the middle-right of the parameter matrix (see Table 1), are for parameter sets E, C, F, and I, since these process parameter sets have intermediate VED, balancing the effects of high and low VED.

4.2. Lattice Structures

Lattice structures were obtained by LPBF and proved to keep their shape almost unchanged after 100 thermal cycles across the solid/liquid transition of the Sn phase. Cracks were observed on as-built lattice surfaces only on horizontal trusses and not on vertical ones. Vertical beams are thin enough to avoid detrimentally high thermal stresses and, so, to prevent vertical crack formation. On the other hand, horizontal segments, show cracks with spacing comparable with that of bulk sample produced with the same process parameter combination (I2). This means that the designer can act both on process parameters and part geometry to reduce or avoid hot cracks.

After thermal cycling, Sn leaked out from the lattice surface. As previously seen for ball-milled and compressed samples [8,9], a fine microstructure without coarse interconnected particles, can help to reduce the risk of significant Sn losses. Nevertheless, the significance of this phenomenon depends on the service condition of the material. Indeed, a feature of interest can be the number of times the transition is activated in component life, i.e., only once (e.g., for safety device) or cyclically, leading to the functional fatigue of the material. Another feature to be considered is the environment where the Al-Sn component works, since Sn leakage could or could not damage other structures in the system.

5. Conclusions

The present work analyzed the effect of LPBF process parameters on Al-20%vol Sn alloy properties. Process parameters affect phase distribution, presence of discontinuities, and geometrical features of samples, while they did not change hardness significantly. To optimize each of these features, an intermediate VED with low hatch distance appears to give the best results, reducing the risk of pore and crack formation.

Furthermore, a lattice structure was successfully produced and proved to be relatively stable even after thermal cycling across Sn melting temperature. Such kind of metal PCM structure could potentially replace homogeneous Al-alloy lattice, providing a “safety function” to the part if temperature increases excessively. It could be inserted for instance in a more complex thermal storage device where a low melting organic PCM (e.g., a paraffin or a fatty acid) fills the Al-Sn alloy lattice, providing also mechanical strength and thermal conductivity.

Considerations on LPBF of Al-Sn alloy and thermal cycling of lattice structures could be extended to other miscibility gap alloys.

Author Contributions: Conceptualization, E.G.; data curation, C.C.; formal analysis, C.C.; investigation, C.C. and R.C.; resources, E.G.; visualization, C.C.; writing—original draft, C.C.; writing—review & editing, C.C., R.C. and E.G. All authors have read and agreed to the published version of the manuscript.

Funding: This research received no external funding.

Institutional Review Board Statement: Not applicable.

Informed Consent Statement: Not applicable.

Data Availability Statement: The raw data required to reproduce these findings cannot be shared at this time as the data also form part of an ongoing study. The processed data required to reproduce these findings cannot be shared at this time as the data also form part of an ongoing study.

Acknowledgments: The Italian Ministry of Education, University and Research is acknowledged for the support through the Project "Department of Excellence LIS4.0—Lightweight and Smart Structures for Industry 4.0.

Conflicts of Interest: The authors declare no conflict of interest.

References

1. Liu, X.; Zeng, M.; Ma, Y.; Zhu, M. Promoting the high load-carrying capability of Al–20wt%Sn bearing alloys through creating nanocomposite structure by mechanical alloying. *Wear* **2012**, *294–295*, 387–394. [CrossRef]
2. Sugo, H.; Kisi, E.; Cuskelly, D. Miscibility gap alloys with inverse microstructures and high thermal conductivity for high energy density thermal storage applications. *Appl. Therm. Eng.* **2013**, *51*, 1345–1350. [CrossRef]
3. Confalonieri, C.; Perrin, M.; Gariboldi, E. Combined powder metallurgy routes to improve thermal and mechanical response of Al−Sn composite phase change materials. *Trans. Nonferrous Met. Soc. China* **2020**, *30*, 3226–3239. [CrossRef]
4. Zhai, W.; Hu, L.; Geng, D.; Wei, B. Thermodynamic properties and microstructure evolution of ternary Al–10%Cu–x%Sn immiscible alloys. *J. Alloys Compd.* **2015**, *627*, 402–409. [CrossRef]
5. Liu, X.; Zeng, M.; Ma, Y.; Zhu, M. Wear behavior of Al–Sn alloys with different distribution of Sn dispersoids manipulated by mechanical alloying and sintering. *Wear* **2008**, *265*, 1857–1863. [CrossRef]
6. Lu, Z.; Zeng, M.; Gao, Y.; Zhu, M. Significant improvement of wear properties by creating micro/nano dual-scale structure in Al–Sn alloys. *Wear* **2012**, *296*, 469–478. [CrossRef]
7. Liu, X.; Zeng, M.; Ma, Y.; Zhu, M. Melting behavior and the correlation of Sn distribution on hardness in a nanostructured Al–Sn alloy. *Mater. Sci. Eng. A* **2009**, *506*, 1–7. [CrossRef]
8. Confalonieri, C.; Grimaldi, A.T.; Gariboldi, E. Ball-milled Al–Sn alloy as composite Phase Change Material. *Mater. Today Energy* **2020**, *17*, 100456. [CrossRef]
9. Confalonieri, C.; Bassani, P.; Gariboldi, E. Microstructural and thermal response evolution of metallic form-stable phase change materials produced from ball-milled powders. *J. Therm. Anal.* **2020**, *142*, 85–96. [CrossRef]
10. Makhatha, M.E.; Fatoba, O.S.; Akinlabi, E.T. Effects of rapid solidification on the microstructure and surface analyses of laser-deposited Al-Sn coatings on AISI 1015 steel. *Int. J. Adv. Manuf. Technol.* **2018**, *94*, 773–787. [CrossRef]
11. Marrocco, T.; Driver, L.C.; Harris, S.J.; McCartney, D.G.; Mc Cartney, G. Microstructure and Properties of Thermally Sprayed Al-Sn-Based Alloys for Plain Bearing Applications. *J. Therm. Spray Technol.* **2006**, *15*, 634–639. [CrossRef]
12. Lucchetta, M.C.; Saporiti, F.; Audebert, F. Improvement of surface properties of an Al–Sn–Cu plain bearing alloy produced by rapid solidification. *J. Alloys Compd.* **2019**, *805*, 709–717. [CrossRef]
13. Kim, W.T.; Cantor, B. Solidification of tin droplets embedded in an aluminium matrix. *J. Mater. Sci.* **1991**, *26*, 2868–2878. [CrossRef]
14. Zhang, W.; Zhao, B.; Zhai, Q.; Gao, Y. Application of Fast Scanning Calorimetry in the Rapid Solidification of Tin Particles Embedded in Al Matrix. In *TMS2013 Supplemental Proceedings*; Wiley: Hoboken, NJ, USA, 2013; pp. 477–484.
15. Zhang, Z.; Wang, Y.; Bian, X.; Wang, W. Orientation of nanocrystals in rapidly solidified Al-based alloys and its correlation to the compound-forming tendency of alloys. *J. Cryst. Growth* **2005**, *281*, 646–653. [CrossRef]
16. Confalonieri, C.; Gariboldi, E. Al-Sn Miscibility Gap Alloy produced by Power Bed Laser Melting for application as Phase Change Material. *J. Alloys Compd.* **2021**, *881*, 160596. [CrossRef]
17. DebRoy, T.; Wei, H.; Zuback, J.; Mukherjee, T.; Elmer, J.; Milewski, J.; Beese, A.; Wilson-Heid, A.; De, A.; Zhang, W. Additive manufacturing of metallic components – Process, structure and properties. *Prog. Mater. Sci.* **2018**, *92*, 112–224. [CrossRef]
18. Kim, W.R.; Bang, G.B.; Park, J.H.; Lee, T.W.; Lee, B.-S.; Yang, S.-M.; Kim, G.-H.; Lee, K.; Kim, H.G. Microstructural study on a Fe-10Cu alloy fabricated by selective laser melting for defect-free process optimization based on the energy density. *J. Mater. Res. Technol.* **2020**, *9*, 12834–12839. [CrossRef]

19. Zafari, A.; Xia, K. Nano/ultrafine grained immiscible Fe-Cu alloy with ultrahigh strength produced by selective laser melting. *Mater. Res. Lett.* **2021**, *9*, 247–254. [CrossRef]
20. Hubert, R.; Matar, O.B.; Foncin, J.; Coquet, P.; Tan, D.; Li, H.; Teo, E.H.T.; Merlet, T.; Pernod, P. An effective thermal conductivity model for architected phase change material enhancer: Theoretical and experimental investigations. *Int. J. Heat Mass Transf.* **2021**, *176*, 121364. [CrossRef]
21. Li, Z.; Gariboldi, E. On the use of effective thermophysical properties to predict the melting process of composite phase change materials with coarse structures. *Int. J. Heat Mass Transf.* **2021**, *180*, 121765. [CrossRef]
22. Vakhshouri, A.R. Paraffin as Phase Change Material. In *Paraffin—An Overview*; IntechOpen: London, UK, 2020.
23. Li, Z.; Gariboldi, E. Modelling the conditions for natural convection onset in open-cell porous Al/paraffin composite phase change materials: Effects of temperature, paraffin type and metallic structure geometry. *Int. J. Heat Mass Transf.* **2021**, *173*, 121279. [CrossRef]
24. Casati, R.; Vedani, M. Aging Response of an A357 Al Alloy Processed by Selective Laser Melting. *Adv. Eng. Mater.* **2019**, *21*, 1800406. [CrossRef]
25. Rasband, W.S. ImageJ. 2018. Available online: https://imagej.net/Welcome (accessed on 20 March 2022).
26. Ferreira, T.; Rasband, W. ImageJ User Guide. 2012. Available online: https://imagej.nih.gov/ij/docs/guide/146.html (accessed on 25 November 2019).
27. Takashimizu, Y.; Iiyoshi, M. New parameter of roundness R: Circularity corrected by aspect ratio. *Prog. Earth Planet. Sci.* **2016**, *3*, 2. [CrossRef]
28. Russ, J.C. *The Image Processing Handbook*; CRC Press: Boca Raton, FL, USA, 2006.
29. Ferro, P.; Meneghello, R.; Savio, G.; Berto, F. A modified volumetric energy density–based approach for porosity assessment in additive manufacturing process design. *Int. J. Adv. Manuf. Technol.* **2020**, *110*, 1–11. [CrossRef]
30. Zhang, J.; Song, B.; Wei, Q.; Bourell, D.; Shi, Y. A review of selective laser melting of aluminum alloys: Processing, microstructure, property and developing trends. *J. Mater. Sci. Technol.* **2019**, *35*, 270–284. [CrossRef]
31. Weingarten, C.; Buchbinder, D.; Pirch, N.; Meiners, W.; Wissenbach, K.; Poprawe, R. Formation and reduction of hydrogen porosity during selective laser melting of AlSi10Mg. *J. Mater. Process. Technol.* **2015**, *221*, 112–120. [CrossRef]
32. Wang, Z.; Ummethala, R.; Singh, N.; Tang, S.; Suryanarayana, C.; Eckert, J.; Prashanth, K.G. Selective Laser Melting of Aluminum and Its Alloys. *Materials* **2020**, *13*, 4564. [CrossRef]
33. Yap, C.Y.; Chua, C.K.; Dong, Z.L. Preliminary investigation on selective laser melting of pure tin. *Proc. Int. Conf. Prog. Addit. Manuf.* **2016**, *1290*, 409–414.
34. Gariboldi, E.; Perrin, M. Metallic Composites as Form-Stable Phase Change Alloys. *Mater. Sci. Forum* **2018**, *941*, 1966–1971. [CrossRef]

quantum beam science

Article

Use of 3D Laser Scanning and Additive Technologies for Reconstruction of Damaged and Destroyed Cultural Heritage Objects

Vadim Parfenov [1,*], Sergei Igoshin [2], Dmitriy Masaylo [2], Alexey Orlov [2] and Dzmitry Kuliashou [3]

[1] Department of Photonic, Faculty of Electronics, St. Petersburg Electrotechnical University, 197376 St. Petersburg, Russia
[2] Institute of Mechanical Engineering, Materials and Transport, Peter the Great St. Petersburg Polytechnic University, 195251 St. Petersburg, Russia; sergei.igosshin@gmail.com (S.I.); dmasaylo@gmail.com (D.M.); orlov_alexey88@mail.ru (A.O.)
[3] Center of Prototyping, 197376 St. Petersburg, Russia; sdimasik1102@gmail.com
* Correspondence: vaparfenov@etu.ru

Abstract: Three-dimensional laser scanning is a novel measurement technique that is frequently used for the documentation of cultural heritage (CH) objects. In the process of 3D scanning, one can obtain computing 3D models of artworks to be documented. It allows one to produce detailed digitized archives of important CH objects. Moreover, the use of 3D scanning enables the digital reconstruction of architectural fragments, sculptures, and other artworks. One more important application of this technique relates to the creation of molds and replicas for replacements of outdoor CH objects in case their preservation requirements do not allow them to remain in their original place due to the influence of environmental factors. One of the most effective ways of creating replicas is the use of laser additive technologies. Therefore, the combination of 3D scanning and additive technologies is a very promising way of preservation of CH. This paper describes several case studies concerned with the combined usage of 3D laser scanning and additive technologies for digital reconstruction and replication and of outdoor sculptures in St. Petersburg city. One of them is the reconstruction of the zinc sculpture "Eva at the fountain" (XIX century, England), which was destroyed during WWII. Its replica was created by means of laser stereolithography. Eventually, one more project is related to the reconstruction of the fragment of the sufficiently damaged cast-iron XIX century monument. This object was reconstructed using two laser technologies: direct metal laser sintering (DMLS), and laser cladding (LC).

Keywords: laser additive technologies; 3D printing; 3D scanning; cultural heritage object; restoration; reconstruction; end-to-end technologies

1. Introduction

In recent decades, one of the most serious challenges in the preservation of cultural and historical heritage has been the rapid decay of exterior monuments due to environmental deterioration, especially in large industrial megapolises. However, in addition to poor environmental conditions, sculptures and other cultural heritage objects also suffer from natural disasters and vandal attacks, which also result in damage and sometimes total loss.

In this context, the question on the need to reconstruct damaged CH objects or to gradually replace them with copies with subsequent transfer of originals to closed museum premises was on the agenda. According to the world practice, today, it is the only opportunity to preserve the most important monuments of the past for descendants, at least their most valuable ones. Although the idea of replacing originals with copies has always caused and still causes an ambiguous attitude in society and even among the museum community, unfortunately, there is no other way to save CH objects from destruction nowadays. It should be noted that the idea of the replication of monuments is not new. Michelangelo's masterpiece, the famous marble sculpture of David, which has remained for almost 370 years in Piazza della Signoria in Florence, was copied in 1873 when the original David was moved for eternal storage in the Gallery of Academy of Fine Arts in the city.

However, nowadays, when museum curators, art experts, and restorers gradually come to an agreement on the need for copying monuments in principle, the question arises of what technologies may be used (and most importantly, are acceptable) when creating copies. Over the years, copies of sculptural monuments were created from different materials. In the 1980s, natural marble was used, and copies were made by "manual" cutting of sculptures and bas-reliefs of stone blocks. Later, cement with marble powder was used, but now various types of synthetic materials are used instead of cement. Such a composition is called "artificial stone". However, this approach, which has been widely adopted in recent years, has many serious shortcomings. The most important of them is that copies made of artificial stone are obtained as a result of forming the original sculpture, and this inevitably leads to a significant physical and chemical impact on its surface. Molding can lead to mechanical damages in the form of fractures and broken small parts of monuments occurring during the mold removal. In addition, the impact of chemical reactions of molding materials with the monument substrate can also be significant.

Now, there is a very attractive alternative to the above-mentioned approach. Innovative 3D laser scanning technology in combination with stone milling machines with numerical software control (CNC) is attractive way of replicating cultural heritage objects. This allows copying sculptural monuments made of natural stone (marble, limestone, granite, etc.). The main advantage of this method is that it is contactless and does not have any negative impact on the original monument. Thanks to this, laser-based contactless copying technology is now widespread in some European countries [1–3].

Ultimately, copying CH objects using natural stone is expensive, and it is not always advisable to use this approach. A different approach can be used to replicate ordinary artifacts and to create copies of lost fragments of works of art for modeling restoration work. Such tasks can be resolved by means of using laser additive technologies. In recent years, several research groups reported case studies where different 3D printing techniques were used, but all known works are not systematic [4–6]. The purpose of this work is to demonstrate the principal possibility of the application and benefits of the use of end-to-end 3D scanning technologies and the reproduction of scan results using CNC and 3D printers with a laser source for repairing and reconstructing cultural heritage objects. In this paper, we describe the results of cases studies on the reconstruction of CH objects in the city of St. Petersburg.

2. Replication and Reconstruction of Sculptures

For the first time in Russia, the non-contact copying of sculptural monuments was carried out by the scientists of St. Petersburg Electrotechnical University (ETU) in collaboration with Italian colleagues in 2008–2010. It was the project on the replication of the XVIII century Italian marble bust "Primavera" from the State-museum preserve "Tsarskoye Selo" collection. This work began with the creation of a 3D computer model of the sculpture obtained using 3D laser scanning. Then, the 3D model was forwarded to our colleagues in Carrara in Italy, who have years of experience in the creation of replicas of historical objects from natural marble using CNC machines. Firstly, they converted 3D model into CAD model requiring for operation of CNC robotic machines. After that, they manufactured a precise copy of the sculpture "Primavera" from a block of white Carrara marble by using a CNC milling robotic machine. The detailed description of this project is given in [3,7], and in Figure 1, one can see photos of the original, the process of carving the marble block, and replica placed in the location of the original sculpture.


(**a**) (**b**) (**c**)

Figure 1. Marble sculpture "Primavera": general view of original, June 2009 (**a**); process of manufacturing the replica by CNC machine (**b**); general view of replica, June 2010 (**c**).

One more project was conducted by the scientific group of the ETU in 2017 when a copy of marble bust of XIX century of the Russian Emperor Peter the Great from the State-museum preserve "Peterhof" collection marble bust was created. This sculpture was given by Russian sponsoring organizations as a present to the French Academy of Sciences in Paris in 2017 on the occasion of the 300th anniversary of the Peter the Great visit to France. During the implementation of this project, 3D scanning of Peter's bust was carried out in the storage facility of the museum "Peterhof", and then, the same as "Primavera", its copy was made of a marble block in Carrara, Italy by using a CNC machine (Figure 2) [8].

Figure 2. Fragments of sculpture "Eve".

The results of the projects on copying marble sculptures of Peter I and Primavera provide a convincing demonstration of the high efficiency of the contactless method for creating physical copies of sculptural monuments made of stone. Its relatively low cost, speed of execution and the full preservation of the original in the process are of such significance that it will inevitably lead to its wide application in museum practice soon.

3. Reconstruction of Damaged Cultural Heritage Objects

Another interesting perspective in modern museum work is connected with the use of 3D scanning for the reconstruction of damaged and even completely destroyed monuments.

3.1. Case Study of Zinc Sculpture "Eve"

One of the case studies of such works is the reconstruction of a totally lost sculpture from the former estate Sergievka in the suburbs of St. Petersburg, which in the XIX century was the country residence of the Duke of Leuchtenberg, the stepson of Napoleon Bonaparte. The Duke of Leichtenberg collected antiquities and possessed the richest collection of masterpieces. Unfortunately, almost all the items of this unique collection were lost during the Great Fatherland War, as Sergievka was in the epicenter of combat activities. Among the many lost masterpieces was a 19th-century zinc sculpture "Eve at the water spring", the fragments of which were discovered underground during construction works in 2007 (Figure 2).

They represented a pile of scattered fragments that did not allow carrying out the reconstruction of this monument by traditional methods of the museum work. However, the use of 3D laser scanning technology, computer simulation, and 3D printing made possible creating a replica of this sculpture, allowing us to judge what the original monument was like (Figure 3). The replica was created from polymer material using additive technology FDM (fused deposition modeling).

Figure 3. Replica of sculpture "Eve".

The results of this project are described in the work [5], but it is worth mentioning that the replication and reconstruction of works of art puts a serious issue on the agenda—what is the accuracy of creating the physical copies of objects? In other words, how precise is the correspondence between surfaces of the same object in its 3D model and replica obtained using additive technologies? This issue is very important from point of view of authenticity of any original CH object and its replica, but it is not considered in the scientific literature in the papers devoted to the replication of sculptures.

We carried out an experimental study on the evaluation of the accuracy of the replication of the sculpture "Eve". In those experiments, we used a laser scanner Surphaser 25SHX (scanning accuracy—2.5 microns) and did find that deviations in the surfaces of the original 3D model and replica were in the range of ±0.7 mm. During a detailed analysis of the 3D model of the replica, a "cellular structure" (resembling honeycomb) was clearly visible on its surface, especially pronounced in the area of the sculpture's back (see Figure 4, where one can see the result of "overlapping" of 3D model of replica and 3D model that was used for the creation of replica).

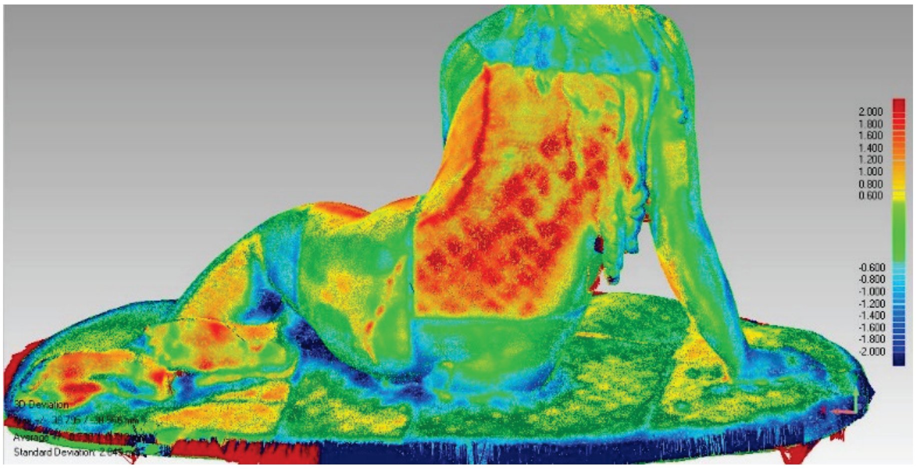

Figure 4. The result of comparing the replica's 3D model and the 3D model that was used to create the replica.

This may be a consequence of the 3D printing technique used, in which, to reduce the cost of replication, we decided to save used material (PLA plastic) by having the sculpture be hollow inside (the volume filling was 10%). Because of this, local "minima" (deflections) of the sculpture surface are observed in the places where the surface layer of the sculpture is attached to the stiffeners, while the sagging areas correspond to local maxima. It was these deformations that were detected by laser scanning.

Thus, the accuracy of reproduction of the sculpture "Eve" can be considered good, but it must be borne in mind that when replicating sculptural monuments, distortions of their geometric shape are possible.

3.2. Case Study of Cast-Iron Star

One of our most recent works relates to the reconstruction of CH objects created from cast-iron. Nowadays, it is a typical conservation problem in CH preservation. There are sculptures, objects of decorative art, grids around historical buildings, parks, and gardens as well as just decorative elements on the facades of buildings. Many of them are highly deteriorated and usually have severely damaged and lost parts (see Figure 5a). Until recently, experts in the field of CH did not attach much importance to such items, and as they fell into complete disrepair, they were replaced with copies. However, in recent years, there has been a reassessment of values, and a new trend has emerged in the work of restorers, which requires the reconstruction of objects damaged by corrosion instead of replacing them with copies.


(**a**) (**b**)

Figure 5. (**a**)—An example of a damaged cast-iron fence; (**b**)—cast-iron star for repairing.

The authors of this article understand this problem and proposed its technical solution based on the use of laser powder coating technology. In our work, we demonstrated the principal possibility of the realization of such an approach.

The object of our studies was a small (10 cm) iron star that is a decorative element of a XIX century cast-iron tombstone fence of the Alexander Nevsky monastery in St. Petersburg. This object is highly deteriorated due to corrosion and has losses of some small elements (see Figure 5b).

The main idea of our project was to recreate the losses of individual elements of the star using a combination of 3D scanning technology, direct metal laser sintering (DMLS), and laser cladding.

Firstly, we analyzed the chemical composition of the star using X-ray fluorescence using XL3t-32280 equipment. The analysis results are shown in Table 1.

Table 1. The result of the chemical analysis of the part.

Element	Fe	Si	Co	Mn	P	Zn	Pb	Ti	Ag	Other
Content, wt. %	91.05	6.38	0.79	0.45	0.34	0.24	0.22	0.17	0.13	0.24

We did find that the main chemical element is Fe (its concentration is of about 91%). Additionally, there are permanent impurities typical for gray cast-iron (the total concentration is only about 7.2%).

Secondly, we removed the corrosion from the star surface. For the removal of corroded layers, we tried to use different treatment techniques: laser cleaning, sand blasting and chemical treatment; the latter gave the best result (see Figure 6a).

(**a**) (**b**)

Figure 6. (**a**)—star after chemical treatment; (**b**)—3D model with added rays.

Then, we carried out 3D scanning of the star using laser triangular scanner Konica Minolta V-910 and created its 3D model. The next stage of our work was the computer modeling. The missing ray of the cast-iron star was modeled with the Zbrush software. The main distinguishing feature of this software is the ability to “sculpt” 3D objects. The surviving cones were projected, processed, and “glued” to the main body of the star in the parts where there were losses (see Figure 6b), where blue ends are reconstructed lost parts of the star.

It was decided to separate those experiments into two stages: firstly, we created one of the star rays, which we proposed to join with the star; the second stage of reconstruction will be based on a reconstruction of the lost end of another star ray by direct metal deposition. It is obvious that such a method of reconstruction is more complicated since the very precise movement of a laser beam is needed, and such a task can be solved by means of the development of specialized software.

A separate ray of the star was grown by the DMLS method according to the CAD model. We used a CW fiber Ytterbium laser with an output power of up to 80 W. Stainless-steel powder 316 L20 (manufacturer—Hoganas, Belgium) with a granule size of 53 µm was used for printing. The result of creating this piece can be seen in Figure 7a.

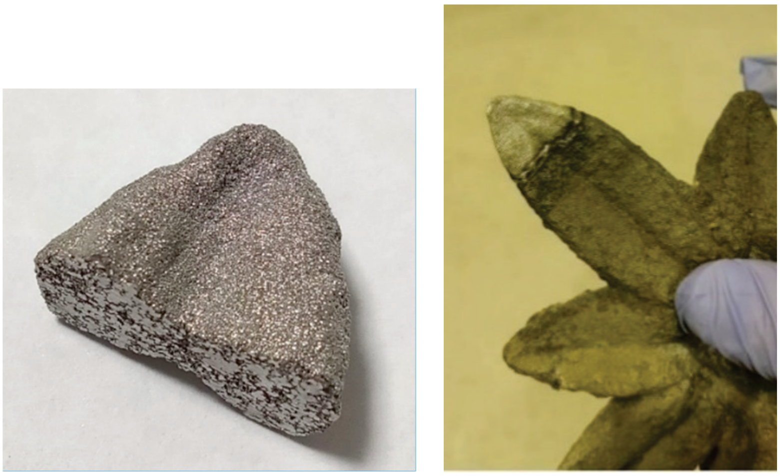
(**a**) (**b**)

Figure 7. (**a**)—DMLS printed star ray; (**b**)—welded star ray.

We then applied direct laser deposition (DLD) [9,10] using the OKTA-Printer machine developed at the Peter the Great St. Petersburg Polytechnic University (see Figure 8). The essence of the DLD method is to directly feed a metal powder or composite powder mixture into a molten bath formed by a laser beam [11–13]. The local action of heating the laser beam, the selective effect, as well as the high accuracy of modern robotic manipulators allow using this technology as an advanced and modern method for repairing and restoring products. The main parts of the OKTA-Printer are the powder cladding head and the CAMAU robot. For joining, we used a nickel alloy powder Inconel 625 (manufacturer—Hoganas, Belgium) with a particle size distribution of 50–150 µm. It is one of the most popular alloys in laser cladding and DLD [14,15]. To connect the two pieces, they were glued to each other with glue, then welded in one pass on each side. The following parameters were used for welding: laser spot width 1.5 mm, laser power 700 W, robot movement speed 1500 mm/s, and powder feed 20 g/min. The result of the stage of the star reconstruction is shown in Figure 7b.

Figure 8. OKTA-Printer implementing DLD technology.

Using the DLD printer, an attempt was made to deposit the missing part of the star's ray on the material from which it is made. For this, a parallel piece was cut off and deposited on it from the same Inconel 625 that was used for welding. As a result of the cladding, an excessive absorption of laser radiation by the star material was detected, which leads to melting and a geometry change in the substrate along the edges, even with a relatively low heat input.

Furthermore, to assess the thermal effect on the structure of the star material, a materials science study of the initial structure and structure after laser cladding was carried out, and the transition zone was also investigated. Additionally, the microhardness was measured at a load of 0.3 kgf with the same step of 200 μm to evaluate the change in metal properties from the nickel alloy overlay to the cast-iron from which the star is made (see Figure 9).

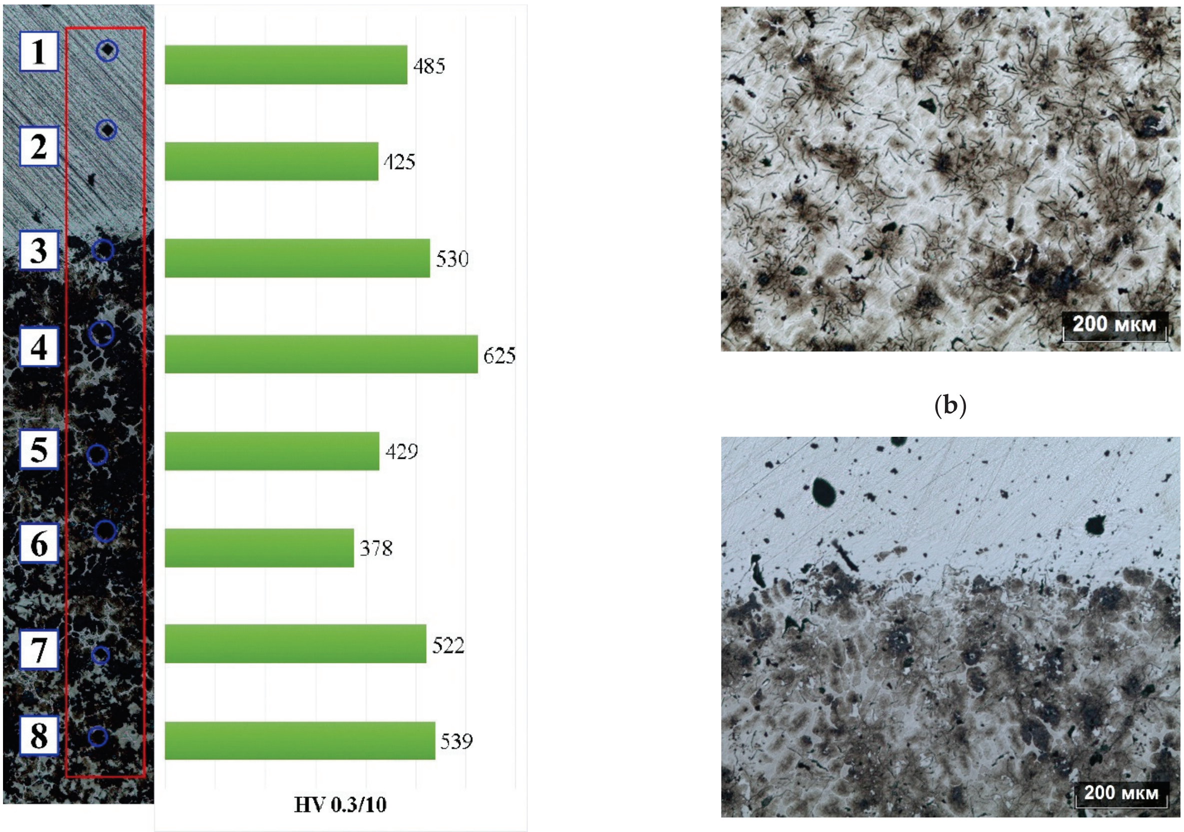

(**a**)

(**b**)

(**c**)

Figure 9. (**a**)—hardness measurement in HV from cladding to cast-iron with a step of 200 μm, the structure of the material was investigated using a Leica optical microscope: (**b**)—structure of cast-iron-before cladding; (**c**)—structure of cast-iron with cladding.

Separate hardness measurements were made at four to five points for each area of interest: cast-iron without surfacing is 240 ± 60 HV, with weld overlay 467 ± 76 HV, hardness of deposited Inconel 625 corresponds to 462 ± 26 HV, hardness in the transition zone is 601 ± 134 HV. Examination of the state of the interface on an optical microscope (Figure 9c) showed a strong metallic bond of the cladding with the star material: there were no cracks or pores at the interface.

Since there are no data on the percentage of carbon in the composition of the studied cast-iron, we assume that the initial microstructure of the star material corresponds to the structure of gray cast-iron on a ferrite base with lamellar-free graphite. Due to the thermal effect of the laser beam, the hardness of cast-iron increased significantly, which can be associated with rapid heating followed by rapid cooling, which leads to the formation of a pearlite structure, as well as the accumulation of thermal stresses. It was noted that at more than 1 mm from the surfacing, the hardness of the cast-iron base was significantly higher than the hardness of the same cast-iron without cladding. This indicates a large heat-affected zone that is not typical for standard cladding materials. Usually, this area is no more than 0.5 mm. This is most likely due to the size of the substrate itself and the low heat-dissipation. For the experiment on direct restoration of the missing part, a substrate with an area of 2 cm^2 was used, whereas the substrates for cladding and DLD are usually at least 100 $cm^{2.}$

4. Conclusions

This article describes several case studies concerned with the reconstruction and replication of CH objects in the city of St. Petersburg. It was shown that such tasks can be effectively achieved by means of the combined use of 3D scanning technologies, CNC milling, and laser additive technologies.

It should be noted that, as far as we know, our work on the reconstruction of the cast-iron star was the first case study that demonstrated the principal possibility of the use of direct metal laser sintering and laser powder cladding technology for the conservation of cast-iron CH objects. Therefore, the combined use of 3D scanning, DMLS, and laser cladding technologies has great potential for exact copying of the texture of metal monuments. The main advantage of this approach is a slight thermal effect on the restoration object at the joining of the reconstructed elements with a damaged object itself by laser cladding. Direct reconstruction of damaged CH objects by the DLD method directly on the object of restoration looks preferable, but it is much more complicated due to the unsuitability of cast iron as a substrate, from which many CH objects are made. Nevertheless, it is no doubt an interesting field for further scientific work, and the authors plan to continue their studies.

Author Contributions: Conceptualization, V.P.; methodology, V.P.; software, D.M.; validation, V.P. and S.I.; formal analysis, V.P.; investigation, V.P., S.I. and D.K.; resources, V.P. and S.I.; data curation, S.I.; writing—original draft preparation, V.P. and D.K.; writing—review and editing, V.P., S.I.; visualization, V.P., D.K. and S.I.; supervision, V.P.; project administration, V.P., A.O.; funding acquisition, V.P. and D.M. All authors have read and agreed to the published version of the manuscript.

Funding: This research received no external funding.

Institutional Review Board Statement: Not applicable.

Informed Consent Statement: Not applicable.

Data Availability Statement: By request to authors.

Acknowledgments: The authors would like to acknowledge Vitaly Tishkin and Anton Zhuravlev for taking part in the experimental studies.

Conflicts of Interest: The authors declare no conflict of interest. The funders had no role in the design of the study; in the collection, analyses, or interpretation of data; in the writing of the manuscript, or in the decision to publish the results.

References

1. Fowles, P.S. The Garden Temple at Ince Blundell: A Case Study in the Recording and Non-Contact Replication of Decayed Sculpture. *J. Cult. Herit.* **2000**, *1*, S89–S91. [CrossRef]
2. la Pensée, A.; Parsons, J.; Cooper, M.; Broadbent, S.; Bingham, R. The Use of 3D Laser Scanning and 3D Modelling in the Realisation of an Artistic Vision; Production of Large Scale Public Art in Tudor Square, Sheffield. In Proceedings of the International Archives of Photogrammetry, Remote Sensing and Spatial Information Sciences, Newcastle upon Tyne, UK, 21–24 June 2010; Volume XXXVIII, pp. 375–380.
3. Parfenov, V.A. Non-Contact Replication of Marble Sculptures Using Laser Technology. In *Sculpture of XVIII-XIX Centuries in Out-Door Environment*; St. Petersburg's Museum of Urban Sculpture Publishing House: St. Petersburg, Russia, 2010; pp. 66–69.
4. Skarlatos, D.; Theodoridou, S.; Hennings, D.; Ville, S. Replication of Marble Exhibits Using Photogrammetry and Laser Scanning (or How to Forge Exhibits). In Proceedings of the XIXth CIPA Symposium, Antalya, Turkey, 30 September–4 October 2003.

5. Wachowiak, M.J.; Karas, B.V. 3d Scanning and Replication for Museum and Cultural Heritage Applications. *J. Am. Inst. Conserv.* **2009**, *48*, 141–158. [CrossRef]
6. Cekus, D.; Kwiatoń, P.; Nadolski, M.; Sokół, K. Quality Assessment of a Manufactured Bell Using a 3D Scanning Process. *Sensors* **2020**, *20*, 7057. [CrossRef] [PubMed]
7. Parfenov, V.A. Laser Techniques in Artworks Conservation in St.Petersburg. *Rev. Cuba. Fis.* **2016**, *33*, E29–E31.
8. Parfenov, V.A. Use of Laser Technologies for Restoration, Documentation and Replication of Sculptural Monuments in Saint Petersburg. *Insight Non-Destr. Test. Cond. Monit.* **2020**, *62*, 129–133. [CrossRef]
9. Thompson, S.M.; Bian, L.; Shamsaei, N.; Yadollahi, A. An Overview of Direct Laser Deposition for Additive Manufacturing; Part I: Transport Phenomena, Modeling and Diagnostics. *Addit. Manuf.* **2015**, *8*, 36–62. [CrossRef]
10. Masaylo, D.V.; Orlov, A.V.; Igoshin, S.D. Effect of Heat Treatment on the Structure and Phase Composition of a High-Temperature Nickel Alloy Obtained by Laser Cladding. *Met. Sci. Heat Treat.* **2019**, *60*, 728–733. [CrossRef]
11. Masaylo, D.V.; Popovich, A.A.; Sufiyarov, V.S.; Orlov, A.V.; Shamshurin, A.I. A Study of Structural Features of a Gradient Material from a Heat-Resistant Nickel Alloy Produced by Laser Cladding. *Met. Sci. Heat Treat.* **2019**, *60*, 739–744. [CrossRef]
12. Schwendner, K.I.; Banerjee, R.; Collins, P.C.; Brice, C.A.; Fraser, H.L. Direct Laser Deposition of Alloys from Elemental Powder Blends. *Scr. Mater.* **2001**, *45*, 1123–1129. [CrossRef]
13. Leyens, C.; Beyer, E. Innovations in Laser Cladding and Direct Laser Metal Deposition. In *Laser Surface Engineering*; Elsevier: Amsterdam, The Netherlands, 2015; pp. 181–192.
14. Todaro, C.J.; Easton, M.A.; Qiu, D.; Zhang, D.; Bermingham, M.J.; Lui, E.W.; Brandt, M.; StJohn, D.H.; Qian, M. Grain Structure Control during Metal 3D Printing by High-Intensity Ultrasound. *Nat. Commun.* **2020**, *11*, 142. [CrossRef] [PubMed]
15. Abioye, T.E.; Folkes, J.; Clare, A.T. A Parametric Study of Inconel 625 Wire Laser Deposition. *J. Mater. Process. Technol.* **2013**, *213*, 2145–2151. [CrossRef]

quantum beam science

Article

Laser Treatment as a New Approach to the Passivation of Iron-Based Historical Monuments

Iuliia Ruzankina [1,2,*], Vadim Parfenov [3], Oleg Vasiliev [4], Oleg Zotov [5] and Alexandra Zotova [5]

[1] Department of Mathematics and Physics, Univesita Cattolica del Sacro Cuore, I-25121 Brescia, Italy
[2] Department of Chemistry, KU Leuven, Celestijnenlaan 200D, 3001 Leuven, Belgium
[3] Department of Photonics, St. Petersburg Electrotechnical University, 197376 Saint Petersburg, Russia; vaparfenov@etu.ru
[4] LLC 'Laser Center', 195176 Saint Petersburg, Russia; tesla_90@mail.ru
[5] Laboratory of Synthesis New Materials and Structures, Peter the Great St. Petersburg Polytechnic University, 195251 Saint Petersburg, Russia; zog-58@mail.ru (O.Z.); zotova_ao@spbstu.ru (A.Z.)
* Correspondence: ruzankinajulia@gmail.com

Abstract: This article is devoted to the study of the possibility of the passivation of iron-based metallic materials. The experimental results obtained for the laser treatment of carbon steel model samples by the radiation of repetitively pulsed and continuous-wave 1.064 µm Nd:YAG lasers are described. It is shown that the laser treatment allows the formation of dense protection films, 62–77 microns thick, on the steel surface. The films enhance the anticorrosion properties of the metal. Exposure to laser radiation reduces the surface roughness (from $R_a = 0.53$ µm to $R_a = 0.38$ µm). Laser radiation power densities of 10.2×10^5 W/cm^2 and 10.7×10^5 W/cm^2 for these two laser generating modes, respectively, correspond to the optimum (in terms of the degree of corrosion resistance) modes of steel treatment. The conducted studies show that the application of Nd: YAG lasers is a promising method for the surface passivation of artworks created from steel and cast iron. One of the most promising applications of the proposed method for the anticorrosion protection of iron is the passivation of the surface of iron-based historical monuments.

Keywords: laser passivation; Nd:YAG laser; anticorrosion coating; steel; cultural heritage; historical monument; artworks; restoration

check for updates

Citation: Ruzankina, I.; Parfenov, V.; Vasiliev, O.; Zotov, O.; Zotova, A. Laser Treatment as a New Approach to the Passivation of Iron-Based Historical Monuments. *Quantum Beam Sci.* **2022**, *6*, 9. https://doi.org/10.3390/qubs6010009

Academic Editors: Swee Leong Sing and Wai Yee Yeong

Received: 20 January 2022
Accepted: 14 February 2022
Published: 16 February 2022

Publisher's Note: MDPI stays neutral with regard to jurisdictional claims in published maps and institutional affiliations.

Copyright: © 2022 by the authors. Licensee MDPI, Basel, Switzerland. This article is an open access article distributed under the terms and conditions of the Creative Commons Attribution (CC BY) license (https://creativecommons.org/licenses/by/4.0/).

1. Introduction

One of the most important practical tasks in modern museum work is the passivation of the surface of cultural heritage (CH) objects made of iron, steel, and cast iron. In the conservation of such objects, restorers frequently have to deal with the removal of corrosion products. This is a very difficult task in itself, since the corrosion layer thickness of many monuments (primarily archaeological objects) can be significant (up to 1 cm). However, this problem is aggravated by the fact that the reoccurring formation of the foci of corrosion on the surface of such objects is possible after the completion of the restoration process. This puts the task of developing effective technologies for creating inhibitory (protective) coatings on the surface of monuments on the agenda.

Corrosion inhibitors are the substances that, when in a corrosive environment in sufficient concentrations, dramatically slow down or even stop the corrosive degradation of metal. There are several different types of inhibitors; however, in terms of restoration-related tasks, the most relevant is the application of coatings which enhance the resistance of museum objects to the effects of atmospheric corrosion. Most often, wax and various types of lacquers are used as inhibitors in the conservation of CH objects; but in recent years special protective materials have emerged, including those made of inorganic materials [1].

According to the mechanism of action, inhibitors can be divided into two types: passivating and adsorption. Adsorption-based corrosion inhibitors are adsorbed on the surface of a protected artifact, forming a film, and inhibit electrochemical reactions (sometimes forming a thin monomolecular film is sufficient for this). Adsorption inhibitors are most often surface-active agents, as well as organic compounds which, owing to their impact on the artifact, additionally enhance the protective properties of the oxide film. The presence of oxygen in a corrosive environment contributes to enhancing the protective effect of adsorption corrosion inhibitors. If the oxide film is unstable, then the adsorption of the inhibitor on the metal surface will be hampered, with the oxygen having no additional impact.

Passivating corrosion inhibitors play an important role in the formation of a protective film on the metal surface. Most often, passivators are inorganic compounds with oxidising properties (nitrites, molybdates, and chromates). Passivating compounds are considered more effective than most non-passivating ones. Thus, the passivation of metals involves the transition of the metal surface into an inactive, passive state, which is associated with the formation of thin surface layers of chemical compounds that prevent corrosion.

In modern technology, passivation refers to methods used to protect metals from corrosion through chemical treatments or technological processes leading to the creation of an oxide film on the treated surface. One of the most advanced approaches for the creation of passivating coatings in industry is the laser treatment of metal surfaces. In particular, from the scientific literature, the possibility of protecting metals from corrosion as a result of the creation of patterned micro- and nanostructures on their surface under the influence of radiation from solid-state lasers with pico- and femtosecond pulse duration has been reported [2,3]. Such a pulse duration can be achieved in the so-called mode-locking generation regime of lasers. However, the laser passivation of metals is still not applied in the restoration of CH objects. One of the possible reasons for this is the fact that pico- and femtosecond laser systems are very expensive, and only highly qualified professionals are able to work with them.

In order to further develop methods for the laser restoration of metals in museums, a study was conducted on the possibility of creating anticorrosive coatings on the surface of iron objects using laser treatment. In this case, unlike in the above-mentioned works, the authors of this article proposed and experimentally proved the possibility of using continuous-wave and repetitively pulsed Nd:YAG lasers for this purpose [2,3]. Lasers operating in such generation regimes are much cheaper than mode-locked laser systems and can be easily exploited even by professional restorers who do not have an engineering background.

It should be noted that research on the possibility of the passivation of metal monuments using pulsed Nd:YAG lasers is also currently being carried out by the scientific group of S. Siano et al. [4,5]. In the works by S. Siano, experiments were carried out focusing on the treatment of iron surfaces using a Nd:YAG laser that generated pulses at a fundamental wavelength of 1.064 μm and operated in three different generating modes: Q-switched mode, long Q-switched mode (LQS—Q-switched mode with increased pulse duration), and Short Free Running mode (SFR—free-running mode with shortened pulse duration). The treatment of the metal was performed using single laser pulses.

Even S. Siano et al. [4,5] themselves consider their results as preliminary, since they explored the task of iron passivation only in relation to model samples and certain types of historical monuments with the foci of corrosion on their surfaces. As a result of the treatment of corroded areas by radiation from a laser operating in SFR mode (with a pulse duration of 20 μs) and heating, the phase transformation of iron oxides occurred—iron oxide (FeO) was converted to magnetite (Fe_3O_4). Although magnetite is a stable iron compound that is affected by corrosion, such an approach to the problem of the passivation of monuments seems to be rather controversial [6]. Firstly, it does not solve the problem of the anticorrosive protection of “clean” (i.e., without foci of corrosion) surfaces. Secondly, the formation of magnetite leads to the appearance of a grey-black colour on the laser-treated surface areas, which may be unacceptable in terms of the aesthetic properties of CH objects.

The approach suggested by the authors of this article is more universal, since it allows the formation of protective anticorrosion layers on “clean” surfaces of monuments made of iron and steel. In addition, in terms of the effect achieved, CW and nanosecond Nd:YAG lasers are alternatives to the above-mentioned pico- and femtosecond laser systems but are simpler to operate and maintain; this is very important from the perspective of routine museum work. It should also be noted that the results obtained in this work are a further development of research on the laser anticorrosion treatment of metals in general, which the authors have devoted themselves to during the last few years [7–11]. This means that the proposed approach is also very useful for iron treatment in industry.

2. Materials and Methods

In order to test the technology involved in the laser passivation of historical monuments made of iron, small carbon steel plates were selected as the model samples (with areas up to 5 cm^2 and thicknesses of 3–5 mm). With electron microscopy, the following chemical composition data were obtained: iron (Fe)—83.4%; carbon (C)—13.5%; silicon (Si)—0.7%; manganese (Mn)—0.5%. In addition to these elements, alloying elements such as nickel (Ni), chromium (Cr), copper (Cu), and cobalt (Co) were also present in the samples in low concentrations. In Russia, a steel grade with such a chemical composition is called Steel20. This steel was chosen for use in experimental studies due to the fact that many historical monuments were created of ferrous metals, which are close to Steel20 in terms of their chemical composition.

Our samples were treated using a Nd:YAG laser at a wavelength of λ = 1064 µm in repetitively pulsed and continuously pulsed modes (Figure 1). A laboratory model developed in the research institute “Polyus” (Moscow) was used in the experiments.

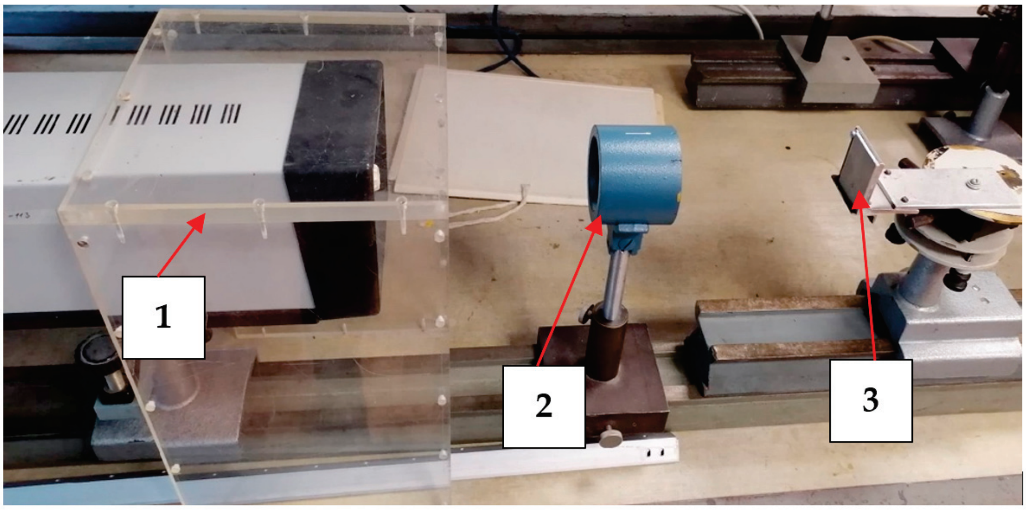

Figure 1. Photo of the optical layout of the Nd:YAG laser experimental setup: (**1**) Nd:YAG laser with a wavelength of 1064 µm, (**2**) focusing lens, and (**3**) sample surface. The laser focuses a 1064 µm beam onto the steel sample.

Laser radiation was focused on the surface of the samples using a special focusing system. The beam was moved across the sample’s surface using a high-speed scanning system based on galvanometer mirrors. The maximum output power of the laser in the pulse-periodic treatment mode varied in the range of 3–20 W (which corresponds to a radiation power density of about 1.5×10^5–11.2×10^5 W/cm^2 and an energy density of about 48–152 J/cm^2) and in the continuous treatment mode varied in the range of 21–22 W (which corresponds to a radiation power density of about 10.7×10^5–11.2×10^5 W/cm^2 and an energy density of about 0.03–0.1 J/cm^2).

The sample processing time was 1–5 s. The metal surface treatment took place at room temperature (23 °C) and 55% relative humidity.

According to the calculations (as seen in Table 1), the average temperature on the sample surface in the laser treatment zone was: 300.3 °C (for a laser operating in a repetitively pulsed mode) and 308.1 °C (for a continuously pulsed laser). The speed of the laser beam was 0.05 m/s in repetitively pulsed mode and from 0.01 m/s to 0.05 m/s in CW mood. The laser spot diameter was 50 µm for both regimes.

Table 1. Nd:YAG laser parameters used to calculate the temperature.

Processing Mode	Power Density, W/cm^2	Temperature, °C	V, m/s
Periodically pulsed laser radiation treatment	1.5×10^5	294.4	0.05
	9.7×10^5	301.8	
	10.2×10^5	302.2	
	11.2×10^5	303.1	
Continuously pulsed laser radiation treatment	10.2×10^5	313.6	0.01
	10.7×10^5	306.7	0.01
		302.7	0.025
	11.2×10^5	315.7	0.01
		307.3	0.025
		303.1	0.05

When a body is heated by laser radiation, various processes are activated. When determining the main parameters of this process, it is sufficient to estimate the threshold radiation power density q_0 (or threshold power P_n, threshold energy W_n). The threshold radiation power density shows the value at which the specified changes begin to occur in the irradiated material. The theoretical value q_n is defined as the value of the incident radiation power density, q_0, at which the maximum temperature of the processed material reaches the value T* corresponding to the beginning of this process. Threshold characteristics can be determined from an expression that determines the temperature on the surface of the body in the centre of the irradiated area in the form of a circle with a radius r_0 at the end of the exposure period. For irradiation in the volume absorption mode, these expressions are presented in Equations (1) and (2). In the presented technological process of laser processing, the treated surface is scanned with a laser beam. The results of thermal exposure depend on the scanning speed used.

The temperature was calculated for the repetitively pulsed and continuously pulsed treatment modes according to Equations (1) and (2):

$$T = \frac{2q_0A\sqrt{D\tau}}{k\sqrt{\pi}} + T_i, \tag{1}$$

$$T = \frac{2}{\sqrt{\pi}} \frac{q_0(1-R)}{K} \frac{\sqrt{2Dr_0}}{V_{sp}} + T_i, \tag{2}$$

where: q_0—laser radiation power density; K—thermal conductivity coefficient; D—temperature conductivity; r_0—spot radius; R—metal surface reflectance coefficient; k—thermal conductivity; τ—duration of exposure; T_i—initial temperature; V_{sp}—speed of the laser beam movement relative to the sample surface (scanning speed); A—absorptive capacity of the material.

The values of all the variables used in the calculations are given in Table 2.

Table 2. Carbon steel parameters used to calculate the temperature on the surface.

R	D, m^2/s	K, W/m·K	r_0, cm	T_0, K
0.63	1.172×10^5	50	0.0025	293

Using a JSM-5610 LV scanning electron microscope (Japan) equipped with the EDX JED-2201 chemical analysis system, SEM images of the treated steel surface were obtained and the elemental composition of the samples was determined.

The change in the surface roughness of the metal was recorded using the contact microprofilometer HOMMEL TESTER T8000 (produced by Hommelwerke GmbH, Germany), and a 3D model of the structure surface was obtained using the stylus profilometer KLA Tencor: P-7 (produced by KLA-Tencor, Milpitas, CA, USA).

In addition, the microstructure of the material surface was examined using an optical light microscope Leica DMI 5000 (produced by Leica Microsystems, Wetzlar, Germany).

3. Results

Figure 2 shows an image of the steel surface before treatment with a laser beam, which was recorded using a scanning electron microscope JSM-5610 LV.

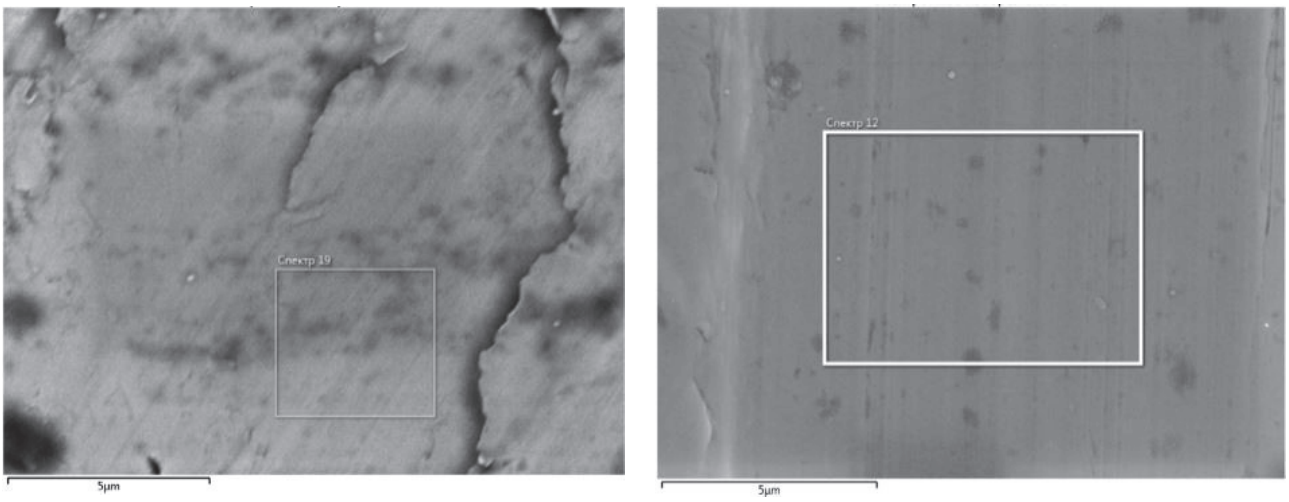

(**a**) (**b**)

Figure 2. SEM image of the surface steel (**a**) before laser treatment and (**b**) after laser treatment (before connection with chemical reagent).

Under the impact of a laser, anticorrosion layers were formed on the steel surface as a result of the microstructure of a thin surface layer of the steel. Figure 2b shows an image of the steel surface after the laser treatment obtained under a microscope. The effect of laser radiation on the surface of Steel 20 contributed to a slight change in the chemical composition. It was found that the laser treatment resulted in a local redistribution of iron and carbon in the surface layer of the steel, leading to the formation of iron carbide (Fe_3C). This effect can be associated with the significant heating of the metal surface.

The changes in the surface roughness of the metal are presented in Table 3. The results obtained allow us to conclude that a significant decrease in the surface roughness of the steel under the influence of a Nd:YAG laser can be obtained using only continuous laser radiation. In Table 3, the samples in which a decrease in surface roughness was observed (from value $R_a = 0.53$ µm to $R_a = 0.38$ µm) are highlighted in green; the best result was obtained for No. 7.

In Table 3, the values R_a and R_z are the arithmetic averages of the absolute values of the deviations of the surface profile within the base length and the sum of the average absolute values of the heights of the five largest profile protrusions and the five largest profile dips within the base length, respectively.

Additionally, the microstructure of the surface of the model samples obtained using an optical light microscope was examined. For metallographic studies, only these samples were selected, the surface roughness of which significantly decreased as a result of laser treatment (in Table 3, they are highlighted in green). For this purpose, the microspecimens used for the qualitative and quantitative analyses of the structure of carbon steel were created. The microspecimens were etched in a 5% solution of nitric acid with the addition of water. Figure 3 shows a general view of the etched surface, and it can be concluded that the steel under examination had a ferrite-pearlite structure.

Table 3. The surface roughness of the model samples before and after laser treatment by Nd:YAG laser.

№	**Processing Mood**	**Treated Material**	
		R_a, μm	**R_z, μm**
1	Treatment with pulsed-periodic laser radiation	1.22	7.20
2	Continuous laser radiation treatment	0.47	2.86
3	Continuous laser radiation treatment	0.44	2.80
4	Treatment with pulsed-periodic laser radiation	1.40	9.05
5	Continuous laser radiation treatment	0.61	4.10
6	Continuous laser radiation treatment	0.60	3.71
7	Continuous laser radiation treatment	0.49	2.76
8	Treatment with pulsed-periodic laser radiation	1.12	7.65
9	Continuous laser radiation treatment	0.38	3.17
10	Continuous laser radiation treatment	0.51	3.62
11	Treatment with pulsed-periodic laser radiation	0.70	5.85
12	Continuous laser radiation treatment	0.40	2.72
	Raw material	0.53	3.66

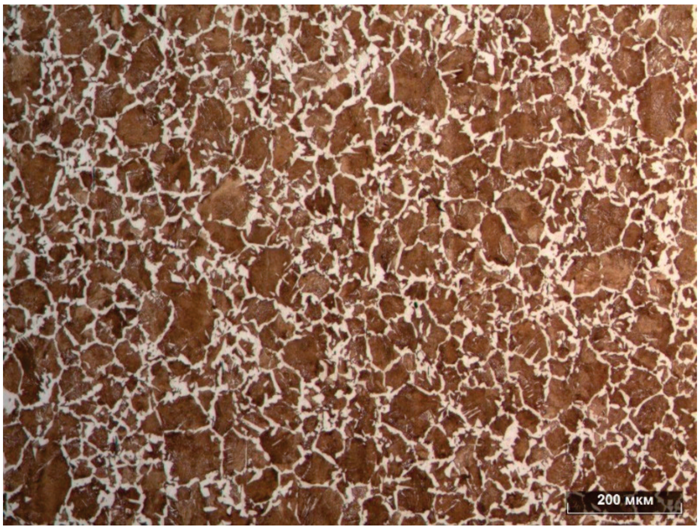

Figure 3. The surface of the etched micro-sections under a microscope at 100× magnification.

Among the analysed samples (Table 3), the best results were shown by samples No. 7 and No. 12.

Figures 4 and 5 show the microstructure of the steel surface treated with an Nd:YAG laser. At the edge of the macrophotography in the cross-section of the micro specimen in Figures 4 and 5, we can clearly see a white stripe, which is a corrosion-resistant layer of steel formed as a result of laser treatment. The best results were obtained with strong carbon diffusion.

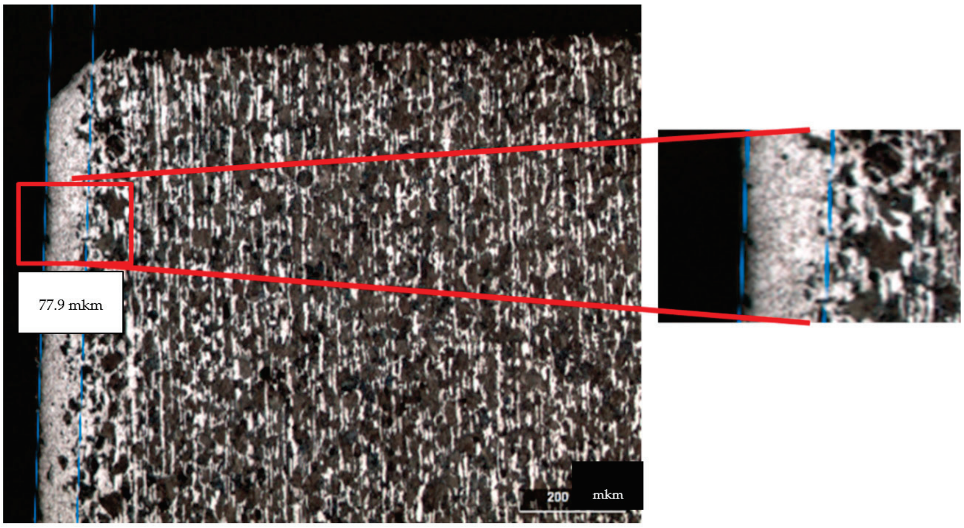

Figure 4. An image of the transverse structure of the microscope of the Nd:YAG laser-treated steel surface obtained with an optical microscope. Sample No. 7.

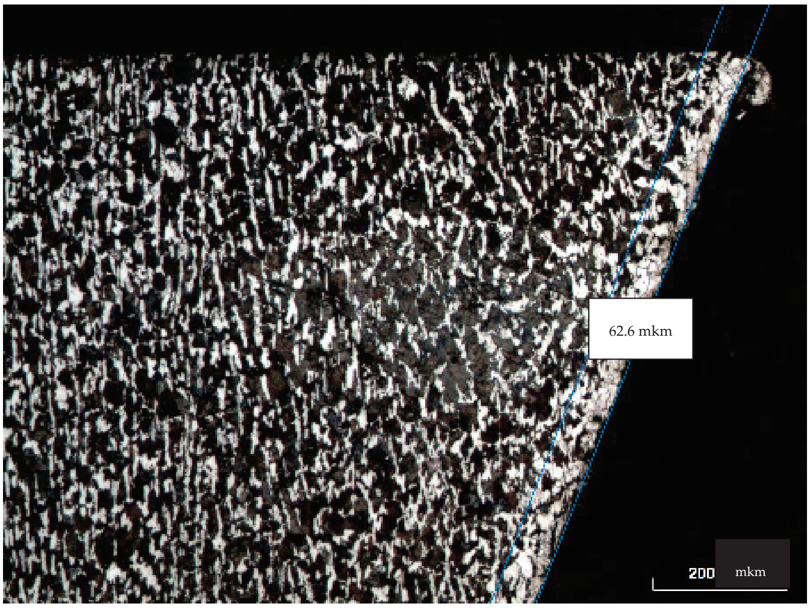

Figure 5. An image of the transverse structure of the microscope of the Nd:YAG laser-treated steel surface obtained with an optical microscope. Sample No. 12.

Sample No. 7 distinguishes itself by a pronounced dense protective layer with an h = 77.9 µm thickness. A decrease and compaction of the grains is evident, which is a positive result and indicates the high quality of the layer and its high corrosion resistance. The disadvantages of this treatment mode (power density $q = 10.2 \times 10^5$ W/cm^2) include the uneven temperature distribution across the sample; as a result, in some places, a decrease in thickness to h = 31.5 µm and a porous structure are observed.

Sample No. 12 is distinguished by a uniformly distributed protective layer with an h = 62.5 µm thickness. A decrease and compaction of the grains can be seen, which is a positive result, as in sample No. 7. The disadvantages of this treatment mode (power density $q = 10.7 \times 10^5$ W/cm^2) include the insufficiently dense anticorrosion coating structure, similar to that of sample No. 7.

Samples with the best treatment results were subjected to corrosion testing. The following solutions were chosen as the electrolyte for the electrochemical method used for determining the corrosion rate: 3% NaCl and 3% Na_2SO_4. These solutions were chosen due to the fact that they simulate the occurrence of real aggressive conditions in the natural environment during the storage and operation of historical monuments. The samples prepared for testing were coated with a layer of hot adhesive compound made of rosin with wax, leaving the untreated area of about 0.54 cm^2, and afterwards were placed into the abovementioned saline solutions. Figure 6 shows the results obtained from measuring the electric potential over time on a steel surface not treated with a laser, which were adopted as standard. The measurements were carried out using the IPC-Pro M potentiostat. As a result of testing in both solutions, an active release of iron (Fe) into the environment was observed, leading to active corrosion processes.

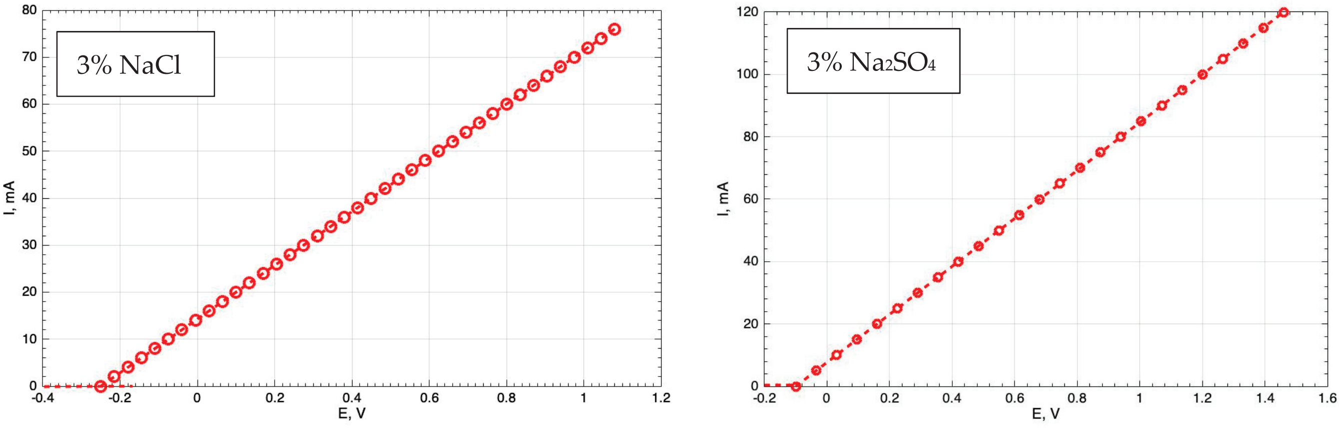

(**a**) (**b**)

Figure 6. Potentiostatic polarisation curves on the untreated laser surface of steel in (**a**) 3% NaCl and (**b**) 3% Na_2SO_4.

It is impossible to create potentiostatic polarisation curves for the samples with protective coatings. However, as a result of these corrosion studies, it was found that the coatings formed on the surface of the steel samples using an Nd:YAG laser do not transmit electric current, and this confirms the fact that the obtained anticorrosion coatings have high protective properties. This is an important advantage of the anticorrosion coatings obtained by laser treatment.

4. Discussion

The conducted studies have shown the potential of enhancing the corrosion resistance of steel through treatment with continuous and repetitively pulsed Nd:YAG laser radiation generated at a wavelength of 1.064 μm. As a result of these experiments, the optimal operating modes of the laser treatment were determined, including the level of radiation power density at which the formation of a protective anticorrosion layer takes place. This is around 10.2×10^5 W/cm^2 and 10.7×10^5 W/cm^2 for the continuous and repetitive laser generating modes, respectively. Under such conditions, a protective anticorrosion coating with a thickness of about 62−77 μm was obtained on the steel surface.

It should be noted that in the experiments an interesting effect was observed. As a result of the laser processing of steel, various colour shades (including blue and light-blue colours) sometimes appeared on its surface; see Figure 7.

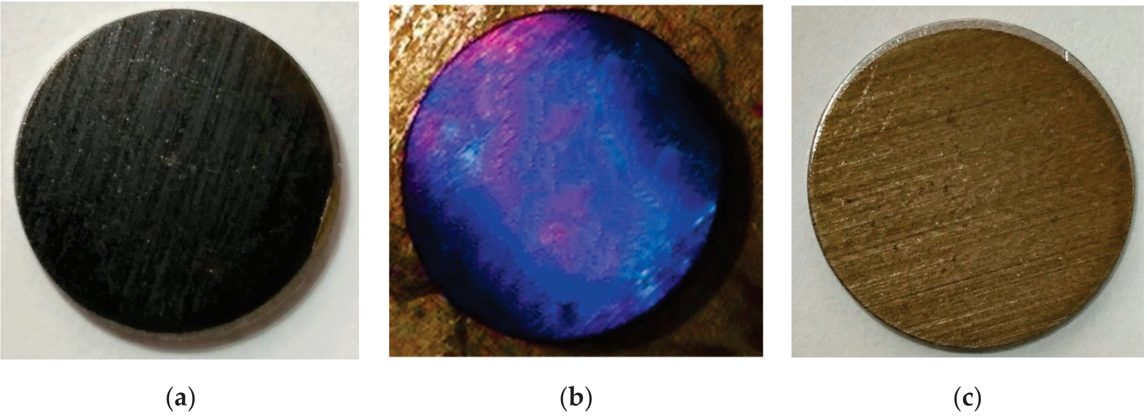
(**a**) (**b**) (**c**)

Figure 7. Colour shades on the steel surface after laser treatment: (**a**) black; (**b**) blue; (**c**) gold.

This opens up possibilities for the use of Nd:YAG lasers to restore the artistic finishing (colour appearance) of decorative art objects made of steel. The possibility of carrying out this restoration task with the help of laser treatment has been discussed previously in one of our articles [12].

Regarding the results obtained in this work, the main conclusion that can be drawn on the basis of the experimental studies conducted lies in the fact that the laser treatment of iron-based metallic materials using continuous-wave and repetitively pulsed Nd:YAG lasers generated at a wavelength of 1.064 μm allows the problem of the passivation of the surface of such materials to be solved. Therefore, the approach proposed in this article may be considered as a promising way to passivate the surface of CH objects created from iron, steel, and cast iron. However, it should be noted that this conclusion is preliminary and needs experimental validation. Since, in these experiments, we used only model samples in order to make our conclusions more general, it is necessary to conduct experiments on the laser passivation of authentic historical artifacts, the surfaces of which are inhomogeneous as a result of weathering and the removal of corrosion layers in the course of conservation works. The authors do plan to carry out such studies in the near future in collaboration with professional restorers.

Meanwhile, it is without doubt that laser treatment allows one to defend newly created metallic artworks against corrosion.

5. Conclusions

The experimental results obtained regarding the laser treatment of carbon steel model samples by the radiation of repetitively pulsed and continuous-wave 1.064 μm Nd:YAG lasers are described in the present article. We can conclude that the laser treatment allows the formation of dense protection films on the steel surface, which enhance the anticorrosion properties of the metal. The application of Nd:YAG lasers is a promising means for the surface passivation of artworks created from steel and cast iron. One possible explanation for this may be that laser treatment results in the local redistribution of iron and carbon in the surface layer of the steel, which leads to the formation of iron carbide (Fe_3C). This effect can be associated with the significant heating of the metal surface. It is known from the scientific literature [13] that, under a temperature change in steel in the range of 600–100 °C (which fits our case), the elements iron (Fe), cobalt (Co) and nickel (Ni) can form carbide iron (Fe_3C) due to chemical reactions with carbon. The specified microstructuring of the steel surface can increase its corrosion resistance. The iron pillar of Delhi is an example of steel with a high percentage of Fe being saved from corrosion.

Author Contributions: Conceptualisation, I.R. and V.P.; methodology, I.R., V.P. and O.V.; validation, I.R., V.P. and O.V.; formal analysis, O.Z.; investigation, O.Z. and A.Z.; resources, O.V.; data curation, I.R.; writing—original draft preparation, I.R.; writing—review and editing, V.P.; visualisation, I.R.; supervision, V.P.; project administration, I.R. All authors have read and agreed to the published version of the manuscript.

Funding: This research received no external funding.

Institutional Review Board Statement: Not applicable.

Informed Consent Statement: Not applicable.

Data Availability Statement: The data supporting the findings of this study are available from the corresponding author upon reasonable request.

Acknowledgments: The authors would like to thank V.G. Bondarenko and S.R. Rustamov (both are with the R&D Institute "Polyus", Moscow) for their assistance in experiments using Nd:YAG lasers.

Conflicts of Interest: The authors declare no financial or commercial conflict of interest.

References

1. Nikitin, M.K.; Melnikova, E.P. *Chemistry in Restoration*; Khimiya: Leningrad, Russia, 1990.
2. Emelyanenko, A.M.; Shagieva, A.G.; Domantovsky, A.G.; Boinovich, L.B. Nanosecond laser micro- and nanotexturing for the design of a superhydrophobic coating robust against long-term contact with water, cavitation, and abrasion. *Appl. Surf. Sci.* **2015**, *332*, 513. [CrossRef]
3. Vorobyev, A.Y.; Ghunlei, G. Multifunctional surfaces produced by femtosecond laser pulses. *J. Appl. Phys.* **2015**, *117*, 3. [CrossRef]
4. Osticioli, I.; Siano, S. Dependence of Nd: YAG laser derusting and passivation of iron artifacts on pulse duration. In Proceedings of the SPIE 9065, Fundamentals of Laser-Assisted Micro- and Nanotechnologies, St. Petersburg, Russia, 24–28 June 2013; p. 906513.
5. Siano, S.; Agresti, J.; Cacciari, I.; Ciofini, D.; Mascalchi, M.; Osticioli, I.; Mencaglia, A.A. Laser cleaning in conservation of stone, metal, and painted artifacts: State of the art and new insights on the use of the Nd: YAG lasers. *Appl. Phys. A* **2012**, *106*, 419. [CrossRef]
6. Tareen, J.; Krishnamurthy, K.V. Hydrothermal stability of hematite and magnetite. *Bull. Mater. Sci.* **1981**, *3*, 9. [CrossRef]
7. Vasiliev, O.V.; Veiko, V.P.; Gornyi, S.G.; Ruzankina, Y.S. Laser apparatus for microstructuring a metal surface, using a fiber laser. *J. Opt. Technol.* **2015**, *82*, 831. [CrossRef]
8. Ruzankina, J.S.; Parfenov, V.A.; Vasiliev, O.S. Anti-corrosion prevention of carbon steel by means of laser treatment. *Laser Phys.* **2019**, *29*, 015203. [CrossRef]
9. Iakovlev, A.; Ruzankina, J.; Kasheev, S.; Vasilyev, O.; Parfenov, V.; Grishkanich, A. Laser anti-corrosion treatment of metal surfaces. In Proceedings of the SPIE 10097, High-Power Laser Materials Processing: Applications, Diagnostics, and Systems VI, San Francisco, CA, USA, 28 January–2 February 2017; p. 100970S.
10. Ruzankina, J.S.; Vasiliev, O.S. Study on possibility for the improvement of corrosion resistance of metals using laser-formed oxide surface structure. *J. Phys. Conf. Ser.* **2016**, *735*, 012050. [CrossRef]
11. Ruzankina, J.S.; Vasiliev, O.S.; Parfenov, V.A. Anti-corrosion treatment of metal surfaces based on photonics methods. *J. Phys. Conf. Ser.* **2017**, *917*, 062039. [CrossRef]
12. Gerashenko, M.D.; Parfenov, V.A. Formation of non-ferrous oxide films on the surface of metals under the influence of laser radiation. *Bull. St. Petersburg State Electrotech. Univ. LETI* **2011**, *3*, 68.
13. Glinka, N.K. *Nauka*; Khimiya: Moscow, Russia, 2017; p. 752.

quantum beam science

MDPI

Article

Laser Peening Analysis of Aluminum 5083: A Finite Element Study

Ali Tajyar [1], Noah Holtham [1], Nicholas Brooks [1], Lloyd Hackel [2], Vincent Sherman [2], Ali Beheshti [3] and Keivan Davami [1,*]

[1] Department of Mechanical Engineering, The University of Alabama, Tuscaloosa, AL 35487, USA; atajyar@ua.edu (A.T.); nholtham@crimson.ua.edu (N.H.); nabrooks1@crimson.ua.edu (N.B.)
[2] Curtiss Wright Surface Technologies, Metal Improvement Company, Livermore, CA 94551, USA; Lloyd.Hackel@cwst.com (L.H.); Vincent.Sherman@cwst.com (V.S.)
[3] Department of Mechanical Engineering, George Mason University, Fairfield, VA 22030, USA; abehesh@gmu.edu
* Correspondence: kdavami@eng.ua.edu

Abstract: In this research, a finite element (FE) technique was used to predict the residual stresses in laser-peened aluminum 5083 at different power densities. A dynamic pressure profile was used to create the pressure wave in an explicit model, and the stress results were extracted once the solution was stabilized. It is shown that as power density increases from 0.5 to 4 GW/cm^2, the induced residual stresses develop monotonically deeper from 0.42 to 1.40 mm. However, with an increase in the power density, the maximum magnitude of the sub-surface stresses increases only up to a certain threshold (1 GW/cm^2 for aluminum 5083). Above this threshold, a complex interaction of the elastic and plastic waves occurring at peak pressures above ≈2.5 Hugoniot Elastic Limit (HEL) results in decreased surface stresses. The FE results are corroborated with physical experiments and observations.

Keywords: laser peening; finite element method; residual stress; Al5083

1. Introduction

Laser technology has been used excessively utilized in material processing and manufacturing techniques such as forming [1], peening [2], additive manufacturing [3], cladding [4], and welding [5]. Among them, laser peening (LP) is an innovative post-processing technique used in the industry to mitigate surface-related failures such as corrosion, fatigue, fretting fatigue, corrosion–fatigue, etc. This versatile technique is also used to form complex shapes and structures [6]. Compared to other similar surface engineering methods such as shot peening [7], water jet peening [8], and ultrasonic peening [9], LP is advantageous as it generates deeper residual stresses with increased thermal stability that is attributed to the lower amount of cold work [10]. However, to achieve the full potential of this technique, a precise understanding of the peening process along with the effects of different process parameters are required [11].

Many experimental studies have focused on parameter optimization of the LP process and the effects of LP on the mechanical properties and material performance [12–15]. However, far fewer attempts have been made to fundamentally understand the wave propagation and corresponding residual stress distribution [16]. This is, of course, anticipated as in situ monitoring of the residual stress distribution during peening is extremely challenging if not impossible [11]. Thus, a hybrid experimental and simulation approach enables an improved understanding of how adjusting various peening parameters affects the pressure wave as it propagates through the material as well as the final state of residual stresses.

The literature contains several studies focused on the numerical simulation of the LP process. Braisted et al. [17] used a combination of explicit and implicit dynamic analysis algorithms in ABAQUS to study the residual stresses induced by the LP process in Ti-6Al-4V as well as 35 CD4. Ding et al. [18] expanded their approach from 2D to 3D and implemented an HEL plastic model to study different LP processing conditions in different metal alloys. Peyre et al. [19] also applied a finite element method (FEM) along with the Johnson–Cook plasticity model to simulate the LP process through 2D axisymmetric FE models for martensitic stainless steel and 7075 aluminum. These studies, among others [20–23], provided improved insight into the LP process and contributed immensely to the process optimization.

In this research, the effects of power density on the magnitude and distribution of the residual stresses in the LPed Al 5083 were studied. Al 5083 is an emerging material of choice for applications in aerospace and marine industries due to its high strength-to-weight ratio as well as other outstanding attributes [24]. While this alloy is widely used in different sectors, the literature has few experimental studies on LP of Al 5083, which are mainly focused on its corrosion cracking behaviors [24,25]. However, no analytical effort has been attempted to quantitatively understand the effect of the LP process on the Al 5083 state of residual stress. This work provides the first combined experimental and numerical analysis on the LP of Al 5083, with new insights on how the laser power density affects the magnitude, depth, and distribution of the induced residual stresses in the alloy.

2. 3D Simulation of the Laser Peening Process

A 3D FE model was created using ABAQUS software to investigate the impact of a single layer LP with different power densities on Al5083 specimens. The overall dimensions of the specimen were modeled to be 12 mm × 12 mm × 7 mm, where an axisymmetric quarter of the block was only considered (Figure 1). Following the experimental conditions discussed later, the simulations were carried out with four power densities of 0.5, 1, 2, and 4 GW/cm^2, which produce peak pressures (P_{Peak}) of 0.72, 1.02, 1.44, and 2.44 GPa. Pressure loading condition was estimated based on the methodology developed by Fabbro et al. [26–28]. Detailed explanation of the method is provided in supplementary materials—Supplementary Information (SI), Section S1.1.

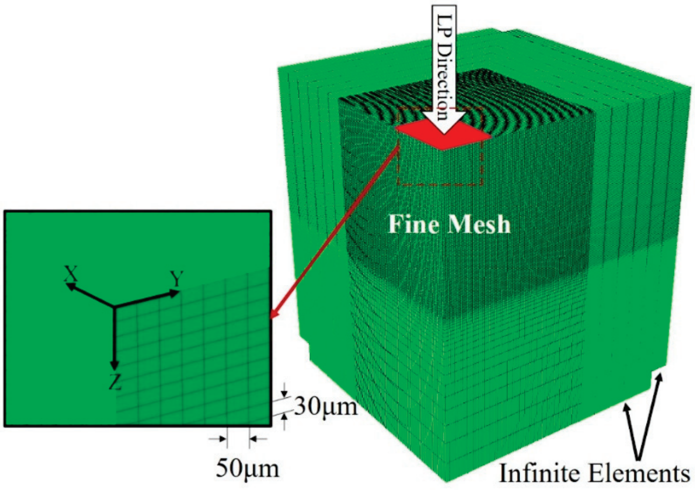

Figure 1. A three-dimensional model used in the FE simulation of the LP process.

The target material was assumed to be initially stress free and considered to be elastic–plastic, homogeneous, and isotropic. It is known that in the LP process, the material becomes deformed at an extremely high strain rate (up to 10^7 s^{-1}); therefore, the constitutive relations obtained from quasi-static conditions are not valid. As a result, herein, the Johnson–Cook (JC) model, being capable of predicting the material response to high strain rates and large deformations, was selected for the simulation. The JC model relates the strain hardening, the strain rate effects, and thermal effects to the flow stress in material expressed as:

$$\sigma = \left[A + B\varepsilon_p^n\right]\left[1 + Cln\frac{\dot{\varepsilon}}{\dot{\varepsilon}_0}\right]\left[1 - \left(\frac{T - T_0}{T_m - T_0}\right)^m\right] \tag{1}$$

where A, B, n, C, and m are the material constants; ε_p represents the equivalent plastic strain; $\dot{\varepsilon}$ and $\dot{\varepsilon}_0$ are the plastic strain rate and the reference plastic strain rate, respectively. A is defined as the yield strength; B denotes the strain-hardening modulus; n is the strain-hardening exponent; and C accounts for the strain rate-hardening effect. T is the temperature in Kelvin and T_0, T_m, and m are the room temperature, the melting point of material, and the power of thermal softening, respectively. Since in the LP technique, the thermal effect of the process is negligible compared to the mechanical effects, the temperature term in the JC model could be eliminated. The properties of Al 5083 used here were adopted from Refs. [29,30] for the dynamic response of Al 5083 and are listed in Table 1.

Table 1. Material properties and Johnson–Cook parameters of Al 5083 [29,30].

Material Properties	
Density, ρ (kg/mm^3)	2.7×10^{-6}
Young's modulus, E (GPa)	70
Poisson's ratio, ν	0.3
Hugoniot elastic limit (HEL), (GPa)	0.57
Johnson–Cook parameters	
A (MPa)	167
B (MPa)	596
C	0.001
m	0.859
n	0.551
$\dot{\varepsilon}_0$	1

To enhance the accuracy of the model as well as facilitate obtaining a converged plastic strain distribution, a finer mesh was used in and around the pulse area where elements of 0.05 mm × 0.05 mm × 0.03 mm were chosen (Figure 1). C3D8R, a continuum solid eight-node reduced integration element, was chosen as the element type. To reduce the analysis time, a coarser mesh was implemented outside of the critical region. Stress waves reflected from the back and bottom surfaces can lead to an error in the analysis; hence, to mitigate this problem, infinite elements (CIN3D8) were implemented along the back and bottom surfaces (Figure 1) so that the stress waves were able to pass through. The numbers of finite and infinite elements in the model were 873,375 and 26,925, respectively.

Each simulation included two steps. In the first step and following the experimental procedure, a square laser spot (3 mm × 3 mm) with a very high pressure was applied on the top surface of the specimen in a short time. In the second step, to assure obtaining a stabilized solution, the stress results were given sufficient time to relax. ABAQUS/Explicit was used for the analysis of both first and second steps. While previously a combination of dynamic explicit analysis and static analysis has been typically used in the literature [16,31–33], it has been also shown that a pure explicit model can be also utilized for both steps if the proper solution time is considered for each step [10,21,34,35]. Further information about the calculation of solution times for step one (to ensure the occurrence of all the plastic deformation in the material), and step two (to obtain the equilibrium of stresses in the material) is provided in SI (Section S1.2).

3. Experiments

3.1. LP Process

A Q-switched Nd:YLF laser was employed to do the laser peening on the AL5083 specimens. The spots had a square shape with dimensions of 3 mm × 3 mm. Specimens were moved using a robotic arm for placing laser impact spots with 100 micron accuracy. A de-ionized (15 M ohm resistance) water layer of ≈1 mm thickness acting as a plasma tamper was flowed over the specimen to be peened. The laser energy passes through the water layer, forms a plasma during the first nanosecond of the pulse, and heats the plasma approximately to 13,000 K. By controlling the distance between the specimen surface and the final imaging lens, the power density was adjusted to achieve a plasma pressure, which was confined by the tamping layer that rises in pressure to above the HEL of the material. It should be added that here, the laser spot was not focused on to the target, so there is no issue of inexact focusing. In addition, breakdown in the current system with the relay imaging was tested where water breakdown only occurred above a power density of 12 GW/cm^2, which is much higher than the power density values used in this study. In this study, four power densities of 0.5, 1, 2, and 4 GW/cm^2 with 18 ns laser pulse duration were selected for the experiments. It is worth noting that given the laser pulse properties and since the heat capacity of the metal is sufficiently high, only a few dozens of microns of the metal experience the heating in the LP process.

3.2. Residual Stress Measurement

A portable X-ray diffraction (XRD) analyzer, Pulstec μ-X360 (Pulstec Industrial Co., Ltd., Hamamatsu, Japan) using the cosα method (detailed information of method are described in the SI, Section S2) was utilized to characterize the surface and in-depth residual stress. A low-intensity Cr $K\alpha$ source was employed to irradiate a 2 mm diameter spot for 30 s, while an image plate was positioned normal to the incident beam at a sample-to-detector distance of ≈39 mm collecting diffracted X-rays. The X-ray incidence angle was set to 25° and the X-ray tube voltage and current were 30 kV and 1.50 mA, respectively. Since the XRD techniques are only able to measure the surface-level stress, material was removed from the surface by an electrolytic polishing machine (Proto, Proto 8818-V3, Proto Manufacturing Inc., Taylor, MI, USA) and a saline electrolyte (Proto Electrolyte A, Proto Manufacturing Inc., Taylor, MI, USA) for in-depth residual stress measurements. The material was carefully etched in four separate regions on each sample corresponding to four different depths of ≈50, 100, 150, and 200 μm, which created circular areas (5 mm diameter) suitable for XRD measurement (Section S2, Figure 2). The precise depth measurement was performed on etched regions with a stylus profilometer (Alpha-Step D-500, KLA-Tencor, Milpitas, CA, USA).

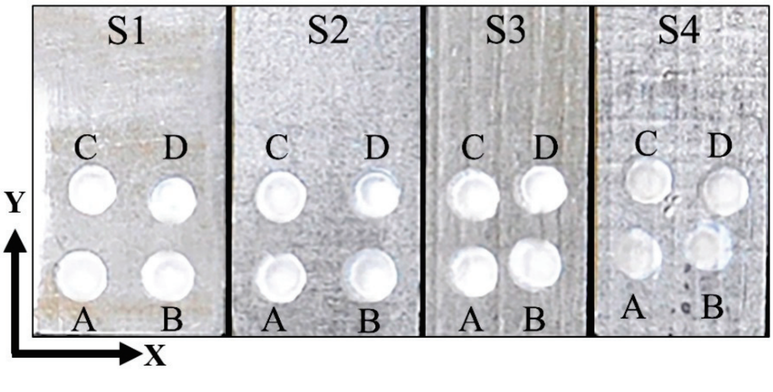

Figure 2. The circular etched regions (A–D) used for residual stress measurement on the four different laser-peened samples (Samples S1–S4 were laser peened with power densities of 0.5, 1, 2, and 4 GW/cm^2, respectively).

4. Results and Discussion

Figure 3 compares the numerical simulation results for the residual stresses along with their experimentally obtained values. The stresses were measured at different depths up to 200 μm. The experimental residual stress values for each point can be considered as the average residual stress within the measured area that is exposed to the X-ray beam. The simulation results were obtained from the average of the residual stress values of nodes along a path from the center to the edge of a peened spot.

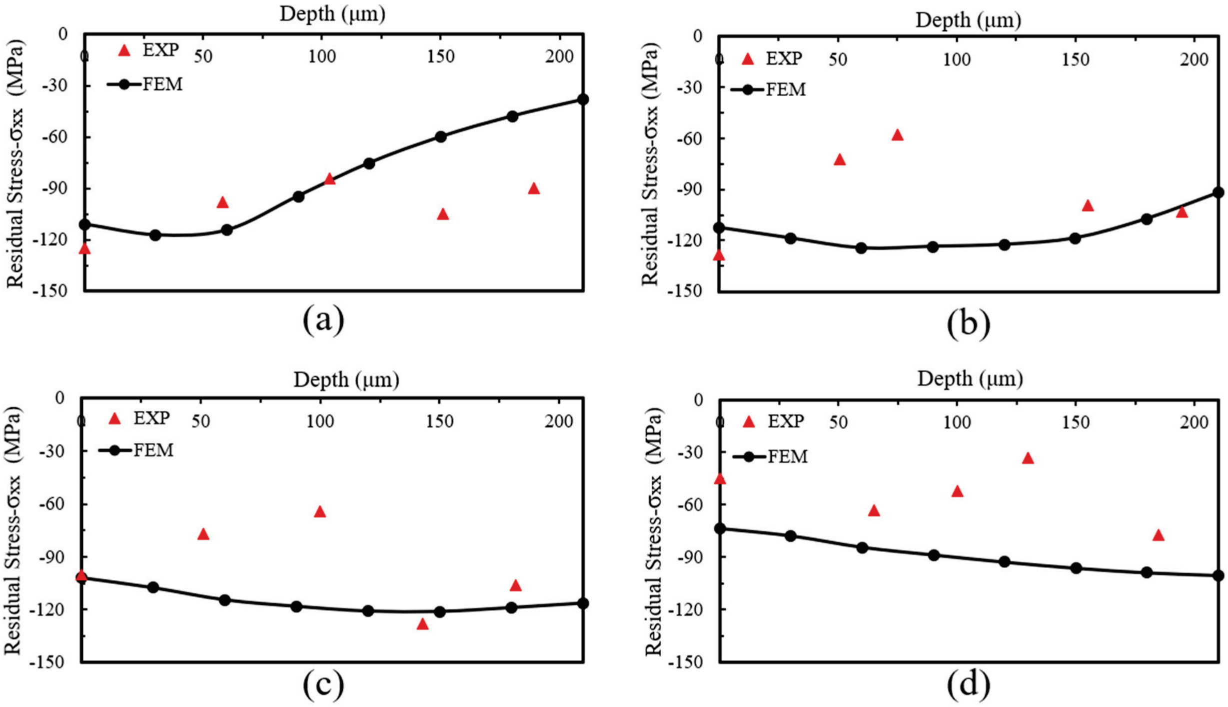

Figure 3. Comparison of residual stresses versus distance (in depth) from the LP face between simulation and experiment for different power densities: (**a**) 0.5 GW/cm^2, (**b**) 1 GW/cm^2, (**c**) 2 GW/cm^2, and (**d**) 4 GW/cm^2.

As shown in Figure 3, only a slight difference in the compressive residual stresses is observed with an increase in power density from 0.5 to 2 GW/cm^2. However, at a power density of 4 GW/cm^2, a considerable decrease in the compressive residual stress values is observed for both simulation and experimental results with a majority of the points having a value less than −90 MPa. While FE analysis is able to successfully predict general experimental trends, there are differences between stress values. The differences might be attributed to couple of factors. The main factor could be that the μXRD patterns might not perfectly represent the global aluminum diffraction constants, since it was mostly obtained from regions inside grains on very small diffracting crystallites [21]. In addition, the experimental residual stress values were calculated from the whole surface of a peened spot, but the simulated residual stress values were obtained from a line (from the center to the outer edge of the spot). Additionally, for aluminum with a relatively low yield strength, XRD measurements might result in even higher errors since the magnitude of the measured stresses are generally low. Another minor contributing factor is the JC model and its sensitivity on several constants. While material properties were obtained directly from the available data in the literature for Al 5083 that was modeled here, inevitable slight differences may exist between current material constants and those of the reported in the literature that might affect the FE results [10,17].

Figure 4a shows the 3D distribution of σ_{xx} residual stresses with a power density of 2 GW/cm^2. It can be seen that compressive and tensile residual stresses have been developed inside and in the neighboring area of the peened spot, respectively. Figure 4b,c show the distribution of σ_{xx} on the surface with different laser power densities along the x (at y = z = 0) and y (at x = z = 0) axes, respectively. The residual stresses in the peened spot are compressive in both x and y directions. This indicates that all four power densities, 0.5 GW/cm^2, 1 GW/cm^2, 2 GW/cm^2, and 4 GW/cm^2, are able to generate peak pressures that exceed the dynamic yield strength of the material and consequently cause plastic deformation that results in the formation of compressive residual stresses [36].

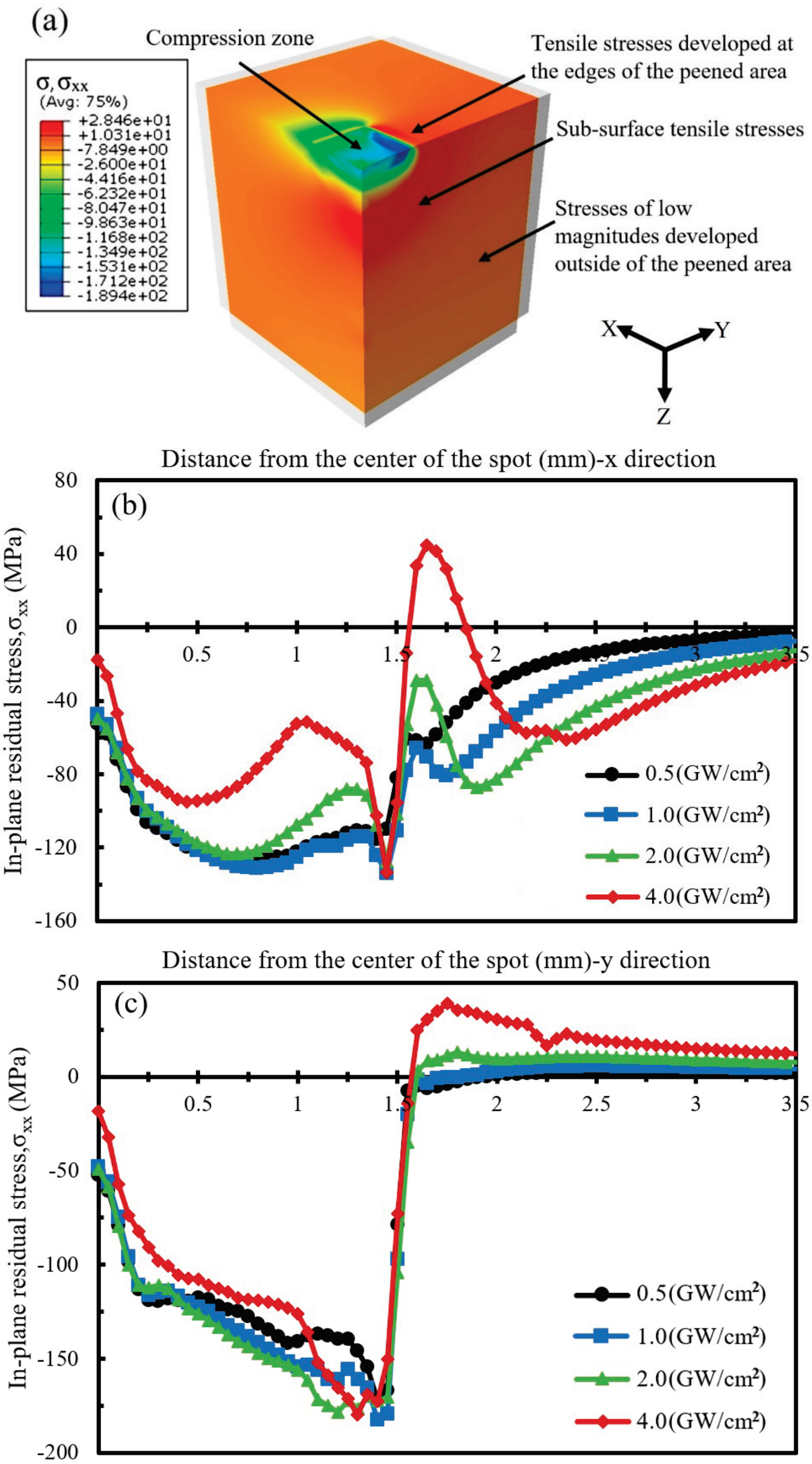

Figure 4. (**a**) In-plane residual stress (σ_{xx}) distribution for specimen with a power density of 2 GW/cm^2, (**b**,**c**) Distribution of σ_{xx} along the x and y axes at the surface for different power densities.

Surprisingly, the maximum value of the residual stresses is not predicted to be at the center of the laser spot (Figure 4a–c). This phenomenon, called residual stress hole (or "stress empty"), was reported for both square and circular spots [37,38]. The residual stress hole may in large part be due to the concentration of the rarefaction waves that are generated by the edges of the peened area at the spot center and reverse plastic deformation. Li et al. [39] explained this phenomenon in a similar way where they attributed the formation of the stress hole to the removal of the compressive stresses at the center of the spot due to the large pulses generated from the surface waves expanding radially to the center of the spot. It was reported that there is a relationship between the magnitude of the stresses in the residual stress hole on the surface and the wave peak pressure, P_{Peak}.

As depicted in Figure 4b, there are spatially abrupt changes in the stress values at the edge of the spot ($x = \approx 1.5$ mm), which are more pronounced when the power density increased from 0.5 to 4 GW/cm^2. It is notable that the residual stresses for the power density of 4 GW/cm^2 in the x direction transition from compressive to tensile to compressive when moving from the spot center to the outside edge. Additionally, the magnitude of surface residual stresses for 4 GW/cm^2 is lower than that for other power densities (Figure 4b). However, along the y direction, more uniform residual stress profiles were observed for all power densities (Figure 4c). There is an intensified peak in compressive stresses around the boundaries of the pulse area, which is followed by a rapid reduction and conversion to tensile stress outside of the spot (Figure 4c). For the power density of 4 GW/cm^2 (P_{Peak} = 2.04 GPa), the residual stress drop at the center is more pronounced in comparison to the other three power densities in both the x and y directions.

Figure 5 shows the variation of σ_{xx} and σ_{yy} with the depth. In order to avoid the effect of the residual stress hole, a position with a distance of 0.75 mm from the center of the peened spot ($x = 0.75$ mm, $y = 0$) and located on the symmetry line was selected to collect residual stress variation in depth. It should be also noted that the magnitude of the stress at other locations with close proximity to the center is checked, and a negligible difference between the residual stress values was observed. It can be seen from Figure 5a that at a power density of 0.5 GW/cm^2, compressive stresses are formed up to a distance of $\approx$0.42 mm from the peened surface, and tensile stresses are generated beneath that ($0.42 < z < 3$ mm) to counter-balance the compressive stresses. With an increase in the power density from 0.5 to 4 GW/cm^2, the depth of the compressive residual stresses also increases (from 0.42 for 0.5 GW/cm^2 to 1.40 mm for 4 GW/cm^2). This was expected, as the depth of the compressive residual stresses in an LPed specimen is closely related to the plastically deformed area [40].

The value and depth of the maximum residual stresses for the power density of 0.5 GW/cm^2 are 135 MPa and $\approx$0.03 mm, respectively. The results show that σ_{xx} compressive residual stresses near the surface achieve magnitudes as high as 140 MPa with increasing power density to 1 GW/cm^2 (P_{Peak} = 1.02 GPa) at a depth of $\approx$0.06 mm (Figure 5a). With increasing the power density to 2 GW/cm^2, although the values of residual stresses decrease slightly, the residual stresses are almost constant (in the range of 119.6–125.4 MPa) to the depth of 0.29 mm. Interestingly, while the compressive residual stresses are observed at a greater distance from the surface for the power density of 4 GW/cm^2 compared with lower power densities, the magnitude of compressive residual stresses on the surface and sub-surface drops remarkably. Similar observations have been reported for A356-T6 alloy as well as Steel 1045 previously [38,41]. As shown in Figure 5b, similar results were observed for the σ_{yy} in-plane residual stress.

The observation here agrees well with the model developed by Peyre et al. [41] where the plastic deformation rises linearly when the peak pressure increases from 1 HEL to 2 HEL and its maximum limit is attained at around 2 to 2.5 HEL. Above that, the surface release waves focus and intensify from the edges of the impacts, and this phenomenon leads to the modification of the residual stress field. Therefore, while a power density of 4 GW/cm^2 (P_{Peak} = 2.04 GPa > 2.5 HEL_{Al5083}) generates deeper residual stresses, its magnitudes are smaller remarkably in comparison to those that the power densities of 1 and 2 GW/cm^2 (P_{Peak} = 1.02 and 1.44 G $\cong$ (2 to 2.5) $\times$ HEL_{Al5083}) can generate. This is in agreement with the previously reported findings that materials can be optimally treated with P_{Peak} in (2 to 2.5) $\times$ HEL range [37,41].

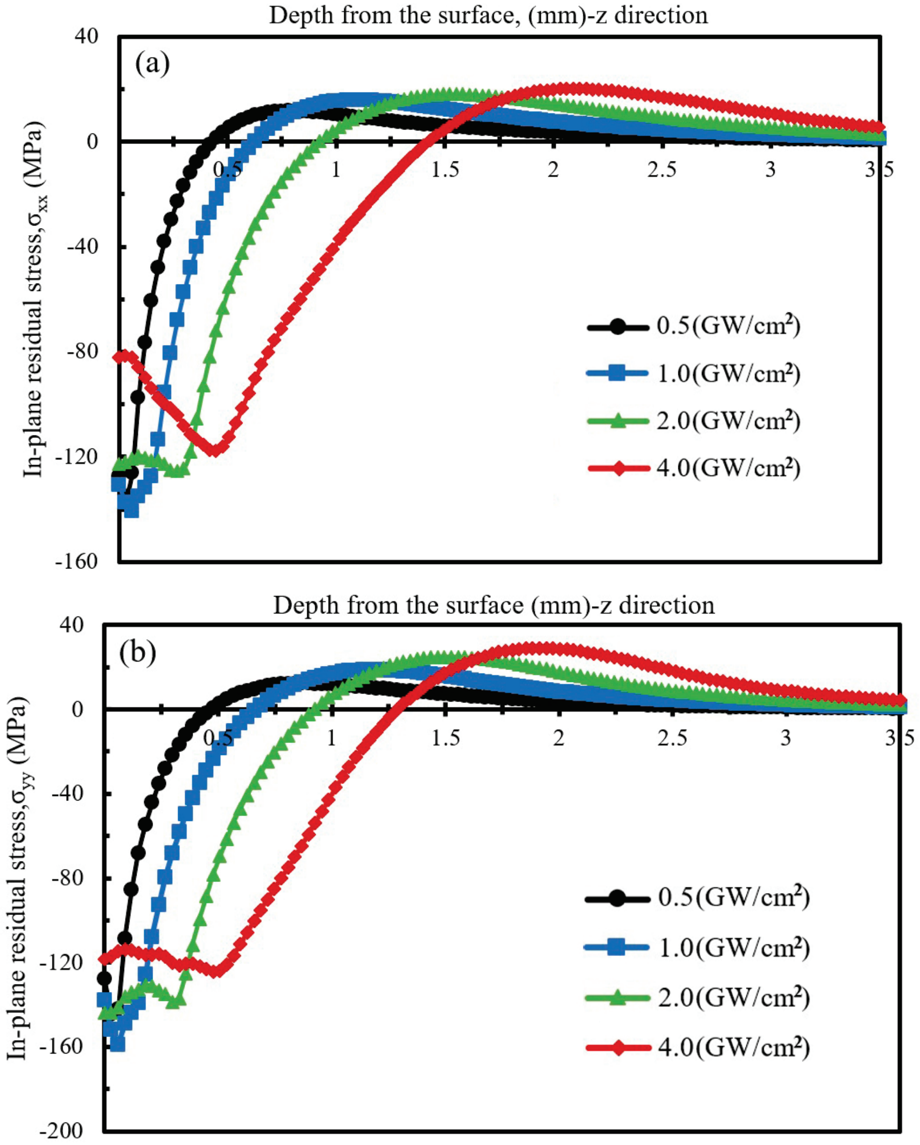

Figure 5. Variation of in-plane residual stress with depth (x = 0.75 mm, y = 0), (**a**) σ_{xx}, (**b**) σ_{yy}.

5. Conclusions

Herein, an explicit model was used to study the effects of four different power densities on the laser peening of aluminum 5083. The magnitude of the generated residual stresses up to a depth of 200 µm was compared with the experimental results. Simulations show a residual stress hole in the middle of the peened spot due to a plastic unloading wave. It was shown that with an increase in the power density from 0.5 to 4 GW/cm^2, residual stresses are generated deeper into the workpiece. At a power density of 4 GW/cm^2, the resulting peak pressure above 2.5 HEL reduced the near surface residual stresses.

Supplementary Materials: The following are available online at https://www.mdpi.com/2412-382X/5/4/34/s1, Figure S1: Temporal pressure profile, Figure S2: (a) History of the internal energy, elastically stored energy, plastically dissipated energy and artificial strain energy during the first step (b) In-plane stress profiles (σxx) versus distance from the center of spot at different calculation times during the second step (A dynamic state towards a residual state). It can be concluded that a quasi-equilibrium state is reached above 100,000 ns. Figure S3: Debye ring measurement schematic.

Author Contributions: Supervision & funding acquisition, K.D.; writing—original draft preparation, A.T.; Formal Analysis, K.D., A.T, N.H., N.B. and A.B.; Methodology, A.T. and K.D.; Review and editing, A.B., L.H., V.S. All authors have read and agreed to the published version of the manuscript.

Funding: Advanced Manufacturing program of the National Science Foundation, award CMMI-AM #2029059.

Institutional Review Board Statement: Not applicable.

Informed Consent Statement: Not applicable.

Data Availability Statement: All the raw data is available upon request.

Acknowledgments: The authors would like to thank Pulstec USA, Inc. and Toshi Suzuki (KLA) for the help with the residual stress measurements. The authors, Russell Rowe and Keivan Davami, extend gratitude to the Alabama Transportation Institute (ATI) for their support of the graduate student involved in this work. Keivan Davami acknowledges the support of the Advanced Manufacturing program of the National Science Foundation, award CMMI-AM #2029059.

Conflicts of Interest: The authors declare no conflict of interest.

References

1. Bachmann, A.L.; Dickey, M.D.; Lazarus, N. Making Light Work of Metal Bending: Laser Forming in Rapid Prototyping. *Quantum Beam Sci.* **2020**, *4*, 44. [CrossRef]
2. Gujba, A.K.; Medraj, M. Laser Peening Process and Its Impact on Materials Properties in Comparison with Shot Peening and Ultrasonic Impact Peening. *Materials* **2014**, *7*, 7925–7974. [CrossRef]
3. Thiede, T.; Mishurova, T.; Evsevleev, S.; Serrano-Munoz, I.; Gollwitzer, C.; Bruno, G. 3D Shape Analysis of Powder for Laser Beam Melting by Synchrotron X-ray CT. *Quantum Beam Sci.* **2019**, *3*, 3. [CrossRef]
4. Zhu, L.; Xue, P.; Lan, Q.; Meng, G.; Ren, Y.; Yang, Z.; Xu, P.; Liu, Z. Recent research and development status of laser cladding: A review. *Opt. Laser Technol.* **2021**, *138*, 106915. [CrossRef]
5. Shobu, T.; Shiro, A.; Kono, F.; Muramatsu, T.; Yamada, T.; Naganuma, M.; Ozawa, T. Internal Strain Distribution of Laser Lap Joints in Steel under Loading Studied by High-Energy Synchrotron Radiation X-rays. *Quantum Beam Sci.* **2021**, *5*, 17. [CrossRef]
6. Munther, M.; Martin, T.; Tajyar, A.; Hackel, L.; Beheshti, A.; Davami, K. Laser shock peening and its effects on microstructure and properties of additively manufactured metal alloys: A review. *Eng. Res. Express* **2020**, *2*, 022001. [CrossRef]
7. Bagheri, S.; Guagliano, M. Review of shot peening processes to obtain nanocrystalline surfaces in metal alloys. *Surf. Eng.* **2009**, *25*, 3–14. [CrossRef]
8. Hayashi, M.; Okido, S.; Suzuki, H. Residual Stress Distribution in Water Jet Peened Type 304 Stainless Steel. *Quantum Beam Sci.* **2020**, *4*, 18. [CrossRef]
9. Malaki, M.; Ding, H. A review of ultrasonic peening treatment. *Mater. Des.* **2015**, *87*, 1072–1086. [CrossRef]
10. Peyre, P.; Chaieb, I.; Braham, C. FEM calculation of residual stresses induced by laser shock processing in stainless steels. *Model. Simul. Mater. Sci. Eng.* **2007**, *15*, 205–221. [CrossRef]
11. Yang, C.; Hodgson, P.D.; Liu, Q.; Ye, L. Geometrical effects on residual stresses in 7050-T7451 aluminum alloy rods subject to laser shock peening. *J. Mater. Process. Technol.* **2008**, *201*, 303–309. [CrossRef]
12. Chupakhin, S.; Klusemann, B.; Huber, N.; Kashaev, N. Application of design of experiments for laser shock peening process optimization. *Int. J. Adv. Manuf. Technol.* **2019**, *102*, 1567–1581. [CrossRef]
13. Palma, T.; Munther, M.; Sharma, M.; Hackel, L.; Beheshti, A.; Davami, K. Nanomechanical Characterization of Laser Peened Additively Manufactured Inconel 718 Superalloy. *Adv. Eng. Mater.* **2019**, *21*, 1900499. [CrossRef]
14. Ren, X.; Chen, B.; Jiao, J.; Yang, Y.; Zhou, W.; Tong, Z. Fatigue behavior of double-sided laser shock peened Ti-6Al-4V thin blade subjected to foreign object damage. *Opt. Laser Technol.* **2020**, *121*, 105784. [CrossRef]
15. Kalainathan, S.; Prabhakaran, S. Recent development and future perspectives of low energy laser shock peening. *Opt. Laser Technol.* **2016**, *81*, 137–144. [CrossRef]
16. Hu, Y.; Yao, Z.; Hu, J. 3-D FEM simulation of laser shock processing. *Surf. Coat. Technol.* **2006**, *201*, 1426–1435. [CrossRef]
17. Braisted, W.; Brockman, R. Finite element simulation of laser shock peening. *Int. J. Fatigue* **1999**, *21*, 719–724. [CrossRef]
18. Ding, K.; Ye, L. FEM simulation of two sided laser shock peening of thin sections of Ti-6Al-4V alloy. *Surf. Eng.* **2003**, *19*, 127–133. [CrossRef]
19. Peyre, P.; Sollier, A.; Chaieb, I.; Berthe, L.; Bartnicki, E.; Braham, C.; Fabbro, R. FEM simulation of residual stresses induced by laser Peening. *Eur. Phys. J. Appl. Phys.* **2003**, *23*, 83–88. [CrossRef]
20. Xiao, Y. Effect of laser shock peening on bending fatigue performance of AISI 9310 steel spur gear. *Opt. Laser Technol.* **2017**, *94*, 15–24. [CrossRef]
21. Hfaiedh, N.; Peyre, P.; Song, H.; Popa, I.; Ji, V.; Vignal, V. Finite element analysis of laser shock peening of 2050-T8 aluminum alloy. *Int. J. Fatigue* **2015**, *70*, 480–489. [CrossRef]
22. Zhou, W.; Ren, X.; Yang, Y.; Tong, Z.; Asuako Larson, E. Finite element analysis of laser shock peening induced near-surface deformation in engineering metals. *Opt. Laser Technol.* **2019**, *119*, 105608. [CrossRef]
23. Cao, Y.; Shin, Y.C.; Wu, B. Parametric study on single shot and overlapping laser shock peening on various metals via modeling and experiments. *J. Manuf. Sci. Eng. Trans. ASME* **2010**, *132*, 0610101–06101010. [CrossRef]

24. Yang, Y.; Zhou, W.; Tong, Z.; Chen, L.; Yang, X.; Larson, E.A.; Ren, X. Electrochemical Corrosion Behavior of 5083 Aluminum Alloy Subjected to Laser Shock Peening. *J. Mater. Eng. Perform.* **2019**, *28*, 6081–6091. [CrossRef]
25. Sun, S. Laser Shock Peening Process to Prevent Stress Corrosion Cracking of 5xxx Aluminum Alloys. Embargoed Master's Thesis, University of Nebraska-Lincoln, Lincoln, NE, USA, April 2018.
26. Ballard, P.; Fournier, J.; Fabbro, R.; Frelat, J. Residual Stresses Induced By Laser-Shocks. *J. Phys. IV* **1991**, *1*, C3-487–C3-494. [CrossRef]
27. Fabbro, R.; Fournier, J.; Ballard, P.; Devaux, D.; Virmont, J. Physical study of laser-produced plasma in confined geometry. *J. Appl. Phys.* **1990**, *68*, 775–784. [CrossRef]
28. Peyre, P.; Fabbro, R. Laser shock processing: A review of the physics and applications. *Opt. Quantum Electron.* **1995**, *27*, 1213–1229. [CrossRef]
29. Elwasli, F.; Zemzemi, F.; Mkaddem, A.; Mzali, S.; Mezlini, S. A 3D multi-scratch test model for characterizing material removal regimes in 5083-Al alloy. *Mater. Des.* **2015**, *87*, 352–362. [CrossRef]
30. Boteler, J.M.; Dandekar, D.P. Dynamic response of two strain-hardened aluminum alloys. *J. Appl. Phys.* **2006**, *100*, 054902. [CrossRef]
31. Wei, X.L.; Ling, X. Numerical modeling of residual stress induced by laser shock processing. *Appl. Surf. Sci.* **2014**, *301*, 557–563. [CrossRef]
32. Kim, J.H.; Kim, Y.J.; Lee, J.W.; Yoo, S.H. Study on effect of time parameters of laser shock peening on residual stresses using FE simulation. *J. Mech. Sci. Technol.* **2014**, *28*, 1803–1810. [CrossRef]
33. Ding, K. Three-dimensional dynamic finite element analysis of multiple laser shock peening processes. *Surf. Eng.* **2003**, *19*, 351–358. [CrossRef]
34. Bikdeloo, R.; Farrahi, G.H.; Mehmanparast, A.; Mahdavi, S.M. Multiple laser shock peening effects on residual stress distribution and fatigue crack growth behaviour of 316 L stainless steel. *Theor. Appl. Fract. Mech.* **2020**, *105*, 102429. [CrossRef]
35. Sealy, M.P.; Guo, Y.B. Surface integrity and process mechanics of laser shock peening of novel biodegradable magnesium-calcium (Mg-Ca) alloy. *J. Mech. Behav. Biomed. Mater.* **2010**, *3*, 488–496. [CrossRef]
36. Sun, R.; Li, L.; Zhu, Y.; Zhang, L.; Guo, W.; Peng, P.; Li, B.; Guo, C.; Liu, L.; Che, Z.; et al. Dynamic response and residual stress fields of Ti6Al4V alloy under shock wave induced by laser shock peening. *Model. Simul. Mater. Sci. Eng.* **2017**, *25*, 065016. [CrossRef]
37. Kim, J.H.; Kim, Y.J.; Kim, J.S. Effects of simulation parameters on residual stresses for laser shock peening finite element analysis. *J. Mech. Sci. Technol.* **2013**, *27*, 2025–2034. [CrossRef]
38. Hu, Y.; Gong, C.; Yao, Z.; Hu, J. Investigation on the non-homogeneity of residual stress field induced by laser shock peening. *Surf. Coat. Technol.* **2009**, *203*, 3503–3508. [CrossRef]
39. Li, P.; Huang, S.; Xu, H.; Li, Y.; Hou, X.; Wang, Q.; Fu, W.; Fang, Y. Numerical simulation and experiments of titanium alloy engine blades based on laser shock processing. *Aerosp. Sci. Technol.* **2015**, *40*, 164–170. [CrossRef]
40. Achintha, M.; Nowell, D. Eigenstrain modelling of residual stresses generated by laser shock peening. *J. Mater. Process. Technol.* **2011**, *211*, 1091–1101. [CrossRef]
41. Peyre, P.; Fabbro, R.; Merrien, P.; Lieurade, H.P. Laser shock processing of aluminium alloys. Application to high cycle fatigue behaviour. *Mater. Sci. Eng. A* **1996**, *210*, 102–113. [CrossRef]

quantum beam
science

MDPI

Review

A Survey of Process Monitoring Using Computer-Aided Inspection in Laser-Welded Blanks of Light Metals Based on the Digital Twins Concept

Ahmad Aminzadeh [1], Sasan Sattarpanah Karganroudi [1,2,*], Mohammad Saleh Meiabadi [3], Dhanesh G. Mohan [4] and Kadiata Ba [5]

[1] Département de Mathématique, Informatique et Génie, Université du Québec à Rimouski, Rimouski, QC G56 3A1, Canada; ahmad.aminzadeh@uqar.ca
[2] Department of Mechanical Engineering, Université du Québec à Trois-Rivières, Trois-Rivieres, QC G8Z 4M3, Canada
[3] Department of Mechanical Engineering, École de Technologie Supérieure, 1100 Notre Dame West, Montreal, QC H3C 1K3, Canada; mohammadsaleh.sheikhmohammadmeiabadi.1@ens.etsmtl.ca
[4] Institute of Materials Joining, Shandong University, Jinan 250061, China; dhanesh@sdu.edu.cn
[5] Applied Sciences Department, Université du Québec à Chicoutimi, 555 boul. Université, Chicoutimi, QC G7H 2B1, Canada; kadiata_ba@uqac.ca
* Correspondence: sattarpa@uqtr.ca

Abstract: The benefits of laser welding include higher production values, deeper penetration, higher welding speeds, adaptability, and higher power density. These characteristics make laser welding a superior process. Many industries are aware of the benefits of switching to lasers. For example, metal-joining is migrating to modern industrial laser technology due to improved yields, design flexibility, and energy efficiency. However, for an industrial process to be optimized for intelligent manufacturing in the era of Industry 4.0, it must be captured online using high-quality data. Laser welding of aluminum alloys presents a daunting challenge, mainly because aluminum is a less reliable material for welding than other commercial metals such as steel, primarily because of its physical properties: high thermal conductivity, high reflectivity, and low viscosity. The welding plates were fixed by a special welding fixture, to validate alignments and improve measurement accuracy, and a Computer-Aided Inspection (CAI) using 3D scanning was adopted. Certain literature has suggested real-time monitoring of intelligent techniques as a solution to the critical problems associated with aluminum laser welding. Real-time monitoring technologies are essential to improving welding efficiency and guaranteeing product quality. This paper critically reviews the research findings and advances for real-time monitoring of laser welding during the last 10 years. In the present work, a specific methodology originating from process monitoring using Computer-Aided Inspection in laser-welded blanks is reviewed as a candidate technology for a digital twin. Moreover, a novel digital model based on CAI and cloud manufacturing is proposed.

Keywords: real-time monitoring; Computer-Aided Inspection (CAI); laser welded blanks (LWBs); digital twin (DT); Industry 4.0

1. Introduction

The transportation industry has dedicated a lot of engineering effort and innovative research into reducing the weight of its products. Air pollution and emission of greenhouse gases from the transportation sector have had detrimental environmental and health effects for decades. For this reason, governments have enacted restrictive regulations on automotive industries to prevent and control the spread of vehicular emissions. Strict regulations have led car manufacturers to look for different solutions and new technologies to solve the problem. One of the strategies that has been adopted in this field is to reduce the weight of cars, leading to fuel consumption and carbon dioxide emission reduction.

Given that the body and other exterior components are a large portion of the car's weight, using light metal structures such as aluminum alloys in automobiles is an effective way to lessen the overall car weight. Aluminum alloys are known for their superior properties, such as strength-to-weight ratio, heat resistance, and corrosion resistance. Laser welding is an effective method of joining materials with high accuracy, good flexibility, and low distortion [1]. However, laser welding of aluminum structures is associated with a range of difficulties due to excessive heat dissipation, the hydrogen solubility of molten aluminum, and an oxide layer inclusion. Manufacturers are motivated by Computer-Aided Inspection (CAI) to ensure high product quality and avoid production defects, which requires automated, rapid, and accurate inspection [2]. CAI commonly refers to automated inspection, among other computer-aided applications extensively used in different industries [3]. By using manufacturing standards and geometric dimensioning and tolerancing (GD&T) criteria, CAI is not only able to detect laser welding defects but also to compensate for these shortcomings. Advances in scanning technology, digital cameras, and controllers have led to a significant increase in real-time monitoring of laser welding processes. A digital twin (DT) aims to build a digital replica of a physical system in a virtual space, such that the digital replica represents the same elements and the same dynamics of a physical system. DT systems can be very helpful for understanding, analyzing, and improving a product, service system, or production [4]. DT systems can also be used to inspect the process, to enable visualization of the impact of variations [5]. Integration of real-time monitoring and real-time simulation in a laser welding process ultimately leads to adopting a DT in laser welding processes. To communicate data, information technology advancements, like the Internet of Things (IoT) and Augmented Reality (AR), can be implemented to link the physical system and its digital twin [6]. Real-time data collection, data analysis, and physics-based simulation are basic phases in defect detection aimed at avoiding the occurrence of defects, and improving the quality of this cutting-edge technology. Thus, a critical review of monitoring technology for the laser welding process is provided. Kong, et al. [7] utilized spectrographic monitoring to control the laser welding process of galvanized high strength steel in two cases, with zinc coating and without zinc coating, in a lap joint configuration. Considering zinc vapor signals as the process feedback, welding defects were identified by the presence of spatters induced by zinc vapor at the faying surface. A series of experiments were conducted to investigate the effects of laser welding parameters on the keyhole dynamics and weld pool, using a high-speed charge-coupled device (CCD) camera with a green laser as an illumination source. The results revealed that welding quality strongly depends on zinc vapor at the faying surface; a higher depth of penetration was also observed in the case of removing the zinc coating. Sebestova, et al. [8] monitored Nd: YAG laser welding by measuring plasma spectral emission lines to calculate the plasma electron temperature. They found a relationship between electron temperature and depth of penetration, which can be used as a controller to identify welding defects and achieve desired penetration depth. Liu, et al. [9] studied laser hot-wire welding of butt joints to assess the molten pool dynamics and the stability of the welding process. A high-speed CCD camera and a spectrometer were used for real-time monitoring of the process through visualization of the molten pool and calculation of the electron temperature according to the Boltzmann plot method. Research established that the contribution of a hot wire facilitates the formation of a molten pool, though laser beams were not able to make the molten pool in butt joints with a large gap. Harooni, et al. [10] conducted real-time spectroscopic monitoring of laser welding of AZ31B magnesium alloy in lap joint configuration. Spectroscopic analysis was performed to study the correlation of the oxide layer on welding sheets and the generation of defects in the interface of overlapped sheets. In addition, a high-speed CCD camera, assisted with a green laser as an illumination source, was employed to monitor the molten pool and the keyhole dynamics due to the oxide layer. The results confirmed that the existing oxide layer on magnesium sheets leads to the generation of pores in the interface area. Blecher, et al. [11] utilized inline coherent imaging for real-time monitoring of keyhole depth in five different alloys. A comparison of real-time keyhole depth measurements and metallographic depth measurements proved that the proposed method was capable of time measurement of keyhole depth except for aluminum alloys. Luo, et al. [12] improvised the acoustic signal monitoring of laser welding by offering a plane microphone array with a time delay recognition. They concluded that the welding process could be monitored and justified using the suggested method even with background noises in the working environment, which had been an obstacle to traditional acoustic signal monitoring. Mirapeix, et al. [13] proposed plasma optical spectroscopy to identify aluminum in the laser welding of Usibor1500 tailor-welded blanks. The estimation of aluminum was done by the line-to-continuum method in real-time. A correlation was identified between aluminum content in real-time monitoring and off-line tests like macrographs or tensile tests. However, the correlation found in the tensile specimen test at lower aluminum contents was not clear because it was affected by other parameters like seam geometry. Recently, our research team developed a new automatic technique to address the distortion in real-time monitoring of aluminum laser-welded blanks [14,15]. The research also provided experimental and numerical investigation of different types of key process parameters and their impact on production quality in automobile applications [16–19]. Wang, et al. [20] developed a real-time monitoring system for disk laser welding based on the feature selection method for pattern recognition, and the Support Vector Machine (SVM) and Back-Propagation (BP) neural network for pattern classification. Images of the plume and spatters were processed, and a sequential forward floating selection (SFFS) algorithm was used for detecting the optimal feature subset. The classification accuracy of BP and SVM were very close to one other; however, the accuracy of SVM reached the maximum of 98.43 using 10 features. It should be noted that the overall processing time remained a challenge for the proposed method. In another study, Wang, et al. [21] used a combination of a Support Vector Machine and a Pearson product-moment correlation coefficient to characterize disk laser welding quality. High-speed photography was employed for image processing, and the area of the plume, the number of spatters, and the horizontal coordinate of the plume centroid were selected among six features to establish an SVM model with 93.58% classification accuracy. The authors concluded that the proposed monitoring system could be used for real-time monitoring of high-power laser welding. De Bono, et al. [22] evaluated two different monitoring methods of laser welding: optical-based and laser interferometry monitoring methods. The optical-based method investigated photodiodes signals of butt welding, and the laser interferometry monitoring took advantage of the In-Process Depth Meter (IDM) sensor from Precitec in stake welding. Photodiode data obtained at the wavelengths between 600 and 850 nm deduced defects correlated to laser power and joint contamination and gap. However, for detecting defects like porosities and cracks, photodiode data need to be decomposed by orthogonal empirical mode decomposition (OEMD) theory. The data acquired by the IDM sensor established a correlation between the IDM signal and the keyhole depth. Chen, et al. [23] employed an SVM model for real-time monitoring in high-power disk laser welding using 15 features of the metal vapor plume and spatters. A high-speed camera was used to capture laser-induced metal vapor for image processing. SVM classification using seven features reached a remarkably accurate 95.93% by 10-fold cross-validation. The authors suggested that the centroid, perimeter, average grayscale value, and quantity of the spatters were critical to improving welding quality. Pasinetti, et al. [24] proposed in-line monitoring of the laser welding process by a smart vision system based on the Industrial Internet of Things (IIoT) approach, to make an interconnection and remotely control the process. Two different setups were used to fulfill two goals. The first setup, called seam tracking, was targeted to keep the laser welding in an optimal position. The second setup, called the keyhole monitor, aimed to detect incomplete keyhole penetration. The researchers suggested that the architecture used enables remote monitoring of multiple welding units from a central unit. Lei, et al. [25] developed a multi-information fused modeling system for predicting weld waist width and the weld back width by a combination of Principal Component Analysis (PCA), genetic algorithm (GA), and neural networks (NN). Images were acquired by a modified optical fiber laser coaxial monitoring system, and pre-processed by the PCA algorithm to effectively remove the redundancy of extracted information. Two morphological features, in addition to laser power and welding speed, were selected as input parameters of the NN. GA was used to optimize the architecture of the NN. Considering the low errors of the developed model, and the short processing time of less than 90 m, the authors proposed that it could be used for real-time monitoring of the laser welding process. Zhang, et al. [26] employed a multiple-optical-sensor system to integrate with a Deep Belief Network (DBN) that was optimized by a genetic algorithm for online monitoring of the high-power disc laser welding process. The multiple-optical-sensor system was able to deliver effectively a thorough insight into the laser welding process. A deep learning model based on the DBN demonstrated more than 10% higher average accuracy compared to the back-propagation neural network (BPNN) model. Haubold [27] offered a monitoring system for remote laser welding using two parallel processing algorithms customized for identifying spatter number and size. The reproducibility of spatter formation was investigated at four different settings of process parameters for ten repetitions. Although a correlation between spatter number and the corresponding standard deviation was established, no resolution for reduction of spatter size and number was made. Shevchik, et al. [28] developed a hybrid monitoring system for data acquisition and processing applied to titanium laser welding. The monitoring system included optical and acoustic sensors combined with machine learning (ML) techniques. M-band wavelets transformation was utilized to decompose optical and acoustic signals, and the normalized energy of the frequency bands was extracted. The Laplacian graph Support Vector Machine (LapSVM) was used to correlate the extracted features with welding quality. The proposed method displayed more than 85.9% classification accuracy, which is notable given the low cost of data preparation. Accordingly, the researchers claimed that the hybrid monitoring system could be used for the industrialization of laser welding monitoring, and they also raised some concerns about sensors selection rather than sensors combination. Zhang, et al. [29] put forward a vision-based monitoring system for laser welding of tailor rolled blanks (TRB) through coaxial visual monitoring and Convolution Neural Network (CNN) processing algorithms. The monitoring system was dedicated to evaluating the penetration quality of the laser welding of TRB. Four statuses for the penetration state were considered for the creation of an image dataset to train and validate the CNN. They advised that with the 2 ms latency of the CNN for TRB, the proposed monitoring system could be effectively employed for real-time monitoring applications. Gonzalez, et al. [30] introduced ConvLBM to monitor laser deposition and welding processes based on medium wavelength infrared (MWIR) imaging. ConvLBM employed a Convolution Neural Network (CNN) to obtain features from MWIR. ConvLBM estimated dilution for the laser deposition process due to its significance on the quality of the process. Defect characterization was also achieved for the laser welding process by ConvLBM for three different materials, proving the adaptability of the monitoring method for different applications. Kaewprachum, et al. [31] employed an infrared camera for real-time monitoring of the laser welding process to apprehend fast dynamic heating phenomena. The images were captured and analyzed to reveal the effects of laser power and welding speed on the average molten pool temperature and the width of the molten pool. Infrared camera measurements were validated by microscopic measurements, and a good correspondence was observed, especially at high powers. Papacharalampopoulos, et al. [32] employed a methodology as a candidate for process-level digital twins (DTs) in laser welding. A simplified laser welding paradigm capable of displaying temperature profiles was studied to assess the employed methodology. The proposed digital twin approach consisted of decomposing spatial domains, adaptation to accuracy, adaptation to measurements, and estimation of inner state, providing intuitiveness to the operator, and real-time function. The methodology was adopted to solve linear partial differential equations, and was validated following measures ensuring the operational performance of a DT.

To the best of the authors' knowledge, the present work is the most comprehensive attempt to present a DT for laser-welded blanks. A virtual system of the physical laser welding system has been developed using CAI to monitor, quality control, and optimize the laser welding process. The developed DT resides in the cloud, and it continuously communicates with physical and virtual systems to provide appropriate commands to operating processes and machines in real-time. In this DT, an evaluation of different aspects of laser welding qualities has been made in order to give a product license to laser-welded blanks.

2. Quality Control Based on 3D Geometrical Inspection

For developing a DT, the raw data of a physical system is collected to extract inspection features and analyze the physical system in real-time. Computer-Aided Inspection (CAI) can help to identify defects and abnormalities occurring in the geometry of a physical system. A 3D scan measurement is one of the CAI tools which provides non-contact, non-destructive, and accurate measurements of a physical system. In other words, it is a 3D geometric inspection technology using data acquisition and data pre-processing to obtain the size and shape of a physical part to display the part in digital space in three dimensions. The 3D scanning provides an opportunity to immediately detect where the digital replica does not match with the 3D CAD model. Three-dimensional scanning is a viable option for the quality control of geometrical features of special welding jigs and fixtures. Using 3D scanning, it is possible to identify where deviations occur, and to measure them instantly. To better understand Geometric Dimensioning and Tolerancing (GD&T), manufacturing standards such as ASME Y14.5 and ISO-GPS have been developed in the era of automation. In addition, as part of its standards and requirements, the American Society of Mechanical Engineers (ASME) also established rules, definitions, defaults, and recommended practices. According to the ASME, parts and workpieces should be evaluated in a free state. Therefore, it is necessary to consider the compliance and deformation of non-rigid parts during the inspection. In response, definitions for geometric dimensioning and tolerancing of non-rigid parts have been developed, based on the ASME Y14.5 and ISO standards. Figure 1 presents the types and tools of CAI algorithms. In fact, inspection 4.0 aims at intelligent inspection by illustrating the basic work that can be implemented. Based on the compliance behavior and inspection parameters, a digital inspection protocol can be implemented onto the cloud, and the appropriate machine and inspection method will be selected. This novel aspect will be presented in the upcoming parts of this article. Generally, components are designed to fit into the right material and mechanical properties based on rigid and non-rigid concepts in computer-aided modeling.

Regarding the compliance behavior of parts, rigid and non-rigid parts, CAI algorithms are developed. CAI is primarily used for comparing the reference geometry, computer-assisted design (CAD), with measured data, scan models [34]. Due to gravity and/or residual stress, some mechanical components often have different shapes in the free-state position compared to the state-of-use position. To make it possible to inspect different types of parts, different registration methods have been developed to classify workpieces into rigid and non-rigid ones. Furthermore, rigid registration is the primary step in computer-assisted inspections of non-rigid parts. In conventional CAI software, it is assumed by default that any data entered into the software is from a rigid part. Therefore, any deviation between the input data and the nominal CAD model should be considered a potential manufacturing defect [35]. Rigid registration has the primary goal of bringing CAD and scan models into a common coordinate system without deforming either model. The model is translated and rotated using an optimal transformation matrix without affecting its shape [36]. Initial CAI approaches were introduced using a rigid registration algorithm with Iterative Close Points (ICP) [37]. The ICP algorithm is known as one of the most robust and efficient rigid registration approaches. Although various methods have been developed over the years—including those described by researchers [38,39]—in different domains, such as aeronautic inspections, the ICP algorithm remains a widely used registration approach [40], thanks to its statistically robust and reliable method of registering. A CAD and a scan of a workpiece that is not presented in the same coordinate systems are shown in Figure 2a, and the ICP algorithm applies the best geometrical fit in Figure 2b. In this regard, the closest point in the reference set (CAD) is first identified for every point the point cloud set contains. The transformation matrix (rotation and translation) is then calculated, to move the CAD model towards scan data. This iteration is repeated until the best geometrical fit is obtained.

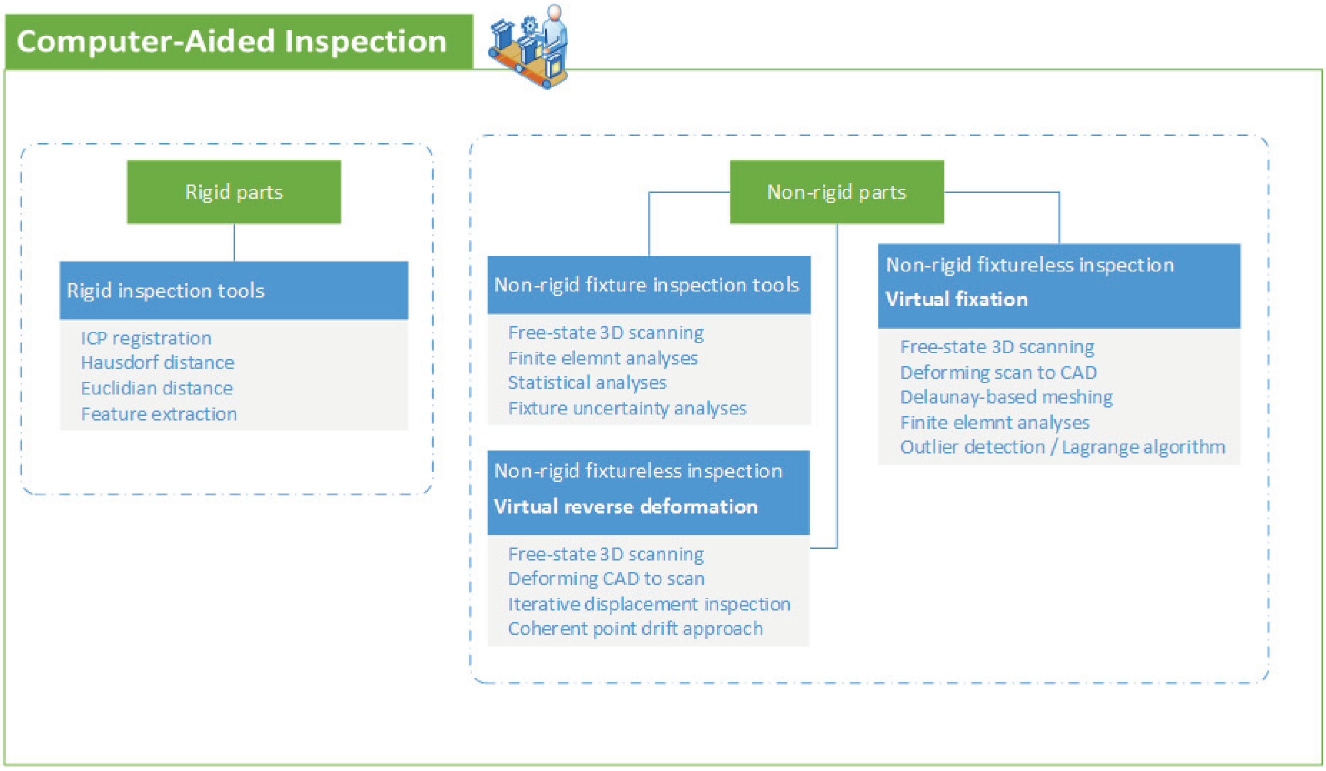

Figure 1. Computer-Aided Inspection methods and tools [33].

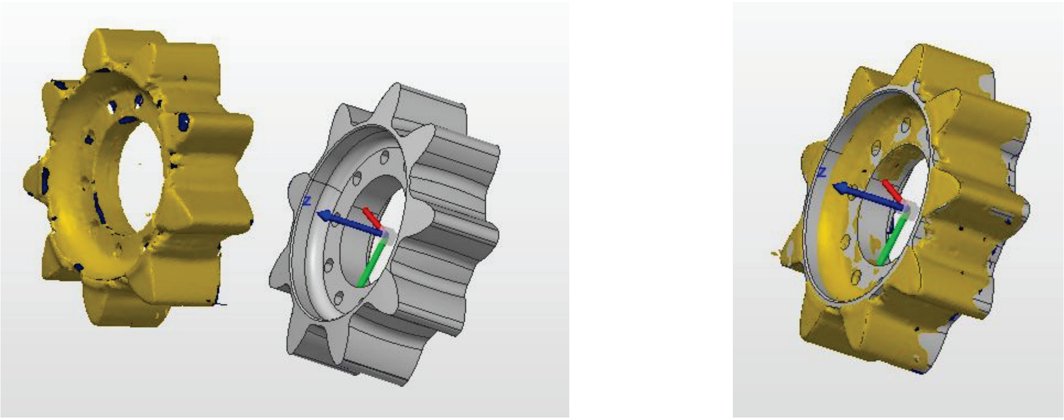

(**a**) (**b**)

Figure 2. CAD and scanned models (**a**) before registration (**b**) after rigid registration using ICP algorithm [33].

Each iteration of the ICP registration minimizes the distance between the two models by estimating and computing the transformation matrix that combines translation and rotation. The Hausdorff distance is the main tool in this algorithm [41]. A distance measure is taken between the CAD mesh and the point cloud data acquired by scanning. In other words, it is the maximum distance between every point of a non-empty set and some point of another non-empty set. Equation (1) illustrates this, where $d_H\ (X,\ Y)$ is the Hausdorff distance and $(X,\ Y)$ are the two non-empty subsets.

$$d_H(X,\ Y) = \max\left\{sup_{x\in X}inf_{y\in Y}d(x,y), sup_{y\in Y}inf_{x\in X}d(x,y)\right\} \quad (1)$$

The ICP algorithm has undergone a lot of improvements and upgrades, as it is one of the most powerful and widely used algorithms. The ICP algorithm was also modified and developed to decrease calculation time [42]. This method proposes a robust solution by applying random sampling to the point clouds. The algorithm also knew the minimization strategy [43] or measured the transformation in a way that minimizes its error. By using the corresponding points in previous iterations of the ICP algorithm, and searching only in the immediate neighborhood of those points, the closest points search was significantly improved in terms of speed [44]. In addition, some techniques have been used to improve the efficiency and speed of the registration process [45]. A variation of the algorithm has also been implemented to enhance the conversion of the sets by taking color information from the workpieces. Even though not all scanners are able to capture the color information from workpieces, this algorithm can still be used. There have been many variants of the algorithm explored and many improvements made by the ICP algorithm [43].

Since non-rigid workpieces have so much more parameters to consider, rigid registration needs to be accompanied by non-rigid algorithms, to take into consideration the part's deviation in its free state [46]. Scanning models cannot be compared to CAD models due to the flexible deformation of parts in a free state. CAI methods can resolve this problem for non-rigid parts where defects (e.g., geometric deviations from the CAD model) are separated from the deformations caused by the compliance or flexible deformation of non-rigid parts. Typically, non-rigid parts are dimensioned and inspected with over-constrained inspection fixtures to compensate for the flexible nature of these components and to ensure that the measurement setup accurately reflects the part's assembly functionality.

3. Verification and Validation of the Methods in CAI

All Computer-Aided Inspection methods cited are based on scan data and computational calculations. It follows that verification and validation of the calculations are imperative due to this aspect of the methods. Both rigid and non-rigid inspection methods are prone to uncertainty in computational simulations and measurement errors due to inaccuracies in data acquisition devices. Due to the technical limitations of devices, optical effects (such as light fraction and reflectivity of surfaces), or the inaccessible features of some parts, scanners are inaccurate. The results of CAI are influenced by these noisy data. Simulation models can be assessed for accuracy, reliability, and robustness by applying verification and validation (V&V) approaches [47]. Validation evaluates the consistency of computed simulation results compared to the actual ones, while verification measures the accuracy of the solution to a problem using a computational model. All numerical methods, including CAI methods, must be thoroughly verified and validated because of various sources of uncertainty in computer codes and simulations. Validating the result of a numerical approach concerning input noise aims at evaluating a computational model's robustness. An effective computational model should be able to produce satisfactory results despite the presence of noises in the input. A robust approach can still produce acceptable results for noise-containing input data compared with noise-free input data. Typically, the input noise in CAI methods comes from measurement noise that is inherent to measuring data acquisition devices. Thus, it is necessary to study the robustness of CAI methods, given the noise generated by scanning devices. A first development model will be generated based on the CAI method, and real feedback will be received during the production process. Furthermore, by combining the concepts of physical and simulation, the human and machine interface theory can make a powerful and self-learning device.

This smart connected modeling is the trigger for Industry 4.0 and intelligent manufacturing by developing a digital twin model.

4. Digital Twins (DT)

Industry 4.0 is the latest revolution in the industrial era, and refers to the digitization of manufacturing by merging physical and virtual (digital) worlds. Digital twins (DTs) are a strategy within Industry 4.0, operating on the virtualization principle [48]. DTs are digitalized integrated systems to monitor, analyze, and simulate the behavior of a physical system. DTs are composed of three main components: the physical system, the virtual system, and the communication layer that connects these two systems. The communication layer is a linkage for data storage, data processing, and data mapping functionalities [49]. The data from the physical and virtual systems must be stored and processed in the communication layer. In this regard, the communication layer needs to be capable of transmitting a big amount of data (big data) in addition to easy fault detection characteristics. Internet of Things (IoT) technology can be used to make interactions between different layers of the integrated systems for real-time data transmission. IoT effectively maintains two-way synchronization of physical and virtual systems, to keep the virtual system updated and to provide real-time control commands for the physical system. The physical system changes are reflected in the virtual system; in other words, the virtual system is updated by employing feedback from the physical system. Real-time control commands are made based on the past and present conditions of the physical system to take care of the consistency of the manufacturing process and the quality of manufactured parts [50]. The constant synchronization between physical and virtual systems through the communication layer ends up in a real-time quality control platform which is also supported and updated by the physical system. As illustrated in Figure 3, all sorts of information originating from physical and virtual systems—GD&T standards, historical data, customer feedback, and fabrication protocols—are communicating with the cloud network to provide enough material to make decisions. Continuous and online communication between different physical and virtual data providers is only made possible by the ability of IoT [51] to transmit large volumes of data.

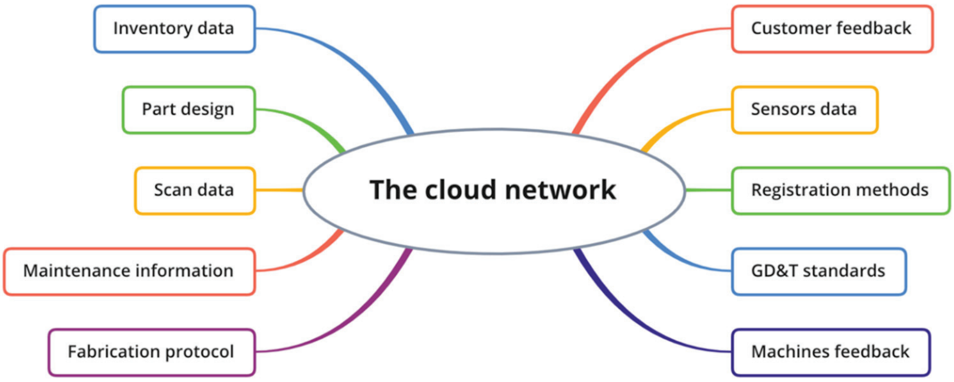

Figure 3. The cloud network in a 4.0 manufacturing factory.

Smart welding is heading inevitably toward the Industry 4.0 paradigm. A schematic of the DT model designed for intelligent laser welding leading to a product license for laser-welded blanks is presented in Figure 4. In this DT, all data from the physical system, including seam tracking, in-process depth meter, and weld inspect data, are communicating with the cloud to update and support the cloud. There is a two-way network of interactions between consequent stages of physical and virtual twins, to transfer and update information, guaranteeing high-quality laser seam according to standards, process command, and specifications defined in the cloud. The application of DTs might facilitate the provision of production licenses for parts manufactured in different production sites, with no need to re-inspect the parts.

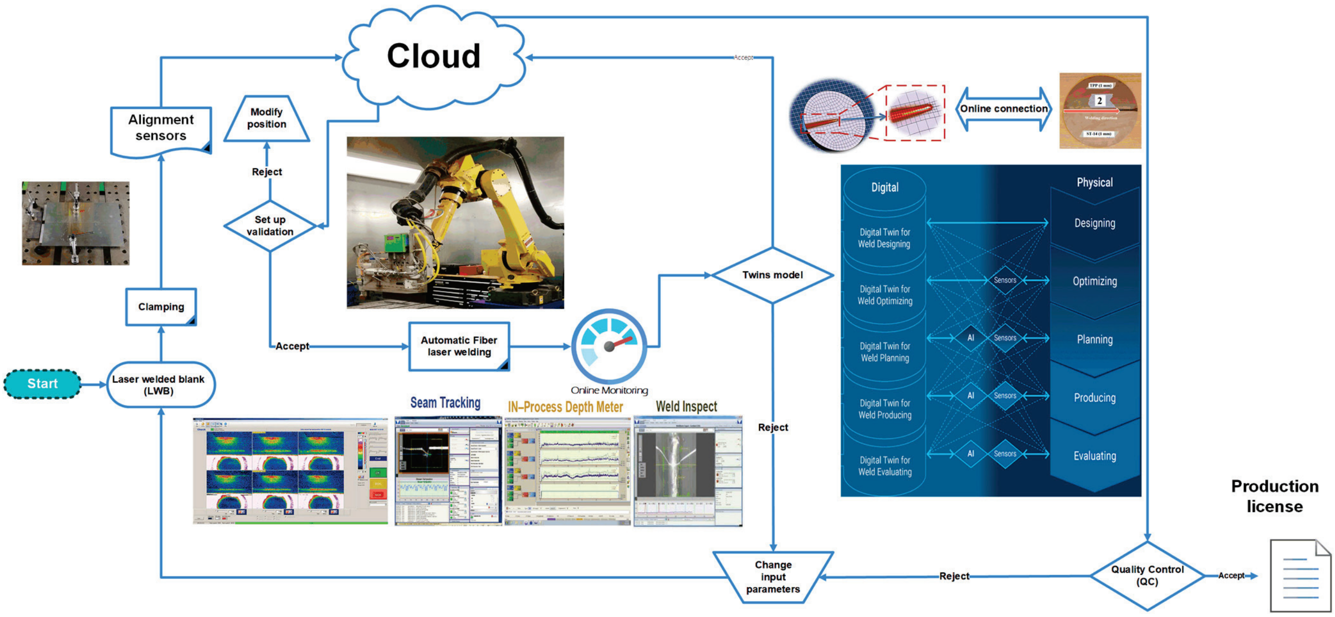

Figure 4. Digital twins model for Inspection 4.0 of laser-welded blanks.

In general, digital twins are efficient platforms for predicting every machine and device's performance, due to their intelligent data processing capability. In a virtual model or DT, physical models of machine operations will be combined with sensor data collected and processed from real assets during real-world operations. In this regard, operators of laser welding machines will benefit from being able to predict structural failure and to plan maintenance activities more effectively. This strategy will result in reduced maintenance costs and operational downtime during welding. As shown in the following model, aluminum sheets are prepared before welding to ensure there is no contamination on the surface. Then, the clamping procedure is adjusted to apply an equivalent force on the surface of the plates. To do so, alignment sensors are used to define the error, and the results are sent to the cloud for future action. By using the validation method, all the process parameters are set, and acceptance/rejection outcomes will be considered, to make a cloud-based smart decision based on the DG&T criteria. If the alignment has been accepted, automatic laser welding will start, and real-time monitoring will be done (seam tracking, in-process depth penetration, weld inspection, etc.). Using sensors and artificial intelligence, digital platforms and physical operations communicate data simultaneously. A cloud platform should be able to process big data and refine it based on pass/fail production criteria. Finally, a license will be issued for the quality assessment of each production. It is worth mentioning that this model can be used in mass production as well as remote manufacturing platforms in any location throughout the world. Thus, this model can be considered the first step toward cloud manufacturing and connected production which can be remotely accessible anytime.

5. Summary and Future Scopes

Investigation of the digital twins market reflects the challenges that have hindered cost-efficient application of digital twins (DTs) in manufacturing. Some of these challenges are due to the complex physics of manufacturing processes and production uncertainties, which in turn leads to difficulties in capturing physical phenomena by a virtual replica. The desire is to set up data-driven digital twins based on a hierarchical structure without any conflict between the physical and virtual systems, which entails appropriate communication and collaboration between them. However, the development of digital twins is still costly due to the restrictions of communication platforms. The ability to predict, prevent and resolve problems and faults also requires the proper implementation of data analysis, decision making, and problem-solving techniques.

In this regard, an overview of computer-aided process monitoring was reviewed, based on the digital twins concept for lightweight laser-welded metals. Different types of 3D geometric inspection, Computer-Aided Inspection (CAI) methods, and tools in the manufacturing industry, are presented and compared in this paper. CAI approaches address automated inspection challenges and requirements for different types of manufactured parts. The development of this process is essential in the production cycle of a part, and therefore should not be ignored. In addition, as moving further toward Industry 4.0, its concepts ought to be incorporated into geometric inspections allowing a comparison between nominal data (CAD model) with respect to a manufactured part, to determine whether it meets specifications without having to apply human judgment. An automated cloud-based Inspection 4.0 is therefore applied. Another objective is to propose an automated production cycle that does not require human intervention. This survey presents an agile approach allowing automation of the laser-welded blanks process. Applying CAI, the process is automated along with the implementation of its DTs. This original model allows remote monitoring of the process, increasing its precision by removing human intervention, increasing productivity, and providing a proper decision-making tool. The challenge now is to integrate artificial intelligence to delegate all redundant work to the machines, and have them provide feedback and auto-maintenance at some point. More research is also needed to develop cost-effective digital twins so that these solutions can meet Industry 4.0 requirements.

Author Contributions: Conceptualization, A.A., S.S.K. and M.S.M.; methodology, S.S.K., D.G.M. and K.B.; validation, S.S.K., M.S.M. and D.G.M.; formal analysis, A.A., S.S.K. and K.B.; investigation, A.A., S.S.K. and M.S.M.; resources, S.S.K. and D.G.M.; data curation, M.S.M. and K.B.; writing—original draft preparation, A.A., S.S.K. and M.S.M.; writing—review and editing, S.S.K., A.A., D.G.M., K.B. and M.S.M.; visualization, A.A., D.G.M. and K.B., supervision and project administration, S.S.K. All authors have read and agreed to the published version of the manuscript.

Funding: We acknowledge the support of the Fonds Québécois de la Recherche sur la Nature et les Technologies (FRQNT) [funding reference number 06351].

Institutional Review Board Statement: This article does not involve human or animal participation or data, therefore ethics approval is not applicable.

Informed Consent Statement: Not applicable.

Data Availability Statement: All data, material, and codes used in this paper are available.

Conflicts of Interest: The authors declare no conflict of interest.

References

1. Katayama, S. *Handbook of Laser Welding Technologies*; Elsevier: Amsterdam, The Netherlands, 2013.
2. Zhao, F.; Xu, X.; Xie, S.Q. Computer-Aided Inspection Planning-The state of the art. *Comput. Ind.* **2009**, *60*, 453–466. [CrossRef]
3. Minetola, P.; Iuliano, L.; Calignano, F. A customer oriented methodology for reverse engineering software selection in the computer aided inspection scenario. *Comput. Ind.* **2015**, *67*, 54–71. [CrossRef]
4. Zhang, L.; Chen, X.; Zhou, W.; Cheng, T.; Chen, L.; Guo, Z. Digital Twins for Additive Manufacturing: A State-of-the-Art Review. *Appl. Sci.* **2020**, *10*, 8350. [CrossRef]
5. Gaha, R.; Durupt, A.; Eynard, B. Towards the implementation of the Digital Twin in CMM inspection process: Opportunities, challenges and proposals. *Procedia Manuf.* **2020**, *54*, 216–221. [CrossRef]
6. Papacharalampopoulos, A.; Michail, C.; Stavropoulos, P. Manufacturing Process Control through a Digital Twin: Encoding Issues. In Proceedings of the TESConf 2020—9th International Conference Through-Life Engineering Services, Cranfield, Bedfordshire, UK, 3–4 November 2020. [CrossRef]
7. Kong, F.; Ma, J.; Carlson, B.; Kovacevic, R. Real-time monitoring of laser welding of galvanized high strength steel in lap joint configuration. *Opt. Laser Technol.* **2012**, *44*, 2186–2196. [CrossRef]
8. Sebestova, H.; Chmelickova, H.; Nozka, L.; Moudry, J. Non-destructive real time monitoring of the laser welding process. *J. Mater. Eng. Perform.* **2012**, *21*, 764–769. [CrossRef]

9. Liu, W.; Liu, S.; Ma, J.; Kovacevic, R. Real-time monitoring of the laser hot-wire welding process. *Opt. Laser Technol.* **2014**, *57*, 66–76. [CrossRef]
10. Harooni, M.; Carlson, B.; Kovacevic, R. Detection of defects in laser welding of AZ31B magnesium alloy in zero-gap lap joint configuration by a real-time spectroscopic analysis. *Opt. Lasers Eng.* **2014**, *56*, 54–66. [CrossRef]
11. Blecher, J.J.; Galbraith, C.M.; Van Vlack, C.; Palmer, T.A.; Fraser, J.M.; Webster, P.J.L.; DebRoy, T. Real time monitoring of laser beam welding keyhole depth by laser interferometry. *Sci. Technol. Weld. Join.* **2014**, *19*, 560–564. [CrossRef]
12. Luo, Z.; Liu, W.; Wang, Z.; Ao, S. Monitoring of laser welding using source localization and tracking processing by microphone array. *Int. J. Adv. Manuf. Technol.* **2016**, *86*, 21–28. [CrossRef]
13. Mirapeix, J.; Vila, E.; Valdiande, J.J.; Riquelme, A.; Garcia, M.; Cobo, A. Real-time detection of the aluminium contribution during laser welding of Usibor1500 tailor-welded blanks. *J. Mater. Process. Technol.* **2016**, *235*, 106–113. [CrossRef]
14. Aminzadeh, A.; Karganroudi, S.S.; Barka, N.; El Ouafi, A. A real-time 3D scanning of aluminum 5052-H32 laser welded blanks; geometrical and welding characterization. *Mater. Lett.* **2021**, *296*, 129883. [CrossRef]
15. Aminzadeh, A.; Karganroudi, S.S.; Barka, N. A novel approach of residual stress prediction in ST-14/ST-44 laser welded blanks; mechanical characterization and experimental validation. *Mater. Lett.* **2021**, *285*, 129193. [CrossRef]
16. Aminzadeh, A.; Nasiri, N.; Barka, N.; Parvizi, A.; Abrinia, K.; Moradi, M.; Sattarpanah Karganroudi, S. Statistical Analysis of Laser-Welded Blanks in Deep Drawing Process: Response Surface Modeling. *J. Mater. Eng. Perform.* **2022**, *31*, 2240–2256. [CrossRef]
17. Aminzadeh, A.; Sattarpanah Karganroudi, S.; Barka, N. Experimental and numerical investigation of forming defects and stress analysis in laser-welded blanks during deep drawing process. *Int. J. Adv. Manuf. Technol.* **2021**, *117*, 1193–1207. [CrossRef]
18. Aminzadeh, A.; Parvizi, A.; Moradi, M. Multi-objective topology optimization of deep drawing dissimilar tailor laser welded blanks; experimental and finite element investigation. *Opt. Laser Technol.* **2020**, *125*, 106029. [CrossRef]
19. Aminzadeh, A.; Parvizi, A.; Safdarian, R.; Rahmatabadi, D. Comparison between laser beam and gas tungsten arc tailored welded blanks via deep drawing. *Proc. Inst. Mech. Eng. Part B J. Eng. Manuf.* **2020**, *235*, 673–688. [CrossRef]
20. Wang, T.; Chen, J.; Gao, X.; Qin, Y. Real-time monitoring for disk laser welding based on feature selection and SVM. *Appl. Sci.* **2017**, *7*, 884. [CrossRef]
21. Wang, T.; Chen, J.; Gao, X.; Li, W. Quality monitoring for laser welding based on high-speed photography and support vector machine. *Appl. Sci.* **2017**, *7*, 299. [CrossRef]
22. De Bono, P.; Allen, C.; D’Angelo, G.; Cisi, A. Investigation of optical sensor approaches for real-time monitoring during fibre laser welding. *J. Laser Appl.* **2017**, *29*, 022417. [CrossRef]
23. Chen, J.; Wang, T.; Gao, X.; Wei, L. Real-time monitoring of high-power disk laser welding based on support vector machine. *Comput. Ind.* **2018**, *94*, 75–81. [CrossRef]
24. Pasinetti, S.; Sansoni, G.; Docchio, F. In-Line Monitoring of Laser Welding Using a Smart Vision System. In Proceedings of the IEEE Metrology for Industry 4.0 and IoT, Brescia, Italy, 16–18 April 2018; pp. 134–139. [CrossRef]
25. Lei, Z.; Shen, J.; Wang, Q.; Chen, Y. Real-time weld geometry prediction based on multi-information using neural network optimized by PCA and GA during thin-plate laser welding. *J. Manuf. Process.* **2019**, *43*, 207–217. [CrossRef]
26. Zhang, Y.; You, D.; Gao, X.; Katayama, S. Online Monitoring of Welding Status Based on a DBN Model During Laser Welding. *Engineering* **2019**, *5*, 671–678. [CrossRef]
27. Haubold, M.W.; Zäh, M.F. Real-time spatter detection in laser welding with beam oscillation. *Procedia CIRP* **2019**, *79*, 159–164. [CrossRef]
28. Shevchik, S.A.; Le-Quang, T.; Farahani, F.V.; Faivre, N.; Meylan, B.; Zanoli, S.; Wasmer, K. Laser welding quality monitoring via graph support vector machine with data adaptive kernel. *IEEE Access* **2019**, *7*, 93108–93122. [CrossRef]
29. Zhang, Z.; Li, B.; Zhang, W.; Lu, R.; Wada, S.; Zhang, Y. Real-time penetration state monitoring using convolutional neural network for laser welding of tailor rolled blanks. *J. Manuf. Syst.* **2020**, *54*, 348–360. [CrossRef]
30. Gonzalez-Val, C.; Pallas, A.; Panadeiro, V.; Rodriguez, A. A convolutional approach to quality monitoring for laser manufacturing. *J. Intell. Manuf.* **2020**, *31*, 789–795. [CrossRef]
31. Keawprachum, B.; Srisungsitthisunti, P. Real-time process monitoring of laser welding by infrared camera and image processing. *Key Eng. Mater.* **2020**, *856*, 160–168. [CrossRef]
32. Papacharalampopoulos, A.; Stavropoulos, P.; Petrides, D. Towards a digital twin for manufacturing processes: Applicability on on laser laser welding. *Procedia CIRP* **2019**, *88*, 110–115. [CrossRef]
33. Sattarpanah Karganroudi, S. *Contribution à L’inspection Automatique des Pièces Flexibles à L’état Libre Sans Gabarit de Conformation*; Université du Québec à Trois-Rivières: Trois-Rivières, QC, Canada, 2017.
34. Sabri, V.; Sattarpanah, S.; Tahan, S.A.; Cuillière, J.C.; François, V.; Pham, X.T. A robust and automated FE-based method for fixtureless dimensional metrology of non-rigid parts using an improved numerical inspection fixture. *Int. J. Adv. Manuf. Technol.* **2017**, *92*, 2411–2423. [CrossRef]
35. Babanezhad, K.; Aidibe, A.; Foucault, G.; Tahan, A.; Bigeon, J. Improved Bi-Criterion flexible registration for fixtureless inspection of compliant parts. *Precis. Eng.* **2020**, *65*, 116–129. [CrossRef]
36. Sattarpanah Karganroudi, S.; Cuillière, J.-C.; François, V.; Tahan, S.-A. “What-if” scenarios towards virtual assembly-state mounting for non-rigid parts inspection using permissible loads. *Int. J. Adv. Manuf. Technol.* **2018**, *97*, 353–373. [CrossRef]

37. Besl, P.J.; McKay, N.D. Method for registration of 3-D shapes. In *Sensor Fusion IV: Control Paradigms and Data Structures*; SPIE: Bellingham, WA, USA, 1992; Volume 1611, pp. 586–606.
38. Li, Y.; Gu, P. Free-form surface inspection techniques state of the art review. *Comput. Des.* **2004**, *36*, 1395–1417. [CrossRef]
39. Savio, E.; Chiffre, L.D.; Schmittc, R. Metrology of freeform shaped parts. *CIRP Ann.* **2007**, *56*, 810–835. [CrossRef]
40. Ravishankar, S.; Dutt, H.; Gurumoorthy, B. Automated inspection of aircraft parts using a modified ICP algorithm. *Int. J. Adv. Manuf. Technol.* **2010**, *46*, 227–236. [CrossRef]
41. Henrikson, J. Completeness and total boundedness of the Hausdorff metric. *MIT Undergrad. J. Math.* **1999**, *1*, 10.
42. Masuda, T.; Yokoya, N. A robust method for registration and segmentation of multiple range images. *Comput. Vis. Image Underst.* **1995**, *61*, 295–307. [CrossRef]
43. Rusinkiewicz, S.; Levoy, M. Efficient variants of the ICP algorithm. In Proceedings of the Third International Conference on 3-D Digital Imaging and Modeling, Quebec City, QC, Canada, 28 May–1 June 2001; pp. 145–152.
44. Greenspan, M.; Godin, G. A nearest neighbor method for efficient ICP. In Proceedings of the Third International Conference on 3-D Digital Imaging and Modeling, Quebec City, QC, Canada, 28 May–1 June 2001; pp. 161–168.
45. Zhu, L.; Barhak, J.; Srivatsan, V.; Katz, R. Efficient registration for precision inspection of free-form surfaces. *Int. J. Adv. Manuf. Technol.* **2007**, *32*, 505–515. [CrossRef]
46. Sattarpanah Karganroudi, S.; Cuillière, J.-C.; Francois, V.; Tahan, S.-A. Automatic fixtureless inspection of non-rigid parts based on filtering registration points. *Int. J. Adv. Manuf. Technol.* **2016**, *87*, 687–712. [CrossRef]
47. Schwer, L.E. An overview of the PTC 60/V&V 10: Guide for verification and validation in computational solid mechanics. *Eng. Comput.* **2007**, *23*, 245–252.
48. Roy, R.B.; Mishra, D.; Pal, S.K.; Chakravarty, T.; Panda, S.; Chandra, M.G.; Pal, A.; Misra, P.; Chakravarty, D.; Misra, S. Digital twin: Current scenario and a case study on a manufacturing process. *Int. J. Adv. Manuf. Technol.* **2020**, *107*, 3691–3714. [CrossRef]
49. Zheng, Y.; Yang, S.; Cheng, H. An application framework of digital twin and its case study. *J. Ambient. Intell. Humaniz. Comput.* **2019**, *10*, 1141–1153. [CrossRef]
50. Mohan, D.G.; Tomków, J.; Sattarpanah Karganroudi, S. Laser Welding of UNS S33207 Hyper-Duplex Stainless Steel to 6061 Aluminum Alloy Using High Entropy Alloy as a Filler Material. *Appl. Sci.* **2022**, *12*, 2849. [CrossRef]
51. Duriagina, Z.; Holyaka, R.; Tepla, T.; Kulyk, V.; Arras, P.; Eyngorn, E. Identification of Fe3O4 nanoparticles biomedical purpose by magnetometric methods. In *Biomaterials in Regenerative Medicine*; InTech: Rijeka, Croatia, 2018; p. 448. [CrossRef]

quantum beam
science

Review

Femtosecond Laser-Based Additive Manufacturing: Current Status and Perspectives

Atiq Basha Kaligar [1,2], Hemnath Anandan Kumar [3], Asghar Ali [2], Wael Abuzaid [2,4], Mehmet Egilmez [1,2], Maen Alkhader [2,4], Farid Abed [2,5] and Ali Sami Alnaser [1,2,*]

[1] Department of Physics, American University of Sharjah, Sharjah 26666, United Arab Emirates; b00090888@aus.edu (A.B.K.); megilmez@aus.edu (M.E.)
[2] Materials Science and Engineering Program, College of Arts and Sciences, American University of Sharjah, Sharjah 26666, United Arab Emirates; aasghar@aus.edu (A.A.); wabuzaid@aus.edu (W.A.); malkhader@aus.edu (M.A.); fabed@aus.edu (F.A.)
[3] Department of Mechanical Engineering, Indian Institute of Information Technology, Design and Manufacturing, Kancheepuram, Chennai 600127, India; hemnathceg@gmail.com
[4] Department of Mechanical Engineering, American University of Sharjah, Sharjah 26666, United Arab Emirates
[5] Department of Civil Engineering, American University of Sharjah, Sharjah 26666, United Arab Emirates
* Correspondence: aalnaser@aus.edu

Abstract: The ever-growing interest in additive manufacturing (AM) is evidenced by its extensive utilisation to manufacture a broad spectrum of products across a range of industries such as defence, medical, aerospace, automotive, and electronics. Today, most laser-based AM is carried out by employing continuous-wave (CW) and long-pulsed lasers. The CW and long-pulsed lasers have the downside in that the thermal energy imparted by the laser diffuses around the irradiated spot and often leads to the creation of heat-affected zones (HAZs). Heat-affected zones may degrade the material strength by producing micro-cracks, porous structures and residual stresses. To address these issues, currently, attempts are being made to employ ultrafast laser sources, such as femtosecond (fs) lasers, in AM processes. Femtosecond lasers with pulse durations in the order of 10^{-15} s limit the destructive laser–material interaction and, thus, minimise the probability of the HAZs. This review summarises the current advancements in the field of femtosecond laser-based AM of metals and alloys. It also reports on the comparison of CW laser, nanosecond (ns)/picosecond (ps) lasers with fs laser-based AM in the context of heat-affected zones, substrate damage, microstructural changes and thermomechanical properties. To shed light on the principal mechanisms ruling the manufacturing processes, numerical predictions are discussed and compared with the experimental results. To the best of the authors' knowledge, this review is the first of its kind to encompass the current status, challenges and opportunities of employing fs lasers in additive manufacturing.

Keywords: femtosecond lasers; additive manufacturing; 3D printing; heat-affected zone; powder bed fusion; direct writing; selective laser sintering

1. Introduction

Additive manufacturing (AM—commonly referred to as 3D printing) has already revolutionised industry and is positioned to make a notable impact across a wide range of sectors [1,2]. This is primarily induced by the significant simplifications and freedom in the design process combined with the adaptability of 3D printing to an impressively wide range of materials not shared by any other manufacturing technique [3]. Although the potential benefits of 3D printing can be exploited in a wide range of applications and industries, including aerospace [4–9], automotive [7,10], defence sectors [11], jewellery making [12], construction [13], electronics [14], food [15], health care [10,16,17], footwear [18], clothing [19], sports [20] and others [21], utilisation in the biomedical is of special interest due to the relatively complex requirements and intricate designs commonly encountered in these fields. The interest in AM continues to grow, and current research and development efforts span across almost all relevant aspects such as the utilised materials, 3D printing technology, post-processing treatments, and optimisation of processing parameters in terms of design and fabrication. One of the major advantages of 3D printing is the ability to adapt and optimise this manufacturing technique to all materials including polymers, ceramics, metals, and composites [1]. Such versatility is not shared by any other manufacturing technique. AM of metals is of particular importance due to the fact of their desirable properties in many applications (e.g., load-carrying capacity). Steel, titanium, aluminium, nickel-based superalloys, iron, copper, gold, and silver have all been successfully processed, even at an industrial scale in some cases [22–24]. Such efforts are no longer limited to lab-scale specimens as adoption by industry continues to grow. The aerospace industry was among the first to adopt AM technology for large-scale production. For example, GE aviation employed AM to print nozzles for its LEAP engines. In addition to reducing the total parts count from 20 to 5, durability was also found to be enhanced by a factor of five [25,26]. Similarly, Boeing is saving millions per plane through the use of AM. As of now, more than 70,000 AM parts fly through Boeing programs [27].

Although various techniques have been developed over the years for AM-based synthesis, including material extrusion (ME), direct energy deposition (DED), powder bed fusion (PBF), fused deposition modelling (FDM), sheet lamination (SL) and binder jetting (BJ) [28], the methods that rely on the utilisation of metal powders have been more widely adopted by industry (i.e., PBF, DED and BJ processes). The metal AM systems are usually composed of a powder delivery system and an energy delivery system [29]. In PBF systems, selective laser melting (SLM) or selective laser sintering (SLS) are key processes. In SLM or SLS, the material will heat up and subsequently melt utilising a laser source. At present, metal AM technologies are predominantly reliant on long-pulsed lasers or CW lasers to process materials [30,31]. In general, CW lasers are utilised for fabricating larger parts, whereas pulsed lasers are considered when fabricating precise and thin parts [32]. In the case of CW laser-based AM, there are certain important process parameters that influence the quality of the produced parts using SLM. This includes hatch spacing, scanning speed, laser power and layer thickness [33,34]. In any SLM process, along with these parameters, the light absorptance and the laser energy density play vital roles in melting and sintering. Despite the significant progress made, there are certain challenges that must be overcome such as accuracy and reduced materials usage [35]. In addition, some materials continue to pose challenges and are difficult to process using AM. For example, some ceramics and refractory metals, due to the fact of their high melting temperatures and high thermal conductivity [36], are still difficult to process using CW or long-pulsed laser-based AM technologies. To process such materials, novel technologies and new processes must be developed to reach very high temperatures while causing minimal heat-affected zones (HAZs), along with good precision and accuracy at sub-micron levels. In this regard, ultrafast lasers (i.e., picosecond (ps) and femtosecond (fs) lasers) are well suited for lifting the shortcomings of the existing additive manufacturing techniques, especially in situations where high melting point materials are involved or extreme precision and reproducibility are required [7,37]. Although AM via ultrafast lasers is a relatively new area, recent works have already highlighted its huge potential and advantages over the use of CW lasers [38]. In short, the main advantages of ultrashort pulsed lasers over CW lasers are increased part resolution [39,40], rapid cooling rate, reduced residual stresses, reduced oxidation effect, lower substrate damage compared to CW laser, suitable to process dielectrics and better wettability [41]. These aspects will be discussed in further detail throughout this article.

The use of ultrafast lasers as a manufacturing tool is gaining notable momentum across various industries. In a recent study, the global ultrafast lasers market was predicted to cross USD 1.43 billion by 2020, a number that is further expected to reach the USD 3.31 billion milestone by 2026 with an estimated compound annual growth rate (CAGR) of 16.6% between 2021 and 2026 [42]. Though the initial investment is high for such laser technologies, the significant advantages (e.g., precise manufacturing and reduced HAZs) provide justification for their use in medical, aerospace and military applications. As noted above, fs lasers are being explored for precise material processing due to the ultrashort pulse duration in the range of a few hundred fs that produces lower laser–matter interaction times and reduces HAZs. In addition to pulse duration, the scanning speed and pulse repetition rate are also major deciding factors for precise AM. Fs laser sources produce higher peak intensities compared to CW lasers or long-pulsed lasers. This allows for rapid energy delivery into the material and paves the way to achieve localised heating [43]. Apart from this, fs lasers have high penetration depth in a short range of time. It is because of these attributes that fs lasers can accurately remove a material, sinter it and can change its properties in a highly localised and controlled manner [44]. Over the past few years, various types of fs lasers, such as fibre laser and solid-state laser systems, have been used in the material processing field. They are capable of producing pulse energies in millijoules and output powers in kilowatts, pulse durations up to 100 s femtosecond and pulse repetition rate can be up to100 MHz [44,45]. With such properties, many applications have already been developed relying on this relatively new technology. Examples include their use in cataract surgeries in the health care sector and in material processing. As fs laser sources are capable of producing precise features at the micro and nano levels in a highly localised and controlled manner, applications at the nanomanufacturing processes [30], and micro fabrications (e.g., fabrication of micro-needles for medical applications [46]) are among the most commonly explored in the literature [47,48]. In addition, various works have explored the potential use of fs lasers for post-processing of 3D printed metallic components (i.e., utilising the associated heat to alter the microstructure) [49,50]. Further, fs laser sources were utilised to modify the flexural strength and surface morphology of materials such as translucent monolithic zirconia (for dental restoration) [51].

Apart from the machining and surface structuring processes, fs laser sources have been explored for the precise 3D printing of various materials such as copper [52–54], silver [55,56], iron [57], tungsten [7,44,58], aluminium alloys [59,60], YSZ [61] and functional ceramics [62]. Some examples include the utilisation of fs lasers in micro sintering to fabricate components at the microscale (e.g., micro engines with materials such as steel, nickel and titanium). Unlike bulk engines, micro engines must be sized down to a few mm, up to a cm, and must be manufactured with remarkable precision at the micro level. Using a CW laser in such a microfabrication process generates HAZs, which limits the process resolution and the finishing quality of the part [46]. In such cases, apart from single-material fabrication, ultrafast laser sources have been utilised in multi-material processing. For example, 12Cr2Si and 9Cr1Mo were reported to give excellent bimetallic structure following fs laser AM. The resulting bimetallic structure between the 12Cr2Si steel and 9Cr1Mo steel exhibited a smooth phase transition between interfaces, which led to excellent strength between the dissimilar metals [63]. Femtosecond laser-based AM is still in its infancy. This review is an attempt to highlight some of the fs laser-based research endeavours, identify the intended industrial applications and outline future prospects of the fs laser AM. We specifically focused on fs laser-assisted sintering and melting of powders, especially metals. We begin with the role of lasers in AM and the important parameters that affect the process. This is followed by a brief discussion on the simulations and models used to elucidate ultrafast laser–material interactions. Subsequently, an account for the role and importance of fs laser powder bed fusion (PBF) and multi-material layered structuring is presented. The reported parameters for sintering different materials are summarised. The review is concluded by spotlighting the future scope and prospects of fs laser AM [64,65].

2. Lasers in Metal Additive Manufacturing

Initially, lasers were employed in cutting and other subtractive manufacturing processes such as milling. Later applications considered the use of laser systems in surface modification and functionalisation. The laser-based AM processes or material deposition became feasible to use only when lasers with increased spatial control of the laser energy input were introduced. This was because these lasers had a high beam quality and enhanced beam delivery [66]. Different AM technologies use lasers as a source to process materials and fabricate complex 3D printed components. Such processes include SLS [22,67,68], SLM [22,69], direct metal deposition (DMD) [22], direct writing (DW) [70] and stereolithography (SLA) [69,70]. All of these, except for the SLA process, are executable with metallic materials [25]. Nowadays, different types of laser sources are being employed in AM. These include diode lasers, Nd:YAG lasers, CO_2 lasers, Yb-doped fibre lasers and excimer lasers [10,29]. The CO_2 lasers, which can run at relatively high power (kilowatt) levels, were widely utilised in metal additive manufacturing and welding processes at the beginning of the AM era. They were followed by Nd:YAG lasers, which are commonly employed as pulsed laser sources. Particularly for metal AM, diode lasers have longer lifetimes and higher efficiency. With relatively compact sizes, high reliability and low maintenance and operation costs, fibre-based lasers attracted significant attention by the AM community, especially for the fabrication and functionalisation of metallic structures [71]. A few commercially available AM machines and their laser systems are listed in Table 1.

Table 1. Commercially available laser-based metal AM machines [72].

Category	Manufacturing Systems	Laser
Direct energy deposition (DED)	Trumpf GmbH: TruLaser series	TruDiode diode laser, up to 6 kW (600 nm)
	Meltio	1200 W diode laser
	BeAM: Modulo series	500–2000 W fibre laser
	Oerlikon Metco Group: MetcoClad systems	1–6 kW diode laser
	InssTek: Fab series	Maximum 2000 W fibre laser
	Optomec Inc.: LENS series	400–1000 W fibre laser
Powder bed fusion (PBF)	Renishaw: AM250	200 or 400 W fibre laser
	SLM Solutions GmbH: SLM systems	400–1000 W fibre laser (for metals)
	EOS GmbH: EOSINT, EOS M and PRECIOUS M machines	30, 70 or 2 × 50 W CO_2 lasers (for thermoplastics) 200 W–1 kW fibre laser (for metals)
	3D Systems Inc.: ProX, sPro and ProX SLM systems	30–200 W CO_2 laser (for thermoplastics) 50–500 W fibre laser (for metals)
	Concept Laser	400–1000 W fibre laser (for metals)
	Aconity ONE	400–1000 W fibre laser
	Trumpf: Truprint 5000	500 W fibre laser

Across industries, many of the aforementioned AM technologies have been utilised for custom and mass production of various components. A summary highlighting the need for AM-based processing in different industrial sectors and the utilised processes are summarised in Table 2.

Table 2. Laser-based AM and its applications in various fields [73,74].

Industry	Trend/Goal	Laser-Based AM Process
Aerospace [12,29]	Demand for lightweight structures	DMD, SLS and SLM
	Rapid tooling, fixturing	DMD and SLS
	Fuel reduction	DMD, SLS and SLM
	Organic features	SLM, SLS and DMD
Automotive [10]	Demand for lightweight structures	SLS, SLM and DMD
Medical (dental, implants) [75]	Minimally invasive surgery	SMS and SLM
	Replication of anatomic structures	SLA and SLS
	Biomaterial manufacturing	SLS and SLA
Electronics [76]	Smart microsystems	SLA and Micro-SLS
	Miniaturisation	SLA and Micro-SLS
	Accelerated product development	SLA and Micro-SLS

Laser Parameters Used in AM

High throughput in manufacturing can be achieved with higher laser absorptivity [74]. In SLM, melting takes place due to the absorption of the thermal energy resulting from the laser–matter interaction. Specific heat capacity and latent heat vary from one material to another and may affect the final product's quality [75]. In some cases, the provision of insufficient energy affects the material build quality, thus leading to detrimental structural impacts. A number of factors, such as laser power, layer thickness, scanning speed and hatch spacing, can be tuned to determine the energy input. An extremely high laser power can result in excessive evaporation of molten material that causes a keyhole effect. In addition, if there is more vaporisation of material in SLM, the vapours may condense and result in laser power disruption [76]. In metal AM, better absorptivity is achieved by shorter wavelengths. CO_2 laser sources have relatively long wavelengths and, hence, lower throughput compared to Nd:YAG lasers. The resolution of the manufacturing method is highly dependent on the focusing ability of the laser source which is dependent on the operating wavelength [77–81].

Energy density is a critical parameter in laser-based AM, as it is closely associated with the occurrence of the underlying physical phenomena, whether it be sintering, melting or solidification [82]. Additionally, some materials that possess high thermal diffusivity and high reflectivity are influenced by energy densities. These energy densities are directly affected by laser power, which serves as the base for determining the build rate. Extremely high laser powers may also worsen the fabrication of parts. Hence, the optimum combination of processing parameters should be chosen to achieve good-quality part fabrication [83,84]. The beam spot size is one important parameter that determines the precision and manufacturing resolution. To calculate the beam quality, AM processes usually use the beam parameter product (BPP), which helps to identify the energy confinement at a point. BPP is usually calculated by the product of the half-angle of beam divergence and beam waist radius [29]. For CW laser-based SLM, the main process parameters, divided into powder-related, powder-bed related and laser related, are detailed in Figure 1 [41].

Different laser sources are classified based on the mode of operation as discussed in an earlier section. The most commonly used laser sources in AM processes, such as SLM, SLS and LENS, are CO_2, Nd:YAG and Yb-fibre lasers. Each laser source has a different wavelength and pulse duration that range from milliseconds ms to ns. On the other hand, ultrafast lasers operate in the range of fs–ps. When it comes to ultrafast laser-based AM, there are several other laser-related parameters that come into the picture such as laser wavelength, pulse duration, pulse energy, repetition rate, spectral bandwidth, average power, beam quality, beam diameter and power stability. Some laser parameters are more critical than the others, for they may greatly affect the finish and quality of the part produced. Some of these critical parameters are average power, pulse energy density, beam quality, spot size and pulse duration. The laser-related parameters and properties are crucial in a CW laser-based SLM process. The laser power source is the main element that provides sufficient energy to melt the powder particles. As discussed earlier, the laser source can be operated at different energy levels, which is denoted by the laser power. If the laser power is not sufficient, powders will not melt properly, and if the laser power is very high, improper melting occurs. The laser spot diameter also plays a major role in determining the energy transfer to melt the powder material [85]. Hatch spacing is the amount of overlap that is present between the adjacent tracks for the layer to improve the bonding [86]. Larger hatch spacing provides insufficient boding between adjacent layers [87]. In any SLM process, the laser moves with a particular velocity in a certain pattern, called a hatch pattern or a scan pattern, that helps to fill in the contours of the particular layer with laser-melted tracks [88]. A summary of the operational parameters specific to different lasers is presented in Table 3.

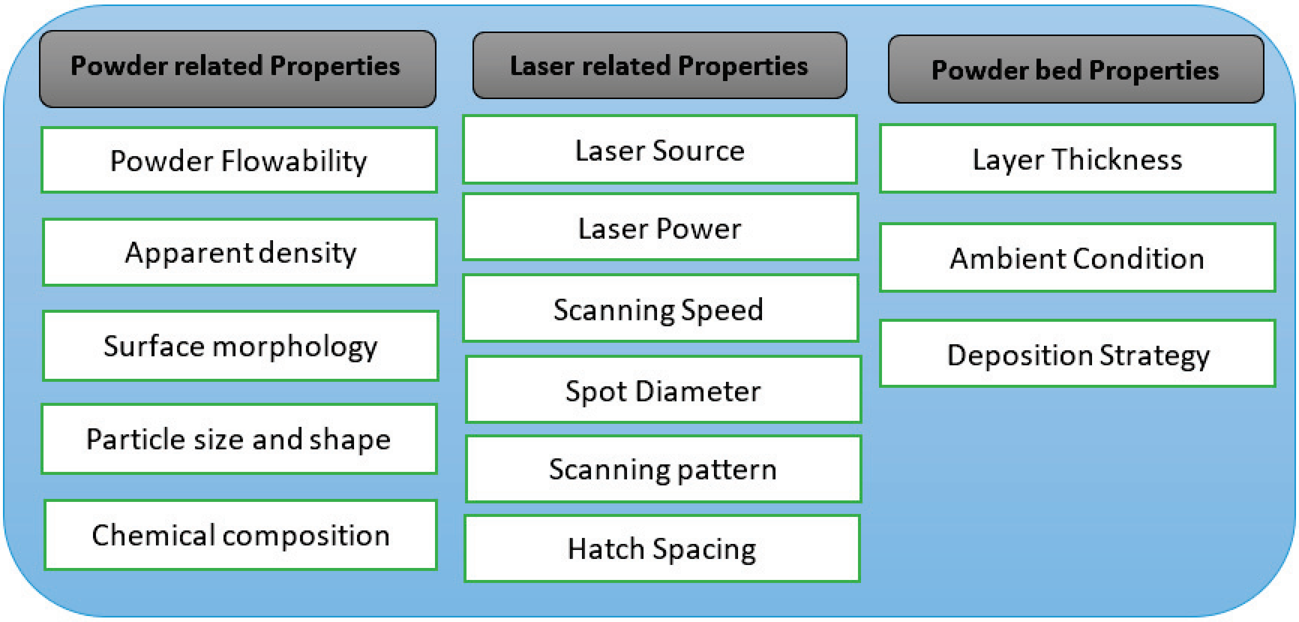

Figure 1. Summary of CW-based SLM process parameters [41].

Table 3. Types of lasers and related parameters used in AM processes [77].

Laser Type	CO_2 Laser	Yb-Fibre Laser	Nd:YAG Laser	Excimer Laser
Type of laser	Pulsed and CW	Pulsed and CW	Pulsed and CW	Pulsed
AM process	SLA, SLM, SLS and LENS	SLS, SLM and LENS	SLS, SLM and LENS	SLA
Wavelength	9.4 and 10.6 µm	1.07 µm	1.06 µm	193, 248 and 308 nm
Output power (CW)	Up to 20 kW	Up to 10 kW	Up to 16 kW	300 W (average)
Pulse duration	100–10 s ns	10 s ns to 10 s ms	Few ns to 10 s ms	10 s ns
Efficiency	5–20%	10–30%	10–20%	1–4%
Beam quality (mm.mrad)	3–5	0–4	0.4–20	0.5–2

Apart from the laser-related properties, powder-related properties are also equally important in determining the quality of the part. The particle size and shape should be within a specific range so that the part quality and surface finish can be assured [89]. The various process response characteristics of laser-based sintered parts are part resolution, surface finish, mechanical properties, microstructure, density and residual stresses, which are important for determining the quality of a 3D printed part [41]. Generated defects, such as cracks, swelling, residual stresses, substrate warping and melt ball formation, reduce the quality of the 3D printed part and should be investigated once the part has been 3D printed [33].

3. Femtosecond Lasers and Laser–Material Interaction

3.1. A Brief History of Ultrafast Laser Development

It is widely accepted that Theodore Maiman demonstrated the first short pulsed laser (i.e., ruby lasers) in the 1960s [64]. In the 1960s and 1970s, revolutionary mode locking research on organic dye lasers and solid-state lasers was published, encompassing both experimental [90,91] and theoretical investigations [92]. With the introduction of fibre amplifiers and fibre lasers in the 1980s, ultrafast fibre lasers became a new class of technology for ultrafast laser sources [93]. Further, Strickland and Mourou developed chirped pulse amplification (CPA) in 1985 that allowed researchers to make ultrashort, ultrahigh intensity laser pulses [66]. During the 1990s, D.E Spence developed a self-mode locked Ti:sapphire laser to produce pulses with pulse durations up to 60 fs, which was a turning point in ultrafast laser development [17,94]. With significant advancements during the 1990s, pulse durations as low as 6.5 fs were achieved [95]. Today's commercial fs fibre lasers can easily deliver pulses of durations less than 100 fs, repetition rates in MHz, and average power in the kW regime. Previously, ultrashort pulse lasers with pulse energy in nanojoules and operating in MHz were mostly reported for communication and information transmission. AM, on the other hand, requires tunable but high pulse energies to process materials [65]. The potential to produce ultrashort pulses with lower HAZs and high peak powers makes fs lasers desirable in industrial applications.

3.2. Mechanisms of Ultrafast Laser–Matter Interaction

Ultrafast lasers are distinguished mainly by three factors: extremely short pulse duration, high intensity and a broad spectral bandwidth [96,97]. In laser–materials interactions, fs lasers allow for rapid energy delivery into the material (in ps) that is significantly faster than plasma expansion time (from ns to µs), causing the local temperature to rapidly rise to temperatures as high as 6000 °C [44]. These factors enable the use of ultrafast lasers in high-quality manufacturing processes with minimal heat dissipation in the surrounding environment. This is a huge advantage compared to nanosecond lasers in which the melted material at the laser focus has time to heat up and diffuse heat into the surroundings, generating large craters with off stoichiometric compositions. Furthermore, during long-pulsed laser processing, micro droplets are generated as a result of the ejected vaporised material, leaving the remaining material to resolidify, which leads to poor processing and generates HAZs, microcracks, dross and recast [64]. For pulse durations in the range of nanoseconds, the absorption of the laser pulse is governed by the linear optical absorption depth of the laser, which causes energy dissipation by heat conduction into the substance [45]. In general, for CW and long-pulsed lasers, the processing would include melting of material, reflow and solidification [64]. Figure 2 shows the comparison of CW, ns and fs-pulsed lasers (i.e., high and low power, respectively) and their material absorption characteristics [57].

When ultrashort pulsed lasers with high laser fluence are applied, ablation of heated matter occurs in a few tens of ps after absorption [47]. In the case of metals interacting with ultrashort lasers, the electron gas absorbs the laser and heats up in less than a hundred fs, whereas the lattice heats up with a delay of 1–100 ps [98,99]. Additionally, HAZ can be less than 5 µm, and for plastic materials, it can be up to 30–50 µm [47]. On the other hand, the penetration depth per pulse for ultrashort pulses is typically between 20 and 100 nm for metals, polymers, and semiconductors but up to 500 nm for glass and transparent materials. Therefore, as the pulse duration decreases, the ablation rate increases, which is also dependent on the laser wavelength, i.e., the absorption spectrum of the material [45,47]. For example, Table 4 shows the maximum ablation rate at 400 fs of pulse duration and 1035 nm wavelength of laser. Generally, with the decrease in pulse duration, the energy and ablation depth increases, while thermal diffusion length become shorter (Figure 3) [47]. Such trends can be advantageous for precise material processing [45].

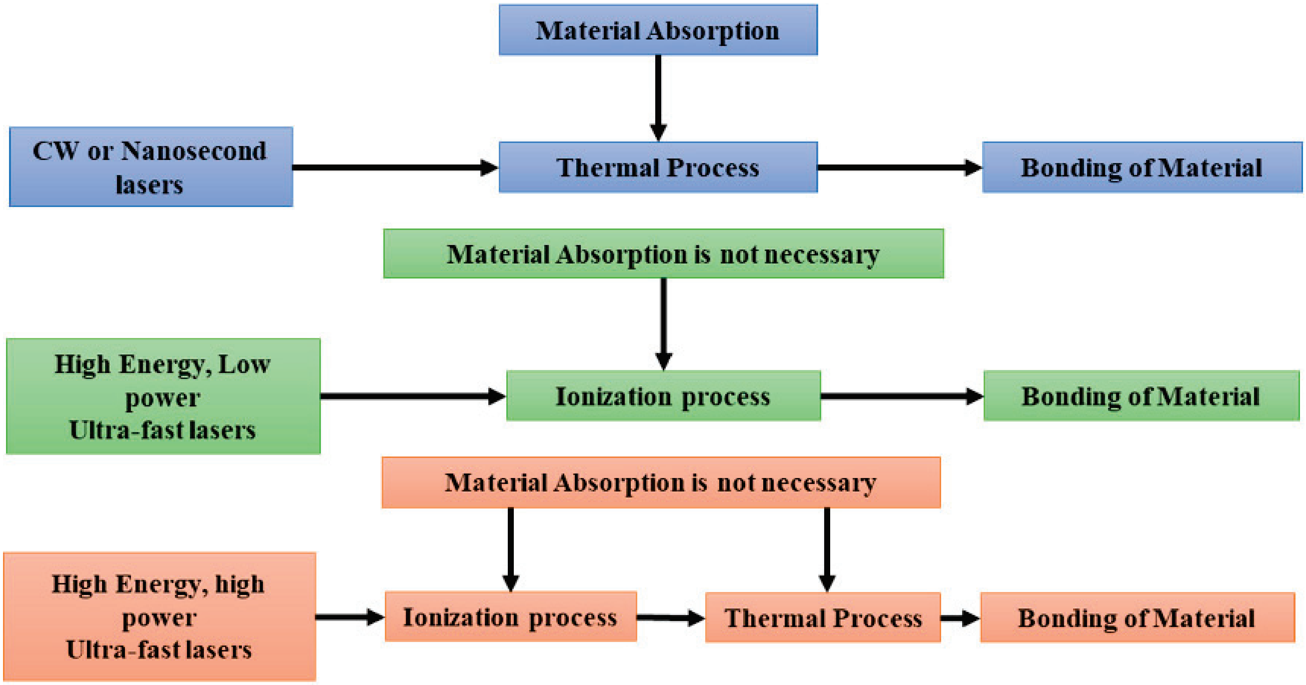

Figure 2. Comparison of CW, ns and fs laser material absorption processes [57].

Table 4. Different maximum ablation rates for various material processes [96].

Material	Optimum Avgerage Fluence at 400 fs and 1035 nm (J/cm^2)	Maximum Ablation Rate at 400 fs and 1035 nm (mm^3/W min)
Steel	0.35	0.22
Nitinol	0.6	0.21
Aluminium	1	0.3
Copper	1.7	0.16
Si	1.3	0.16
SiC	0.7	0.13
PET	0.7	8
Fused silica	3	0.4
Sapphire	4	0.3

The data in Table 4 are included in [44] as a basis for estimating ablation rates, which may be useful for micromachining, structuring and other industrial applications. However, in the case of SLS, ablation of the material may be unfavourable for additive manufacturing, because it requires melting or partial fusing of particles to print layer by layer. Therefore, by appropriately tuning the fs laser parameters and utilising the most important characteristics of fs laser sintering (i.e., generating reduced HAZs and lower heat dissipation), it was possible to print different materials such as copper [52,53], iron [100], silver [55,56], tungsten [7,44,101] and aluminium [38,60]. Additive manufacturing of parts utilising fs lasers is complex and comprises various factors/parameters as shown in Table 5.

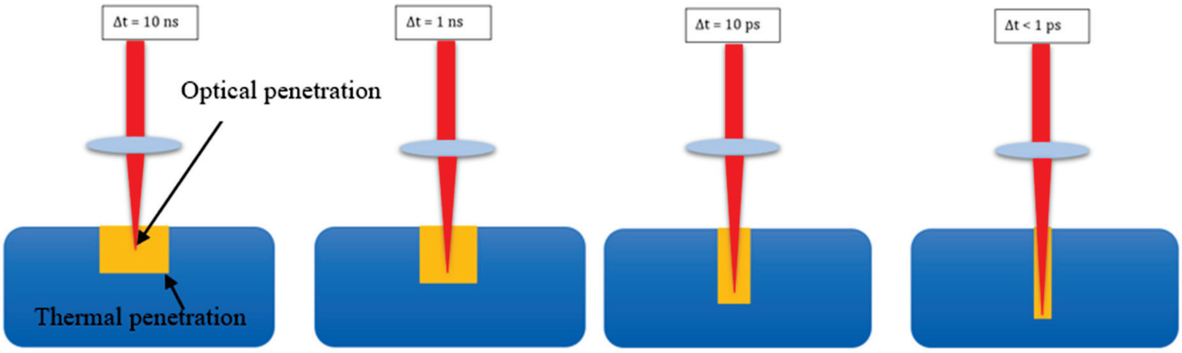

Figure 3. Energy penetration (red) and volume heated via heat conduction (yellow) or different pulse durations [47].

Table 5. Various factors that influence fs laser material processing [44].

Various Factors	Description
Pulse energy	Depends on the average output power and pulse repetition rate
Pulse width	Called pulse duration also and, in general, varies a few hundred femtoseconds in the case of fs laser material processing
Average power	Total average output power utilised in material processing
Pulse repetition rate	Number of pulses per second, in general, between kHz and a few MHz will be utilised during material processing
Peak power	Maximum peak power attained by a single pulse
Focus spot area/volume	The laser spot area or volume is the exposed area/volume, which is important to consider during precise processing
Hatch spacing	The spacing between each line exposed during area-wise material processing
Scanning velocity	The scan velocity is the speed of the laser travelling during processing; it is the most critical parameter to control because the exposure time depends on this parameter
Operation mode	The environment during processing
Wavelength	The laser operating wavelength
Powder particle size	The powder size is important to consider, depending on the application
Shape of the powder particle	In general, for SLS/M spherical powder particles are considered
Powder morphology	The uniformity of powder size distribution

Pulsed lasers produce discrete pulses of laser energy at a specified repetition rate. In Table 5, pulse energy is defined as the energy per each pulse, which is proportional to the average power and inversely proportional to the repetition rate of the laser. The full width at half maximum (FWHM) in the laser's optical power vs. time plot is defined as the laser pulse duration, or pulse width. The average power of a pulsed laser is calculated as the energy of the pulse divided by the pulse duration. The number of pulses released per second is defined as the pulse repetition rate. Higher repetition rates result in less thermal relaxation time at the surfaces, which leads to more rapid material heating. The maximum laser power that a single pulse attains is known as laser peak power. The laser spot at the focal plane of a focusing lens is described by the spot size of a focused laser beam [102]. In general, the goal of many applications, such as materials processing, is having a minimum spot size. In materials processing, different materials will have different wavelength-dependent absorption characteristics, resulting in distinct interactions with the substance. The operation mode relates to the laser processing environment; in many situations, argon or nitrogen gas purging has been used to avoid oxidation issues [89,103]. It is also necessary to consider and monitor the powder quality and size distribution before processing. The powder quality depends upon the size and shape of the powder. The powder size distribution is crucial in facilitating the sintering of powder particles and, as such, the powder particles should be of uniform shape, because dissimilar-shaped powder particles will lead to poor melting and will affect the quality of the fabricated part [104,105]. Both powder size and laser spot diameters determine the precision of 3D printed parts generated by fs laser-based 3D printing [77].

As for metallurgical aspects, melting in general refers to particle–particle fusion during fs laser melting or sintering. Phase change refers to change in phase during sintering process. This is dependent on the uniform cooling that happens in the process and on the material's thermo-physical properties. Cracking and residual stresses, in general referred to as defects generated in the printed parts, need to be analysed once the part is fabricated. Thermal diffusion depends on the material property, i.e., thermal conductivity. For example, due to the fact of its high thermal conductivity, when copper interacts with the laser, a large amount of heat is dissipated into the surroundings.

A simplified illustration of the temporal evolution of the fs-laser-based AM process was developed by Shaung et al. [44]. As shown in Figure 4, fs laser ablation causes ionisation of materials and the development of new grains and microstructures during cooling and solidification, which occur on a ps–μs time scale. When the pulse duration is at the lowest pulse duration (i.e., at the start and less than ps), the laser–matter interaction is mainly dominated by ionisation of materials, ablation and plasma formation. When the pulse duration is, in general, between fs and ns, the local temperature may exceed 10,000 K. Similarly, as the pulse duration increases, there will be thermal energy dominance. Finally, correlation between the pulse number and temperature shows that it is possible to reach higher temperatures with higher pulse repetition rates.

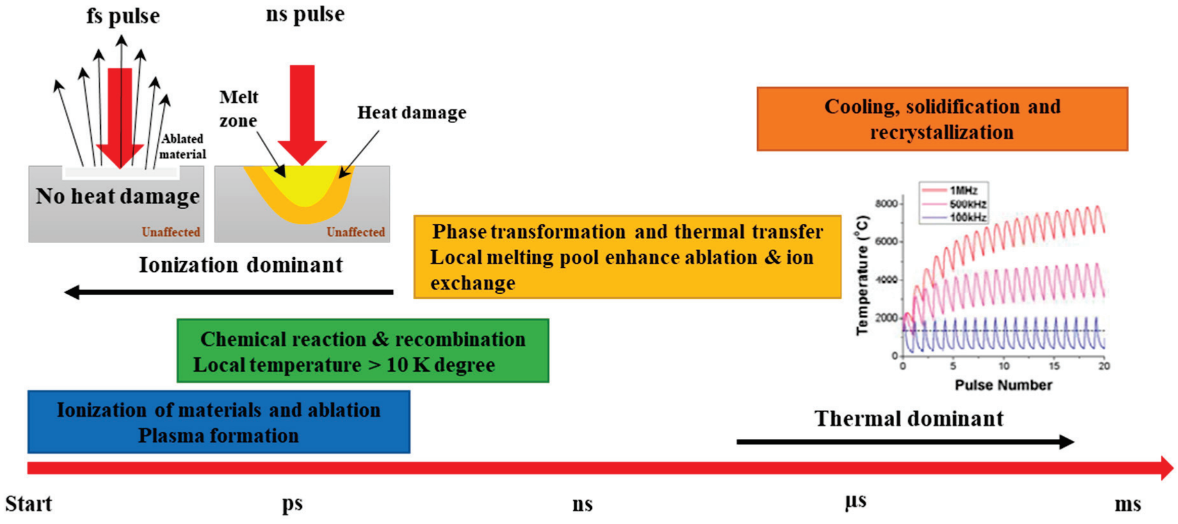

Figure 4. Temporal evolution of an fs-laser-based AM process [44]. The inset shows the correlation between pulse number and temperature for different repetition rates.

3.3. Modelling and Numerical Analysis of Laser-Based AM

To better understand the principal physical interactions and the governing mechanisms of a manufacturing process, it is essential to develop numerical-based models that capture the underlying physical phenomena of the process. Such models, for instance, can provide details about the temporal and spatial distribution of the temperature, deformation and stress fields resulting from the material–tool (e.g., laser or cutting tool) interaction during the manufacturing process. These fields are difficult and often impossible to obtain experimentally; however, they allow for realising a better understanding of the processes' underlying physical interactions and their effects on the quality of the manufactured part. The latter is needed to optimise the manufacturing process (e.g., increase its sustainability, throughput or reduce its cost) and improve the quality of the manufactured parts (e.g., enhance their surface finish and mechanical properties).

Developing an accurate physically informed numerical model of a manufacturing process requires identifying and including the physical laws and equations that describe the evolution, interaction and equilibrium of the physical parameters pertaining to the physical phenomena associated with the manufacturing process. Applying this to laser-based material processing techniques proved challenging as they are intrinsically multi-physical problems and involve complex coupled governing equations. Thus, different strategies for modelling laser-based material processing were developed. The different strategies, which are overviewed in the following, included different assumptions and used different numerical schemes (e.g., finite element and molecular dynamics). Most importantly, each approach was designed to investigate a certain aspect of laser-based material processing.

The mostly used strategy to model laser-based processing of materials simplifies the modelling process by modelling the laser–material interaction as an intense heat source. Subsequently, the response of the material to the intense heat source is modelled using thermo-mechanical equilibrium and constitutive equations that compute the temperature and deformation fields in the vicinity of the heat source. Later, temperature and deformation fields are used to determine the processed material microstructure (e.g., grain size and dislocation density). This approach, which was mostly used to model CW laser-based processing, was applied successfully to model laser welding [106], DED [107] and SLM [108].

The aforementioned thermo-mechanical approach was extended to model fs laser processing of metals. The extension involved emphasising more on the heat and mass transfer and applying the analysis at two length scales: one at the microscale and another at the nanoscale. Modelling heat transfer and temperature distributions at small scales (i.e., nano and micro) is of great importance, as the fabrication process is highly dependent on phenomena occurring at those small scales. However, at the microscale level and below, additional challenges arise. Using fundamental and phenomenological laws, such as Fourier's law of heat conduction, become highly challenging as the heat transfer time characteristics vary for various heat carriers, which may align with the energy excitation time [109]. In addition, modelling heat transfer at the microscale is computationally challenging, as it requires considering micro time steps, which increases the computational costs. Even with the aforementioned challenges, many preliminary modelling-based studies have been conducted over the past two decades to analyse the capability of fs lasers to precisely cut materials. These showed that fs lasers can be used to precisely cut materials [110,111] and produce "precise cuts" with minimal damage [112]. In addition, models showed that the HAZ and the rate of heat can be precisely controlled in fs laser processing in comparison with the processing of materials using long-pulsed lasers [113].

Developing more capable thermo-mechanical models that better describe the interaction of fs lasers with the processed material necessitated representing the fs-laser induced energy and heat transfer process more accurately. During fs laser processing of materials, three different types of heat transfer regimes exist [114] and should be accounted for in the models. In the primary stage, the energy from the laser is absorbed by the electrons of the processed material. At this stage, the excited electrons are in a state of thermal non-equilibrium. In the second stage, the electrons gradually attain a state of thermal equilibrium, and fermi distribution can be used to represent the density of the existing states. But the lattice and electrons will be at two different states of temperature regimes. During the second stage, heat transfer mainly occurs due to the diffusion of hot electrons. In the third and final stage, the lattice and electrons reach a state of thermal equilibrium.

In this stage, the energy is carried into the bulk through a normal thermal diffusion process [115]. In general, when an fs laser interacts with any metal, the electron subsystem absorbs the laser pulse energy, which increases the electrons' temperature to very high temperatures in the range of thousands of degrees kelvin. However, during irradiation, the lattice temperature lags behind that of the electrons, and the lag remains for the next few ps. Eventually, the laser energy transferred to the electron subsystem is carried to the lattice subsystem. Models that account for the aforementioned three stages have been developed and used to describe fs laser–material interaction during the processing of copper [116].

Specialised models were also developed to investigate specific physical mechanisms pertaining to laser–material interaction. For instance, to better understand and predict fs–laser–induced ablation during fs-laser-based processing of materials, numerical and theoretical models were developed. These included molecular dynamics [117,118] and hydrodynamics models [119,120] (continuous thermodynamics model). Predicted ablation depth, using a hydrodynamics model, for copper and aluminium subjected to an fs laser is shown in Figure 5. This figure shows a relatively good correlation between the experimental and numerical results, underscoring the importance of numerical models. The molecular dynamics models include the kinematic equations of each atom present in the ablation entity. Whereas the hydrodynamics model uses a set of equations in a Lagrangian form that represent hydrodynamics along with the multiphase equation of the state. Though these models are able to represent the underlying physics of the process, they are complex and consume large amounts of computational time.

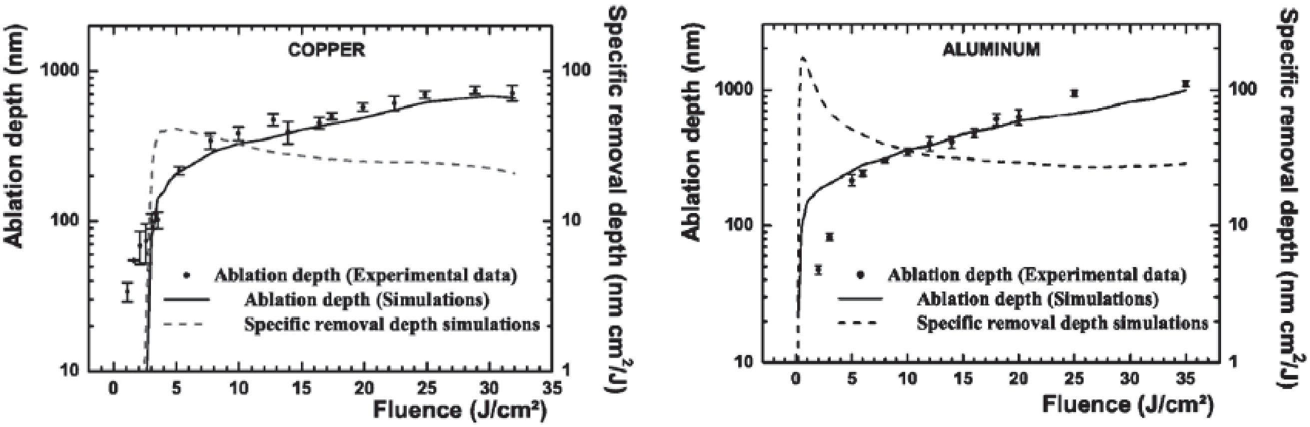

(a) **(b)**

Figure 5. Experimental and numerical results of ablation depth as a function of laser fluence using a hydrodynamics model for (**a**) copper and (**b**) aluminium with a 170 fs laser pulse (Adapted from reference [119]).

To study the complex process of ablation and to predict the non-equilibrium temperature distribution between the lattice and electrons regime, while avoiding the computational complexities of hydrodynamics and molecular dynamics models, a two-temperature numerical model was developed by Anisimov et al. [121]. Due to the fact of their computational efficiency, two-temperature models (TTMs) are widely used to model fs laser processing of metals [99,122]. The two-temperature model was developed from the Boltzmann equation and is composed of the following coupled PDEs (partial differential equations) [123]:

$$C_e(T_e)\frac{\partial T_e}{\partial t} = K_e\nabla^2 T_e - G(T_e - T_l) + Q(r,t) \tag{1}$$

$$C_l\frac{\partial T_l}{\partial t} = K_l\nabla^2 T_l + G(T_e - T_l) \tag{2}$$

where C_e is the electron heat capacity, C_l is the lattice heat capacity, K_l is the lattice thermal conductivity, K_e is the electron thermal conductivity, $Q(r,t)$ is the laser energy density absorbed per unit time, and G is the electron–phonon coupling constant. In these equations, the temperature-dependent variables are G, K_e, and C_e. Equations (1) and (2) represent the mechanics of heat transfer in the electron and lattice reservoirs, respectively, and they are composed of the diffusion equations for both reservoirs and the coupling term that represents the temperature difference between the two (i.e., electrons and lattices). Accordingly, these are the energy balance equations that represent the absorption of the laser pulse by the metal. The basic TTM, represented by Equations (1) and (2), has been subjected to various modifications and adaptations, to increase its accuracy or investigate a particular physical interaction.

TTM was adapted to account for additional physical properties. For instance, Ahmed et al. [124] developed a numerical model to simulate fs laser ablation of copper. In this effort, a TTM model that accounts for the thermophysical and dynamic optical properties was used. The important process parameters considered in their work included pulse number, laser fluence and the time interval between pulses. The laser pulse chosen was Gaussian with the FWHM mode having a wavelength of 800 nm. In addition, electron temperature and lattice heat capacity were considered in calculating the dynamic thermal properties. For both single- and multi-pulse laser irradiation with varying process settings, numerical simulations were carried out. It was concluded that during ablation of copper, while keeping the fluence constant, the ablation depth increases with the increase in the number of pulses.

Attempts were made to implement TTMs in commercial modelling packages that could enable a wide range of users to model laser–material interactions. For instance, Lee et al. implemented a TTM in the finite-element-based commercial software ABAQUS [125,126]. Temperature predictions obtained by the implemented model were validated using analytical results of the linear two-temperature model. The low and high fluences were also validated using nonlinear simulations and data values taken from literature [123]. The overall research concluded that a pulse repetition rate in the range of 0.1–1 GHz aids in maximising ablation and reducing melt pool generation. The latter two conditions enabled a more precise metal cutting process [125,126]. Limitations and potential improvements to TTMs attracted the interest of the research community. For instance, Jian et al. analysed an existing TTM and found that it was limited only by low fluence, which is used for the estimation of important parameters such as electron heat capacity and reflectivity [127]. To improve the prediction of the existing TTM, some parameters, such as electron relaxation time, absorption coefficient, electron heat capacity, reflectivity and electron conductivity, were introduced. The modified model was used to predict the initiation of melting in gold metal and to study the effect of pulse duration on predicting the fluence threshold for initiation of damage [127]. Davydov et al. also attempted to improve the accuracy of TTMs using a semi-empirical equation for the state [128]. However, this approach was less efficient than Jian et al.'s model [127]. A TTM was also modified and used to investigate the effect of the angle of incidence. For studying the temperature and ablation depth during the ablation of copper at an oblique angle of incidence using an fs laser, a numerical simulation was developed by Dasallas et al. [129]. The used model was an improved model of the TTM. Improvements included accounting for laser spot size, laser fluence and the dynamic changes in the reflectivity of the target. Simulation results showed that threshold energy of ablation was highly dependent on the angle of polarisation and the polarisation of incident light. However, the model did not predict the topography of the crater ablation in detail. TTM-based simulations were found to be useful in studying rapid melting and solidification using laser-based processing. Kuo et al. used a TTM to study the melting and solidification of materials using ultrafast lasers and found that if pure conduction is considered, after turning off the laser pulse, melted layers near the heating surface will solidify [130]. Fischer et al. [131] and Konrad et al. [132] conducted similar investigations but for SLM of metal powders using ultrashort pulses. A one-dimensional TTM that considers the thermophysical properties and temperature-dependent material properties was developed by Cheng et al. to study and simulate fs-laser-induced melting of copper nanoparticles [133]. This model included the extended Drude model with dynamic optical properties. The model was successfully validated using experimental results [52]. Cheng et al. [133] also experimented with fs laser processing of silver nanoparticles and simulated the sintering process using TTM. Jia et al. developed another one-dimensional TTM and used it to investigate the dependence of ablation depth in gold, copper and aluminium on various process parameter settings [134]. In this model, the spatial temperature distribution of the lattice was used to determine the ablation depth. Both TTM- and molecular dynamics (MD)-based models have been used to model laser–material interaction for ultrafast and ultrashort pulsed lasers. However, each approach has its advantages and limitations [135]. For instance, MD better represents the underlying physical interactions, while TTM is less complex and computationally demanding, and it is more compatible with widely used modelling software. In order to overcome the individual limitations of each method, hybrid models that better represent the underlying physics of laser–material interactions were developed. Hybrid models comprising the advantages of both TTM and MD were used to study laser–material interactions for processes utilising ultrashort lasers [136,137].

4. Femtosecond Laser-Based Additive Manufacturing—Powder Bed Fusion

As mentioned previously, the use of ultrashort pulsed lasers in AM results in lower thermal damages to the surrounding environment due to the high peak intensities and short pulse duration. Those result in rapid transfer of energy into the material, causing ionisation that is much quicker than plasma expansion (in the range of ns) [44]. Fs lasers in AM have been employed mainly in two processes, namely, PBF and DW technology. The DW technology is explained in detail in Section 5, and Figure 6 shows the overall schematic of an fs laser source integrated with PBF, i.e., (SLS/M).

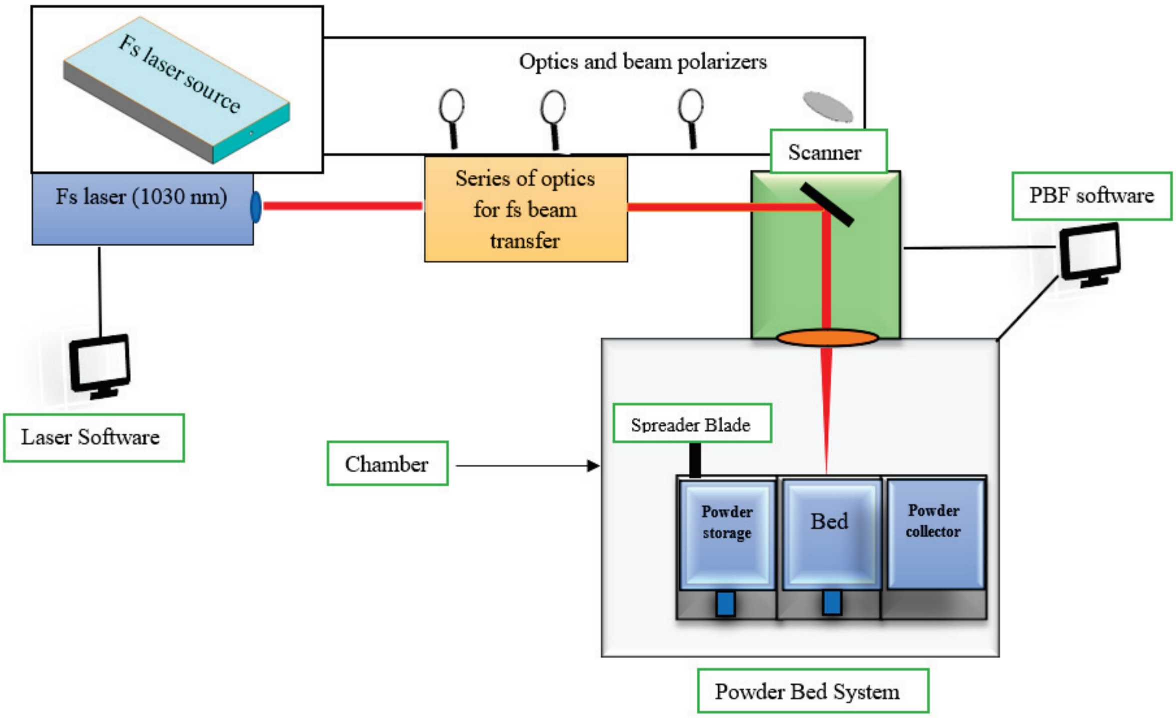

Figure 6. Schematic of the fs-laser-based selective laser sintering–powder bed fusion process.

The main heating or melting source element during fs laser processing is the fs laser source that is usually operated by the inbuilt laser software. Through this software, laser parameters, such as pulse duration, pulse repetition rate and beam profile, can easily be controlled. When laser parameters are set and the laser beam is allowed to pass through a series of optical elements, the beam is directed towards the scanner system. The required average output power is usually regulated by the beam polariser. The scanner software is utilised to set the scanning speed, hatch spacing, part geometry and the other aspects of the 2D drawing. The laser light is then focused through the scanner onto the powder bed system. The powder system consists of a spreader, powder bed, powder storage and powder collector. Before the laser light falls on the powder bed, the recoater mechanism spreads the powder on the powder bed with a set layer thickness. Then printing is conducted layer by layer. The PBF system could be enclosed in a chamber with an inert gas environment to eliminate oxidation issues. By employing further optimised parameters in fs laser AM, successful manufacturing of more precise functional parts for diverse applications, such as in the microelectronics, aerospace, automotive and biomedical industries, have already been demonstrated [130].

5. Femtosecond Laser Additive Manufactured Powder Materials, Print Qualities and Characterisation

As discussed earlier, laser-based AM has shown great potential in the last few decades for fabricating complex 3D geometries with diverse functional materials and with relative ease. Continuous wave laser-based 3D printing has been the industry standard in the field of laser additive manufacturing. However, and despite the significant advantages associated with the use of CW lasers, there still remain challenges related to heat affected zones and the development of cracks that tend to result in defective parts with poor quality. Many research and development efforts focus on optimising the CW laser processing parameters and conditions to address these issues. More recently, the use of ultrafast femtosecond lasers (pulse duration = 10^{-15} s) in SLS/SLM (PBF techniques) [54,138] and DW technology [52,53,139,140] is being considered. The use of short laser pulses reduces the developed thermal gradients and would, consequently, reduce the heat affected zones and limit thermal stress levels (associated with the development of cracks during printing). In addition, the smaller spot size in femtosecond lasers allows for a greater precision in the submicron range. Such accuracy and resolution are not typically offered by CW laser systems, which have spot sizes in the mm range. Some of the most recent developments in fs-based AM are discussed below. As different materials bring along different sets of challenges and requirements, this review is presented in sections based on the considered base metal for fabrication. Combined, the sections below provide a comprehensive review of relevant works on fs laser-based AM.

5.1. Femtosecond Laser Sintering of Copper

Copper and copper alloys are widely utilised in industry because of their remarkable properties such as thermal, electrical and corrosion resistance [141]. The utilisation of this metal in AM has diverse applications in various sectors including electronics [142], aerospace [143], automotive [141], heat exchangers [143] and MEMs [142]. Due to the high thermal conductivity of copper (i.e., 400 W/m·K), this material has historically been considered as one of the most difficult to print due to the large heat dissipation into the substrate [143], which prevents a sufficient temperature rise to melt the powders during printing. Additionally, sintering copper-based materials has been reported to be challenging with CW laser sources due to the fact of its high reflectivity that reduces effective energy deposition into the material [144]. Nevertheless, various attempts with certain levels of success have been reported in the literature for AM of Cu-based materials. For example, Pogson et al. [144] investigated the sintering of pure copper through PBF process utilising CW and ns lasers but failed to produce high-density parts [144]. Sciammarella et. al. [145] fabricated 12 cubic mm volume of C1100 copper onto a 4142-steel substrate utilising CW laser at a 900 W laser power [145]. NASA has also reported the successful fabrication of the first full-scale copper rocket part utilising AM methods and copper-based alloys [143]. NASA further fabricated combustion chamber liners, integral channels and closeouts with a high conductive and high-strength copper-alloy i.e., GRCop-42 (copper–chrome–niobium) utilising the PBF (SLM) process [143,146]. Cu–Cr–Zr–Ti alloy powders were also used in the SLM process to produce parts that have applications in the combustion chamber liner of a rocket engine and as heat sinks of the components of the first wall and diverter of the international thermonuclear experimental reactor (ITER) [147]. In addition, Colopi et al. [148] utilised a 1 kW CW laser to fabricate a heat exchanger consisting of complex geometries and fine critical features, where the use of high power was meant to overcome the limitation of poor laser absorptivity [148].

In the current era of the fourth industrial revolution, and with the growing demand for functionality and performance in MEMs devices, an increasing number of transistors must be packed and interconnected on electronic boards, resulting in smaller chips and interconnects [141,148]. To fabricate transistors and interconnects, traditional manufacturing techniques have been utilised. However, the fabrication of miniaturised features using such traditional techniques is limited [142]. Currently available macroscale metal AM techniques, such as PBF utilising CW lasers, are reported to produce a minimum feature with sizes up to 100 µm, which is still too large. The minimum feature size of a back-end-of-line (BEOL) wafer interconnect is in the range of 15–20 µm [149]. To address this issue, nowadays, a new technique called microscale AM is being employed to fabricate parts at the micro- and nanoscales. The DW process is a widely used AM technology for such microfabrication of conductive micropatterns using Ag, Au and Cu metals [150,151]. Among these, Cu is considered to be the key material for low-cost printing [152]. Further, the ultrafast lasers, such as ns and fs lasers, are preferred over CW lasers in micro-level fabrication because of the smaller spot sizes, lower HAZs, and less substrate damage [149,153]. Copper has been most widely in fs laser sintering due to the fact of its wide range of applications in MEMS [116], microsensors [53], complex cooling structures [138], among others. Cheng et al. [52] demonstrated experimentally and theoretically the sintering of copper nanoparticles (NPs) utilising a femtosecond laser. The fs laser sintering was carried out on a copper-coated substrate with a pulse repetition rate of 80 MHz, pulse width of 100 fs and a wavelength of 800 nm. Figure 7 shows SEM images of copper patterns generated at two average powers of 195 and 210 mW, and a scanning speed of 0.1 mm/s [52]. The experimental and theoretical results for copper nanoparticles sintered by fs laser reported by Cheng et al. were found to be in good agreement demonstrating the great potential of this technique in the field of micro- and nanoscale manufacturing.

N Roy et al. (2017) utilised microscale SLS techniques to investigate and compare the processing capabilities of CW, ns, and fs lasers to achieve miniaturised features of 1 µm sized interconnect transistors [142,149,150]. The oxidation issues were reported to be more severe in CW laser sintered parts compared to the ns and fs laser sintered parts. The HAZs were also minimal and there was lower substrate damage for the ns and fs lasers compared to CW laser sintering [142]. Mizoshiri [53,152] utilised an fs-laser-based DW additive manufacturing process to fabricate copper-based microsensors for temperature sensing. This was achieved through reductive sintering of CuO. In this experiment, Cu_2O-rich sensing parts and Cu-rich electrodes were 3D printed. Though laser reductive sintered metal oxide NPs were reported to have higher resistivity than laser sintered metal NPs, their absorption of irradiated light was higher [152]. Figure 8 shows the Cu NPs spin-coated substrate irradiated with a femtosecond laser to form Cu- and Cu_2O-rich micropatterns. The film was spun-coated at 7000 rpm on a substrate with a thickness of 1 mm with different materials, i.e., CuO NPs at 60 wt%, ethylene glycol at approximately 27 wt% and PVP solution at approximately 13 wt%, respectively. Later, the unsintered part was removed by ethylene glycol and ethanol.

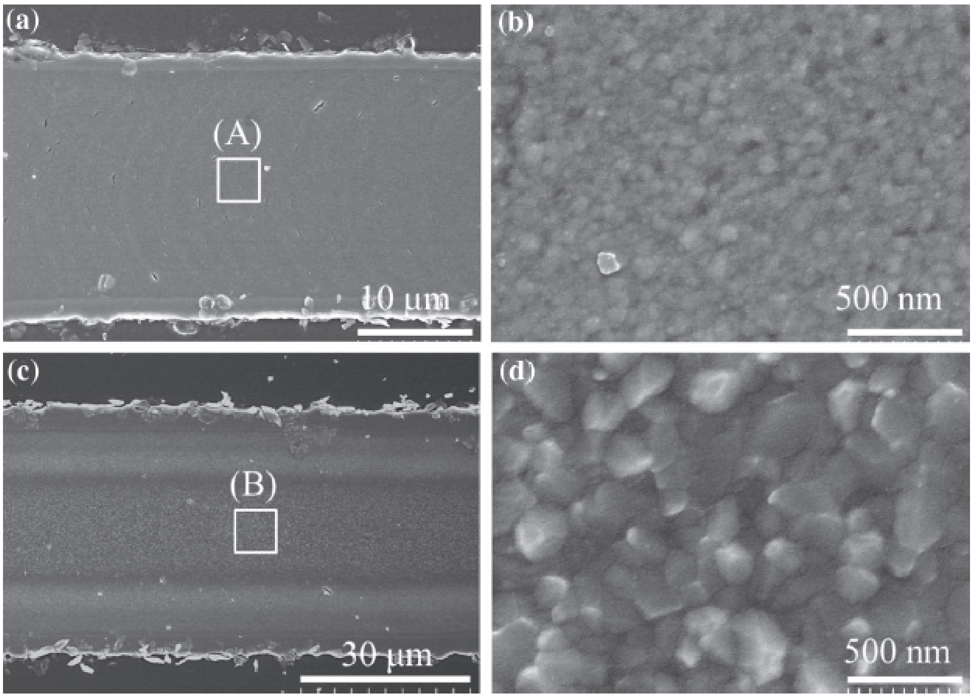

Figure 7. SEM images of Cu line patterns at a constant speed of 0.1 mm/s and laser fluences of (**a**) 12.8 mJ/cm^2 at 195 mW; (**c**) 13.8 mJ/cm^2 at 210 mW where (**b**,**d**) are magnified images of regions (**A**) and (**B**) (Adapted from reference [52]).

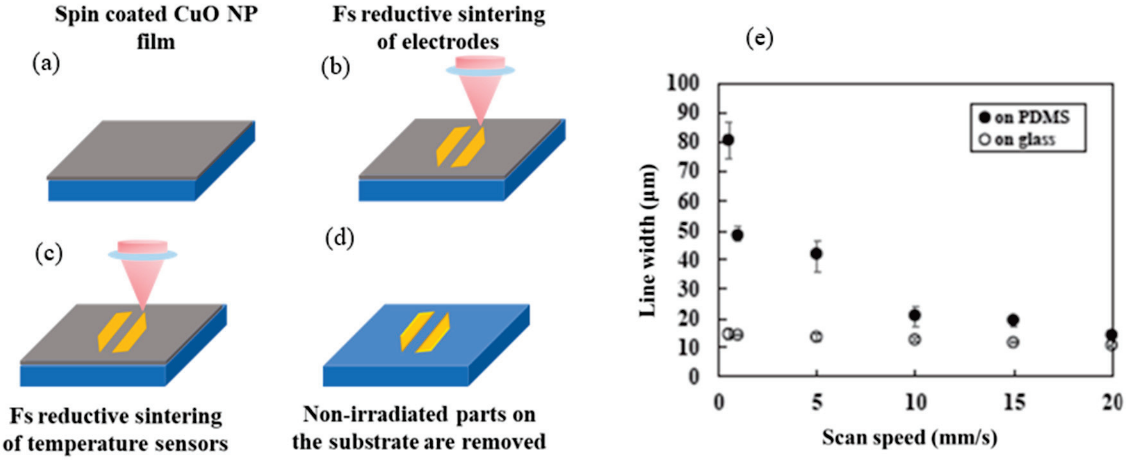

Figure 8. (**a**) Spin-coated CuO NP film; femtosecond reductive sintering of (**b**) electrodes, (**c**) temperature sensors and (**d**) non-irradiated parts on the substrate were removed; (**e**) fs laser reductive sintered line width on PDMS vs. glass as a function of the scanning speed [53].

As for the laser processing parameters, a pulse repetition rate of 80 MHz, pulse duration of 120 fs and a max pulse energy up to 0.62 nanojoules, operating at an 800 nm wavelength, were used [53]. It is evident from Figure 8e, that in the case of both the glass and the PDMS substrates, the width of the printed lines decreased with the increase in the scanning speed. In addition, the authors noted that at a particular scanning speed, the line width on the PDMS substrate was broader than on glass. This was due to the higher thermal conductivity in the case of the PDMS substrate. Cu, Cu_2O and CuO were present in all of the sintered micropatterns. The micropatterns, characterised using XRD, showed that the Cu peak was stronger at a 5 mm/s scanning speed compared to a 1 mm/s. The ratio of Cu_2O to CuO peak intensities in the XRD spectra of the sintered sample was considered to evaluate Cu_2O generation. According to the XRD spectra, the maximum

Cu_2O generation occurred at a scanning speed of 1 mm/s. Therefore, the Cu_2O-rich sensing part of the micro-temperature sensors has been demonstrated in this paper under these conditions. Therefore, in the aforementioned work, Cu-rich and Cu_2O-rich micropatterns were selectively fabricated by optimising the laser parameters [53]. This work paves a new way for better manufacturing techniques utilising fs laser reductive patterning for the manufacturing of microdevices. Mizoshiri et al. [154] further investigated the effect of various parameters, such as scanning speed and laser fluence, during fs laser reductive sintering of NiO and CuO mixtures on heat accumulation during sintering. It was identified that short pulsed laser irradiation at higher fluence reduces the metal oxide content in the fabricated pattern. Further, n-type and p-type thermoelectric micropatterns were fabricated using fs sintering, which may serve as metal electrodes in flexible displays.

Figure 9 depicts the surface morphologies of the micropatterns sintered at various scanning speeds while keeping fluence constant at 0.059 J/cm^2. At lower scanning speeds, more pronounced ablation was observed. Furthermore, at scanning speeds of 5 mm/s, instead of full melting, the powder particles were properly sintered. It was discovered that even when the fluence was kept constant, the scanning speed could affect the content of the Ni and Cu percentages in the sintered micropatterns. It was further mentioned that Cu converts to CuO when temperatures rise above 673 K [154]. When compared to the single exposed sintered sample, the double-exposed sintered sample contained more metal oxides. The heat accumulation and thermal history (single or multiple times exposed) during sintering are important in determining the composition and thermoelectric properties of the sintered sample [155]. Similarly, by utilising near-infrared fs laser pulses, three-dimensional copper-based microstructures were fabricated [156–158]. Mizoshiri et al. [158] expanded their research and printed Cu-based micropatterns inside Cu_2O nanosphere films using a femtosecond laser. To minimise the thermal diffusion, the line width was maintained to be the same as the diameter of the laser spot, i.e., 0.7 μm. Copper-based microstructures were printed via thermochemical reduction of Cu_2O by varying the focal plane along the z-axis, and the laser spot was focused inside the Cu_2O film (Figure 10). Different micropatterns have been demonstrated by varying the focus spot in the z-direction as shown in Figure 10. The laser peak intensity was set at 204 GW/cm^2 and the scanning speed was 0.01 mm/s [158]. Square micropatterns of a size 1.8×1.8 mm^2 were fabricated at a laser peak intensity of 163 GW/cm^2 and a scanning speed of 100 m/s.

Mizoshiri et al. [152] carried out laser-reduced sintering patterning in an inert gas (N_2/Ar) environment and were able to produce lower copper oxide (CuO/Cu_2O) generation in the fabricated sample. They used a pulse duration of 120 fs, a laser wavelength of ~780 nm, a scanning speed from 5 to 10 mm/s, a pulse energy of 0.74 nJ and a pulse repetition rate of 80 MHz [152]. Their investigations revealed that as the injection rate of inert gases (N_2 and Ar) increased, lower metal oxides were produced, but the fabricated samples had lower surface densities. The XRD results show that the fabricated pattern was greatly reduced (i.e., Cu rich) and the degree of reduction was maximised at a scanning speed of 8 mm/s. Furthermore, the Cu generation in the composition of the fabricated pattern increased with the rate of gas injection, while the degree of reduction was unaffected by the type of gas (N_2/Ar). However, as the gas injection rate increased (i.e., higher than 100 mL/min), the porosity in the patterns increased. Using fs laser reductive sintering, the copper micropatterns could be fabricated with a much lower pulse energy of approximately 0.5 nJ and a lower average power of approximately 50 mW, but, in the case of CW and nanosecond pulse lasers, a minimum of 0.2 W would be needed.

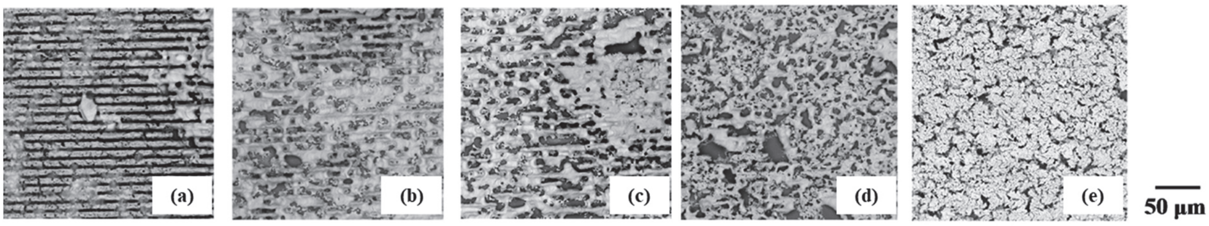

Figure 9. SEM images of sintered CuO–NiO NP micropatterns at different scanning speeds: (**a**) 0.1; (**b**) 0.5; (**c**) 1; (**d**) 3; (**e**) 5 mm/s [154].

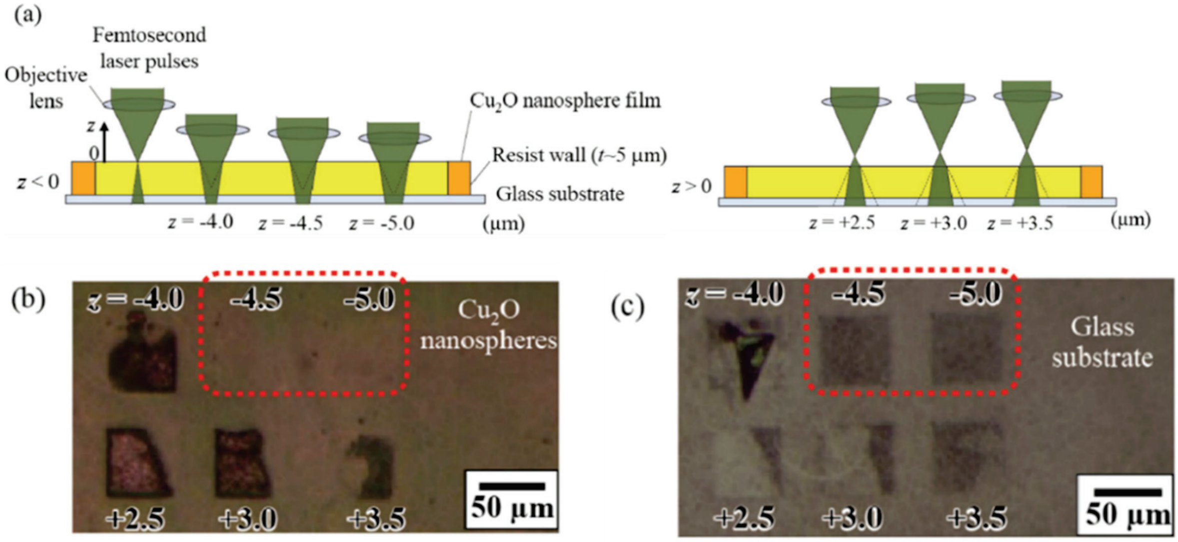

Figure 10. (**a**) Schematic of microfabrication of Cu-based patterns within a Cu_2O film. Microscopic images of (**b**) sintered patterns and (**c**) after Cu_2O nanosphere film removal (Adapted from reference [158]).

Although DW technology has been successful in producing Cu micropatterns using the fs laser sintering technique, the process appears to be time-consuming, requiring the preparation of film coated on substrate, sintering and, finally, removing the unsintered area from the substrate. However, in the PBF process, using layer-by-layer sintering, 3D structures can be produced that could have applications in cooling structures and heat exchangers. Kaden et al. [54] demonstrated printing of copper by PBF process, i.e., printing layer by layer utilising an fs laser with a 1030 nm wavelength and a focal spot of 35 μm [54]. The experiment was carried out in a nitrogen gas environment. Powder layer thickness was maintained manually at approximately 30 micrometres using a squeegee. The results were benchmarked and compared with different repetition rates utilising the energy per unit length (line energy) given by:

$$\text{Line Energy (El)} = \frac{P_{avg}}{V_{scan}} = \frac{E_{pulse} \times F_{rep}}{V_{scan}}$$

where El is the energy per unit length, P_{avg} is the average power, V_{scan} is the scanning speed, E_{pulse} is the pulse energy and F_{rep} is the repetition rate.

In general, with lower repetition rates, insufficient melting occurs, resulting in poor fusion of the metal particles to the substrate. By increasing the pulse repetition rate to 20 MHz and maintaining the pulse energy to 1 μJ, proper bonding of the copper powder to the substrate has been demonstrated [54]. Blasting and ablation effects were reported when the pulse energy increased by more than 1.5 μJ. It was also found that the thermal accumulation effect could be responsible for successful fusing of metal particles to the substrate at higher repetition rates. The line energy also had an impact on the resulting print quality. Further, printing of thin-walled web-like structures at a scanning speed of 666 mm/s and a pulse energy of 1 microjoule was reported. These thin walls were reported to have an aspect ratio of approximately 15:1 and a thickness of less than 100 µm. Figures 11 and 12 show samples fabricated using fs sintering of copper particles with ultrashort laser pulses. At higher line energies, the HAZ increased significantly which, consequently, negatively impacted the local precision. As a result, the line energy was reported to be kept below 100 J/m in their subsequent experiments [138].

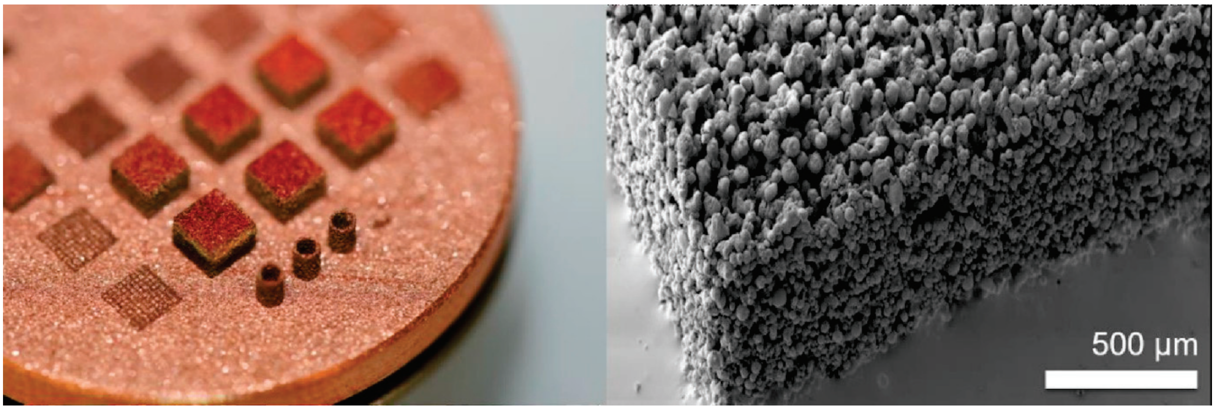

(**a**) (**b**)

Figure 11. (**a**) The samples fabricated with cuboids of a 2 × 2 mm^2 size, and total height of 1.4 mm; (**b**) SEM images of the sample (Adapted from reference [54]).

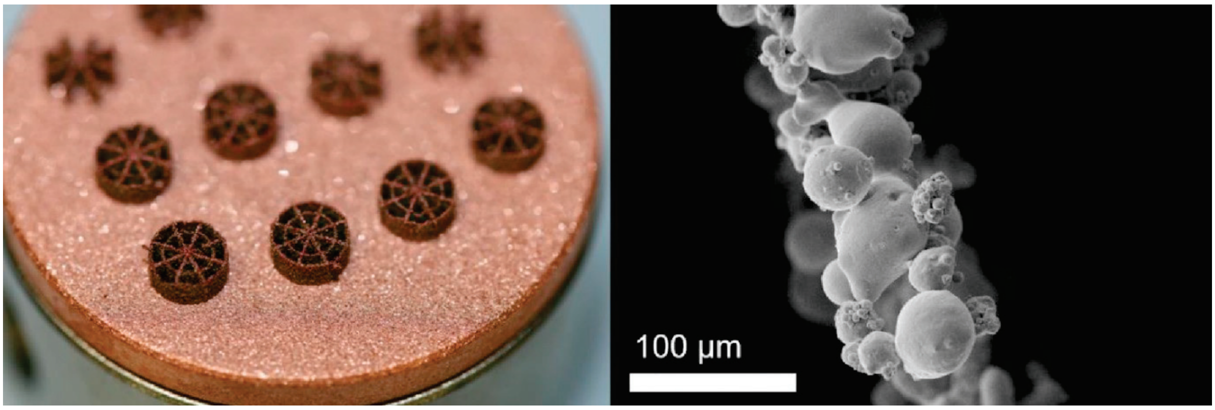

(**a**) (**b**)

Figure 12. (**a**) Thin-walled circular samples; (**b**) SEM image of a single wall (Adapted from reference [54]).

5.2. Femtosecond Laser Sintering of Iron and Tungsten

Tungsten and its alloys have diverse applications in various fields such as lighting engineering, aerospace, electronics, medical, nuclear and military [159,160]. This refractory material possesses exceptional intrinsic properties such as high tensile strength, high hardness, high melting temperature, high density, high thermal conductivity, high recrystallisation temperature and low thermal expansion [159–161]. These properties make tungsten ideal for high-temperature, high heat flux applications in radiation environments such as collimators, radiation shields in imaging systems (CT, SPECT, MRI and X-ray) [162], plasma-facing components (PFCs) in future nuclear fusion devices, such as the International Thermonuclear Experimental Reactor (ITER), and high-performance rocket nozzles [159–161,163,164]. However, tungsten's main disadvantage is its lack of room-temperature ductility that restricts its machinability and limits its use as a structural material. The brittle-to-ductile (BDT) transition temperature of tungsten, which is typically between 200 and 400 °C, limits its fabricability [162]. Because of this BDT transition temperature, tungsten products are conventionally manufactured by chemical vapour deposition (CVD), spark plasma sintering (SPS), powder metallurgy (PM) and hot isostatic pressing (HIP). These techniques, however, have limitations when it comes to complex internal and external structures [159]. SLM/S was used to overcome these limitations. Though it was not an easy process in the early stages, since the AM of tungsten is hindered by almost all of the difficult challenges in metal SLM/S processing such as high melting point, high thermal conductivity, affinity for oxygen at high temperatures, high viscosity, and brittle nature at room temperature, resulting in cracks and porous microstructures of fabricated parts [161].

Despite the listed challenges with processing tungsten, successful examples are reported in the literature. For example, Ghosh et al. [165] utilised a pulsed Nd:YAG laser with a pulse duration of approximately 1000 ns to investigate SLS of tungsten carbide and cobalt powder alloys. Porous samples were produced in this experiment. Dianzheng et al. [166] utilised CW laser-based SLM to fabricate pure tungsten material parts with densities of up to 96 percent; however, this was accompanied by some microcracks in the printed components. Chaolin et al. (2018) utilised CW laser to fabricate pure tungsten samples by SLS processes. The produced parts possessed dense microstructures without balling but a few microcracks still existed [159]. Muller et al. (2019) carried out experiments to fabricate pure tungsten powder parts utilising CW laser-based PBF with laser power up to 400 W and by preheating the substrate up to 1000 °C. The produced parts had a relative density of up to 98 percent, and cracks were minimised but not eliminated completely. The same research team also fabricated honeycomb-like structures with tungsten–copper composite materials, which were utilised as heat sink materials for PFCs with high heat loads [164]. Li et al. (2020) investigated various process parameters in CW laser-based SLS, such as scanning speed, hatch spacing and laser power, and their effect on the surface microstructure, densification and morphology of fabricated tungsten samples. With the optimum parameters of a scanning speed of 400 mm/s, hatch spacing of 0.08 mm and laser power of 300 W, the produced tungsten samples had densities of up to 98.31 percent [160]. As noted from the aforementioned studies considering CW laser-based AM of tungsten, and despite the reported success, shortcomings in terms of cracking still represent a challenge. The studies utilising fs lasers aimed to improve the relative density, hardness and strength of SLS/M-produced tungsten parts. The high peak power and the ultrashort pulse duration of fs lasers make them an emerging technology in melting/sintering high-temperature metals such as tungsten [7,44,58,101]. Due to the phenomena of fast cooling, localised heating, lower HAZs and greater precision in the submicron range, these ultrafast lasers have many advantages over CW and long-pulsed lasers. 3D printing of such high-temperature metals would benefit industries, including the automotive, biomedical and aerospace, that require high-temperature materials with outstanding mechanical qualities and accuracy [7].

In an early study, Ebert et al. (2012) initially investigated fs laser processing of tungsten powder and was able to report sintered structures. In these experiments, the fs laser used had an operating wavelength of 1030 nm and 180 fs pulse duration. The laser repetition rate was tuned from 0.125 to 1 MHz, and the laser spot diameter was ~36 microns. The layer thickness was reported to be maintained around 1 mm and was irradiated from 1 to 50 times. The experiments were carried out in vacuum at 0.05 Pa, with helium used as a residual gas during the sintering process [101]. It was reported that when the line spacing was at approximately 0.01 mm, the sintering of continuous surfaces was possible, and the sintered structures were in the range of 1 to 10 μm. The SEM images of the sintered part under different processing settings are shown in Figure 13a–d. These results demonstrate some sintering phenomena utilising fs lasers but do not provide precise and optimum laser parameters on the quality of the sintered structures.

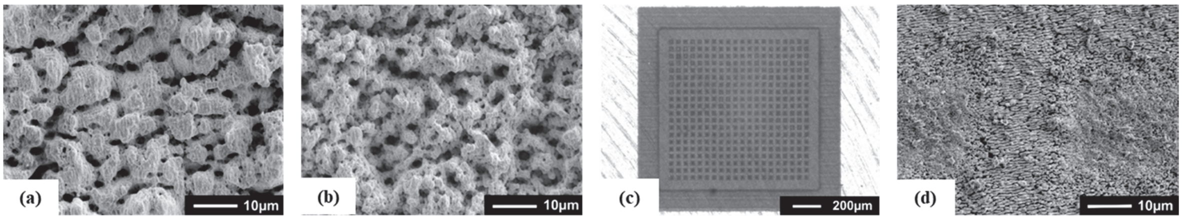

Figure 13. (**a**) SEM image of sintered samples, operated at max intensity = 6.74 × 10^{12} W/cm^2, energy per unit length = 0.7 J/m, scanning speed = 1250 m m/s, line spacing = 10 μm and pulse repetition rate = 125 kHz, 10 scans; (**b**) SEM image of sintered samples, operated at max intensity = 6.74 × 10^{12} W/cm^2, energy per unit length = 0.23 J/m, scanning speed = 3750 m m/s, line spacing = 10 μm and pulse repetition rate = 125 kHz, 10 scans; (**c**) optical image of sintered grid-like structures, operated at max intensity = 1.77 × 10^{12} W/cm^2, energy per unit length = 3 J/m, scanning speed = 600 m m/s, line spacing = 10 μm, and pulse repetition rate = 1 MHz, 6 scans; (**d**) SEM image of sintered grid-like structure sample (Adapted from reference [101]).

Furthermore, Huan Huang (2015) [7] carried out fs laser sintering/melting experiments with tungsten and iron powders to produce 3D structures fused to the substrate. To compare the mechanical properties and microstructure of fs-laser-fabricated samples, similar 3D structures were fabricated using a CW laser source while maintaining the same average power of 50 W, and the scanning speeds for both the CW and fs pulse lasers operated at 80 MHz. The particle sizes of the iron and tungsten powders were in the range of 1–5 μm. For analysing the properties of the printed structures, the 3D printed samples were vertically cut as shown in Figure 14.

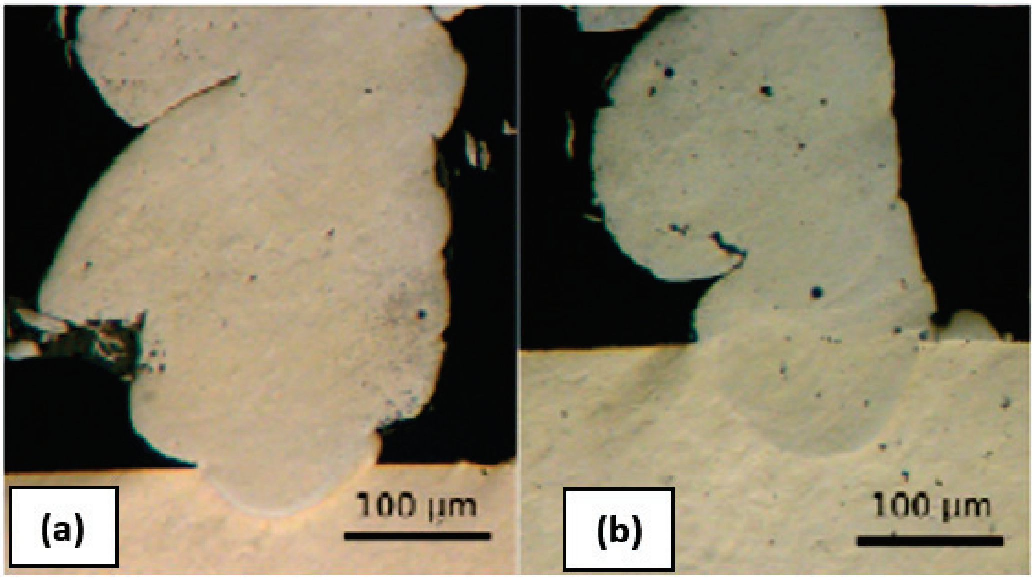

Figure 14. Iron rings fabricated by (**a**) an 80 MHz fs laser; (**b**) a CW laser (Adapted from reference [7]).

The penetration depth of the fs-laser-fabricated iron-powder sintered sample was approximately 30 μm, while the penetration depth of the CW fabricated sample was 75 μm. This difference was attributed to the smaller HAZ in the case of fs laser-based 3D printing. Using the same 50 layer printing, the size of the sample fabricated using an fs laser was 0.8 mm tall, with a wall thickness of 300 μm, and the sample size fabricated using a CW laser was 1.03 mm tall with a wall thickness of 380 μm. This paper demonstrated how localised heating in an fs laser can result in the precision printing of 3D structures. Furthermore, the microhardness of the fs-laser-fabricated iron sample was higher than that of the CW-laser-fabricated sample, because the average grain size in the fs-laser-fabricated sample was smaller at all heights compared to the CW laser 3D printed samples. This is due to the well-known fact that hardness increases as grain size decreases. The grains in CW-laser-fabricated samples were reported to be slightly bigger due to the lower cooling rates and greater HAZs [57]. The next challenging material, tungsten, was fabricated in cube structures by the same research group [7]. With tungsten's higher melting temperature compared to iron, 1 MHz pulse repetitions at 45 W, a pulse duration of 400 fs, a layer thickness of 15 µm and scanning at a speed of 25 mm/s yielded strongly fabricated parts fused to the substrate (Figure 15). On the other hand, 80 MHz fs laser and CW laser operating at higher power failed to completely melt and fuse tungsten powder to the substrate.

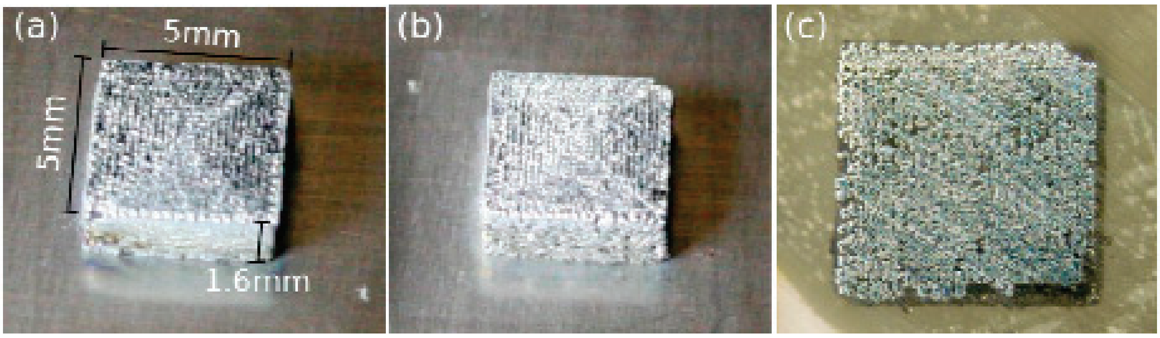

Figure 15. (**a**,**b**) The fs laser 3D printed tungsten cube with fs laser viewed from different angles; (**c**) polished top surface (Adapted from reference [7]).

The mechanical properties, such as average ultimate tensile strength (388.4 MPa), were determined from three sample locations. However, because of the porosity and potential oxidation during 3D printing, the microhardness values were reported to be unsatisfactory. Further, three-dimensional structures utilizing tungsten material were fabricated [44]. Different tungsten samples, including 100 µm thin walls, were 3D printed using fs laser source as shown in Figure 16 [44].

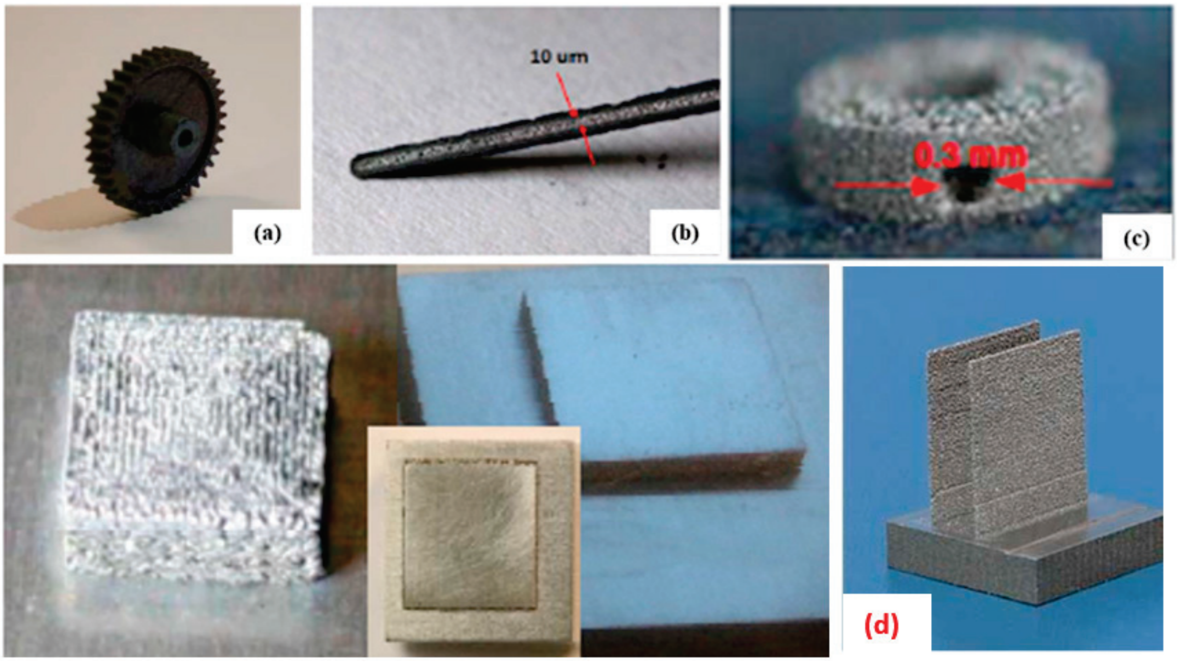

Figure 16. (**a**) A gear a half-inch in diameter 3D printed by fs laser; (**b**) fs sintered tungsten feature; (**c**) fs sintered tungsten with a small circular feature with a hole; (**d**) 3D printed thin wall of a 100 microns (Adapted from reference [44]).

For comparison, 20 ps and 200 ps pulsed lasers as well as a 750 fs laser and a CW laser system were employed in the 3D printing of tungsten [44] while keeping all other parameters similar. Figure 17 shows the average grain area versus pulse duration for fs, 20 ps, 200 ps and CW laser sintered samples, where the left is for the top surface and the right is for the cross-section. Comparing the microhardness in the case of pulsed lasers at different durations with the CW laser showed that fs-laser-based AM had the highest hardness as displayed in Table 6.

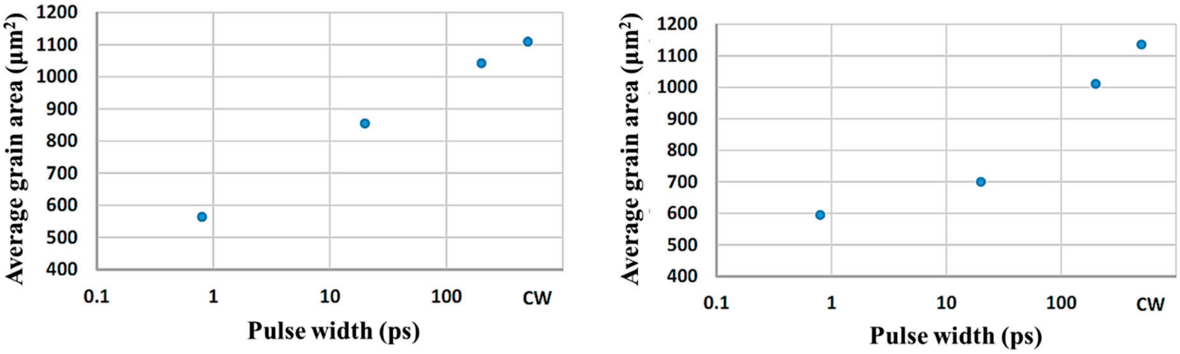

Figure 17. Average grain size area as a function of pulse width (Adapted from reference [44]).

Table 6. Hardness values for the tungsten sample processed with different lasers [44].

Hardness (HRC)	Fs Sample	CW Sample	20 ps Sample	200 ps Sample	Tungsten Sample
Cross-section	47.7	44.7	41.8	45.1	45.8
Top	45.4	44.9	44.1	42.4	44.9

The aforementioned work also revealed that the fs laser sintered samples had lower cracks and defects compared to the other laser printed samples. Similarly, fs laser sintering of iron powder coated on a glass substrate was demonstrated by Liu et al. (2016) [100]. Melting and fusing both (i.e., iron and glass) materials is challenging because of the glass' brittleness and the different thermal expansion coefficients of iron and glass. In this study, the fs laser was utilised to overcome this issue, because of its localised heating, high temperature generated in a shorter time and quick cooling rate, The sintering parameters, such as average power of 37 W, powder layer thickness of 40 μm and 20 μm line spacing were used during the sintering process at various scanning speeds [100]. The reflectance was measured for the fabricated samples at different values of the laser power and scanning speeds. It was found that at lower scanning speeds, the reflectance was reduced, while noting that glass was prone to breaking at lower scanning speeds. The reported findings suggest that fs laser AM could be a new way to achieve an excellent blackening effect with a reflectance of less than 1%, rendering it useful for applications in stray light reduction.

5.3. Femtosecond Laser Sintering of Silver

Nowadays, electronics has seen substantial improvements in the field of sensors, printed electronic components and flexible electronics. These flexible sensors are rapidly evolving, where they can be used in many applications [167]. In the medical sector, these flexible electronics have a large impact, as they can be low-cost, tactile, low-weight and non-pervasive wearable systems; in addition, they can be used as monitors to observe patients' health conditions on a regular basis. Hence, there is an existing special need to manufacture such flexible devices using appropriate manufacturing technology. This can be facilitated by using AM technologies, such as SLS, that can process metal NPs and also in direct writing technology. Initially, the SLS process was used for NPs of noble metals like silver and gold, but later it was also expanded to more cost-effective materials such as copper and nickel [151]. Silver material has been utilised by inkjet technology-based AM process for fabrication of temperature sensors [168–170]. Hong et al. processed silver particles via a laser sintering process to fabricate a large and flexible transparent conductor based on microgrid structures that can be used in touch screen panels and optoelectronic devices [171]. In 2011, using direct writing technology, Lee et al. fabricated conductive metal films made out of silver nanoparticles. Femtosecond laser characteristics aid in the fabrication of metal conductors with submicron-sized features and high conductivity. Due to the fact of its reduced HAZ, femtosecond laser-based metal patterns on transparent and flexible polymer substrates has garnered special attention owing to its several practical applications in photonic devices and flexible electronics [41,56,167,172]. Fs laser has also been utilised to fabricate SERS (surface enhanced Raman scattering) substrates [172]. SERS is an analytical tool for detecting molecular fingerprints and integrating them into microfluidic platforms that allow for liquid sample analysis for biological and medical diagnosis. Traditionally, lithographic techniques have been used to produce SERS substrates with significant Raman enhancements. However, fabricating them, on the other hand, entails a number of time-consuming steps. Furthermore, using lithographic techniques to achieve ordered arrays of nanostructures of arbitrary size can be expensive [56], challenging [56], hazardous and incompatible with sensitive substrates [172]. To address these issues, fs lasers have been used to fabricate SERS substrates sintered with silver nanoparticles [56]. Based on the process parameter set and the layer thickness, sintering of nanoparticles may lead to three different phenomena: surface necking, full melting of silver particles and balling. Kurnoothala et al. [56] sintered silver nanoparticles on a silica-based microfluidic channel via the surface necking phenomenon using an fs laser source to fabricate the SERS substrate. The width of the fabricated lines at various laser powers and scanning speeds were reported [56] and are shown in Figure 18. The utilised fs laser system operated at a wavelength of 1030 nm, a 370 fs pulse duration and had a pulse repetition rate of 1 MHz.

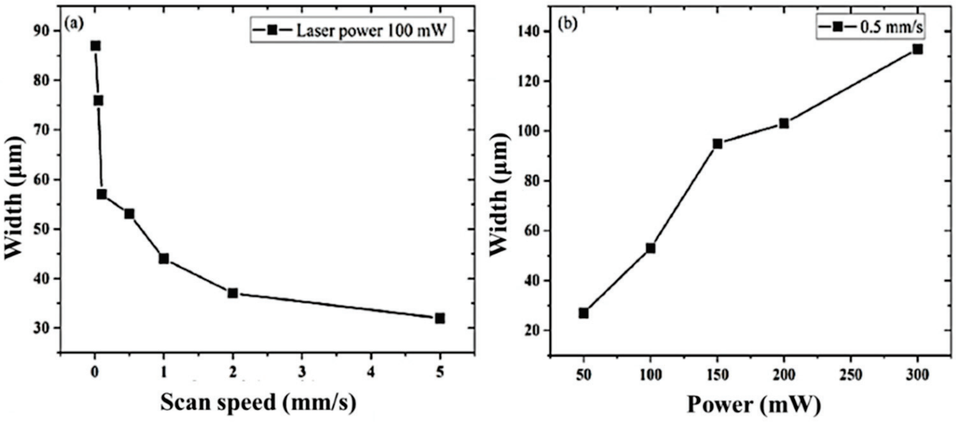

Figure 18. (**a**) Track width as a function of varying scan speeds with a constant laser power of 100 mW; (**b**) track width as a function of varying laser powers with a constant scan speed of 0.5 mm/s (Adapted from reference [56]).

Due to the ultrashort pulse durations in fs laser sintering, the thermal diffusion effect is suppressed, and sintering of metal nanoparticles can be restricted to the laser focal spot. This largely reduces the heat-affected zone and enables the fabrication of submicron-sized metal patterns on flexible substrates [55]. Noh et. al. [173] utilised a Ti:sapphire laser system operating at an 800 nm wavelength, a 50 fs pulse duration and a pulse repetition rate of 1 kHz to fabricate silver NPs on a flexible substrate. The laser fluence and effective pulse number were 10–120 mJ/cm^2 and 1000–10,000, respectively. The scanning speed, V, varied between 20 and 200 μm/s, and the beam size was 200 μm. The hatch space between the scanning lines was set to 200 μm [173]. The reported SEM images of sintered microstructures of the Ag NPs on the PET substrates after fs laser irradiation are shown in Figure 19 [173]. Noha et. al. also compared the results obtained with a KrF excimer nanosecond laser operating at a 248 nm wavelength, a 25 ns pulse duration and a repetition rate of 10 Hz. The experiments were carried out with a fluence = 10–40 mJ/cm^2 and a pulse number of 1–1000. The effective pulse number was varied by varying scanning speeds in the 0.015–15 mm/s range at f = 10 Hz and d = 1.5 mm [41].

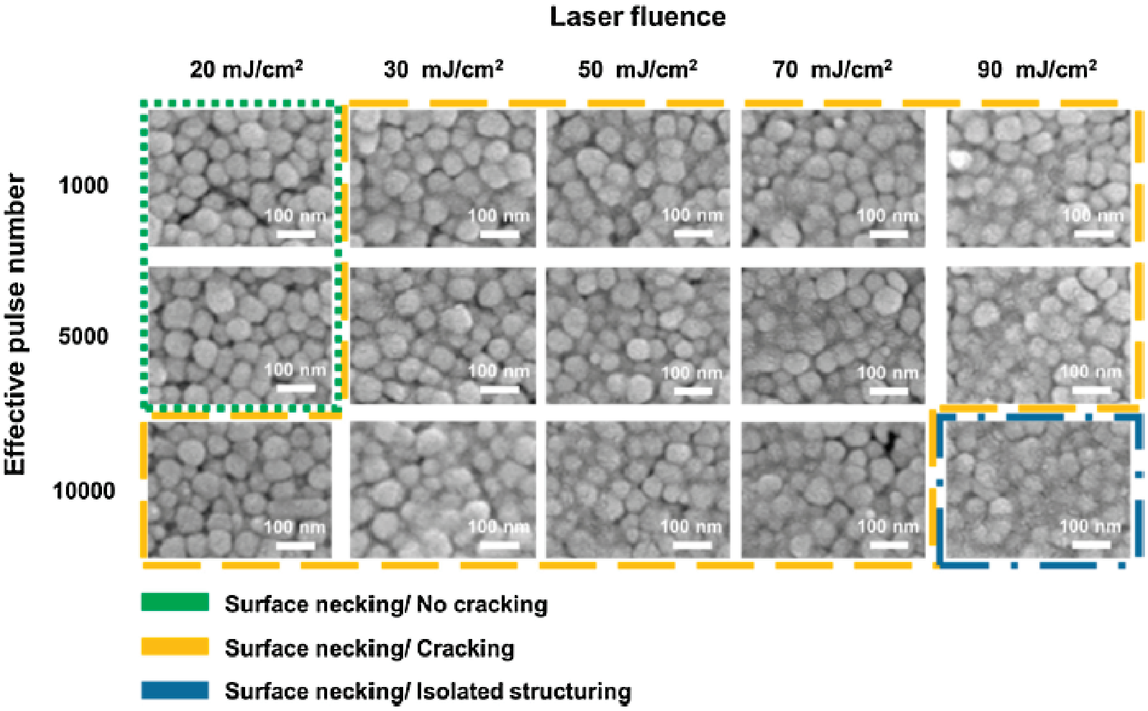

Figure 19. SEM images of fs Ag NPs sintered at various laser fluences (Adapted from reference [173]).

For the entire fluence range reported in [173], fs laser irradiation sintered the Ag NPs without completely melting them, instead creating necks between the particles by solid-state diffusion. As the fluence increased, the significant neck growth arose by grain boundary and volume diffusion. At fluence = 20 mJ/cm^2 and an effective pulse number = 1000, the Ag NPs were reported to form necks with an average neck diameter of 12 ± 2 nm. At fluence = 90 mJ/cm^2 and an effective pulse number = 10,000, the average neck diameter increased to 36 ± 3 nm. The increased neck formation was reported to reduce the porosity by blocking open pores in the particle bed [173]. As depicted in Figure 20, with the increasing fluence and EPN (effective pulse number), the fraction of the exposed area rose to 40%. This study showed that EPN was less significant in film cracking than laser fluence [173]. It also suggests that the formation of the interparticle necking after laser sintering greatly decreases the electrical resistance. The resistance decreased as fluence and EPN increased until the fluence = 40 mJ/cm^2. At a fluence = 30 mJ/cm^2 and an EPN = 1000, the lowest resistance was reported as shown in Figure 20c. The mechanical properties of fs laser sintered Ag particles were also examined in this paper for interfacial characteristics between Ag NPs and the PET substrate. The cross-sectional SEM images are also presented as shown in Figure 21 [173].

The aforementioned work reported that fs laser irradiation resulted in substantial embedding of the Ag NPs into the PET layer, which led to an increase in the contact area (Figure 21b) and would significantly improve the adhesion strength [173]. At fluence of 90 mJ/cm^2, the embedded depth was found to be approximately half the particle size. Additionally, the reported comparative results of the fs and ns laser-sintered samples showed that due to the low substrate damage and fewer film cracks, fs-laser-generated films were of higher electrical conductivity compared to the ones generated with an ns laser [173]. The surface topography AFM analysis results showed that in the case of ns laser sintering, the average affected spot was 1.2 µm wide and 500 nm deep, whereas in case of fs laser sintering, the average affected spot was 200 wide and 90 nm deep [173].

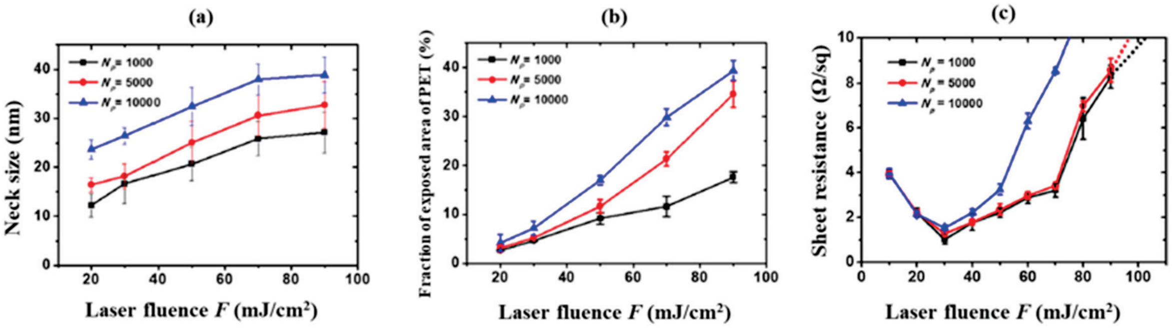

Figure 20. (**a**) Neck size; (**b**) fraction of the exposed area of the PET substrate after fs laser sintering; (**c**) sheet resistances of the fs laser sintered Ag particles [173].

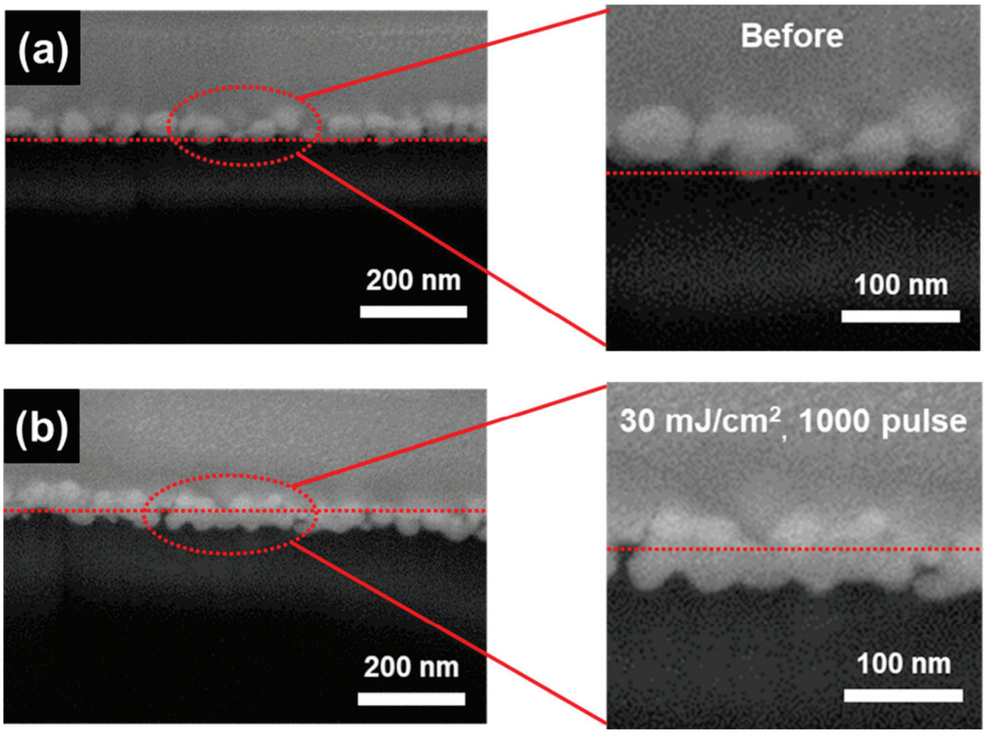

Figure 21. Cross-sectional SEM images (**a**) before fs laser sintering and (**b**) after fs laser sintering (F = 30 mJ/cm^2, effective pulse number = 1000) (Adapted from reference [173]).

Noh et al. further investigated the correlation between different process parameters and the conductivity, microstructure and adhesion strength of the sintered films [172]. Melting, interparticle necking, balling and film cracking were analysed by varying the EPN, fluence and layer thickness. It was found that both adhesion strength and electrical conductivity increased by increasing the fluence up to the maxim when melting of particles began [174]. By varying the spin-coated layer's thickness from 350, 200 and to 100 nm, different conclusions were drawn from this study. For the 350 nm layer thickness, short thermal penetration helped in the fabrication of thin-film samples. In the case of the 200 nm layer thickness, the highest thermal conductivity was reported when melting just began in NPs. Whereas with the 100 nm layer thickness, complete melting of particles deteriorated the conductivity due to the capillary instability of the molten film and, therefore, the highest conductivity was reported just before melting started as shown in Figure 22b,c [172]. Moreover, fine patterns of a few hundred nanometre line widths utilising ultrashort lasers were fabricated in other sequel studies [175]. Microstructure formation by varying the sintering parameters of Ag NPs utilising ultrashort pulses was presented and revealed that the fs laser sintering process was similar to typical thermal sintering processes.

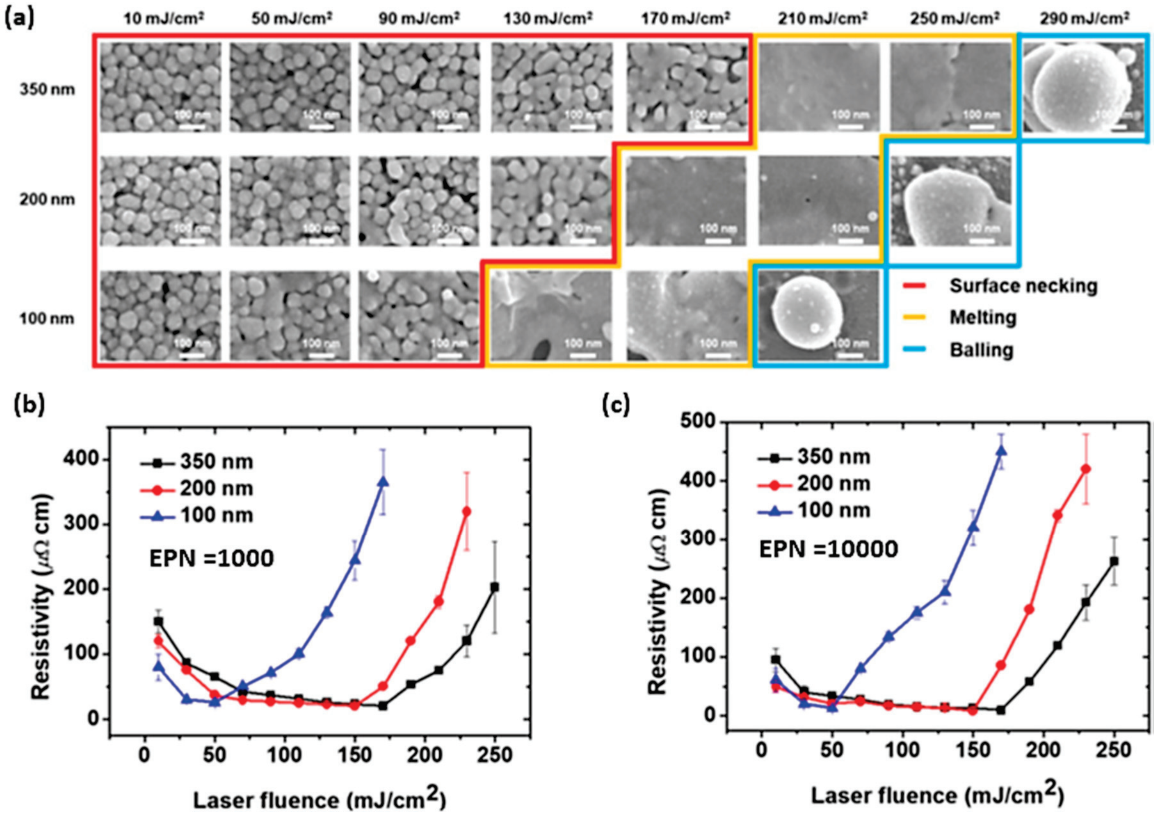

Figure 22. (**a**) Microstructures of fs sintered Ag particles during surface necking and melting stages. Variations in the resistivity of sintered Ag films as a function of fluence; (**b**) Np = 1000; (**c**) Np = 10,000 (Adapted from reference [172]).

5.4. Femtosecond Laser Sintering of Aluminium Alloy

Aluminium is one of the lightest materials that is used for many burgeoning applications such as in automotive parts, electricity lines, defence and aerospace, and food and beverages containers. Conventional manufacturing processes are capable of processing pure aluminium while processing them using SLM is quite difficult. This is because of challenges such as high reflectivity of the laser beam, oxidation and flowability. In addition, pure aluminium has high thermal conductivity compared to its alloys, making it more challenging to fabricate in the SLM process. Additive manufacturing of Al and its alloys has various applications in the automotive and aerospace fields, where fabricating light-weight structures with complex geometries is challenging using other traditional methods [59]. SLM processing of Al and its alloys has been found to be beneficial for hard-to-machine materials. To make Al fabrication possible through PBF process, additives were included [80,176]. Using one of aluminium's common alloys, AlSi10Mg, parts were fabricated using SLM process. This alloy has a very good hardness and strength and, hence, it is suitable for parts containing thin walls subjected to high loads, especially in aerospace applications [177]. AM-made Al parts are actively used in consumer products [178]. Various Al alloys were processed using the SLM technique including Al6061 and AA2024, among others [179]. These alloys possess good fatigue resistance as well as resistance to stress, corrosion and cracking. In 2010, AlSi12 alloy was processed using the SLM technique to achieve a denser part, but there were oxidation issues [180]. Micromechanical models were developed to quantitatively link aluminium material fracture properties, to microstructure features at multiple lengths scales, and manufacturing conditions [181]. An attempt was made by adding Cu to the Al powders to reduce oxidation, and the control was better when compared to conventional processes [179]. Al–Li alloys are reported to have great potential in light-weight construction, as the lithium content in the alloy significantly increases the stiffness at a lower mass, and the elastic modulus rises dramatically as the lithium concentration increases [59]. However, in traditional casting processes, a maximum Li fraction, up to 2 wt.%, has been reported due to the precipitation of the brittle δ-Al–Li [8]. Recently, it was reported that an ultrashort pulsed laser with a 500 fs pulse duration was used to 3D print the binary element Al–Li with Li content up to 4 wt.% [60]. The high content of Li generated during fs laser 3D printing of Al–Li alloys could be attributed to the high cooling rate within the melt pool during fs laser sintering, which has much shorter laser–matter interaction times. This also, in turn, supresses excessive Li evaporation during sintering. As the Li content increases in the Al–Li alloy, a significant increase in elasticity was found as depicted in Figure 23.

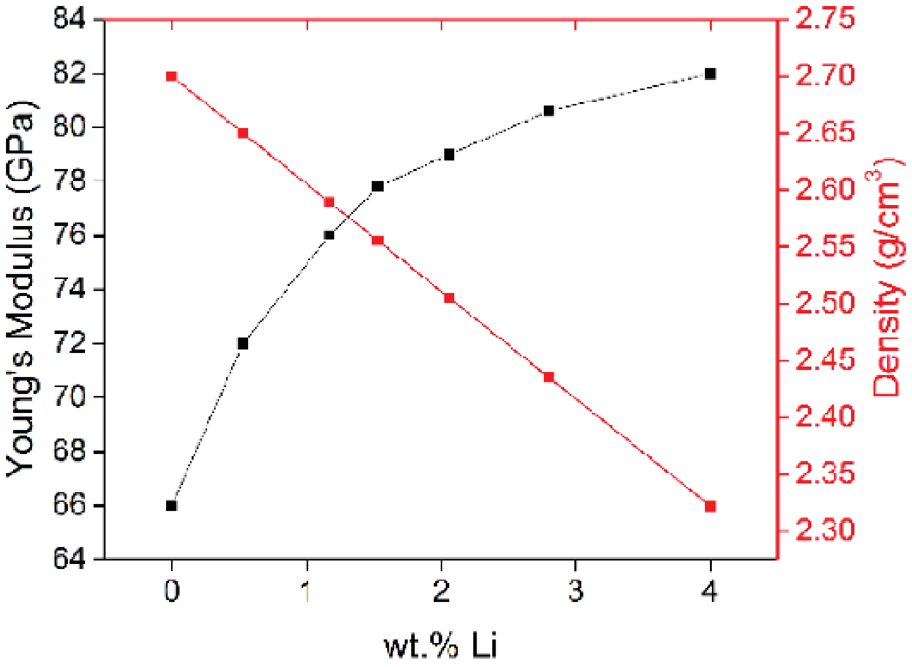

Figure 23. Lithium content versus density and Young's modulus in Al–Li alloys [60].

Furthermore, Al 3D parts were printed with an fs laser operating at a 20 MHz repetition rate and a pulse energy of 1.5 µJ at four different scanning speeds (Figure 24). The layer thickness during fabrication was reported to be 40 µm, and the hatching spacing was 30 µm. Complex gear wheels were fabricated by the same research group to prove the feasibility of the fs laser sintering process as shown in Figure 25.

Further, Ullsperger (2017) [38] utilised an fs laser operating at a 1030 nm wavelength, a pulse duration of 500 fs, an average power of 30 W at a pulse repetition ratio of 20 MHz to 3D print AlSi4O alloys. Higher concentrations of Si in AlSi4O served to primarily reinforce the material and to reduce thermal expansion during sintering. Previously, a CW laser was used in additive manufacturing of AlSi4O. However, when the CW laser additively manufactures hypereutectic alloys, such as AlSi4O, low cooling rates cause decomposition due to the low Si solubility in Al and poor precision due to the larger melting zone. To achieve minimal structural sizes, single tracks fabricated by CW laser were reported to be up to 150 µm [182]. To address these challenges, researchers utilised ultrafast laser sources of picosecond and femtosecond pulse durations to fabricate these alloys with reduced HAZs. The 3D printing process was carried out in a nitrogen gas environment to avoid oxidation issues, such that the oxygen concentration in the chamber was below 0.5 percent. The powder bed fusion technique has been utilised, and the powder layer-by-layer spreading was conducted manually with a rubber blade with the layer height maintained between 25 and 50 µm. In the sub-picosecond regime, the single pulse ablation threshold for Al–Si alloy operating at a 1030 nm wavelength was reported to be 0.12 J/cm^2 [38]. Ullsperger et al. found that for a layer thickness of 30 µm and at fluence greater than 0.13 J/cm^2, the powder layer was blasted from the substrate, indicating possible limitations due to the effect of higher pulse energies. By increasing the pulse repetition rate, the blasting effect was slightly reduced, and sintering and melting were found to start with a laser fluence below 0.13 J/cm^2. The experiments were carried out at a 20 MHz pulse repetition rate, initially single tracks were fabricated with a laser power ranging from 3 to 30 W, corresponding to the energy per unit length of 50–1000 J/m [38] as shown in Figure 26.

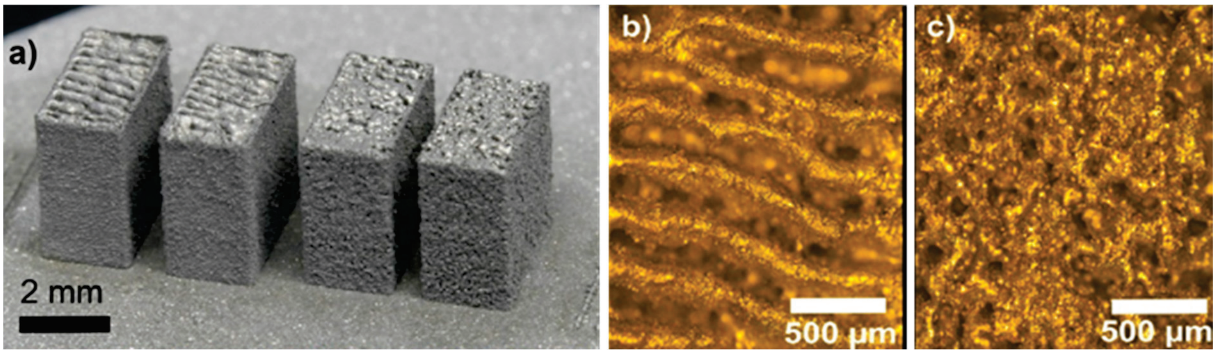

Figure 24. (**a**) Samples fabricated at different scan velocities (0.2, 0.3, 0.5 and 0.7 m/s, from left to right); Printed structure's microscopic images with a scan velocity of (**b**) 0.3 m/s and (**c**) 0.7 m/s [60].

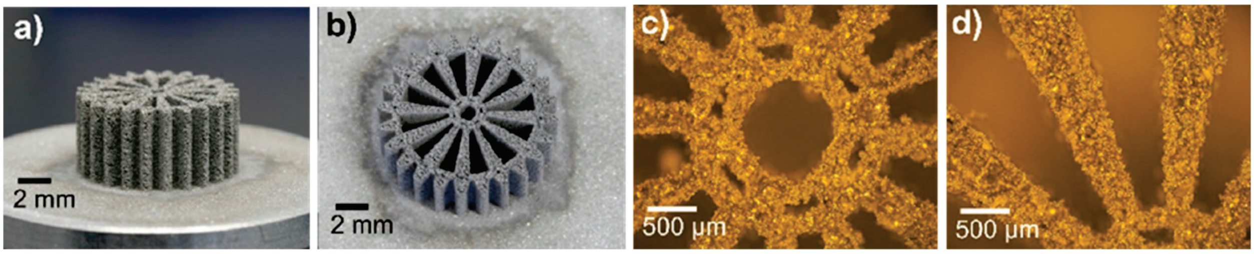

Figure 25. (**a**,**b**) Figures of a gear wheel fabricated at a scanning speed of 0.7 m/s, pulse energy of 1.5 µJ and 20 MHz pulse repetition rate; (**c**,**d**) light microscope images at different locations on the gear [60].

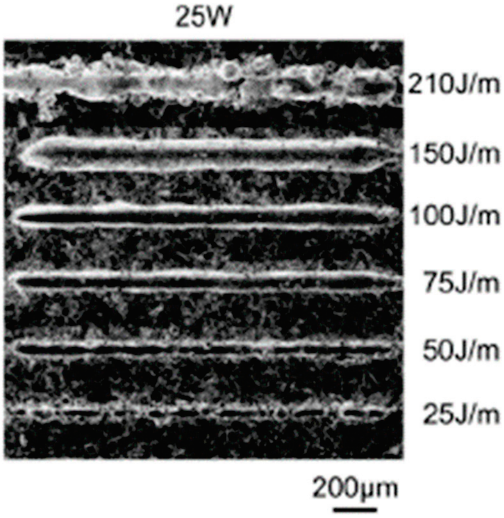

Figure 26. SEM images of single tracks at different parameters at a pulse energy of 1.25 µJ (Adapted from reference [38]).

The reported results in [38] showed that at lower scanning speeds (i.e., less than 120 mm/s (>210 J/m)) the fs laser sintering resulted in melt warps and extensive HAZs were observed with line widths in the range of 150–250 microns. Whereas at higher scanning speeds (i.e., more than 800 mm/s (<30 J/m)), irregular tracks with droplets were formed. Furthermore, with laser powers lower than 6 W, only a surface sintering effect was reported, with no fully formed melt pools. Good structures with lower roughness were formed when the laser power was set to be from 12 to 25 W with an energy per unit length from 40 to 170 J/m. With stable and reproducible single rings of 1.5 mm in diameter with 50 layers, each layer was fabricated with a thickness of 30 microns. The wall thickness produced was 54 µm with an average laser power of 12 W, whereas a 95 µm thickness was produced with a laser power of 25 W [38]. Based on these studies, light-weight 3D structures were demonstrated with a laser power of 25 W at a scanning speed of 200 mm/s as shown in Figure 27. These 3D structures fabricated were 8 mm in diameter, consisting of 120 layers with 30 microns for each layer thickness and a final wall thickness of 100 microns [38].

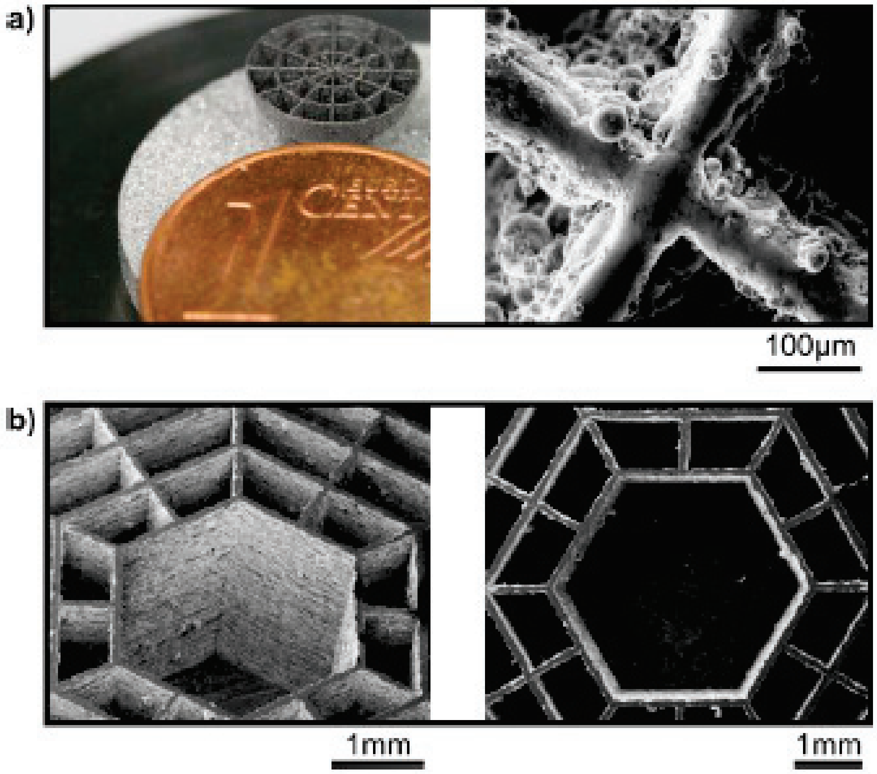

Figure 27. (**a**) Hollow thin-walled structure fabricated using fs-based AM; (**b**) hexagonal structure fabricated to a height of 5 mm (Adapted from reference [38]).

Moreover, Ullsperger et al. [183] carried out comparative studies on laser-assisted powder bed fusion of Al–40Si (40 percent Si by weight). They utilised an fs laser source operating at a 1030 nm wavelength with a repetition rate between 6 and 20 MHz as well as a CW laser operating at a 1070 nm wavelength. The laser spot diameter was approximately 50 microns, the average power around 25 W, the layer height was 15 µm and a scanning speed of 200 mm/s were set for the fs laser additive manufactured parts 1 mm height (Figure 28). The experiments were reported by setting the layer thickness to 30 µm at different pulse durations, i.e., 500 fs, 20 ps and 800 ps. It was reported that generating a stable melt pool on a thin powder layer requires an average power of more than 10 W and a pulse repetition rate of more than 1 MHz as shown in Figure 29. Higher ablation has been reported with a fluence greater than 0.4 J/cm^2. With ultrafast laser pulses of 500 fs and 20 ps operating at 20 MHz, the lowest melting pool width of 70 μm was formed, and enhanced fabricated parts with higher hardness were reported [183].

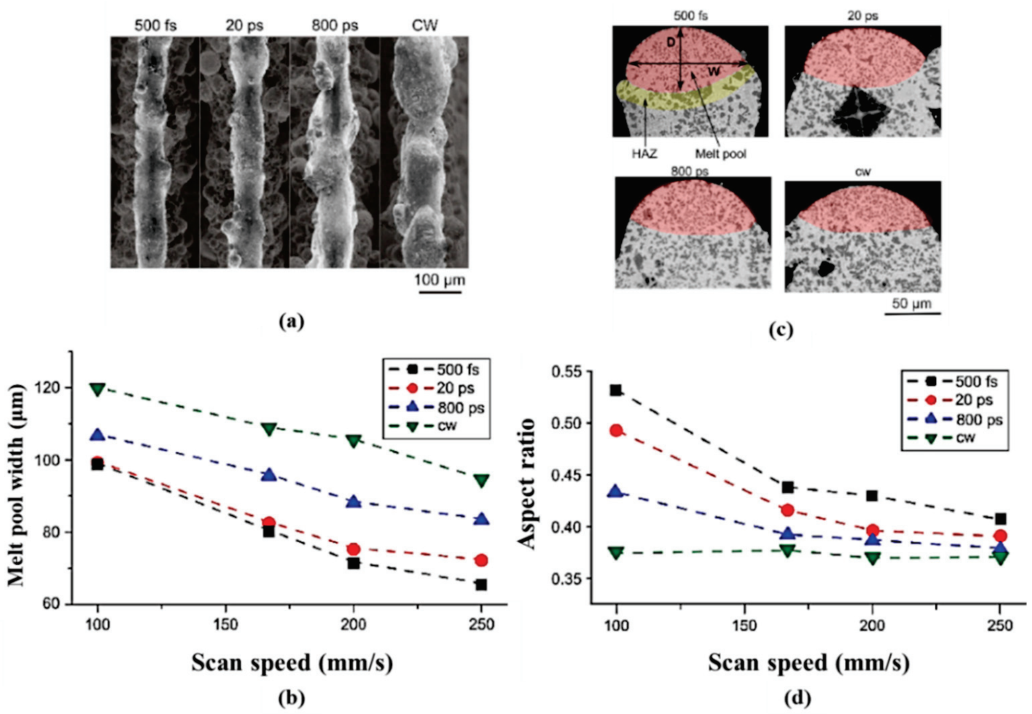

Figure 28. (**a**) SEM images of the walls (top view) above the parameters and a layer thickness of 15 microns; (**b**) scan speed versus melt pool width for different lasers; (**c**) melt pool width at the tip of the wall captured by optical microscopy; (**d**) scan speed versus aspect ratio between melt pool depth and width (increases for shorter pulse duration) (Adapted from reference [183]).

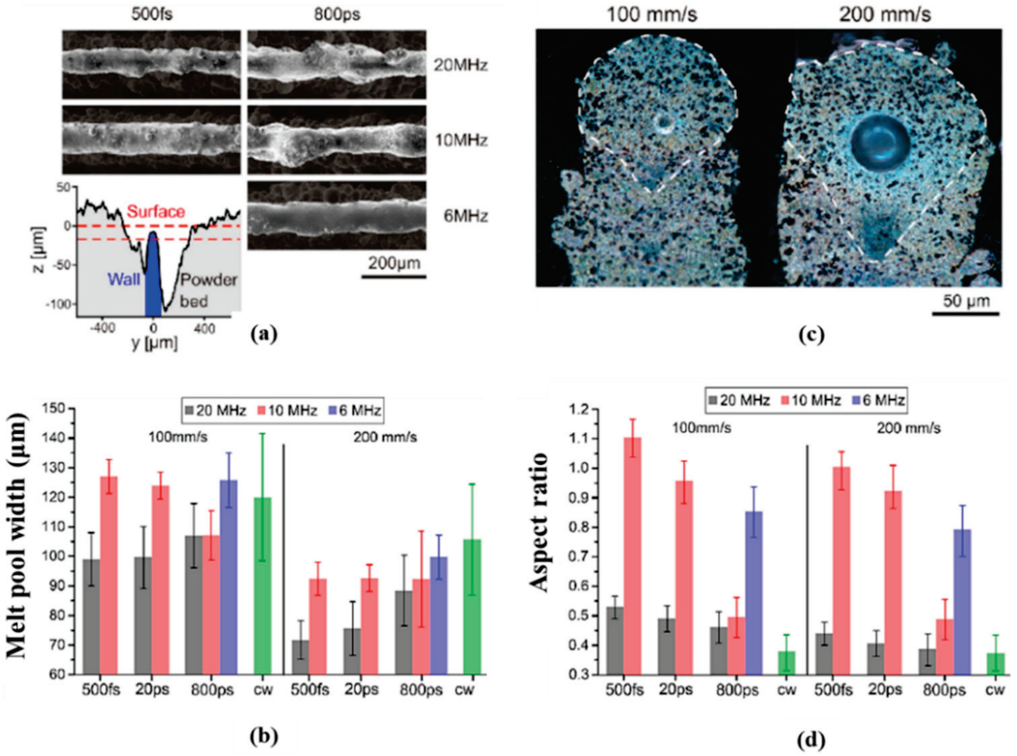

Figure 29. (**a**) SEM images of the tip of wall with a constant scanning speed of 200 mm/s; (**b**) different pulse durations versus melt pool width; (**c**) cross-section of two polished walls at 500 fs and 10 MHz repetition rate; (**d**) different scanning speeds versus aspect ratio [183].

5.5. Femtosecond-Pulsed-Laser Sintering in Hard Tissue Engineering

Tissue engineering and bone grafting have proven to be a promising approach in developing compatible tissues required at the repair site. There are different types of bone grafts that can be mainly divided into allografts (same species), autograft (same individual) and synthetic (alloplast). The latter is made of biomaterials (biocompatible polymers, ceramics, metals and composites) that are required to heal damaged or traumatised human body tissues [184]. However, there are significant drawbacks in the case of allografts and autografts such as the lack of prior donor tissue, lack of bioactivity and graft rejection. [185,186]. These issues could be resolved with alloplast-type bone grafting. In AM processes, SLS techniques have been employed for bone tissue repair using biopolymers, composites and ceramics [186]. Tan et al. (2003) utilised SLS of polyethereherketone–hydroxyapatite biocomposite blends to fabricate bone scaffolds [187]. SLS can also be used to fabricate scaffolds for the repair or regeneration of dental tissues in addition to bone tissue engineering scaffolds. SLS can be considered a versatile technology in biomaterials and tissue engineering for restoring and reconstructing tooth and bone deformities as well as for enhancing existing implants and scaffold coatings [62]. Fine powder composites formed by combining epoxy resin E-12 (as a binder) with K_2O–Al_2O_3–SiO_2 series dental glass–ceramic were used to fabricate dental restoration devices utilising SLS [186]. Sintering of hard tissues must be safe enough not to damage the delicate tissues nearby. However, there are few biomaterials that can undergo thermal effects during sintering. They include proteins, such as melanin and haemoglobin that are capable of absorbing UV spectra, and the hydroxyl group members that absorb infrared radiation [62]. Taking into account all of the aforementioned factors, it has been reported that sintering hard tissue requires a short pulsed laser with an emitted wavelength between the visible and infrared [62]. This range was selected to avoid the absorption properties of melanin (N700 nm) and haemoglobin (N600 nm) as well as water. Further, the smaller HAZs, lower irradiation time and shorter pulse durations with ultrashort lasers play key role in such fabrication.

A.D. Anastasiou et al. utilised femtosecond (100 fs) pulsed lasers operating at a wavelength of 1045 nm for sintering ceramic-based synthetic, i.e., calcium phosphate minerals such as brushite (DCPD: $CaHPO_4 \cdot 2H_2O$) and hydroxyapatite (HAP: $Ca_{10}(PO_4)6(OH)_2$) [62]. The calcium phosphate minerals (i.e., brushite and hydroxyapatite) were further doped with iron (10%) to improve the sintering phenomenon with an fs laser [62]. It was reported that microstructural sintering and densification were observed when doping with Fe^{3+}-ions, and the laser absorption of the materials increased. After sintering, Fe^{3+}-doped brushite transformed to β-calcium pyrophosphate and Fe^{3+}-doped HAP transformed to calcium–iron–phosphate. It was observed that a temperature increase of 1000 °C occurred over a 30 µm diameter during irradiation; however, it was localised because it was estimated to decline to 40 degrees within 500 µm. From this work [62], it implies that soft tissues located more than 500 µm away from the irradiation zone are safe from thermal damage. Highly porous calcium pyrophosphate has been reported to have applications in bone regeneration, such as coatings or scaffold construction, and a dense layer of calcium–iron–phosphate might be used in acid eroded enamel restoration and for the treatment of tiny bone defects [62]. This shows a new way for alloplast grafting (i.e., synthetic bone grafting), which effectively lowers damage to the surrounding soft tissues, and the quality of sintering using fs lasers.

5.6. Femtosecond Laser-Based Additive Manufacturing Multi-Material Layered Structure

A solid oxide fuel cell (SOFC) is an electrochemical system that converts chemical energy from hydrogen fuel to electrical energy, in general, operating at high temperatures [188,189]. An anode, electrolyte and cathode are the three primary components of the SOFC. Currently, several traditional manufacturing techniques, such as chemical vapour deposition (CVD), tape casting, electrophoretic deposition (EPD), physical vapour deposition (PVD), screen printing, spray pyrolysis, sputtering and inkjet printing, were utilised to fabricate SOFCs [188,189]. Each of these processes has its own set of limitations such as tape casting's inability to produce layers thinner than 10 µm, in addition to the high cost (e.g., PVD, EPD and CVD). Furthermore, SOFCs' traditional fabrication methods involve a number of fabrication steps. A single-step fabrication approach that can provide reproducibility, flexibility and durability of SOFCs is much needed to address all of these limitations and further the commercialisation of SOFCs [188]. As a result, AM techniques have been recognised as a viable alternative that could address these shortcomings. Inkjet printing, stereolithography, aerosol jet printing, fused deposition modelling and SLS are among the AM techniques utilised in SOFC fabrication, with inkjet printing being the most prevalent because of its low-cost processing [188]. M. Lomberg et al. (2015) utilised CW laser-based SLS approach to produce SOFC electrodes with a laser power of 120 W and a scan speed of 400 mm/s. SOFCs with Ni powder as fuel electrodes, YSZ electrolyte, and LSCF-GDC air electrodes were successfully fabricated. The results reveal that the microcracks existed in SOFC electrodes manufactured using SLS [189]. Similarly, Arianna Pesce et al. (2020) used the SLA technique to fabricate the planar and conjugate LSM–YSZ/YSZ/Ni–YSZ SOFC layers. The results demonstrated that fully dense YSZ electrolytes with low cracks were produced [190]. Further, to overcome the limitations of CW laser-based SLS techniques, researchers utilised an fs laser-based SLS system to fabricate SOFCs. Bai et al. [191] utilised fs laser sintering to fabricate multilayer YSZ samples without the use of binders or heat treatment. The schematic of a multi-layered solid oxide fuel cell is shown in Figure 30. A high-power mode-locked Yb-doped fibre laser was employed with an average output power of 250 W, spot size of 25 µm, pulse duration of 800 fs, wavelength at 1030 nm and pulse repetition rate (PRR) of 80 MHz. The Ni-YSZ supporting layers were fabricated (Figure 31). High-density Ni-YSZ was fabricated when a scanning speed of 300 mm/s and laser power of 130 W were used. After first sintering of the Ni-YSZ supporting structure, a thin film of YSZ (powder or dye) was spread and laser-processed. Clear melting and fusing to the anode base were achieved, and the YSZ ink type had better uniformity. A thin coating of LSM (ink type) was put on top of the YSZ electrolyte layer and melted to act as the SOFC's cathode [191,192].

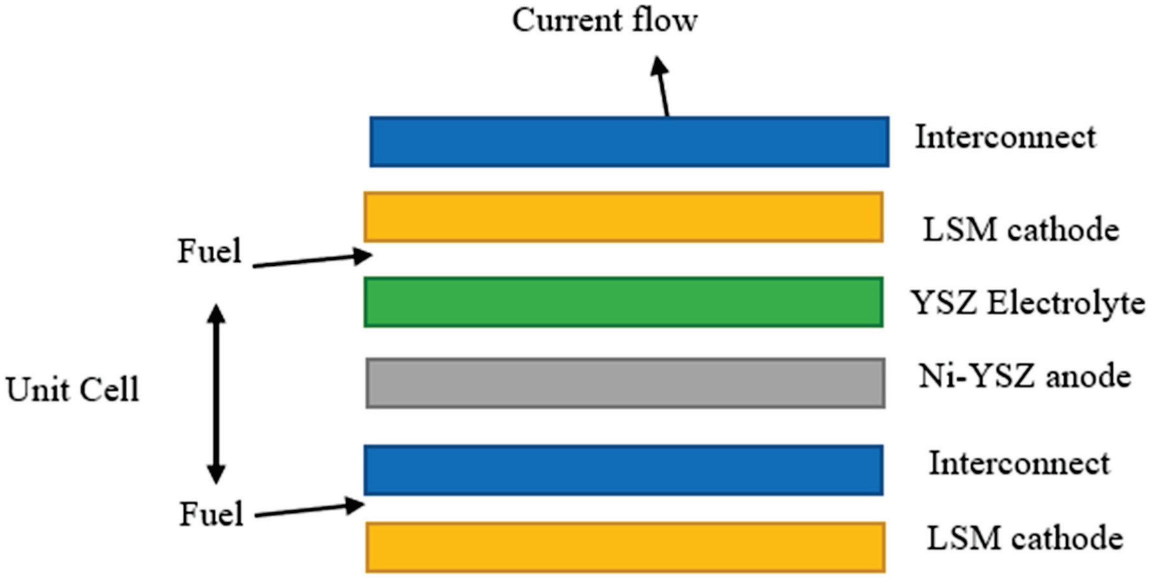

Figure 30. Schematic of a solid oxide fuel cell.

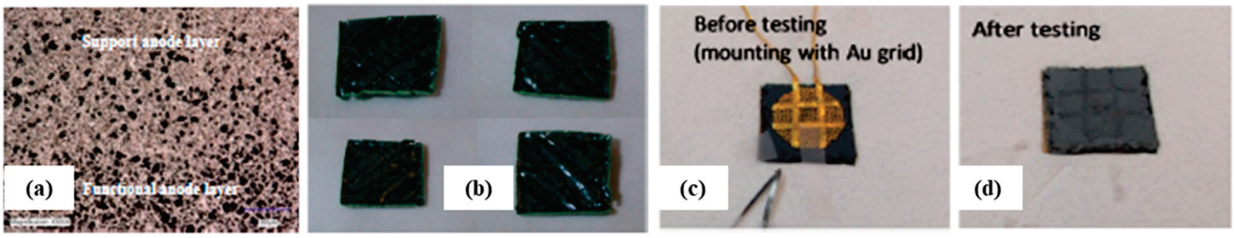

Figure 31. (**a**) Cross-section SEM image of the interface between the functional layer and support layer of an anode; (**b**) Ni-YSZ anode samples with the cell sample mounted on an Au grid for testing the I-V curve and EIS; (**c**) sample mounted on grid with Au before testing (**d**) cell sample after testing (Adapted from reference [191]).

5.7. Femtosecond Laser Processing of Titanium and Titanium Alloys

Titanium and its alloys have been widely utilised in automobile [193,194], biomedical [194,195], and aerospace [194,195] industries because of its key properties such as corrosion resistance [195], light weight [194,195], high strength [194,195], wear resistance [194] and high fracture toughness [195]. Further, because of its good biocompatibility, biostability, durability and mechanical properties, Ti has been widely used in dental and orthopaedic implants [196]. Several research studies have been carried out with pure titanium and its alloys (mainly Ti6Al4V) using CW laser-based SLM process [194,195,197]. Meanwhile, fs lasers have been mainly utilised in surface structuring and post-processing of 3D printed Ti parts. Surface treatment processes, meant to optimise surface roughness and dimensional accuracy, are of great importance in the field of AM to ensure that printed parts are useful for a large of number of applications. Post-processing techniques, such as CNC milling and polishing, can also be required to improve surface finishing [198]. However, these traditional processes may be challenging for thin walled, microscale and complex structures [49]. Further, the wettability behaviour of additive manufactured parts is also an important factor to consider, as it does impact the corrosion-resistance and water–material interaction [199]. To address these issues, researchers have been exploring ultrafast pulsed lasers (i.e., fs lasers), which enable efficient surface treatments or post-processing of additive manufactured parts. A.Y Vorobyev (2007) performed surface treatment of Ti utilising an fs laser, and they were able to produce a large variety of nanostructures on the surface of Ti material with sizes less than 20 nm [196]. Mingareev et al. (2013) also reported the utilisation of an fs laser to improve the surface quality of additive manufactured of Ti- and Ni-based alloy parts [49]. Jiao et al. (2018) observed that fs laser processing on Ti6Al4V material produced nanostructures that paved the way for AM part self-cleaning and hydrophobic properties [199]. Similarly, other research studies have been carried out utilising an fs laser to structure and treat Ti surfaces [200–202]. Yet, studies utilising femtosecond lasers to 3D print Ti parts are still scarce, which leaves a good room for exploration.

5.8. Femtosecond Laser Processing of Graphene

The unique properties of fs lasers make them attractive to be employed particularly in nano- and microfabrication. The applications of micro- and nanofabrication include microfluidic devices, medical and tissue engineering, metal micro- and nanostructures, photonic devices and micro and nano machining [203]. Fs lasers are also used in the fabrication of commonly used graphene products. Nowadays, many modern electronic devices have been developed that are flexible and smart electronics, have curved screens for mobiles and televisions, wearable displays, and electronic skins, making them particularly interesting for many researchers [204–206]. To produce such flexible electronics, materials such as graphene have unique and favourable properties. Graphene, a thin layer of carbon material, has numerous unique properties that make them suitable for many advanced electronic applications. Some of the unique properties include biocompatibility, mechanical strength, carrier mobility, conductivity and flexibility. There are different methods in which graphene can be processed and produced. Those methods include chemical vapour deposition (CVD), electron beam lithography, chemical synthesis and solvent exfoliation of graphene. Though these technologies exist, they are still in the early stage. Apart from these, AM technology has been successfully employed in the development of two-dimensional graphene structures. Yet, the development of graphene 3D structures remains a challenge. Direct writing and photolithography are two common AM technologies that are employed in the graphene development [207]. Attempts have been made by Chen et al., in 2018, to produce a composite from graphene oxide (GO), thermoplastic polyurethane and lactic acid [208]. These composites exhibited good biocompatibility and carrier mobility. Additionally, CW and pulsed lasers have been used to effectively process graphene materials [209]. The combined technology of an fs laser and DW technology was proposed by Bi et al., where they successfully fabricated varieties of complex micro-organic light-emitting diodes (OLEDs) [210]. As an application of electronic skins, based on the femtosecond laser-reduced graphene oxides (LRGOs), An et al. developed a graphene-based non-contact humidity sensor [211]. These LRGOs were also used in the development of strain sensors having a gauge factor greater than 400 by Wang et al. in 2016 [212]. Followed by this research, Qiao et al. fabricated an ultra-high gauge factored strain sensor which can be used to detect finger bends, pulse and respirational signals [213]. Fs laser-induced graphene (LIG) is another electronic skin similar to LRGOs. These LIGs were used in the fabrication of gas permeable temperature sensors as well as the throat sensors which are used in fabrication of artificial throats. These aforementioned findings on femtosecond laser-reduced LIGs and LRGOs demonstrate the great potential of fs lasers when employed in the electronic and health care industries.

5.9. A summary of the fs Laser AM Parameter Sets for Various Materials

The above discussions revealed that fs parameters play a crucial role in AM. It is evident that each set of parameters is specific to each material and the intended application. The various process parameters involved in fs laser AM, such as the wavelength, pulse duration, pulse repetition rate, laser power, scan speed, focus spot diameter, layer thickness, line spacing, pulse energy, fluence and energy density, were retrieved from the above discussed studies and are detailed in Table 7. These values can be used as a guide when planning fs laser-based AM with different materials:

Table 7. Showing materials processed through femtosecond lasers with different process settings.

Sample Number	Material	Wavelength (nm)	Pulse Duration (fs)	Pulse Repetition Rate (MHz)	Power (W)	Scan Speed (mm/s)	Spot Diameter (microns)	Layer Thickness (microns)	Line Spacing (μm)	Pulse Energy (J) (or) Fluence (J/cm^2) (or) Energy Density (W/cm^2)	Reference
1	Al–40Si	1030	500	6–20 MHz	25	200	50	15 to 30	-	<0.4 J/cm^2	[183]
2	Al–Li Alloy	1030	500	10–20 MHz	30	100–700	35	20 to 40	-	1.5–3 μJ	[60]
3	AlSi4O (40 microns)	1030	500	20 MHz	12 to 25	200	50	35 to 50	-	40–170 J/m	[38]
4	Calcium Phosphate	1045	130–190	1000	0.4	0.1	30	-	-	0.4 nJ	[62]
5	Copper (10 nm)	800	100	80 MHz	0.195–0.210	0.1	6.97	-	-	12.8–13.8 mJ/cm^2	[52]
6	Copper (35 microns)	1030		200–20 MHz	-	833 and 666	35	30	15	1, 1.25 μJ, 100 J/m	[54,138]
7	Copper (CuO)	780	120	81 MHz	-	0.5–20	-	1000	-	0.54 nJ	[53]
8	Cu_2O	780	120	83 MHz	-	100	0.7		-	163 GW/cm^2	[158]
9	CuO and NiO	780	120	82 MHz	-	0.1–5	1.3	10	-	0.059 J/cm^2	[154]
10	CuO/Cu_2O	780	120	84 MHz	-	10	-		-	0.74 nJ	[152]
11	Iron (1–5 microns)	1030	350	80 MHz	50	50	-		-	-	[7]
12	Iron on glass	1060	800	80 MHz	37 and 53	300 and 400	-	40	-	-	[100]
13	Monolithic zirconia	1030	400	200 kHz	5		-	-	-	25 μJ	[51]
14	Silver (Ag) NP	1030	370	1 MHz	0.05–0.3	0.01–5	-	-	-	-	[56]
15	Silver (Ag) NP	780	100	80 MHz	0.1–0.4	0.1–0.6	-	-	-	-	[174]
16	Silver (Ag) NP	800	50	1 kHz	-	0.02–4	-	-	-	10–300 m J/cm^2	[172]
17	Silver (Ag) NP	800	50	1 kHz	-	0.02–0.2	-	-	200	10–120 m J/cm^2	[173]
18	Silver (Ag) NP	780	100	1 kHz	0.5, 0.6	0.1–0.6	-	-	-	-	[55]
19	SS 316 L	793	150–200	1 kHz	0.15	-	-	-	-	-	[46]
20	Tungsten	1030	180	0.125–1 MHz	0.4 to 0.875	100–5000	36	-	10	0.4–7.5 μJ, 0.07–1.3 J/cm^2	[101]
21	Tungsten	1030	400	1 MHz	35	20	20	25–50	-	22.5 μJ	[58]
22	Tungsten	1030	750	100 kHz to 100 MHz	Maximum 1 kW	-	-	-	-	maximum 500 J	[44]
23	Tungsten	1030	400	1 MHz	45	25	-	-	-	-	[7]
24	YSZ, Ni-YSZ	1030	800	80 MHz	130	300	25	5–600	-	-	[191]

6. Summary

AM, one of the most rapidly evolving advanced manufacturing technologies is outpacing all other non-traditional manufacturing techniques, and it is positioned to make a major positive impact across all industries. This highly versatile technology represents one of the major enablers in the ongoing transformation of the fourth industrial revolution. The extreme flexibility and design freedom offered by AM, along with the wide selection of suitable materials (polymers, metals, ceramics and composites) and synthesis techniques positions 3D printing as the fabrication method of choice for an impressively wide range of applications. The fabrication of metallic parts is obviously of huge practical significance due to the fact of their desirable mechanical, electrical, thermal and magnetic properties. The development of various processing methods, metallic alloy compositions and optimising parameters for desirable properties are all active areas of research and development. Among the many recently developed AM techniques, selective laser sintering/melting represents one of the most promising methods capable of producing standard quality parts for various applications. The majority of current research efforts considering the SLM/S process has been carried out with CW and long-pulsed lasers to produce quality components. The process capabilities of SLS/M utilising different lasers sources, such as CW and pulsed lasers, were discussed in detail. The use of ultrafast lasers (picosecond and femtosecond lasers in particular), however, represents a major deviation and paves the way towards further enhancements by capitalising on shorter pulses, smaller HAZs, and superior resolution through significantly smaller spot sizes and shorter interaction times offered by fs lasers. Currently available commercial machines that utilise CW or pulsed lasers were compared to fs laser-based ones to highlight the benefits and shortcomings. Further, the main advantages of pulsed lasers over CW lasers were listed, which helps in orienting the research scope towards fs laser-based AM process. Though CW lasers have been proven to produce quality parts with various materials, there are still limitations such as HAZs, residual stresses, substrate damage, not being suitable for micro- and nanoscale parts, difficulty in processing materials with high thermal and melting points such as copper and tungsten. To address the issues mentioned in the case of CW and long-pulsed lasers, researchers utilised ultrashort pulsed lasers such as fs lasers in SLS/M.

***Fs laser science*:** To clearly understand the science behind these ultrafast lasers (i.e., fs lasers), a brief history, the fundamentals and fs laser–matter interaction were thoroughly discussed. In comparison with CW and ns lasers, fs lasers produce minimal HAZs, lower residual stresses and can produce miniaturised parts. Further, the fs laser-based AM and its different essential parameters affecting the AM parts were discussed. The ultrafast laser–material interaction studied by various researchers was consolidated and presented. Various numerical modelling approaches, such as the two-temperature model, molecular dynamics model, hydrodynamics model, hybrid model combining TTM and MD models and modified TTM models, were discussed to study the process in detail. In this review article, two major SLS/M techniques (i.e., powder bed fusion and direct writing) were utilised for fs laser-based AM. In the direct-writing technique, a pre-coated substrate is selectively sintered using a laser source. Similarly, to better understand the process of fs laser powder bed fusion technique, a schematic with components of the fs laser-based selective laser sintering/melting method was discussed.

***Materials*:** An fs laser source has been utilised for processing various materials that were challenging with CW or long-pulsed lasers. The different materials that were processed utilising fs laser source included copper, silver, aluminium, iron, tungsten, biomaterials, and ceramics. Copper material has been used for fs laser-based SLS/M utilising both DW and PBF techniques. Copper has been challenging to print using traditional CW lasers due to its high thermal conductivity and high reflectivity. A limitation that was clearly alleviated through the use of fs laser sintering process. Mainly in the case of miniaturised electronic devices, CW and long-pulsed laser failed to achieve parts at the micron or submicron levels because of HAZs, beam size, residual stresses and substrate damage. It was also reported that oxidation issues are much more prevalent in CW laser sintering than ns and fs laser sintering. Fs laser-reductive sintering of copper oxide material using DW technique has been reported to produce functional parts for temperature sensors applications. Attempts have also been made to fabricate micropatterns using copper–nickel alloys. Further sintering of copper particles utilising the PBF technique reported that at lower repetition rates, there was low melting, resulting in poor fusing of metal particles to the substrate. By increasing the pulse repetition rate and maintaining the pulse energy, proper bonding of copper powder to the substrate was achieved, which could have major applications in microdevices, heat sinks, and others. Further Very high melting point materials such as tungsten was also processed utilising the fs laser based PBF technique. Tungsten has eye-catching major applications in the aerospace, medical and nuclear sectors, among others. A few years back, AM of tungsten was a major challenge because of its high melting point, high thermal conductivity, and low thermal expansion. Since 2015, researchers have started utilising high-power CW laser sources to fabricate tungsten material to meet specific applications. Though they succeeded in fabricating the tungsten parts with CW laser source, there were still issues related to lower relative density, and micro-cracks were still prevalent. Research group explored the fabrication of tungsten parts utilising the fs laser-based PBF technique to address these issues. They demonstrated how processing parameters, including pulse repetition rate, laser spot diameter and layer thickness, played a crucial role in sintering tungsten particles. The capability of producing fine features using fs-laser-based AM, thin walls of 100 microns, smaller gear shapes and circular features with holes were fabricated with good accuracy. Comparing fs laser sintered parts with CW laser sintered and ps laser sintered parts, it was found that the defects present in fs laser sintered samples were fewer compared to other types of lasers. Further fs laser produced greater hardness and higher density parts as compared to CW laser sintered parts. One of the special features of fs lasers is localised heating, which was used to fuse iron powder onto a glass substrate that possesses extremely different material properties.

Furthermore, other precious metals, such as silver, also have been processed using an fs laser for specific applications in photonic devices and flexible electronics. It is fascinating to note that the silver nanoparticles were fabricated on a silica-based microfluidic channel utilising an fs laser to fabricate the SERS substrate. Researchers have also utilised both ns and fs laser sources to fuse silver nanoparticles on a PET substrate and compared the results by varying the effective pulse number and fluence. The results showed that in the case of the fs laser source, because of the low substrate damage and less film cracking, the produced parts had a higher electrical conductivity than ns laser sintered parts. Similarly, other experiments utilising fs laser sintering of silver nanoparticles were dedicated to analysing the effect of process parameters and varying spin-coated layer thicknesses on conductivity, microstructure and adhesion strength.

Aluminium and its alloys which are utilised in lightweight structures in different fields like aerospace, automotive, etc., were also investigated by utilising fs laser-based AM. In the case of Al and Li alloys for aerospace application, as the Li content increases in Al–Li alloy, the stiffness increases significantly at a lower mass. It was reported that the traditional casting process of Al–Li could process up to a max of 2 percent due to the precipitation of brittle δ-Al–Li. To address these issues, researchers utilised key factors of high cooling rates in fs laser-based technique to fabricate Al–Li alloy and produce Al–Li alloy with higher Li content. Similarly, other alloys such as AlSi4O, Al–40Si were also reported to fabricate parts utilising the fs laser-based AM technique. It is reported that in the case of AlSi4O, by properly optimising the process parameters, the minimum feature size of 50 μm was achieved utilising fs laser processing.

Fs laser based AM poses great potential in biomedical and tissue engineering to effectively fabricate hard tissues, which could have major dental and bone repair applications. The most important factors of fs laser sintering are the lower HAZs, lower irradiation time and localised heating, which play critical roles in fabricating or repairing the damaged tissues without affecting the surrounding area. The fs laser-based AM technique has also been utilised in the fabrication of multi-material SOFCs, which has solved a few limitations, such as microcracks that occur in CW laser-based-fabricated SOFCs. By utilising fs lasers, sintering of dense multi-material SOFCs was reported.

7. Conclusions

Fs laser-based sintering processes enhance the material processing library of conventional techniques based on CW or long-pulsed lasers by adding full control over the processing parameters. In particular, challenging materials, such as copper, silver, YSZ and tungsten, were reported to produce standard functional parts meeting the requirements of many applications. The fs laser sintering of copper has proven to have significant applications in the fabrication of micropatterns for interconnects on transistor IC chips. Further, the oxides of copper and nickel were utilised by the fs reductive sintering process to produce micropatterns that are sensitive to temperature and which could find applications in micro-sensing devices. Similarly, pure copper powder has also been investigated utilising fs lasers, which could have applications in heat sinks or cooling devices used in micro-robotic engines. Yet, this is still in the early stage because, as such, no quality parts have been fabricated utilising an fs laser source. Fs laser sintering of tungsten material has been reported to produce dense parts that could have significant applications in rocket parts, plasma-facing components in nuclear fusion reactors and radiation shielding in imaging systems. However, only a single research group has claimed to produce such dense parts with higher hardness, strength, etc. But the process parameters are not much evident, and there is a need to develop optimum process conditions to fabricate fs laser-based tungsten parts because tungsten material has much scope and applications in most emerging fields. In the case of aluminium and its alloys, Al–Li and AlSi4O, the reported results are encouraging. However, as these materials are utilised for structural applications in aerospace and automobile, the large-scale production may or may not be possible with the current research in fs laser sintering. Moreover, in the case of ceramics, which have significant applications in challenging tissue fabrication, fs laser sintering could be ideal, as it does not cause damage to the surrounding soft tissues during fabrication. Yet, more research is needed to identify the proper equipment and techniques that need to be developed to be able to commercialise the fabricated ceramic parts. For SOFCs, while inkjet printing process and other traditional manufacturing techniques are mainly employed to develop them at cheaper costs, the need for much more miniaturised parts with higher efficiency necessitates the application of fs laser sintering.

Author Contributions: Conceptualization, A.S.A.; investigation, A.A., H.A.K. and A.S.A.; validation, M.A., M.E., W.A. and A.S.A.; writing—original draft preparation A.B.K. and H.A.K.; writing—review and editing, M.A., M.E., W.A., F.A. and A.S.A.; Supervision, A.S.A. All authors have read and agreed to the published version of the manuscript.

Funding: This work was supported by the American University of Sharjah through FRG grant #FRG19-L-S61.

Institutional Review Board Statement: Not applicable.

Informed Consent Statement: Not applicable.

Data Availability Statement: Data underlying the results presented in this paper are not publicly available at this time but may be obtained from the corresponding authors upon reasonable request.

Conflicts of Interest: The authors declare no conflict of interest.

References

1. Gibson, I.; Rosen, D. *Additive Manufacturing Technologies*, 17th ed.; Springer: New York, NY, USA, 2014.
2. Dilberoglu, U.M.; Gharehpapagh, B.; Yaman, U.; Dolen, M. The Role of Additive Manufacturing in the Era of Industry 4.0. *Procedia Manuf.* **2017**, *11*, 545–554. [CrossRef]

3. Thompson, M.K.; Moroni, G.; Vaneker, T.; Fadel, G.; Campbell, R.I.; Gibson, I.; Bernard, A.; Schulz, J.; Graf, P.; Ahuja, B.; et al. Design for Additive Manufacturing: Trends, opportunities, considerations, and constraints. *CIRP Ann.* **2016**, *65*, 737–760. [CrossRef]
4. Barroqueiro, B.; Andrade-Campos, A.; Valente, R.; Neto, V. Metal Additive Manufacturing Cycle in Aerospace Industry: A Comprehensive Review. *J. Manuf. Mater. Process.* **2019**, *3*, 52. [CrossRef]
5. Katz-Demyanetz, A.; Popov, V.V.; Kovalevsky, A.; Safranchik, D.; Koptyug, A. Powder-bed additive manufacturing for aerospace application: Techniques, metallic and metal/ceramic composite materials and trends. *Manuf. Rev.* **2019**, *6*, 5. [CrossRef]
6. Mohanavel, V.; Ali, K.A.; Ranganathan, K.; Jeffrey, J.A.; Ravikumar, M.M.; Rajkumar, S. The roles and applications of additive manufacturing in the aerospace and automobile sector. *Mater. Today Proc.* **2021**, *47*, 405–409. [CrossRef]
7. Huang, H.; Nie, B.; Wan, P.; Yang, L.-M.; Bai, S.; Liu, J. Femtosecond fiber laser additive manufacturing and welding for 3D manufacturing. In *Laser 3D Manufacturing II*; Proc. SPIE: San Francisco, CA, USA, 2015; Volume 9353, p. 93530A. [CrossRef]
8. Rioja, R.J.; Liu, J. The Evolution of Al-Li Base Products for Aerospace and Space Applications. *Metall. Mater. Trans. A* **2012**, *43*, 3325–3337. [CrossRef]
9. Byskov-Nielsen, J.; Savolainen, J.-M.; Christensen, M.S.; Balling, P. Ultra-short pulse laser ablation of metals: Threshold fluence, incubation coefficient and ablation rates. *Appl. Phys. A* **2010**, *101*, 97–101. [CrossRef]
10. Chua, C.K.; Matham, M.V.; Kim, Y.-J. *Lasers in 3D Printing and Manufacturing*; World Scientific Publishing Company: Singapore, 2017. [CrossRef]
11. Dordlofva, C. A Design for Qualification Framework for the Development of Additive Manufacturing Components—A Case Study from the Space Industry. *Aerospace* **2020**, *7*, 25. [CrossRef]
12. Pinkerton, A.J. [INVITED] Lasers in additive manufacturing. *Opt. Laser Technol.* **2016**, *78*, 25–32. [CrossRef]
13. Paolini, A.; Kollmannsberger, S.; Rank, E. Additive manufacturing in construction: A review on processes, applications, and digital planning methods. *Addit. Manuf.* **2019**, *30*, 100894. [CrossRef]
14. Saengchairat, N.; Tran, T.; Chua, C.-K. A review: Additive manufacturing for active electronic components. *Virtual Phys. Prototyp.* **2017**, *12*, 31–46. [CrossRef]
15. Godoi, F.C.; Prakash, S.; Bhandari, B.R. 3d printing technologies applied for food design: Status and prospects. *J. Food Eng.* **2016**, *179*, 44–54. [CrossRef]
16. Huang, S.H.; Liu, P.; Mokasdar, A.; Hou, L. Additive manufacturing and its societal impact: A literature review. *Int. J. Adv. Manuf. Technol.* **2013**, *67*, 1191–1203. [CrossRef]
17. Sibbett, W.; Lagatsky, A.A.; Brown, C.T.A. The development and application of femtosecond laser systems. *Opt. Express* **2012**, *20*, 6989–7001. [CrossRef]
18. Application Spotlight: 3D Printing for Footwear, AMFG. 2019. Available online: https://amfg.ai/2019/09/18/application-spotlight-3d-printing-for-footwear/ (accessed on 30 October 2021).
19. Wong, K.V.; Hernandez, A. A Review of Additive Manufacturing. *ISRN Mech. Eng.* **2012**, *2012*, 208760. [CrossRef]
20. Meier, M.; Tan, K.H.; Lim, M.K.; Chung, L. Unlocking innovation in the sport industry through additive manufacturing. *Bus. Process. Manag. J.* **2019**, *25*, 456–475. [CrossRef]
21. Wimpenny, D.I.; Pandey, P.M.; Kumar, L.J. (Eds.) *Advances in 3D Printing & Additive Manufacturing Technologies*; Springer: Singapore, 2017; pp. 9–28. [CrossRef]
22. Das, S.; Bourell, D.L.; Babu, S. Metallic materials for 3D printing. *MRS Bull.* **2016**, *41*, 729–741. [CrossRef]
23. Frazier, W.E. Metal Additive Manufacturing: A Review. *J. Mater. Eng. Perform.* **2014**, *23*, 1917–1928. [CrossRef]
24. Herderick, E. Additive manufacturing of metals: A review. *Mater. Sci. Technol. Conf. Exhib.* **2011**, *2*, 1413–1425. Available online: http://www.scopus.com/inward/record.url?eid=2-s2.0-84856301323&partnerID=40&md5=e02018d10b2ca37a7e2ae1773e4fcaec (accessed on 30 November 2021).
25. Liu, R.; Wang, Z.; Sparks, T.; Liou, F.; Newkirk, J. Aerospace applications of laser additive manufacturing. In *Laser Additive Manufacturing: Materials, Design, Technologies, and Applications*; Woodhead Publishing: Sawston, UK, 2017; ISBN 9780081004340.
26. Najmon, J.C.; Raeisi, S.; Tovar, A. Review of additive manufacturing technologies and applications in the aerospace industry. In *Additive Manufacturing for the Aerospace Industry*; Elsevier: Amsterdam, The Netherlands, 2019; pp. 7–31.
27. Saracyakupoglu, T. The Qualification of the Additively Manufactured Parts in the Aviation Industry. *Am. J. Aerosp. Eng.* **2019**, *6*, 1. [CrossRef]
28. Vafadar, A.; Guzzomi, F.; Rassau, A.; Hayward, K. Advances in Metal Additive Manufacturing: A Review of Common Processes, Industrial Applications, and Current Challenges. *Appl. Sci.* **2021**, *11*, 1213. [CrossRef]
29. Lee, H.; Lim, C.H.J.; Low, M.J.; Tham, N.; Murukeshan, V.M.; Kim, Y.J. Lasers in additive manufacturing: A review. *Int. J. Precis. Eng. Manuf. Technol.* **2017**, *4*, 307–322. [CrossRef]
30. Deckers, J.; Meyers, S.; Kruth, J.; Vleugels, J. Direct Selective Laser Sintering/Melting of High Density Alumina Powder Layers at Elevated Temperatures. *Phys. Procedia* **2014**, *56*, 117–124. [CrossRef]
31. Kruth, J.; Froyen, L.; Van Vaerenbergh, J.; Mercelis, P.; Rombouts, M.; Lauwers, B. Selective laser melting of iron-based powder. *J. Mater. Process. Technol.* **2004**, *149*, 616–622. [CrossRef]
32. Biffi, C.; Fiocchi, J.; Bassani, P.; Tuissi, A. Continuous wave vs. pulsed wave laser emission in selective laser melting of AlSi10Mg parts with industrial optimized process parameters: Microstructure and mechanical behaviour. *Addit. Manuf.* **2018**, *24*, 639–646. [CrossRef]

33. Kumar, H.; Kumaraguru, S. Distortion in Metal Additive Manufactured Parts. In *3D Printing and Additive Manufacturing Technologies*; Springer: Berlin/Heidelberg, Germany, 2019; pp. 281–295.
34. Oliveira, J.P.; LaLonde, A.; Ma, J. Processing parameters in laser powder bed fusion metal additive manufacturing. *Mater. Des.* **2020**, *193*, 108762. [CrossRef]
35. Yeong, W.; Yap, C.; Mapar, M.; Chua, C. State-of-the-art review on selective laser melting of ceramics. In *High Value Manufacturing: Advanced Research in Virtual and Rapid Prototyping*; CRC Press: Boca Raton, FL, USA, 2013; pp. 65–70.
36. Lonergan, J.M.; Fahrenholtz, W.; Hilmas, G. Zirconium Diboride with High Thermal Conductivity. *J. Am. Ceram. Soc.* **2014**, *97*, 1689–1691. [CrossRef]
37. In't Veld, B.H.; Overmeyer, L.; Schmidt, M.; Wegener, K.; Malshe, A.; Bartolo, P. Micro additive manufacturing using ultra short laser pulses. *CIRP Ann.* **2015**, *64*, 701–724. [CrossRef]
38. Ullsperger, T.; Matthäus, G.; Kaden, L.; Rettenmayr, M.; Risse, S.; Tünnermann, A.; Nolte, S. Selective laser melting of AlSi40 using ultrashort laser pulses for additive manufacturing applications. In Proceedings of the Lasers in Manufacturing Conference 2017, Munich, Germany, 26–29 June 2017.
39. Neuenschwander, B.; Jaeggi, B.; Schmid, M.; Dommann, A.; Neels, A.; Bandi, T.; Hennig, G. Factors controlling the incubation in the application of ps laser pulses on copper and iron surfaces. In *Laser Applications in Microelectronic and Optoelectronic Manufacturing (LAMOM) XVIII*; Proc. of SPIE: San Francisco, CA, USA, 2013; Volume 8607, p. 86070D. [CrossRef]
40. Nedialkov, N.; Atanasov, P. Molecular dynamics simulation study of deep hole drilling in iron by ultrashort laser pulses. *Appl. Surf. Sci.* **2006**, *252*, 4411–4415. [CrossRef]
41. Nagarajan, B.; Hu, Z.; Song, X.; Zhai, W.; Wei, J. Development of Micro Selective Laser Melting: The State of the Art and Future Perspectives. *Engineering* **2019**, *5*, 702–720. [CrossRef]
42. Ultrafast Lasers Market-Growth, Trends, COVID-19 Impact, and Forecasts (2021–2026), Mordor Intell. 2020. Available online: https://www.mordorintelligence.com/industry-reports/ultrafast-lasers-market (accessed on 25 November 2021).
43. Eaton, S.M.; Zhang, H.; Herman, P.R.; Yoshino, F.; Shah, L.; Bovatsek, J.; Arai, A.Y. Heat accumulation effects in femtosecond laser-written waveguides with variable repetition rate. *Opt. Express* **2005**, *13*, 4708–4716. [CrossRef]
44. Bai, S.; Liu, J.; Yang, P.; Huang, H.; Yang, L.-M. Femtosecond fiber laser additive manufacturing of tungsten. In *Laser 3D Manufacturing III*; Proc. of SPIE: San Francisco, CA, USA, 2016; Volume 9738, p. 97380. [CrossRef]
45. Hodgson, N.O.R.M.A.N.; Laha, M.I.C.H.A.E.L.; Lee, T.S.; Steinkopff, A.L.B.R.E.C.H.T.; Heming, S.E.B.A.S.T.I.A.N. Industrial femtosecond lasers and material processing. In *Industrial Laser Solutions*; PennWell Publishing: Nashville, TN, USA, 2019.
46. Gieseke, M.; Senz, V.; Vehse, M.; Fiedler, S.; Irsig, R.; Hustedt, M.; Sternberg, K.; Nölke, C.; Kaierle, S.; Wesling, V.; et al. Additive Manufacturing of Drug Delivery Systems. *Biomed. Tech. Eng.* **2012**, *57*, 398–401. [CrossRef]
47. Birnbaum, M. Semiconductor Surface Damage Produced by Ruby Lasers. *J. Appl. Phys.* **1965**, *36*, 3688–3689. [CrossRef]
48. Hodgson, N.; Laha, M.; Lee, T.S.; Haloui, H.; Heming, S.; Steinkopff, A. Industrial Ultrafast Lasers–Systems, Processing Fundamentals, and Applications. In *CLEO: QELS_Fundamental Science*; Optical Society of America: San Jose, CA, USA, 2019. [CrossRef]
49. Mingareev, I.; Bonhoff, T.; El-Sherif, A.; Meiners, W.; Kelbassa, I.; Biermann, T.; Richardson, M. Femtosecond laser post-processing of metal parts produced by laser additive manufacturing. *J. Laser Appl.* **2013**, *25*, 052009. [CrossRef]
50. Mingareev, I.; Bonhoff, T.; El-Sherif, A.; Biermann, T.; Meiners, W.; Kelbassa, I.; Richardson, M. Ultrafast laser-based post-processing of parts produced by additive manufacturing. *Int. Congr. Appl. Lasers Electro-Opt.* **2013**, *2013*, 787. [CrossRef]
51. Liang, S.; Ye, H.; Yuan, F. Changes in Crystal Phase, Morphology, and Flexural Strength of As-Sintered Translucent Monolithic Zirconia Ceramic Modified by Femtosecond Laser. *Appl. Sci.* **2021**, *11*, 6925. [CrossRef]
52. Cheng, C.W.; Chen, J.K. Femtosecond laser sintering of copper nanoparticles. *Appl. Phys. A* **2016**, *122*, 1–8. [CrossRef]
53. Mizoshiri, M.; Hata, S. Direct Writing of Cu-based Micro-temperature Sensors onto Glass and Poly(dimethylsiloxane) Substrates Using Femtosecond Laser Reductive Patterning of CuO Nanoparticles. *Res. Rev. J. Mater. Sci.* **2016**, *4*, 47–54. [CrossRef]
54. Kaden, L.; Matthäus, G.; Ullsperger, T.; Engelhardt, H.; Rettenmayr, M.; Tünnermann, A.; Nolte, S. Selective laser melting of copper using ultrashort laser pulses. *Appl. Phys. A* **2017**, *123*, 596. [CrossRef]
55. Son, Y.; Yeo, J.; Ha, C.W.; Hong, S.; Ko, S.H.; Yang, D.Y. Fabrication of submicron-sized metal patterns on a flexible polymer substrate by femtosecond laser sintering of metal nanoparticles. *Int. J. Nanomanuf.* **2013**, *9*, 468. [CrossRef]
56. Kurnoothala, R.; Sai, M.V.; Vishnubhatla, K.C. Facile fabrication of integrated microfluidic SERS substrate by femtosecond laser sintering of silver nano particles. *Opt. Mater.* **2021**, *111*, 110518. [CrossRef]
57. Song, B.; Dong, S.; Deng, S.; Liao, H.; Coddet, C. Microstructure and tensile properties of iron parts fabricated by selective laser melting. *Opt. Laser Technol.* **2014**, *56*, 451–460. [CrossRef]
58. Nie, B.; Huang, H.; Bai, S.; Liu, J. Femtosecond laser melting and resolidifying of high-temperature powder materials. *Appl. Phys. A* **2014**, *118*, 37–41. [CrossRef]
59. Olakanmi, E.O.; Cochrane, R.; Dalgarno, K. A review on selective laser sintering/melting (SLS/SLM) of aluminium alloy powders: Processing, microstructure, and properties. *Prog. Mater. Sci.* **2015**, *74*, 401–477. [CrossRef]
60. Yürekli, B.; Schade, L.; Ullsperger, T.; Seyfarth, B.; Kohl, H.; Matthäus, G.; Liu, D.; Rettenmayr, M.; Nolte, S. Additive manufacturing of binary Al-Li alloys. *Procedia CIRP* **2020**, *94*, 69–73. [CrossRef]
61. Ferrage, L.; Bertrand, G.; Lenormand, P. Dense yttria-stabilized zirconia obtained by direct selective laser sintering. *Addit. Manuf.* **2018**, *21*, 472–478. [CrossRef]

62. Anastasiou, A.; Thomson, C.; Hussain, S.; Edwards, T.; Strafford, S.; Malinowski, M.; Mathieson, R.; Brown, C.; Brown, A.; Duggal, M.; et al. Sintering of calcium phosphates with a femtosecond pulsed laser for hard tissue engineering. *Mater. Des.* **2016**, *101*, 346–354. [CrossRef]
63. Bai, S.; Liu, J. Additive manufacturing of bimetallic structures. *SN Appl. Sci.* **2020**, *2*, 1152. [CrossRef]
64. Lei, S.; Zhao, X.; Yu, X.; Hu, A.; Vukelic, S.; Jun, M.B.G.; Joe, H.-E.; Yao, Y.L.; Shin, Y.C. Ultrafast Laser Applications in Manufacturing Processes: A State-of-the-Art Review. *J. Manuf. Sci. Eng.* **2020**, *142*, 031005. [CrossRef]
65. Mottay, E.; Liu, X.; Zhang, H.; Mazur, E.; Sanatinia, R.; Pfleging, W. Industrial applications of ultrafast laser processing. *MRS Bull.* **2016**, *41*, 984–992. [CrossRef]
66. Strickland, D.; Mourou, G. Compression of amplified chirped optical pulses. *Opt. Commun.* **1985**, *56*, 219–221. [CrossRef]
67. Bakshi, K. A Review on Selective Laser Sintering: A Rapid Prototyping Technology. *IOSR J. Mech. Civ. Eng.* **2016**, *4*, 53–57. [CrossRef]
68. Hong, S. Selective Laser Sintering of Nanoparticles. *Sinter. Funct. Mater.* **2018**, 147–164. [CrossRef]
69. Ruszaj, A. Additive methods in micro and nano manufacturing technologies. *Mechanik* **2019**, *92*, 386–390. [CrossRef]
70. Engstrøm, D.; Porter, B.; Pacios, M.; Bhaskaran, H. Additive nanomanufacturing–A review. *J. Mater. Res.* **2014**, *29*, 1792–1816. [CrossRef]
71. Milewski, J.O. *Lasers, Electron Beams, Plasma Arcs*; Springer: Singapore, 2017; pp. 85–97.
72. Jamie, D. A Comprehensive List of all the Metal 3D Printer Manufacturers, 3D Nativ. 2021. Available online: https://www.3dnatives.com/en/metal-3d-printer-manufacturers/#! (accessed on 13 November 2021).
73. Schmidt, M.; Merklein, M.; Bourell, D.; Dimitrov, D.; Hausotte, T.; Wegener, K.; Overmeyer, L.; Vollertsen, F.; Levy, G.N. Laser based additive manufacturing in industry and academia. *CIRP Ann.* **2017**, *66*, 561–583. [CrossRef]
74. Yap, C.Y.; Chua, C.K.; Dong, Z.L.; Liu, Z.H.; Zhang, D.Q.; Loh, L.E.; Sing, S.L. Review of selective laser melting: Materials and applications. *Appl. Phys. Rev.* **2015**, *2*, 041101. [CrossRef]
75. Mosadegh, B.; Xiong, G.; Dunham, S.; Min, J.K. Current progress in 3D printing for cardiovascular tissue engineering. *Biomed. Mater.* **2015**, *10*, 034002. [CrossRef]
76. Vaezi, M.; Seitz, H.; Yang, S. A review on 3D micro-additive manufacturing technologies. *Int. J. Adv. Manuf. Technol.* **2013**, *67*, 1721–1754. [CrossRef]
77. Majumdar, J.D.; Manna, I. *Laser-Assisted Fabrication of Materials*; Springer: Berlin, Germany, 2012.
78. Gu, D.; Meiners, W.; Wissenbach, K.; Poprawe, R. Laser additive manufacturing of metallic components: Materials, processes and mechanisms. *Int. Mater. Rev.* **2012**, *57*, 133–164. [CrossRef]
79. Mukherjee, T.; Zuback, J.S.; De, A.; Debroy, T. Printability of alloys for additive manufacturing. *Sci. Rep.* **2016**, *6*, 19717. [CrossRef] [PubMed]
80. Karia, M.C.; Popat, M.A.; Sangani, K.B. Selective laser melting of Inconel super alloy-a review. In *AIP Conference Proceedings*; AIP Publishing: Melville, NY, USA, 2017.
81. Garban-Labaune, C.; Fabre, E.; Max, C.E.; Fabbro, R.; Amiranoff, F.; Virmont, J.; Weinfeld, M.; Michard, A. Effect of Laser Wavelength and Pulse Duration on Laser-Light Absorption and Back Reflection. *Phys. Rev. Lett.* **1982**, *48*, 1018–1021. [CrossRef]
82. Buchbinder, D.; Schleifenbaum, J.H.; Heidrich, S.; Meiners, W.; Bültmann, J. High Power Selective Laser Melting (HP SLM) of Aluminum Parts. *Phys. Procedia* **2011**, *12*, 271–278. [CrossRef]
83. Sing, S.L.; Yeong, W.Y.; Wiria, F.E.; Tay, B.Y.; Zhao, Z.; Zhao, L.; Tian, Z.; Yang, S. Direct selective laser sintering and melting of ceramics: A review. *Rapid Prototyp. J.* **2017**, *23*, 611–623. [CrossRef]
84. Ke, L.; Zhu, H.; Yin, J.; Wang, X. Effects of peak laser power on laser micro sintering of nickel powder by pulsed Nd:YAG laser. *Rapid Prototyp. J.* **2014**, *20*, 328–335. [CrossRef]
85. Sufiiarov, V.; Popovich, A.; Borisov, E.; Polozov, I.; Masaylo, D.; Orlov, A. The Effect of Layer Thickness at Selective Laser Melting. *Procedia Eng.* **2017**, *174*, 126–134. [CrossRef]
86. Aboulkhair, N.T. Additive Manufacture of an Aluminium Alloy: Processing, Microstructure, and Mechanical Properties. Ph.D. Dissertation, University of Nottingham, Nottingham, UK, 2015.
87. Aboulkhair, N.T.; Everitt, N.; Ashcroft, I.; Tuck, C. Reducing porosity in AlSi10Mg parts processed by selective laser melting. *Addit. Manuf.* **2014**, *1–4*, 77–86. [CrossRef]
88. Thijs, L.; Kempen, K.; Kruth, J.-P.; Van Humbeeck, J. Fine-structured aluminium products with controllable texture by selective laser melting of pre-alloyed AlSi10Mg powder. *Acta Mater.* **2013**, *61*, 1809–1819. [CrossRef]
89. Aboulkhair, N.T.; Simonelli, M.; Parry, L.; Ashcroft, I.; Tuck, C.; Hague, R. 3D printing of Aluminium alloys: Additive Manufacturing of Aluminium alloys using selective laser melting. *Prog. Mater. Sci.* **2019**, *106*, 100578. [CrossRef]
90. DeMaria, A.J.; Stetser, D.A.; Heynau, H. Self mode-locking of lasers with saturable absorbers. *Appl. Phys. Lett.* **1966**, *8*, 174–176. [CrossRef]
91. Shank, C.V. Subpicosecond kilowatt pulses from a mode-locked cw dye laser. *Appl. Phys. Lett.* **1974**, *24*, 373. [CrossRef]
92. Haus, H.A. Theory of mode locking with a fast saturable absorber. *J. Appl. Phys.* **1975**, *46*, 3049–3058. [CrossRef]
93. Fermann, M.E.; Hartl, I. Ultrafast fibre lasers. *Nat. Photonics* **2013**, *7*, 868–874. [CrossRef]
94. Spence, D.E.; Kean, P.N.; Sibbett, W. 60-Femtosecond pulse generation from a self-mode-locked Ti:sapphire laser. *Opt. Lett.* **1991**, *16*, 42–44. [CrossRef] [PubMed]

95. Sutter, D.; Jung, I.; Kartner, F.; Matuschek, N.; Morier-Genoud, F.; Scheuer, V.; Tilsch, M.; Tschudi, T.; Keller, U. Self-starting 6.5-fs pulses from a Ti:sapphire laser using a semiconductor saturable absorber and double chirped mirrors. *IEEE J. Sel. Top. Quantum Electron.* **1998**, *4*, 169–178. [CrossRef]
96. Hamad, A.H. *Effects of Different Laser Pulse Regimes (Nanosecond, Picosecond and Femtosecond) on the Ablation of Materials for Production of Nanoparticles in Liquid Solution*; IntechOpen: London, UK, 2016.
97. Byskov-Nielsen, J. Short-Pulse Laser Ablation of Metals: Fundamentals and Applications for Micro-Mechanical Interlocking. Ph.D. Dissertation, University of Aarhus, Aarhus, Denmark, 2010.
98. Hu, A.; Li, R.; Bai, S.; Yu, Y.; Zhou, W.; Bridges, D.; Deng, Y.; Zhang, L. *Introduction to Laser Micro-to-Nano Manufacturing*; Springer: Singapore, 2020; pp. 1–74.
99. Wellershoff, S.-S.; Hohlfeld, J.; Güdde, J.; Matthias, E. The role of electron-phonon coupling in femtosecond laser damage of metals. *Appl. Phys. A* **1999**, *69*, S99–S107. [CrossRef]
100. Liu, J.; Deng, C.; Bai, S. Glass surface metal deposition with high-power femtosecond fiber laser. *Appl. Phys. A* **2016**, *122*, 1064. [CrossRef]
101. Ebert, R. Laser Processing of Tungsten Powder with Femtosecond Laser Radiation. *J. Laser Micro/Nanoeng.* **2012**, *7*, 38–43. [CrossRef]
102. Phillips, K.C.; Gandhi, H.H.; Mazur, E.; Sundaram, S.K. Ultrafast laser processing of materials: A review. *Adv. Opt. Photonics* **2015**, *7*, 684–712. [CrossRef]
103. Key Parameters of a Laser System, EDMUND Opt. (n.d.) Available online: https://www.edmundoptics.com/knowledge-center/application-notes/lasers/key-parameters-of-a-laser-system/ (accessed on 25 November 2021).
104. Zhang, B.; Li, Y.; Bai, Q. Defect Formation Mechanisms in Selective Laser Melting: A Review. *Chin. J. Mech. Eng.* **2017**, *30*, 515–527. [CrossRef]
105. Wang, L.; Wei, Q.; He, W.; Shi, Y. Influence of powder characteristic and process parameters on SLM formability. *J. HuaZhong Univ. Sci. Technol. (Nat. Sci. Ed.)* **2012**, *2*. [CrossRef]
106. Lindgren, L.-E.; Lundbäck, A. Approaches in computational welding mechanics applied to additive manufacturing: Review and outlook. *Comptes Rendus Mécanique* **2018**, *346*, 1033–1042. [CrossRef]
107. Francois, M.; Sun, A.; King, W.; Henson, N.; Tourret, D.; Bronkhorst, C.; Carlson, N.; Newman, C.; Haut, T.; Bakosi, J.; et al. Modeling of additive manufacturing processes for metals: Challenges and opportunities. *Curr. Opin. Solid State Mater. Sci.* **2017**, *21*, 198–206. [CrossRef]
108. Liu, J.; Jalalahmadi, B.; Guo, Y.; Sealy, M.P.; Bolander, N. A review of computational modeling in powder-based additive manufacturing for metallic part qualification. *Rapid Prototyp. J.* **2018**, *24*, 1245–1264. [CrossRef]
109. Wang, G.-X.; Prasad, V. Microscale heat and mass transfer and non-equilibrium phase change in rapid solidification. *Mater. Sci. Eng. A* **2000**, *292*, 142–148. [CrossRef]
110. Hopkins, J.-M.; Sibbett, W. Ultrashort-pulse lasers: Big payoffs in a flash. *Sci. Am.* **2000**, *283*, 72–79. [CrossRef]
111. Momma, C.; Chichkov, B.; Nolte, S.; von Alvensleben, F.; Tünnermann, A.; Welling, H.; Wellegehausen, B. Short-pulse laser ablation of solid targets. *Opt. Commun.* **1996**, *129*, 134–142. [CrossRef]
112. Zhang, Y.; Tzou, D.Y.; Chen, J.K. Micro-and nanoscale heat transfer in femtosecond laser processing of metals. *arXiv* **2015**, arXiv:1511.03566. Available online: https://arxiv.org/abs/1511.03566 (accessed on 25 November 2021).
113. Hirayama, Y.; Obara, M. Heat-affected zone of metals ablated with femtosecond laser pulses. In *Photon Processing in Microelectronics and Photonics II*; Proc. of SPIE: San Jose, CA, USA, 2003; pp. 417–425.
114. Hohlfeld, J.; Wellershoff, S.-S.; Güdde, J.; Conrad, U.; Jähnke, V.; Matthias, E. Electron and lattice dynamics following optical excitation of metals. *Chem. Phys.* **2000**, *251*, 237–258. [CrossRef]
115. Chowdhury, I.H.; Xu, X. Heat transfer in femtosecond laser processing of metal. *Numer. Heat Transf. Part A Appl.* **2003**, *44*, 219–232. [CrossRef]
116. Ji, P.; Zhang, Y. Multiscale modeling of femtosecond laser irradiation on a copper film with electron thermal conductivity from ab initio calculation. *Numer. Heat Transf. Part A Appl.* **2017**, *71*, 128–136. [CrossRef]
117. Povarnitsyn, M.; Fokin, V.B.; Levashov, P.R. Microscopic and macroscopic modeling of femtosecond laser ablation of metals. *Appl. Surf. Sci.* **2015**, *357*, 1150–1156. [CrossRef]
118. Perez, D.; Lewis, L.J. Molecular-dynamics study of ablation of solids under femtosecond laser pulses. *Phys. Rev. B* **2003**, *67*, 184102. [CrossRef]
119. Colombier, J.P.; Combis, P.; Bonneau, F.; Le Harzic, R.; Audouard, E. Hydrodynamic simulations of metal ablation by femtosecond laser irradiation. *Phys. Rev. B* **2005**, *71*, 165406. [CrossRef]
120. Rethfeld, B.; Ivanov, D.S.; E Garcia, M.; I Anisimov, S. Modelling ultrafast laser ablation. *J. Phys. D Appl. Phys.* **2017**, *50*, 193001. [CrossRef]
121. Anisimov, S.I.; Kapeliovich, B.L.; Perel-man, T.L. Electron emission from metal surfaces exposed to ultrashort laser pulses. *Zh. Eksp. Teor. Fiz* **1974**, *66*, 375–377.
122. Qiu, T.; Tien, C. Femtosecond laser heating of multi-layer metals—I. Analysis. *Int. J. Heat Mass Transf.* **1994**, *37*, 2789–2797. [CrossRef]
123. Qiu, T.Q.; Tien, C.L. Heat Transfer Mechanisms During Short-Pulse Laser Heating of Metals. *J. Heat Transf.* **1993**, *115*, 835–841. [CrossRef]

124. Abdelmalek, A.; Bedrane, Z.; Amara, E.-H.; Sotillo, B.; Bharadwaj, V.; Ramponi, R.; Eaton, S.M. Ablation of Copper Metal Films by Femtosecond Laser Multipulse Irradiation. *Appl. Sci.* **2018**, *8*, 1826. [CrossRef]
125. Lee, D.; Kannatey-Asibu, E. Numerical Analysis of Ultrashort Pulse Laser-Material Interaction Using ABAQUS. *J. Manuf. Sci. Eng.* **2009**, *131*, 021005. [CrossRef]
126. Lee, D.; Kannatey-Asibu, E. Numerical Analysis on the Feasibility of Laser Microwelding of Metals by Femtosecond Laser Pulses Using ABAQUS. *J. Manuf. Sci. Eng.* **2008**, *130*, 061014. [CrossRef]
127. Jiang, L.; Tsai, H.-L. An improved two-temperature model for metal thin film heating by femtosecond laser pulses. *Int. Congr. Appl. Lasers Electro-Opt.* **2004**, *2004*, M602. [CrossRef]
128. Davydov, R.; Antonov, V.; Angelina, M. Computer Simulation of Metal Ablation by Single and Multiple Ultrashort Laser Pulses. In *2018 IEEE International Conference on Electrical Engineering and Photonics (EExPolytech)*; IEEE: Piscataway, NJ, USA, 2018; pp. 236–239.
129. Dasallas, L.L.; Garcia, W.O. Numerical simulation of femtosecond pulsed laser ablation of copper for oblique angle of incidence through two-temperature model. *Mater. Res. Express* **2018**, *5*, 016518. [CrossRef]
130. Kuo, L.S.; Qiu, T. *Microscale Energy Transfer during Picosecond Laser Melting of Metal Films*; American Society of Mechanical Engineers: New York, NY, USA, 1996.
131. Fischer, P.; Karapatis, N.; Romano, V.; Glardon, R.; Weber, H. A model for the interaction of near-infrared laser pulses with metal powders in selective laser sintering. *Appl. Phys. A* **2002**, *74*, 467–474. [CrossRef]
132. Konrad, C.; Zhang, Y.; Shi, Y. Melting and resolidification of a subcooled metal powder particle subjected to nanosecond laser heating. *Int. J. Heat Mass Transf.* **2007**, *50*, 2236–2245. [CrossRef]
133. Cheng, C.-W.; Chang, C.-L.; Chen, J.-K.; Wang, B. Femtosecond laser melting of silver nanoparticles: Comparison of model simulations and experimental results. *Appl. Phys. A* **2018**, *124*, 371. [CrossRef]
134. Jia, X.; Zhao, X. Numerical study of material decomposition in ultrafast laser interaction with metals. *Appl. Surf. Sci.* **2019**, *463*, 781–790. [CrossRef]
135. Li, X.; Guan, Y. Theoretical fundamentals of short pulse laser–metal interaction: A review. *Nanotechnol. Precis. Eng.* **2020**, *3*, 105–125. [CrossRef]
136. Ji, P.; Zhang, Y. Melting and thermal ablation of a silver film induced by femtosecond laser heating: A multiscale modeling approach. *Appl. Phys. A* **2017**, *123*, 671. [CrossRef]
137. Wu, H.; Wu, C.; Zhang, N.; Zhu, X.; Ma, X.; Zhigilei, L.V. Experimental and computational study of the effect of 1 atm background gas on nanoparticle generation in femtosecond laser ablation of metals. *Appl. Surf. Sci.* **2018**, *435*, 1114–1119. [CrossRef]
138. Kaden, L.; Seyfarth, B.; Ullsperger, T.; Matthäus, G.; Nolte, S. Selective laser melting of copper using ultrashort laser pulses at different wavelengths. In *Laser 3D Manufacturing V*; Proc. of SPIE: San Francisco, CA, USA, 2018; Volume 10523, p. 1052312.
139. Paeng, D.; Lee, D.; Yeo, J.; Yoo, J.-H.; Allen, F.I.; Kim, E.; So, H.; Park, H.K.; Minor, A.M.; Grigoropoulos, C. Laser-Induced Reductive Sintering of Nickel Oxide Nanoparticles under Ambient Conditions. *J. Phys. Chem. C* **2015**, *119*, 6363–6372. [CrossRef]
140. Kang, B.; Han, S.; Kim, J.; Ko, S.; Yang, M. One-Step Fabrication of Copper Electrode by Laser-Induced Direct Local Reduction and Agglomeration of Copper Oxide Nanoparticle. *J. Phys. Chem. C* **2011**, *115*, 23664–23670. [CrossRef]
141. Jiang, Q.; Zhang, P.; Yu, Z.; Shi, H.; Wu, D.; Yan, H.; Ye, X.; Lu, Q.; Tian, Y. A Review on Additive Manufacturing of Pure Copper. *Coatings* **2021**, *11*, 740. [CrossRef]
142. Roy, N.; Dibua, O.; Foong, C.S.; Cullinan, M. Preliminary Results on the Fabrication of Interconnect Structures Using Microscale Selective Laser Sintering. In *ASME 2017 International Technical Conference and Exhibition on Packaging and Integration of Electronic and Photonic Microsystems*; American Society of Mechanical Engineers: New York, NY, USA, 2017.
143. Singer, F.; Deisenroth, D.C.; Hymas, D.M.; Ohadi, M.M. Additively manufactured copper components and composite structures for thermal management applications. In Proceedings of the 2017 16th IEEE Intersociety Conference on Thermal and Thermomechanical Phenomena in Electronic Systems (ITherm), Orlando, FL, USA, 30 May–2 June 2017; IEEE: Piscataway, NJ, USA, 2017; pp. 174–183.
144. Pogson, S.; Fox, P.; Sutcliffe, C.; O'Neill, W. The production of copper parts using DMLR. *Rapid Prototyp. J.* **2003**, *9*, 334–343. [CrossRef]
145. Sciammarella, F.; Gonser, M.J.; Styrcula, M. Laser Additive Manufacturing of Pure Copper. In Proceedings of the SME RAPID Conference and Exposition, Dearborn, MI, USA, 10–13 June 2013; Volume 71, pp. 1241–1248.
146. Gradl, P.R.; Protz, C.S.; Cooper, K.; Ellis, D.; Evans, L.J.; Garcia, C. GRCop-42 Development and Hot-fire Testing Using Additive Manufacturing Powder Bed Fusion for Channel-cooled Combustion Chambers. In Proceedings of the AIAA Propulsion and Energy 2019 Forum, Indianapolis, IN, USA, 19–22 August 2019. [CrossRef]
147. Polozov, I.A.; Borisov, E.V.; Sufiiarov, V.S.; Popovich, A.A. Selective laser melting of copper alloy. *Mater. Phys. Mech.* **2020**, *43*, 65–71. [CrossRef]
148. Colopi, M.; Caprio, L.; Demir, A.; Previtali, B. Selective laser melting of pure Cu with a 1 kW single mode fiber laser. *Procedia CIRP* **2018**, *74*, 59–63. [CrossRef]
149. Roy, N.; Jou, W.; Feng, H.; Jeong, J.; Wang, Y.; Cullinan, M. Laser Sintering of Copper Nanoparticles: A Simplified Model for Fluence Estimation and Validation. In *International Manufacturing Science and Engineering Conference*; American Society of Mechanical Engineers: New York, NY, USA, 2017.

150. Roy, N.K.; Dibua, O.G.; Jou, W.; He, F.; Jeong, J.; Wang, Y.; Cullinan, M.A. A Comprehensive Study of the Sintering of Copper Nanoparticles Using Femtosecond, Nanosecond, and Continuous Wave Lasers. *J. Micro Nano-Manuf.* **2017**, *6*, 010903. [CrossRef]
151. Lim, J.; Kim, Y.; Shin, J.; Lee, Y.; Shin, W.; Qu, W.; Hwang, E.; Park, S.; Hong, S. Continuous-Wave Laser-Induced Transfer of Metal Nanoparticles to Arbitrary Polymer Substrates. *Nanomaterials* **2020**, *10*, 701. [CrossRef]
152. Mizoshiri, M.; Yoshidomi, K. Cu Patterning Using Femtosecond Laser Reductive Sintering of CuO Nanoparticles under Inert Gas Injection. *Materials* **2021**, *14*, 3285. [CrossRef]
153. Le Harzic, R.; Huot, N.; Audouard, E.; Jonin, C.; Laporte, P.; Valette, S.; Fraczkiewicz, A.; Fortunier, R. Comparison of heat-affected zones due to nanosecond and femtosecond laser pulses using transmission electronic microscopy. *Appl. Phys. Lett.* **2002**, *80*, 3886–3888. [CrossRef]
154. Mizoshiri, M.; Nishitani, K.; Hata, S. Effect of Heat Accumulation on Femtosecond Laser Reductive Sintering of Mixed CuO/NiO Nanoparticles. *Micromachines* **2018**, *9*, 264. [CrossRef] [PubMed]
155. Constantin, L.; Wu, Z.; Li, N.; Fan, L.; Silvain, J.F.; Lu, Y.F. Laser 3D printing of complex copper structures. *Addit. Manuf.* **2020**, *35*, 101268. [CrossRef]
156. Mizoshiri, M.; Kondo, Y. Direct writing of Cu-based fine micropatterns using femtosecond laser pulse-induced sintering of Cu2O nanospheres. *Jpn. J. Appl. Phys.* **2019**, *58*, SDDF05. [CrossRef]
157. Mizoshiri, M.; Kondo, Y. Direct writing of two- and three-dimensional Cu-based microstructures by femtosecond laser reductive sintering of the Cu_2O nanospheres. *Opt. Mater. Express* **2019**, *9*, 2828–2837. [CrossRef]
158. Mizoshiri, M.; Tanokuchi, A. Direct writing of Cu-based micropatterns inside Cu_2O nanosphere films using green femtosecond laser reductive sintering. *Opt. Mater. Express* **2020**, *10*, 2533–2541. [CrossRef]
159. Tan, C.; Zhou, K.; Ma, W.; Attard, B.; Zhang, P.; Kuang, T. Selective laser melting of high-performance pure tungsten: Parameter design, densification behavior and mechanical properties. *Sci. Technol. Adv. Mater.* **2018**, *19*, 370–380. [CrossRef]
160. Li, J.; Wu, Y.; Zhou, B.; Wei, Z. Laser Powder Bed Fusion of Pure Tungsten: Effects of Process Parameters on Morphology, Densification, Microstructure. *Materials* **2020**, *14*, 165. [CrossRef]
161. Iveković, A.; Omidvari, N.; Vrancken, B.; Lietaert, K.; Thijs, L.; Vanmeensel, K.; Vleugels, J.; Kruth, J.-P. Selective laser melting of tungsten and tungsten alloys. *Int. J. Refract. Met. Hard Mater.* **2018**, *72*, 27–32. [CrossRef]
162. Selective Laser Melting (AM), Wolfmet. (n.d.) Available online: https://www.wolfmet.com/applications/slm/selective-laser-melting-tungsten/ (accessed on 25 November 2021).
163. Hirai, T.; Escourbiac, F.; Carpentier-Chouchana, S.; Fedosov, A.; Ferrand, L.; Jokinen, T.; Komarov, V.; Kukushkin, A.; Merola, M.; Mitteau, R.; et al. ITER tungsten divertor design development and qualification program. *Fusion Eng. Des.* **2013**, *88*, 1798–1801. [CrossRef]
164. Müller, A.V.; Schlick, G.; Neu, R.; Anstätt, C.; Klimkait, T.; Lee, J.; Pascher, B.; Schmitt, M.; Seidel, C. Additive manufacturing of pure tungsten by means of selective laser beam melting with substrate preheating temperatures up to 1000 °C. *Nucl. Mater. Energy* **2019**, *19*, 184–188. [CrossRef]
165. Ghosh, S.K.; Das, A.K.; Saha, P. Selective Laser Sintering: A Case Study of Tungsten Carbide and Cobalt Powder Sintering by Pulsed Nd:YAG Laser. *Funct. Graded Mater.* **2015**, 441–459. [CrossRef]
166. Wang, D.; Yu, C.; Zhou, X.; Ma, J.; Liu, W.; Shen, Z. Dense Pure Tungsten Fabricated by Selective Laser Melting. *Appl. Sci.* **2017**, *7*, 430. [CrossRef]
167. Zacharatos, F.; Theodorakos, I.; Karvounis, P.; Tuohy, S.; Braz, N.; Melamed, S.; Kabla, A.; De La Vega, F.; Andritsos, K.; Hatziapostolou, A.; et al. Selective Laser Sintering of Laser Printed Ag Nanoparticle Micropatterns at High Repetition Rates. *Materials* **2018**, *11*, 2142. [CrossRef] [PubMed]
168. Khosravani, M.R.; Reinicke, T. 3D-printed sensors: Current progress and future challenges. *Sens. Actuators A Phys.* **2020**, *305*, 111916. [CrossRef]
169. Courbat, J.; Kim, Y.; Briand, D.; De Rooij, N. Inkjet printing on paper for the realization of humidity and temperature sensors. In Proceedings of the 2011 16th International Solid-State Sensors, Actuators and Microsystems Conference, Beijing, China, 5–9 June 2011; pp. 1356–1359. [CrossRef]
170. Dankoco, M.; Tesfay, G.; Benevent, E.; Bendahan, M. Temperature sensor realized by inkjet printing process on flexible substrate. *Mater. Sci. Eng. B* **2016**, *205*, 1–5. [CrossRef]
171. Hong, S.; Yeo, J.; Kim, G.; Kim, D.; Lee, H.; Kwon, J.; Lee, H.; Lee, P.; Ko, S.H. Nonvacuum, Maskless Fabrication of a Flexible Metal Grid Transparent Conductor by Low-Temperature Selective Laser Sintering of Nanoparticle Ink. *ACS Nano* **2013**, *7*, 5024–5031. [CrossRef]
172. Noh, J.; Kim, D. Femtosecond laser sintering of silver nanoparticles for conductive thin-film fabrication. *Appl. Phys. A* **2020**, *126*, 1–7. [CrossRef]
173. Noh, J.; Ha, J.; Kim, D. Femtosecond and nanosecond laser sintering of silver nanoparticles on a flexible substrate. *Appl. Surf. Sci.* **2020**, *511*, 145574. [CrossRef]
174. Son, Y.; Lim, T.W.; Yeo, J.; Ko, S.H.; Yang, D.-Y. Fabrication of Nano-scale Conductors by Selective Femtosecond Laser Sintering of Metal Nanoparticles. In Proceedings of the 10th IEEE International Conference on Nanotechnology, Ilsan, Korea, 17–20 August 2010; IEEE: Piscataway, NJ, USA, 2010; pp. 390–393.
175. Son, Y.; Yeo, J.; Moon, H.; Lim, T.W.; Hong, S.; Nam, K.H.; Yoo, S.; Grigoropoulos, C.P.; Yang, D.-Y.; Ko, S.H. Nanoscale Electronics: Digital Fabrication by Direct Femtosecond Laser Processing of Metal Nanoparticles. *Adv. Mater.* **2011**, *23*, 3176–3181. [CrossRef]

176. Kimura, T.; Nakamoto, T. Thermal and Mechanical Properties of Commercial-Purity Aluminum Fabricated Using Selective Laser Melting. *Mater. Trans.* **2017**, *58*, 799–805. [CrossRef]
177. Manfredi, D.; Calignano, F.; Krishnan, M.; Canali, R.; Paola, E.; Biamino, S.; Ugues, D.; Pavese, M.; Fino, P. Additive Manufacturing of Al Alloys and Aluminium Matrix Composites (AMCs). In *Light Metal Alloys Applications*; InTech: Rijeka, Croatia, 2014.
178. DebRoy, T.; Wei, H.L.; Zuback, J.S.; Mukherjee, T.; Elmer, J.W.; Milewski, J.O.; Beese, A.M.; Wilson-Heid, A.; De, A.; Zhang, W. Additive manufacturing of metallic components–Process, structure and properties. *Prog. Mater. Sci.* **2018**, *92*, 112–224. [CrossRef]
179. Kannan, C.S.; Chandra, S.S.S.; Krishnan, G.P.; Raj, S.P. *A Review on Additive Manufacturing of AA2024 and AA6061 Alloys Using Powder Bed Fusion*; IOP Publishing: Bristol, UK, 2020; Volume 988, p. 012002.
180. Louvis, E.; Fox, P.; Sutcliffe, C.J. Selective laser melting of aluminium components. *J. Mater. Process. Technol.* **2011**, *211*, 275–284. [CrossRef]
181. Lassance, D.; Fabregue, D.; Delannay, F.; Pardoen, T. Micromechanics of room and high temperature fracture in 6xxx Al alloys. *Prog. Mater. Sci.* **2007**, *52*, 62–129. [CrossRef]
182. Grigoriev, S.N.; Tarasova, T.V.; Gvozdeva, G.O.; Nowotny, S. Structure Formation of Hypereutectic Al-Si-Alloys Produced by Laser Surface Treatment. *Stroj. Vestn.-J. Mech. Eng.* **2014**, *60*, 389–394. [CrossRef]
183. Ullsperger, T.; Liu, D.; Yürekli, B.; Matthäus, G.; Schade, L.; Seyfarth, B.; Kohl, H.; Ramm, R.; Rettenmayr, M.; Nolte, S. Ultra-short pulsed laser powder bed fusion of Al-Si alloys: Impact of pulse duration and energy in comparison to continuous wave excitation. *Addit. Manuf.* **2021**, *46*, 102085. [CrossRef]
184. Dinçel, Y.M. Bone Graft Types. In *Bone Grafting-Recent Advances with Special References to Cranio-Maxillofacial Surgery*; IntechOpen: London, UK, 2018; pp. 27–40.
185. Shivalkar, S.; Singh, S. Solid Freeform Techniques Application in Bone Tissue Engineering for Scaffold Fabrication. *Tissue Eng. Regen. Med.* **2017**, *14*, 187–200. [CrossRef]
186. Duan, B.; Wang, M. Selective laser sintering and its application in biomedical engineering. *MRS Bull.* **2011**, *36*, 998–1005. [CrossRef]
187. Tan, K.; Chua, C.; Leong, K.; Cheah, C.; Cheang, P.; Abu Bakar, M.; Cha, S. Scaffold development using selective laser sintering of polyetheretherketone–hydroxyapatite biocomposite blends. *Biomaterials* **2003**, *24*, 3115–3123. [CrossRef]
188. Masaud, Z.; Khan, M.Z.; Hussain, A.; Ishfaq, H.A.; Song, R.-H.; Lee, S.-B.; Joh, D.W.; Lim, T.-H. Recent Activities of Solid Oxide Fuel Cell Research in the 3D Printing Processes. *Trans. Korean Hydrog. New Energy Soc.* **2021**, *32*, 11–40. [CrossRef]
189. Tai, X.Y.; Zhakeyev, A.; Wang, H.; Jiao, K.; Zhang, H.; Xuan, J. Accelerating Fuel Cell Development with Additive Manufacturing Technologies: State of the Art, Opportunities and Challenges. *Fuel Cells* **2019**, *19*, 636–650. [CrossRef]
190. Pesce, A.; Hornés, A.; Núñez, M.; Morata, A.; Torrell, M.; Tarancón, A. 3D printing the next generation of enhanced solid oxide fuel and electrolysis cells. *J. Mater. Chem. A* **2020**, *8*, 16926–16932. [CrossRef]
191. Bai, S.; Liu, J. Femtosecond Laser Additive Manufacturing of Multi-Material Layered Structures. *Appl. Sci.* **2020**, *10*, 979. [CrossRef]
192. Liu, J.; Bai, S. Femtosecond laser additive manufacturing of YSZ. *Appl. Phys. A* **2017**, *123*, 293. [CrossRef]
193. Furuta, T. Automobile applications of titanium. In *Titanium for Consumer Applications*; Elsevier: Amsterdam, The Netherlands, 2019; pp. 77–90. [CrossRef]
194. Singh, N.; Hameed, P.; Ummethala, R.; Manivasagam, G.; Prashanth, K.; Eckert, J. Selective laser manufacturing of Ti-based alloys and composites: Impact of process parameters, application trends, and future prospects. *Mater. Today Adv.* **2020**, *8*, 100097. [CrossRef]
195. Agius, D.J.; Kourousis, K.I.; Wallbrink, C. A Review of the As-Built SLM Ti-6Al-4V Mechanical Properties towards Achieving Fatigue Resistant Designs. *Metals* **2018**, *8*, 75. [CrossRef]
196. Vorobyev, A.Y.; Guo, C. Femtosecond laser structuring of titanium implants. *Appl. Surf. Sci.* **2007**, *253*, 7272–7280. [CrossRef]
197. Löw, K.; Leong, K.F.; Sun, C. Review of Selective Laser Melting process parameters for Commercially Pure Titanium and Ti6Al4V. In *High Value Manufacturing: Advanced Research in Virtual and Rapid Prototyping*; CRC Press: Boca Raton, FL, USA, 2013; pp. 71–76.
198. Kumbhar, N.N.; Mulay, A.V. Post Processing Methods used to Improve Surface Finish of Products which are Manufactured by Additive Manufacturing Technologies: A Review. *J. Inst. Eng. India Ser. C* **2018**, *99*, 481–487. [CrossRef]
199. Jiao, L.; Chua, Z.Y.; Moon, S.K.; Song, J.; Bi, G.; Zheng, H. Femtosecond Laser Produced Hydrophobic Hierarchical Structures on Additive Manufacturing Parts. *Nanomaterials* **2018**, *8*, 601. [CrossRef]
200. Worts, N.; Jones, J.; Squier, J. Surface structure modification of additively manufactured titanium components via femtosecond laser micromachining. *Opt. Commun.* **2019**, *430*, 352–357. [CrossRef]
201. Cheng, C.W.; Huang, C.J.; Cheng, H.T.; Kuo, C.N. Fabrication of porous Ti structures with nanostructures from Ti powders by femtosecond laser pulses. *J. Laser Micro Nanoeng.* **2015**, *10*, 310. [CrossRef]
202. Hammouti, S.; Holybee, B.; Zhu, W.; Allain, J.P.; Jurczyk, B.; Ruzic, D.N. Titanium nitride formation by a dual-stage femtosecond laser process. *Appl. Phys. A* **2018**, *124*, 411. [CrossRef]
203. Sugioka, K.; Cheng, Y. Femtosecond laser three-dimensional micro- and nanofabrication. *Appl. Phys. Rev.* **2014**, *1*, 041303. [CrossRef]
204. Han, T.-H.; Kim, H.; Kwon, S.-J.; Lee, T.-W. Graphene-based flexible electronic devices. *Mater. Sci. Eng. R Rep.* **2017**, *118*, 1–43. [CrossRef]

205. You, R.; Liu, Y.; Hao, Y.; Han, D.; Zhang, Y.; You, Z. Laser Fabrication of Graphene-Based Flexible Electronics. *Adv. Mater.* **2020**, *32*, e1901981. [CrossRef]
206. Liu, Y.-Q.; Chen, Z.-D.; Mao, J.-W.; Han, D.-D.; Sun, X. Laser Fabrication of Graphene-Based Electronic Skin. *Front. Chem.* **2019**, *7*, 461. [CrossRef] [PubMed]
207. Li, Y.; Feng, Z.; Huang, L.; Essa, K.; Bilotti, E.; Zhang, H.; Peijs, T.; Hao, L. Additive manufacturing high performance graphene-based composites: A review. *Compos. Part A Appl. Sci. Manuf.* **2019**, *124*, 105483. [CrossRef]
208. Chen, Q.; Mangadlao, J.D.; Wallat, J.; De Leon, A.; Pokorski, J.K.; Advincula, R.C. 3D Printing Biocompatible Polyurethane/Poly(lactic acid)/Graphene Oxide Nanocomposites: Anisotropic Properties. *ACS Appl. Mater. Interfaces* **2017**, *9*, 4015–4023. [CrossRef] [PubMed]
209. Fu, X.-Y.; Chen, Z.-D.; Han, D.-D.; Zhang, Y.-L.; Xia, H.; Sun, H.-B. Laser fabrication of graphene-based supercapacitors. *Photonics Res.* **2020**, *8*, 577. [CrossRef]
210. Bi, Y.-G.; Feng, J.; Li, Y.-F.; Zhang, Y.-L.; Liu, Y.-S.; Chen, L.; Liu, Y.-F.; Guo, L.; Wei, S.; Sun, H.-B. Arbitrary Shape Designable Microscale Organic Light-Emitting Devices by Using Femtosecond Laser Reduced Graphene Oxide as a Patterned Electrode. *ACS Photonics* **2014**, *1*, 690–695. [CrossRef]
211. An, J.; Le, T.-S.D.; Huang, Y.; Zhan, Z.; Li, Y.; Zheng, L.; Huang, W.; Sun, G.; Kim, Y.-J. All-Graphene-Based Highly Flexible Noncontact Electronic Skin. *ACS Appl. Mater. Interfaces* **2017**, *9*, 44593–44601. [CrossRef]
212. Wang, D.-Y.; Tao, L.-Q.; Liu, Y.; Zhang, T.-Y.; Pang, Y.; Wang, Q.; Jiang, S.; Yang, Y.; Ren, T.-L. High performance flexible strain sensor based on self-locked overlapping graphene sheets. *Nanoscale* **2016**, *8*, 20090–20095. [CrossRef] [PubMed]
213. Qiao, Y.; Wang, Y.; Tian, H.; Li, M.; Jian, J.; Wei, Y.; Tian, Y.; Wang, D.-Y.; Pang, Y.; Geng, X.; et al. Multilayer Graphene Epidermal Electronic Skin. *ACS Nano* **2018**, *12*, 8839–8846. [CrossRef]

quantum beam science

Review

Making Light Work of Metal Bending: Laser Forming in Rapid Prototyping

Adam L. Bachmann [1,2], **Michael D. Dickey** [2] **and Nathan Lazarus** [3,*]

[1] Fellowship Program at US Army Research Laboratory, Oak Ridge Associated Universities (ORAU), Adelphi, MD 20783, USA; abachma@ncsu.edu
[2] Department of Chemical and Biomolecular Engineering, North Carolina State University, Raleigh, NC 27603, USA; mddickey@ncsu.edu
[3] Sensors and Electron Devices Directorate, US Army Research Laboratory, Adelphi, MD 20783, USA
* Correspondence: nathan.lazarus2.civ@mail.mil

Received: 18 November 2020; Accepted: 10 December 2020; Published: 14 December 2020

Abstract: Lasers can be used to bend 2D metal sheets into complex 3D objects in a process called 'laser forming.' Laser forming bends metal sheets by locally heating the sheets to generate plastic strains and is an established metal bending technology in the shipbuilding industry. Recent studies have investigated the laser forming of thin metal parts as a complementary rapid prototyping technology to metal 3D printing. This review discusses the laser forming process, beginning with the mechanisms before covering various design considerations. Laser forming for the rapid manufacturing of metal parts is then reviewed, including the recent advances in process planning, before highlighting promising future research directions.

Keywords: laser forming; rapid prototyping; self-folding origami; metal bending

---

1. Introduction

Fabricating complex 3D structures is a difficult task, as many materials and processes are inherently 2D. Flat structures need to be carefully assembled to produce the desired 3D shape, whether a ship, an automobile, or a solar array. One of the oldest ways to produce 3D structures from flat objects is origami, the Japanese art of paper folding [1,2]. Origami principles can apply to other sheets of material, often with the goal of assembling the final 3D structure far from the point of production of the 2D pattern [3–5].

Researchers have developed algorithms to achieve complex 3D shapes from 2D fold patterns [6]. These algorithms are not limited to paper, although the algorithms typically neglect the effect of substrate thickness and, thus, work best on materials that are thin and inextensible, like paper. Oftentimes, the desired structures need to be made of materials that have a non-negligible thickness [7,8]. Folding rigid materials is typically done by attaching rigid facets with compliant hinges [9], but this places restrictions on what can be produced, a term called rigid foldability [10]. One of the most common rigid folding patterns is the Miura-ora pattern (Figure 1a,b), as it allows large area structures to be compactly stored before deployment, which is valuable for space applications [5,7,11,12]. In many applications, actuation (folding) is done manually (Figure 1c,d) [13]; however, researchers are exploring ways to create hinges that fold in response to external stimuli (e.g., light, electricity, heat, moisture), allowing for self-folding (Figure 1e) [3,14–17].

Origami manufacturing using computational design algorithms is a relatively new method for rapid prototyping. Rapid prototyping is defined as the direct translation of computer aided design (CAD) files into 3D objects, with 3D printing the most common approach [18]. Three-dimensional printing is a popular technology that additively builds objects through the layered deposition of material [19,20]. 3D printing allows highly customized metal parts to be fabricated with minimal waste (Figure 1f), making it an attractive technology for 'mass customization' [21]. Many metal 3D printing methods use a focused energy beam (laser or electron beam) to fuse metal powders together, building the part layer by layer, but the process is long and has a limited build volume [20,22,23] and metal 3D printers are also relatively expensive (to the order of hundreds of thousands of dollars for a commercial printer) [23]. The unfused powder acts a support, allowing pieces to be built with moderate overhangs, but sharp bends remain challenging [23], as well as thin shells [24]. Origami folding, which allows rapid and cheap creation of 3D shells of material, is therefore an important complementary technology, well-suited for many devices, such as antennas, waveguides, and other systems that rely on thin layers of metal. Thin metal sheets are easy to bend, and overhangs can be generated with almost any degree of bend angle, enabling the production of complex shapes with simple folds and cuts (Figure 1g).

Successful metal origami requires precise control over the bending of the sheets of metal. There are multiple ways to bend metal, the most common methods use expensive equipment, such as press brakes (Figure 2a), or roll formers (Figure 2b) [25–27]. Press brakes involves placing the sheet metal over a shaped die and then applying intense mechanical pressure to force the metal into the die. Roll forming involves the gradual bending of the sheet metal by passing through successively narrower rollers. Both processes rely on mechanically deforming the sheet, which leads to a spring-back effect that causes the final bend angle to differ from the dies and rollers, as a result of residual elastic strains after the mechanical pressure is removed [28–31]. Proper control for spring-break often involves extensive testing of how the brakes and substrates interact [29]. A change of design shape or material means this testing would need to be repeated, making this a poor choice for rapid prototyping.

Another method of metal bending involves thermal stress-induced bending called line heating [34]. Line heating uses a gas torch to carefully heat a piece of metal followed by cooling the part rapidly in water to generate plastic strains that bend the metal. This process, unlike press break forming, is highly labor intensive. Line heating also depends on the craftsmanship of the bender, since the gas torch is a diffuse heat source, which can lead to large heat-affected zones and degraded material properties [35]. Aiming to automate this process, researchers suggested replacing the skill of a bender and flame torches with the highly controllable heat of a laser [35]. The process is similar to line forming, but uses lasers to localize the heating. Thus, these early researchers called this process 'laser forming' [36,37].

Laser forming is defined as the use of a laser beam to locally heat and introduce thermal stresses to plastically deform a work piece [38]. The interaction of a laser beam and a substrate generates localized thermal gradients (Figure 2c) [36,37] that cause unequal material expansions. The thermal expansions generate stresses large enough to cause the heated material to yield, generating plastic response stresses [39,40]. As the piece cools, the scanned area returns to its normal size and stops straining the surrounding material, but the compressive stresses remain leading to a permanent deformation in the substrate without a spring-back effect [37]. Laser forming consists of several related mechanisms, and is most commonly used for bending but can also be used for shortening/adjusting a work piece [41,42].

While this review uses the term "laser forming" for thermal metal forming processes, as accepted in the related research community, we want to address potential confusion in terminology. Another technique also used for laser bending is laser peen forming (also known as laser shock forming). In laser peen forming (Figure 2d), a short-pulsed laser is focused on a sacrificial coating on top of the workpiece [43]. When the coating ablates, it generates a plasma plume that attempts to expand in all directions [43]. The laser peen forming setup confines this expanding plume, usually with a layer of water, and redirects this energy as a shockwave into the workpiece, leading to bending [43]. This process is entirely mechanical and, thus, susceptible to the similar drawbacks of more conventional fabrication. A recent review of the field can be found elsewhere [44], and this approach will not be covered further here. The term 'laser forming' has also been used by researchers in reference to other technologies based on producing (i.e., forming) a material with a laser, including powder bed fusion [45], or laser metal cladding (Figure 2e) [46]. Both techniques use a laser to selectively heat metal powders, causing them to coalesce, but 'laser forming' is not the preferred terminology in those fields.

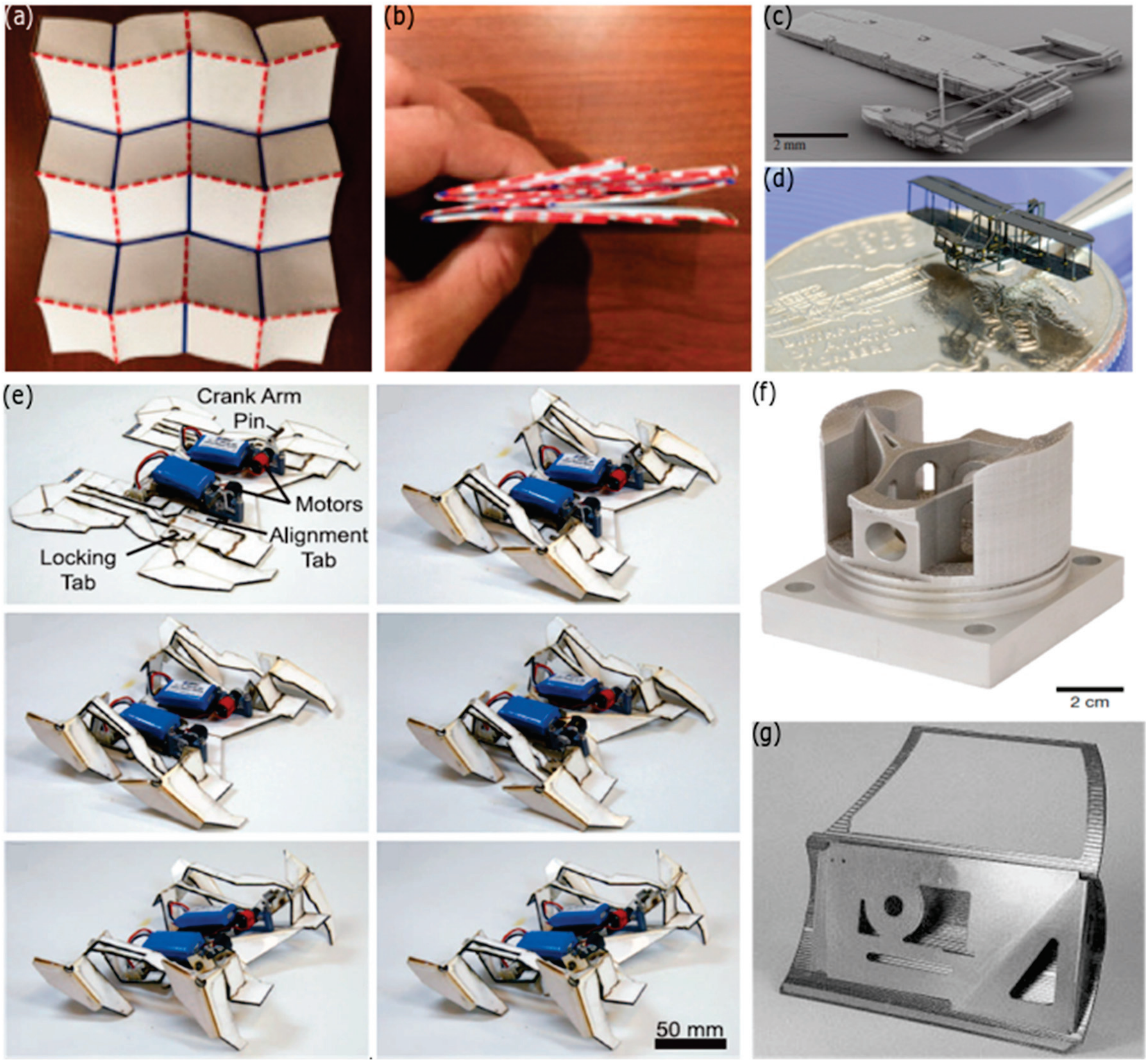

Figure 1. Complex 3D origami requires fold patterns such as the Miura-ori, which compresses a (**a**) large sheet in the unfolded sheet into a (**b**) compact folded state [1]. Copyright SAGE publications, 2016. Origami principles can be used to produce complex structures. A (**c**) folded microelectromechanical systems (MEMS) structure becomes a (**d**) scale replica of the Wright flyer once the unfolding is complete [13]. © IOP Publishing. Reproduced with permission. All rights reserved. Self-folding (**e**) has been used to produce crawling robots from flat sheets [3]. Reprinted with permission from AAAS. Rapid prototyping of metallic 3D structures can be done with (**f**) 3D printing [32]. Reprinted with permission from Springer Nature, copyright 2017. Metal products can also be formed by the (**g**) laser forming of sheet metal [33]. Reproduced with permission from Emerald Publishing, copyright 1997.

Laser forming was first developed in the 1980s [35], and much of the early research was focused on understanding the complex interaction between the laser and the material properties with a goal of developing formulas that can accurately predict the final bend angle [37,48,49]. A number of studies now exist on modelling of laser forming, including a notable review [38], so we refrain from focusing on these research efforts here. Instead, we aim to survey laser forming as a rapid prototyping strategy for developing 3D structures from flat substrates. The most recent review focusing on the manufacturing applications of laser forming is almost two decades old [50], and there have been many advances in the field since then.

This review of laser forming begins with a discussion of the three dominant sub-mechanisms of laser forming, before discussing how to select appropriate process parameters to achieve a desired bend shape. We then survey the application space of laser forming, from larger scale fabrication to smaller scale rapid prototyping and adjustment, before providing an outlook on current challenges and unresolved problems in the field.

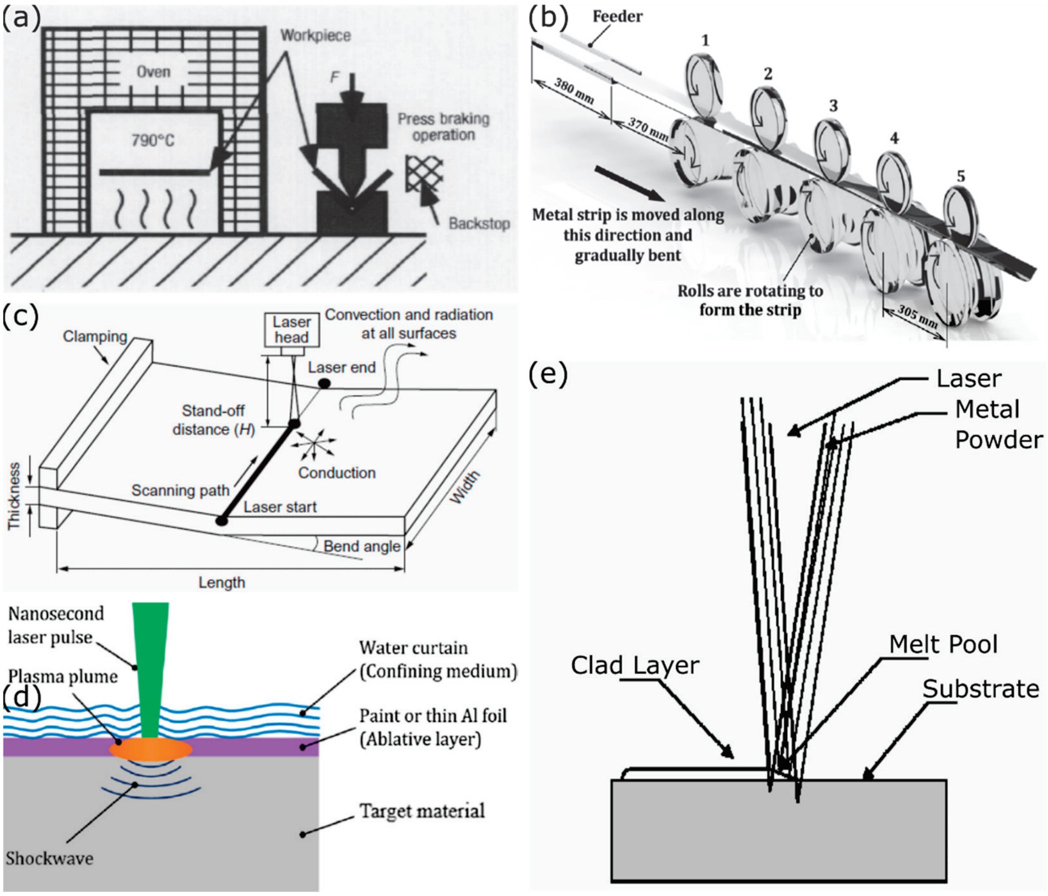

Figure 2. Common metal forming techniques include (**a**) press brake forming [27] over dies to produce sharp bends. Brittle materials, such as titanium, require a preheating step to exceed the ductile-brittle transition temperature, so they can be bent without breaking. Reprinted with permission of Elsevier, copyright 2000. Long sheets of metal can be (**b**) roll formed [31] to generate pieces with a constant cross-section. Reprinted with permission of Elsevier, copyright 2000. Laser forming is term that is commonly used to describe many processes, but is used in this review to refer to (**c**) the process by which a laser-induced thermal gradient generates plastic stresses in a workpiece that leads to a permanent deformation [47]. Reprinted with permission of Elsevier, copyright 2016 Some other process that are sometimes (erroneously) referred to as laser forming include (**d**) laser peen (shock) forming [44], where a laser-induced shockwave mechanically deforms a workpiece. Reprinted with permission of Elsevier, copyright 2018. Some author have also used laser forming to describe (**e**) laser metal cladding [46]. Reprinted with permission of Taylor and Francis, copyright 2000.

2. Laser Forming Mechanisms

Laser forming is a relatively broad term that refers to the plastic deformation of a workpiece resulting from laser-induced thermal stresses. From experimental studies and finite element modelling of laser forming, three main sub-mechanisms have been identified for understanding laser forming: the temperature gradient mechanism (TGM), the buckling mechanism (BM), and the upsetting (shortening) mechanism, (UM) [36–38]. All three mechanisms arise from plastic strains generated in the work piece as a result of the absorbed laser energy, but the dominance of one mechanism over the others depends on how that energy propagates in the work piece [51]. This energy propagation depends on the workpiece geometry and the lasing parameters.

2.1. Temperature Gradient Mechanism (TGM)

The temperature gradient mechanism is dominant when a thermal gradient is generated through the thickness of the work piece through laser heating [37]. This vertical gradient is achieved with a higher laser scan speed and a thicker substrate (or a thinner substrate with relatively poor thermal conductivity) [52]. The thickness of the material in the TGM case is typically on the order of the laser beam diameter [53,54]. For example, a researcher laser formed sheets between 0.5 and 4 mm thick, using a laser with a beam diameter of 5.2 mm travelling at 1.5 m/min [52]. Once the laser energy is absorbed by the surface of the metal, the temperature rises rapidly (Figure 3a). In most materials, the hotter areas expand, generating stresses on the cooler sections [55]. As the top of the workpiece is much hotter than the bottom, the top of the workpiece expands more than the bottom, leading to a small counter-bend (Figure 3b) away from the laser [38,52]. At these high temperatures, the mechanical properties, such as the Young's modulus, drop precipitously [56]. At these elevated temperatures, the thermal expansion stresses exceed the flow stress, which means the thermal stresses are large enough to maintain plastic deformation [36,39,40]. The work piece surrounding the thermally expanded portion is stiff and resists the expansion by exerting an equal compressive force [52,55]. Initially, the material bends away from the laser (the counter-bend), and is a consequence of the thermal expansion combined with the decreased yield stress of metals at higher temperatures [36]. Once the piece has time to cool, the material scanned by the laser returns to its normal volume, but the compressive stresses remain in the piece. Consequently, the laser scanned volume is under compression causing the work piece to develop a final bend angle, θ, toward the laser [36,50]. At the cooler temperatures, the mechanical properties return to their higher values which prevents the formation of new plastic stresses, so this bend angle is permanent [38,52,55]. The TGM mechanism, therefore, always results in a bend toward the laser source.

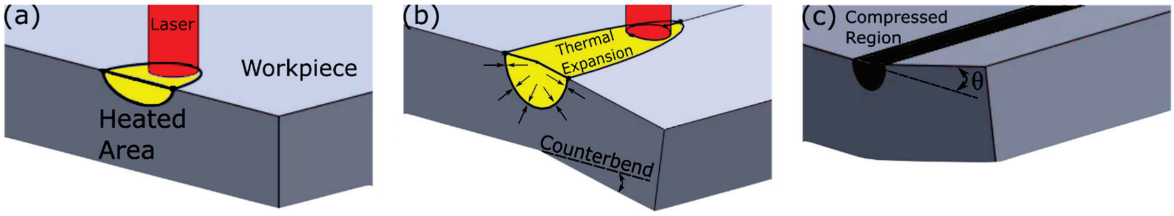

Figure 3. Schematic of the temperature gradient mechanism during the immediate laser exposure (**a**) showing the thermal gradient established through the thickness of the substrate, while (**b**) the thermal expansion causes a counter-bend that also generates plastic, compressive strains. After the laser has passed and the area locally cools, (**c**) the compressive forces remain, causing the substrate the bend toward the laser and generating a bend angle, θ.

2.2. Buckling Mechanism (BM)

The buckling mechanism also relies on a thermal gradient, but in this mechanism, the work piece is either thinner or has a high thermal conductivity relative to the laser scan speed [36]. The first report of laser forming using the buckling mechanism used a laser beam with a diameter of 0.12 mm traveling at 5 mm/s to laser form 0.1 mm thick steel foils [57]. In this case, there is essentially no temperature gradient through the thickness of the substrate, but rather, the thermal gradient spreads outward from the scan line (Figure 4a) [57]. This means the resulting compressive forces are pushing against each other, generating a buckling instability (Figure 4b) [57]. Consequently, the work piece can bend either toward or away from the laser (Figure 4c) [57]. As an instability, the bending direction should be random, but this assumes the sheet has no residual stresses prior to laser forming [57]. Commercially available materials have a complex internal stress state, because of the hot and cold working that the sheet experiences during manufacturing, and this stress state determines the buckling direction [58]. Complete knowledge of this stress state would allow the bending direction to be predicted [57,58], though this is usually unknown. Beyond predicting the bending direction, researchers have also developed ways to control the buckling direction. Such methods include pre-bending the metal sheet [52,59], or through judicious choice of the lasing parameters [60,61]. The ability to generate bidirectional bending expands the design space for laser forming [62,63], without the need for human input, i.e., flipping the work piece [50]. As bending with the buckling mechanism can occur both toward and away from the laser, there can be some ambiguity which mechanism is occurring. Downward bending currently remains the best confirmation that buckling is occurring, because the TGM only bends the workpiece toward the laser. It has been reported that buckling can lead to larger bend angles per pass [57,58], which suggests the bend angle can be another way to differentiate the mechanisms, though visual downward bending is the easier method.

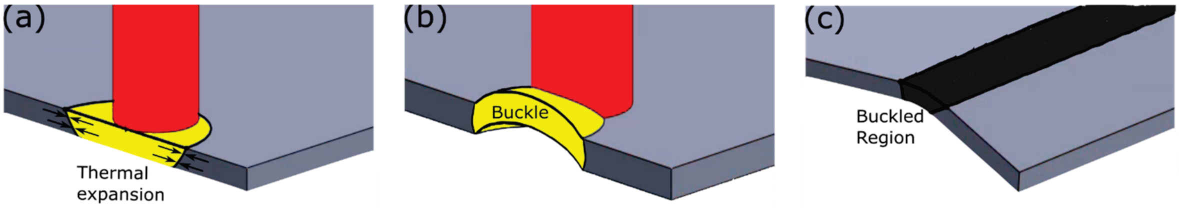

Figure 4. When laser forming thinner materials, the thermal gradient is unable to be established through the thickness of the material, so (**a**) the material expands outward. The compressive forces (**b**) are pushing opposite of each other, causing the workpiece to buckle. Once the buckling has formed, it (**c**) propagates and leads to bending in the direction opposite to the buckle. As the buckle is an instability, it can buckle in either direction.

2.3. Upsetting Mechanism (UM)

The third mechanism of laser forming is the upsetting mechanism [37,64]. The upsetting mechanism begins in a similar manner to the buckling mechanism. The laser scan speed is kept low to prevent a thermal gradient from developing through the thickness of the substrate, generating similar stresses to the buckling mechanism [54]. In the upsetting mechanism, however, the substrate is much stiffer along the scan path, preventing an out-of-plane bend [36,64] (Figure 5). This stiffness can be the result of using a thicker workpiece or one where the material has a higher Young's modulus [50]. Since the flow stress has been reached, but the substrate is unable to bend, the laser scan path becomes locally thicker and the substrate becomes, consequently, shorter [42]. One of the more comprehensive studies on the upsetting mechanisms reliably shortened 2 mm thick steel plates using 12 mm laser beams scanning at speeds around 1 mm/s [51]. The upsetting mechanism allows for in-plane substrate adjustments, which expands what shapes are laser formable by producing a change in the Gaussian curvature [53,65].

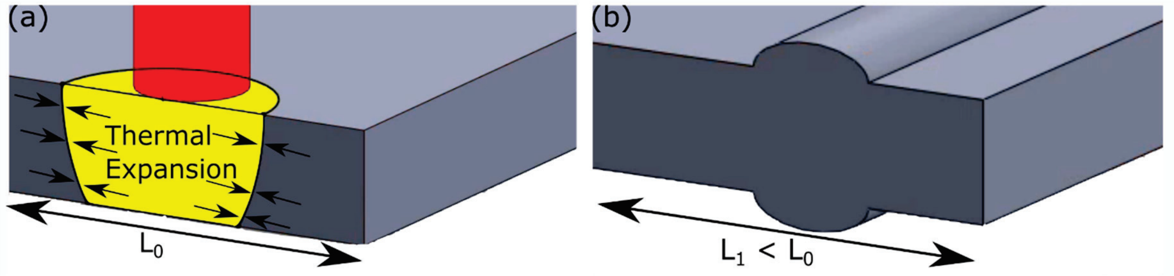

Figure 5. A slow laser scan speed (**a**) is used to minimize the thermal gradient through the thickness of the workpiece. Instead, the thermal gradient is established horizontally. The plastic compressive forces that resist the thermal expansion are insufficient to cause buckling, as the bending moment is too large. This results in the (**b**) scanned area locally thickening. Since volume is conserved, the workpiece shortens and changes its Gaussian curvature.

2.4. Coupling Mechanism

Some recent reports have suggested that the three mechanisms described above are not sufficient to capture the full range of experimental results, so they have proposed a coupling mechanism that combines both TGM and the upsetting mechanism [51,64,66]. This combination of forming mechanisms was already discussed [36,57] in early reports, but was not considered a separate mechanism. The proposed coupling mechanism is a consequence of the mechanisms above being idealized, limiting cases. As the laser forming parameters are adjusted, it is reasonable that the other mechanisms might start to play an increasingly important role, especially near the transition region between TGM and buckling [36]. For this reason, the proposed coupling mechanism will not be treated as a distinct mechanism of laser forming here, but it is still important to consider when designing a laser forming process, and is even useful for laser forming certain structures [66].

3. Design Considerations for Laser Forming

3.1. Laser and Substrate Selection

Since its first reports, laser forming has been used to bend sheets of common metals, such as stainless steel [67–69] and aluminum [70–72], out of plane without mechanical inputs [36,37,67]. As the understanding of the process developed, more varied substrates were explored such as titanium, [27,73] and copper alloys [74,75], hoping to develop new ways to form 3D structures for aerospace and electrical applications. Researchers have also explored laser forming on non-metallic substrates and have bent typically brittle materials such as silicon [76–78], ceramics [41,79], and glass [79,80]. More recently, there have also been demonstrations of the laser forming of more complex structures, such as metal foams [81,82] and laminates [83]. Despite the success of laser forming non-metals, metal bending has remained the primary application of laser forming, due to the use of metals as engineering materials in applications such as ship hulls [35,54,84]. There have also been some reports of laser forming of a limited number of polymers [85,86], although polymer laser forming remains relatively rare. Laser forming, therefore, is a general process reliant on controlled heating to generate plastic stresses, and appears possible for most materials. Large bending angles are more readily realized in metals as their ductility helps avoid crack formation at the bend line, [80,82] though experimental results suggest that the maximum bend angle is a strong function of material thickness with thinner samples being able to demonstrate larger bend angles [79,82,87]. Studies of many of the more well-studied substrates have been able to demonstrate deformation by all three mechanisms. Laser forming of the more exotic materials tends to be realized using the TGM, [76,80,82] though BM has been demonstrated in glass [79] and UM in silicon.

Critical to the success of the laser forming process is appropriate coupling of the laser energy to the material being formed. This coupling can be achieved by selecting the appropriate laser wavelength that corresponds to the absorption maximum of the substrate [75,88], by using a much higher power laser, so sufficient energy is absorbed by the substrate even with low absorptivity, or by using an absorbing coating layer that is matched with the laser wavelength being used (Figure 6) [85,89]. Metals thicker than 100 nm are optically opaque [90] and do not transmit appreciable amounts of light, so the metal substrates that have been used in laser forming will primarily either reflect or absorb the laser energy. The percentage of the incoming laser energy that is reflected is called the reflectance and these values have been measured as a function of wavelength [91]. The most common lasers [27] used for laser forming are Nd:YAG lasers that operate at 1.064 μm [57,58,76,78,85,86,92,93] and CO_2 lasers that emit at 10.6 μm [39,50,54,68,89,94–96]. CO_2 lasers are common in industrial setting, as they were one of the first gas lasers developed [97] and exhibit a high energy efficiency, while operating as a continuous-wave mode at high average powers (>1 kW); however, their absorption into metals is low and an absorbing coating is often required. Nd:YAG lasers are popular in industry as the 1.064 μm output wavelength is better absorbed by metals for cutting and welding, so absorbing coatings are not needed.

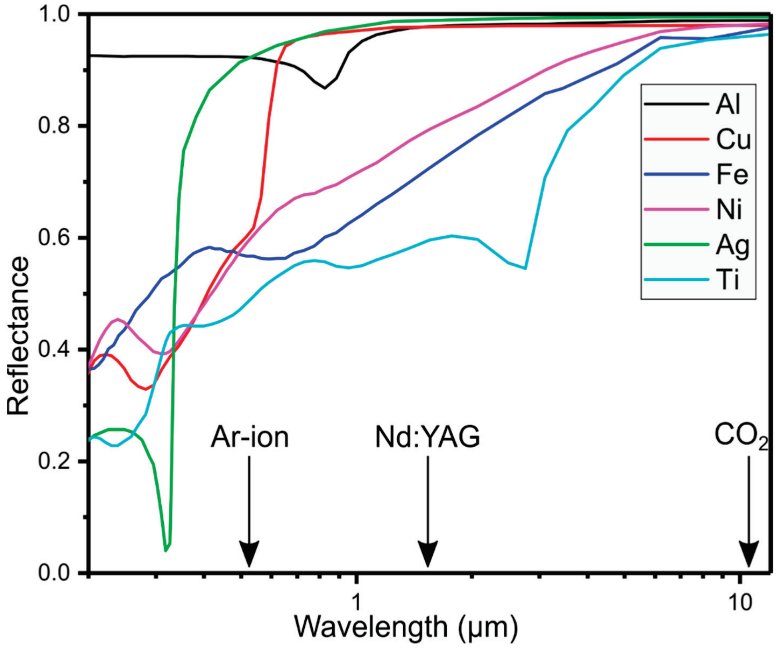

Figure 6. The spectral reflectance of metals, plotted from the data in [91], with the wavelength of some common lasers also identified. Almost all metals are entirely reflective to the 10.6 µm light of CO_2 lasers, while metals tend to be less reflective to the 1.064 µm light of the Nd:YAG laser, though copper, aluminum, and silver are still fairly reflective. Copper has a much higher absorbance to the 514 nm beam from an Ar-ion laser.

The early reports focused on using high power (>1 kW) lasers [40,60,61,70,71,98–103], as the intent was to bend large sheets as part of the ship building process [35]. The laser forming of thinner substrates enables the use of lower power (<100 W) lasers, such as those found in commercial metal marking laser systems [57,63,67,76,85,88,93,104].

Studies on the laser forming of plastics took advantage of the high transmissivity of high-density polyethylene (HDPE) to the wavelength of the Nd:YAG laser [85,86]. The laser energy was absorbed by a resinous black coating applied to the surface of the plastic. The laser power was kept low and the scan speed high, to ensure that the bending occurred through the temperature gradient mechanism, which reliably generates bending toward the laser. As expected, this was observed when the resin was on the side of the plastic exposed to the laser. With the same process parameters, but the coating placed on the opposite side, the plastic was reliably bent away from the laser. This downward bending should not be possible if using the TGM, but the optical transparency of HDPE to the laser made the system behave as if it was exposed to a laser on the underside and the TGM was causing the plastic to bend that direction. This same technique could be adopted for laser systems with multiple wavelengths, as glass absorbs the radiation from a CO_2 laser, but is transparent to the light from a Nd:YAG laser. Thus, sealed metal structures could still be bent if there is a glass window for the laser to pass through [105]. As seen in Figure 6, some metals, such as copper, are highly reflective to the fundamental wavelength of the Nd:YAG laser (1.064 µm). Consequently, laser forming copper with a Nd:YAG laser requires a substantially higher power or the use of a different wavelength. Recently, laser forming was demonstrated with other laser systems that might be commonly found in research environments, such as fiber lasers [106], exciplex lasers [74], and even Ar-ion lasers [67], which expand the substrate choice for laser forming.

Once the appropriate laser/substrate matching has been done, judicious selection of process parameters is essential to the laser forming process, as the laser power and scan speed control which mechanism is dominant [37]. Typically, laser power is kept low and speeds high to ensure that the substrate is being bent by the TGM, generating reliable bending toward the laser. As the TGM only generates a bend of one or two degrees per pass or less [38,74,101], many passes are needed to create structures with large bend angles, sometimes taking as many as 150 passes to produce a full 90 degree bend [88].

3.2. Cooling Effects in Laser Forming

To ensure that the same thermal gradient is established with each laser pass, an appropriate cooling time must also be built into the laser forming process. Consistent laser forming requires that the workpiece be cooled to the same thermal state in between each laser pass. The majority of laser forming setups use free convection with the surrounding air to cool the workpiece, which is relatively slow and leads to a pronounced increase in processing time (Figure 7a). In fact, cooling can be the longest part of a laser forming process [52,59,86,107]. To reduce the processing time, researchers have proposed multiple methods for forced cooling such as forced convection with compressed gas streams aimed at either side (Figure 7b) [92,108], passive water cooling with the bottom of the workpiece being placed in a water bath (Figure 7c) [109–111], and forced liquid cooling, such as a circulated cooling fluid placed in contact with the bottom of the substrate (Figure 7d) [112–115]. All these methods showed a pronounced reduction in the total processing time, as the workpieces cooled to room temperature in a matter of seconds, with active water cooling showing the largest reduction in processing time.

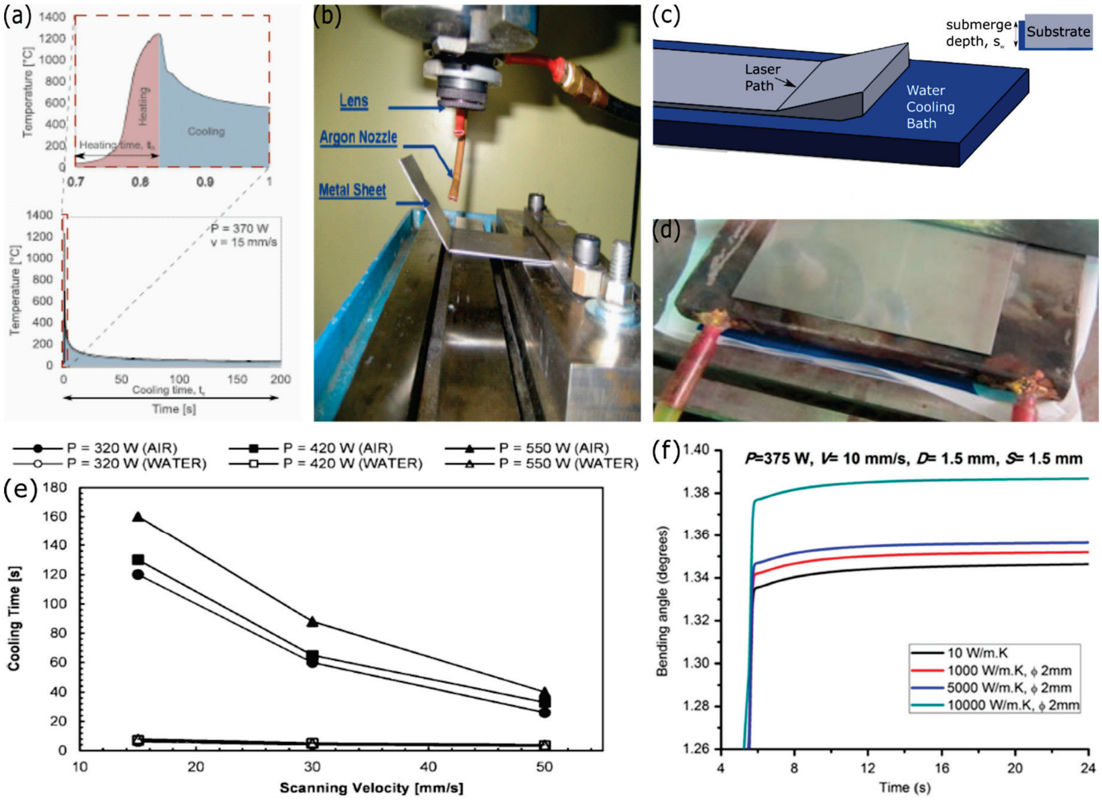

Figure 7. Most of the processing time (**a**) while laser forming is cooling the workpiece back to its initial state after each laser pass which is usually done by free convection [114]. Reprinted with permission from Springer Nature, copyright 2015. This time can be reduced by building in other cooling mechanisms, such as (**b**) forced air cooling [92], (**c**) passive water cooling [109] on the unexposed side, or (**d**) forced liquid cooling [115]. (**b**) Reprinted with permission from Elsevier, copyright 2013 (**d**). Reprinted with permission from Cambridge University Press, copyright 2017. Passive water cooling leads to a (**e**) dramatic reduction in cooling time for most processing conditions [109]. Reprinted with permission from Springer Nature, copyright 2012. Sometimes, cooling offers a small increase (**f**) in the bending angle achieved per pass [112]. Reprinted with permission from Springer Nature, copyright 2017.

Active cooling systems are not typically desirable when designing manufacturing processes, as they require pumps that increase both capital and operating costs of the process, but they are acceptable if the active cooling offers a substantial decrease in processing time or improvement in the reliability of a process. Fortunately, passive water cooling has also been demonstrated to provide sufficient reductions in processing time (Figure 7d) that active cooling may not be needed [109]. Some researchers have reported that forced cooling can lead to an increased bend angle per pass (Figure 7e) under the same lasing conditions, but reports differ on how pronounced this effect is, with some arguing there is no measurable effect [35,108,109,112,113]. Overall, integrated cooling systems offer a way to increase the throughput of laser forming by greatly reducing the time needed to establish thermal equilibrium in between laser passes for multi-pass forming.

The processing time can be further decreased by using the buckling mechanism as buckling is capable of generating larger bending angles per pass than the TGM, because more energy is put into the workpiece [56,57]. Typically, laser forming using the buckling mechanism is avoided as the mechanism is fundamentally an instability and so the workpiece can bend either toward the laser or away from it [57]. This instability is theoretically random but can be controlled by multiple factors, such as external loads [57,104], or the relaxation of internal stresses that exist because of the cold-working of common metal sheets [57]. The main reason to use the buckling mechanism is the downward bending, which greatly broadens the number of structures that can be laser formed [59,61].

3.3. Macro-Scale Laser Forming

Early research efforts were focused on macro-scale laser forming of sheet metals that are millimeters thick [35,50,103]. Among the macro-scale design targets were ship hulls [35,84], fuselage panels [70], and car doors (Figure 1g) [33]. These structures highlight different uses for laser forming in a manufacturing environment, as ship hulls and fuselage panels are low-volume parts, whereas car doors are high-volume components. Laser forming is considered less desirable for manufacturing high-volume metal parts, as it cannot compete with the speed of conventional methods, because the laser forming process is dominated by the cooling time needed between laser passes [33,50,52,114].

Both high-volume and low-volume products need to be joined to other parts, which is the second use for laser forming in manufacturing of macro-scale objects. Metal parts are often joined via welding, which can introduce distortions and lead to misalignment [35,116]. These distortions arise from two main contributions. First, the high heat of welding introduces thermal stresses similar to laser forming [116]. Second, the heat of welding releases stored plastic strains that result from mechanical forming [35]. While the distortions from welding are often small, they still need to be corrected, and laser forming offers a way to address these problems in a process known as hybrid laser forming [50,54,117,118]. Accurate manipulation of metals near weld lines is, however, challenging, because the local weld distortion is not uniform due to the complex stress state generated during welding [119].

The ability to shape large 3D objects using only a laser offers promising opportunities, such as remote deployment, the production of replacement parts where they are needed rather than at a centralized facility and shipped. In the 1980s, it was proposed that laser forming would be a valuable technology in space [103]. A laser system is more compact than a hydraulic press and the high energy efficiency of CO_2 and diode lasers lowers the energy consumption required for metal bending. Laser systems also offer the potential for cutting the workpiece [59] and joining [120] it with other pieces that traditional press brakes do not, making laser systems valuable for areas with minimal electricity generation or limited space.

3.4. Laser Forming Curved Surfaces

Ship hulls are an example of a doubly curved structure and so researchers needed to design methods of introducing curvature into laser formed parts [53]. Currently, there are two main methods for developing curvature in laser formed parts. The first is to make multiple bend lines close to each other [33,68,121], approximating a smooth curve as the limit of many bend lines close together (Figure 8d). By adjusting the distance between the laser passes, bends of varying curvature are able to be produced, as the heat affected zone is not limited to the laser pass line [68]. As this curvature is produced by simple bends, the resulting structures are considered developable surfaces [65]. Developable surfaces are the family of surfaces that can be produced by transforming a plane as long as the Gaussian curvature remains unchanged (Figure 8a) [65]. This means bending, rolling, and cutting are permitted, but stretching or compressing a region are forbidden [65]. As developable surfaces are produced from bending and folding, much of the knowledge gained in origami engineering is applicable to producing structures with laser forming [1,14,26,122,123].

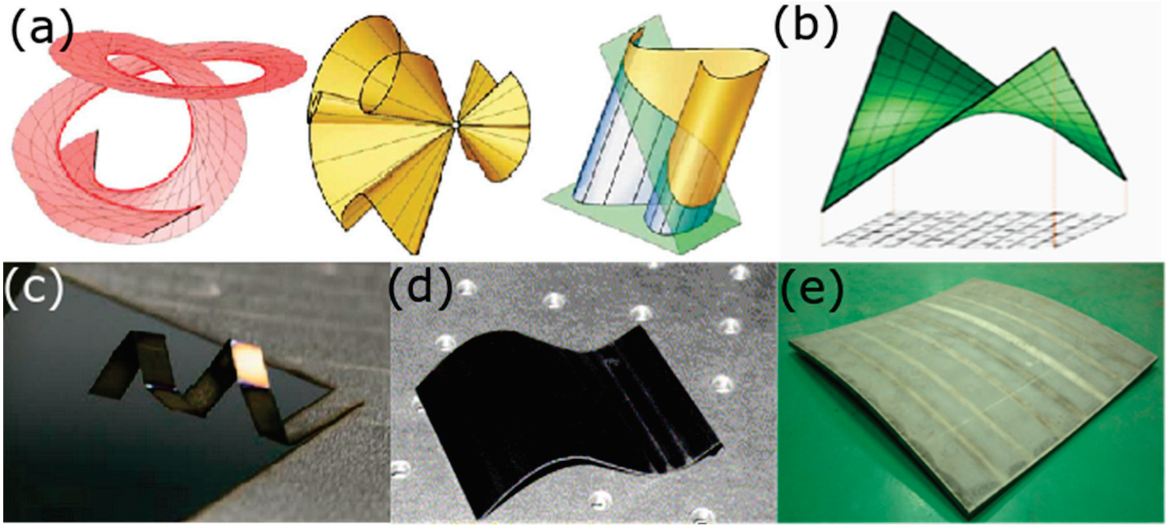

Figure 8. Some (**a**) developable surfaces [65] which are surfaces with zero Gaussian curvature, which means they can be produced from flat sheets, while non-developable surfaces, such as the (**b**) hyperbolic paraboloid [65] or "saddle shape", cannot be formed by bending and cutting inelastic sheets, as they have a non-zero Gaussian curvature. (**a**,**b**) Published under a CC BY License. Laser forming with the temperature gradient mechanism (TGM) or buckling mechanisms can produce developable surfaces, such as (**c**) a coil [59] or (**d**) a cubic spline curve [99], which only require simple bends to produce from a metal sheet. (**d**) Reproduced with permission from Elsevier, copyright 2003. The upsetting mechanism causes a shortening of the workpiece, which changes the Gaussian curvature, so (**e**) a doubly curved saddle shape can be successfully laser formed [84]. Reproduced with permission from Elsevier, copyright 2013.

The second method to produce curved structures relies on the upsetting mechanism that produces in-plane strains [53]. These planar strains cause local distance to be distorted, changing the Gaussian curvature of the workpiece [53,124], which simple bending does not. Since the strain changes the Gaussian curvature, the final workpiece is considered a non-developable surface,, as developable surfaces have zero Gaussian curvature [65]. Non-developable surfaces include hyperbolic paraboloids (Figure 8b) and hyperboloids, which are often called saddles (Figure 8e) [53,84] and pillows [53], respectively, in the laser forming literature. The ability to generate these surfaces from flat sheets using laser forming greatly expands the design space of 3D structures that can be rapidly prototyped.

While the majority of laser forming research has been done on planar substrates, some researchers have investigated laser forming as a means to bend metal tubes for heat exchangers and engines [40,125–127]. Laser formed tubes bend toward the laser, though researchers disagree about what mechanism is causing the bending. Some suggest the TGM is causing the bending [126], while others suggest that the stiff nature of metal pipes means that the upsetting mechanism is dominant, leading to a local shortening, which causes the tube to bend toward the laser without a spring-back effect [40,128]. Like the laser forming of sheets, laser tube bending is a highly flexible method that does not require specially designed dies. This makes laser tube bending valuable for rapid prototyping, as well as low volume, customized production [126]. When bending tubes, it is important to consider the distortion of the tube cross-section, or ovalization [40]. Multiple reports have confirmed that laser tube bending tends to produce less ovalization than mechanical bending, as the laser induced stresses are less than the mechanical forces used when cold bending the tubes [40,126].

Matching the optical absorbance of the substrate with the laser output allows the energy to couple more effectively, lowering the laser power required for successful laser forming. As lower powered (<100 W) laser cutting systems proliferated, researchers hoped to use these systems for laser forming as well as laser cutting. Laser cutting requires high laser fluences, so the beam size needs to be small to achieve clean cuts. Since the output power is lower, the fluence is kept high by decreasing the spot size. For successful laser forming, the laser spot size is typically the same order of magnitude as the substrate being bent which has led researchers to experiment with the laser forming of smaller and thinner substrates [67,72,129].

3.5. Micro-Laser Forming

Complex, 3D silicon microstructures are difficult to produce because silicon is a brittle material that requires high temperatures and specialized tools to produce the desired shape [130]. Laser forming has been applied to adjusting silicon microstructures [76]. The precise control of heating enables silicon microstructures to be bent out of plane, even with more thermally sensitive components, as long as the thermally sensitive components are not located near the laser scan path. Laser forming is not heavily used for the rapid prototyping of MEMS structures, but has been found tremendously successful as a quality control technique called laser micro-adjustment [64,131]. Laser micro-adjustment is a valuable application of laser forming, as evidenced by the industrial adoption of the technique [41,131,132].

Laser micro-adjustment uses a laser to make submicron final adjustments to microstructures [106,133]. Any of the mechanisms can be used for this adjustment, but the smaller bending angle per pass makes the TGM preferable to the buckling mechanism for out-of-plane bends [38,64]. The upsetting mechanism is useful for shortening the workpiece locally which has been used for aligning actuators [42,133]. The laser forming mechanism can be easily determined by adjusting the lasing parameters [36], but the size of the sheets being micro-adjusted makes edge effects more common [134], and increases the coupling between the TGM and the upsetting mechanism [64,101,106,135]. This coupling leads to both in-plane shortening and out-of-plane bending, which is especially common in actuators. Bridge actuators are micromechanical structures that hold functional components and allow fine adjustments to the final positioning to be made. Bridge actuators are produced by removing most of the structural material in a small area, so that they are connected by thin strips called bridges. When laser forming a two-bridge actuator, the scan path effectively creates two hot and two cold sides, the usual irradiated and unirradiated sides of the work piece, as well as a hot bridge and a cold bridge. The usual irradiated sides produce the out of plane bending, while the hot bridge causes an in-plane bend [42,135]. While actuators are one of the most common pieces laser micro-adjusted, the process is general and has been applied to multiple devices [136] and companies have filed for patents on using laser adjustments based on these reports [137–139]. There has also been a promising report of the laser forming of shape memory alloys, a material commonly used for MEMS actuators, although this forming has not yet been done on MEMS structures [140].

One application of laser micro-adjustment is the precise alignment of optical fibers to ensure optimal coupling with a photonic integrated circuit (PIC) [141]. While glass has been successfully laser formed [81,82], laser forming the optical fiber would only produce bends into the fiber, rather than aligning it. To align the optical fiber, the researchers sheathed the fiber into a thin metal tube and the tube was then laser formed [141,142]. The optical fiber is flexible, so the bend in the metal tube will cause a deflection in the fiber tip. In effect, the metal tube is being used as an alignment actuator with sub-micron precision, owing to the controllability of laser forming [141,142].

3.6. Laser Forming for Rapid Prototyping

The flexibility of laser forming makes it a promising technology for rapid prototyping, and researchers have identified rapid prototyping as one of the areas where laser forming is most likely to make meaningful contributions in the industrial product lifecycle [50]. This promise remains largely unfulfilled compared to more conventional 3D printing for various reasons. Despite the many different methods for 3D printing, such as fused filament fabrication [143,144] and stereolithography [145,146], 3D printing follows the same general workflow to produce a printed object from a computer aided design (CAD) file (Figure 9a). Once the engineer has designed the object they want to be 3D printed using a CAD software, they need to export it to a format that can be 3D printed [19]. The default file format for the additive manufacturing community is the STL file format, which approximates the surface of the CAD object as a collection of tessellated triangles [147]. Since 3D printers build structures in a layer-by-layer fashion, the STL file needs to be passed to a slicer, which converts the 3D object to the build layers. From this file, the scan path is developed, and support structures are calculated if the object needs them. For modern 3D printing, the conversion of the CAD file to printed object is entirely automated [19,147]. Critical to the broad adoption of laser forming for rapid prototyping is developing a similar software structure that can convert a CAD file into a path planning program, which also calculates the appropriate lasing setting to produce the desired 3D object without human intervention. Extensive research efforts have been undertaken to achieve this goal, with recent results suggesting that this goal might be realized soon [62].

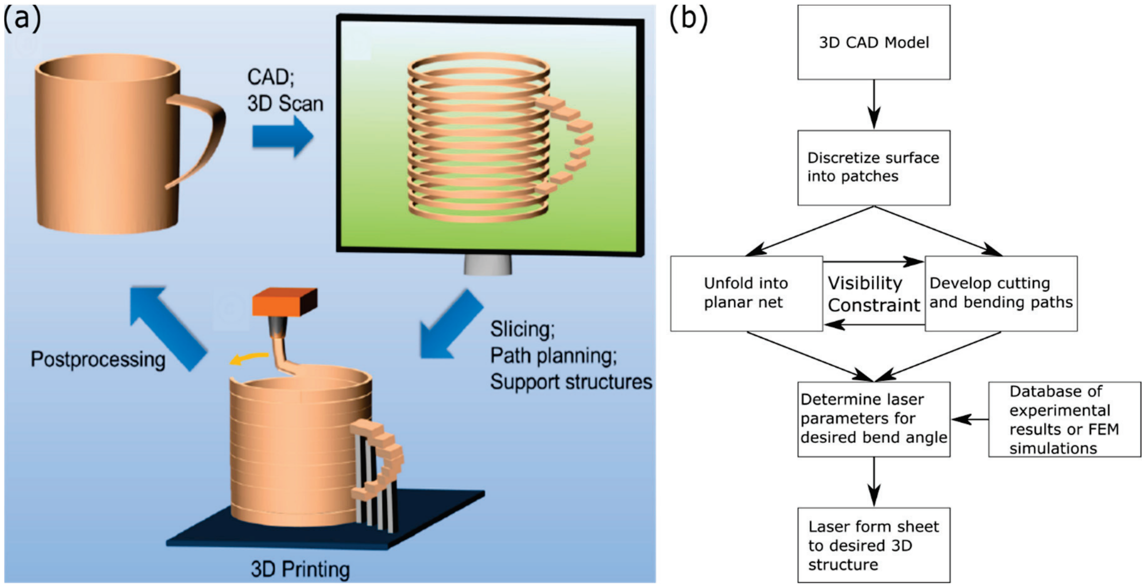

Figure 9. Comparison of workflows for (**a**) conventional 3D printing [19] showing the slicer and path planner, compared to (**b**) proposed workflow for the automated laser forming of arbitrary convex polyhedra. (**a**) Image originally published under a CC BY license. Unlike 3D printing, path planning for laser forming is strongly dependent on the material being formed, which requires a database to determine laser power and speed settings. For more advanced structures, laser forming algorithms need to consider the optical path of the laser beam, as this couples the unfolding algorithm and the path planning.

One of the first complex objects successfully prototyped using laser forming was a car door (Figure 1g) [33]. This demonstration is notable for many reasons, chiefly the entire production was done in the laser system. The researchers started from a blank sheet of metal that was laser formed to produce the desired bends, and the final structure was cut from the sheet using the same laser. As the buckling mechanism was only recently reported and control strategies were limited, the researchers were laser forming only using TGM. The complex shape of the car door required both concave and convex bending, so the workpiece needed to be manually flipped to produce the bi-directional bending needed for the car panel. While these experiments involved no prediction of laser settings, the researchers introduced a novel feedback system, where the scanning speed was adjusted to produce the desired bend angle. Additionally, a car panel might be considered far from an arbitrary design, so the scan pattern was relatively easy to design.

To produce more complex objects via laser forming, it is necessary to know which bend lines are needed to produce a given shape, a classic origami problem [1]. To this end, the inverse design of scan strategies to generate a desired laser formed structure has been a productive research topic [53,66,84,99,148–151]. The design of irradiation paths involves more than planning where the beam needs to be applied to generate a desired shape, but also the laser power and travel speed, to produce the desired degree of bending using the appropriate forming mechanism. These requirements remain a challenge, and have required researchers to design algorithms that plan a scan path and guesses appropriate lasing settings by consulting a database from experiments [99] or finite element simulations (Figure 9b) [53,121,150]. Despite the known disagreement between experimental results and simulations [38], these scan strategies are able to produce the final desired structures with a high degree of accuracy [53,121]. One limitation of these design systems is the limited degree of bending required in the validation structures. As the bend angles required per point are small to moderate, the relationships between bend angle and line energy (laser power divided by scan speed) is approximately linear [98,99]. As the laser spot size gets smaller and the required bending angle approaches 90 degrees, this linear relation fails to hold [88,152] and none of these design strategies account for this deviation. These limitations are more prominent, as engineers have started using laser forming to produce highly complex structures.

Realizing that laser forming was not limited to moderate bending, but could be used for larger folds (up to ninety degrees or higher), our group began envisioning what origami structures can be produced with laser forming. Laser forming with TGM is limited to ninety-degree bends, as further bending results in the workpiece blocking the laser path, but this limitation does not exist if using the buckling mechanism to bend away from the laser. Using both mechanisms, we were able to produce complex objects, such as cubes (Figure 10a) and airplanes, (Figure 10b), without the need for human intervention [59]. Similar to the car door forming [33], the outline of the shape was manufactured from metal sheets by using the laser to also cut the final structure, releasing it from the sheet. By using a Nd:YAG laser instead of a CO_2 laser, an absorbing coating was not needed, allowing for marking of the metal at low powers. Rapidly producing these structures from a blank metal sheet using multiple bending modes and laser cutting demonstrated the potential for laser forming to be a viable rapid prototyping strategy.

Soon after, we showed that laser forming could be used to produce electronic devices, such as antennas [153] and inductors [88]. When producing the antennas, a blank metal sheet was clamped on all sides, before laser cutting the slots for the array antenna and the perimeter of the waveguide was laser cut from the metal sheet, before the entire structure was bent to produce the final structure: a rectangular prism (Figure 10c) [153]. It was worth noting that the laser cutting made more precise cuts than electro-discharge machining, the usual technology used to produce the slots in the waveguide. In fact, the entire laser process of cutting and bending was faster than conventional machining that only produces the slots. Efficient waveguides require smooth surfaces to minimize losses [154], so new manufacturing techniques need to show that they do not greatly alter the metal surface. The impact of laser forming is limited to the laser scan paths and even after 100 passes only showed a modest increase of the surface roughness of 0.5 μm [155]. Similarly, the coils for the inductor were cut from a blank piece of copper before being bent out of plane to generate a toroidal inductor (Figure 10d) [88]. Laser forming can also be used to produce an inductor with an overpass or bending the inductor out of plane. Bending inductors out of plane offers a way to improve the Q-factor as eddy currents and skin effects are minimized [156], which is especially important for integrating these elements on semiconductor integrated circuits. Both reports demonstrated that laser forming could be used to rapidly prototype functional devices, as the designs can easily be iterated, as it only requires changing the location or size of lines in a 2D CAD drawing. This process, however, still requires human input to exchange the metal sheets between design iterations, which would limit the industrial adoption of laser forming for rapid prototyping or producing custom parts.

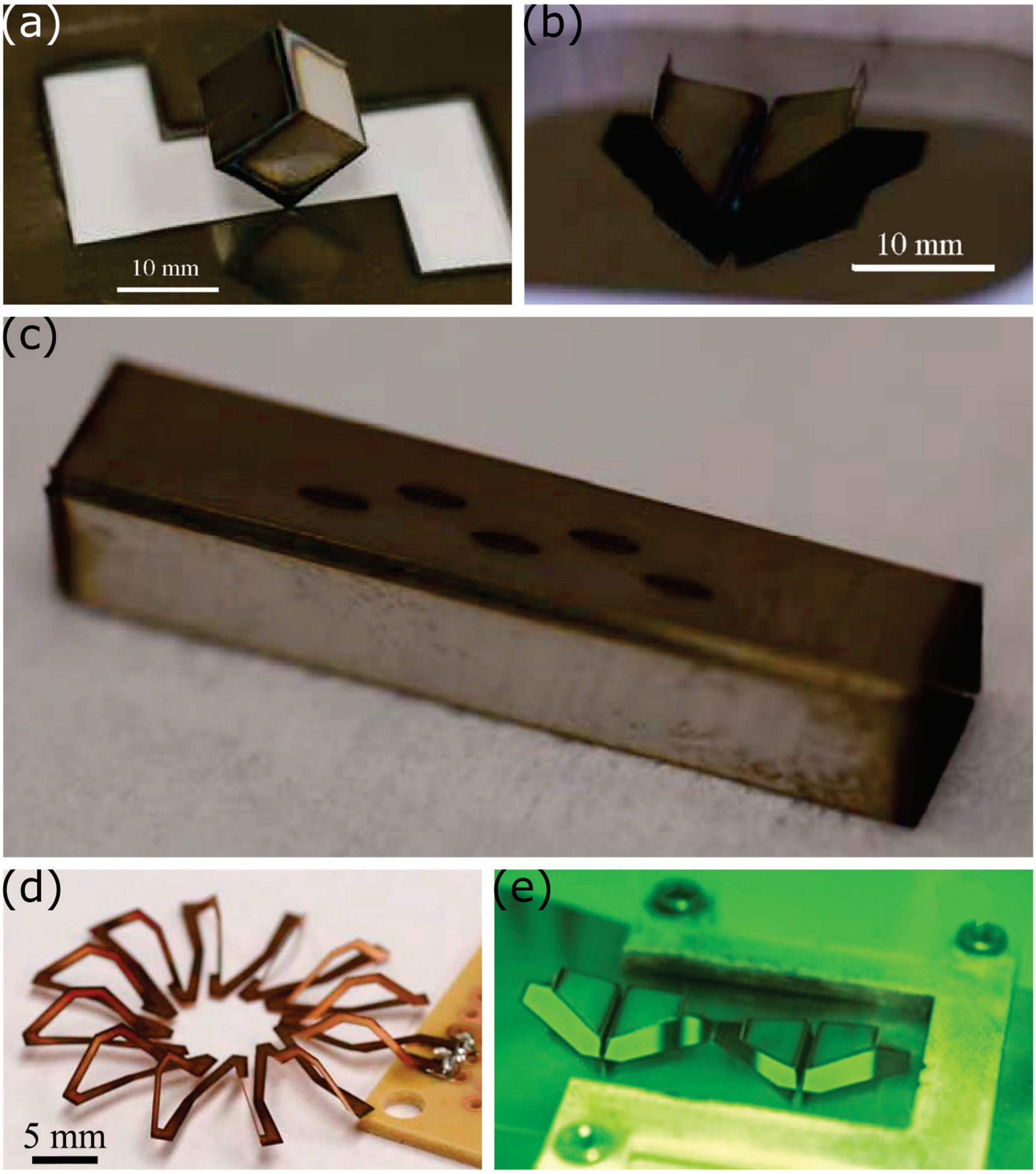

Figure 10. Laser forming can be used to produce complex and functional structures without the need for mechanical input. Three-dimensional structures that were cut and laser formed from nickel foil using a 20W Nd:YAG laser include (**a**) cubes and (**b**) airplanes [59]. (**a**,**b**) Reprinted with permission from John Wiley and Sons, copyright 2013. Laser forming can be used to produce functional structures as well, such as (**c**) a slotted waveguide for antennas from stainless steel [153] and even (**d**) toroidal inductors from copper [88]. (**c**) Reprinted with permission from IEEE, copyright 2018. (**d**) Reprinted with permission from IEEE, copyright 2018. New metal sheets are required between samples, but (**e**) continuous laser forming can be realized by combining it with roll-to-roll processing [63]. Reprinted with permission from Springer Nature, copyright 2018.

Working to automate the entire laser forming process, our group developed a roll-to-roll laser forming system, with the metal feedstock passing through the focal plane of the laser [63]. This set up allowed features to be readily cut and folded from the sheet metal using the TGM. Additionally, the metal sheet had a pre-strain from being wound onto a roll that was used to reliably generate downward bending using the buckling mechanism, producing the same complex shapes from our previous work in an automated process (Figure 10e). Once the piece was formed, it was released from the sheet and fell down a chute, before the rolls were spun to introduce a new working area. This was the first demonstration of a fully automated laser forming process to produce complex 3D structures. While impressive, producing these structures relied on our previously designed scan paths and laser settings. For many of the structures, we relied on the self-limiting nature of ninety-degree bends, so that precise control over the laser settings was not needed. Accurately determining the laser power, speed, and number of passes would be required, if the desired structures included intermediate bends.

Figuring out what scan path and what lasing setting are needed to produce a desired structure is known as the inverse design problem, and has been intensively studied [53,66,99,148–150]. Part of the difficulty of designing laser scan strategies is the highly-coupled and nonlinear thermo-mechanical nature of laser forming, so many of the previously proposed strategies are limited in the number of scan lines [66,99,150] or are computationally intensive, relying on full finite-element models [148,149]. Recently, researchers introduced an algorithm that takes a desired 3D structure as an input, and simultaneously unfolds the structure into a planar net and plans the cutting and bending paths for this net [62]. For normal origami, the planar net and the bending path can be solved for separately, because the craftsmen is able to access all needed fold lines at any given time [6]. As current laser forming setups rely on an unobstructed optical path between the laser and the fold line, this visibility constraint effectively couples the two problems.

Over the years, laser forming has emerged as a viable rapid prototyping strategy that is complementary to metal 3D printing. Understanding of the sub-mechanisms has allowed researchers to develop scan strategies for many 3D shapes, but the complex thermomechanical process makes it near mandatory to automate this process. This need becomes most pronounced when more complex 3D structures and devices are being laser formed, especially ones that require multiple forming mechanisms. Solutions to this inverse design problem are rapidly developing, and will hopefully make laser forming as accessible as 3D printing.

4. Conclusions and Outlook

Laser forming has developed dramatically over the past forty years, from a mechanistic understanding of the process to the successful laser origami of complex 3D shapes and the algorithms to design their laser scan patterns. As the field matures and laser forming is adopted as a viable rapid prototyping strategy, new research opportunities abound. Like any other prototyping technology, laser forming is valuable for certain structures, while not being preferable for others. Deciding if laser forming is the preferred fabrication methods requires design heuristics that have yet to be clarified. Continued research efforts should be focused on clarifying these heuristics, while expanding the capabilities of the laser forming by developing it as a robust technology that is able to reliably produce functional, near-arbitrary 3D structures from flat substrates in an automated manufacturing environment. To this end, researchers will need to address current gaps in the understanding of the laser forming process, which will inform the design and control algorithms.

Laser forming involves rapid heating and cooling cycles that can cause changes in the microstructure of the metal during the process. Microstructural control is very important for titanium pieces in the aerospace industry, as the mechanical properties and fatigue resistance of titanium and its alloys are highly dependent on having precise control over the grains. Preliminary reports suggest that laser forming leads to unfavorable grain structures in titanium [27,95,157]. Other industries and applications might not have as stringent requirements on the grain structure, but these reports suggest there may be some degradation in the mechanical properties of laser formed parts compared to mechanically bent structures, an area that needs further investigation.

The microstructure of a material influences more than mechanical properties, so these other properties need to be considered when deciding to laser form an object. Of particular concern to the shipbuilding industry might be corrosion resistance to the salty ocean water. The corrosion resistance of some laser formed metals has been briefly investigated [96,115,158,159], with many metals demonstrating a reduced corrosion resistance resulting from the disturbed microstructure. Interestingly, some alloys showed an increased corrosion resistance after being laser formed [159], though the role of the lasing parameters on this phenomenon was underexplored. There is a need to study systematically the suitability of a laser formed material for use in a corrosive environment as a function of the material's properties, the nature of the corrosive species, and the laser forming parameters. Applications could include ship hulls in salt water, or a laser bent tube in a chemical processing plant.

For laser forming to move from academic research to an industrial process, stronger control schemes and predictive modelling need to be developed. The state-of-the-art algorithms either develop the optimal laser settings for relatively simple shapes based on finite element modelling, or they use experimental data to develop a laser scan path to produce near-arbitrary 3D shapes. The next step would be to develop an algorithm that combines these methods to develop a scan path for near-arbitrary shapes and the optimal laser settings to produce this shape, as some regions might only need bending, while others require shortening. Combining these algorithms would enable additional constraints to be designed around, as the laser-substrate interaction does more than just bend the workpiece.

Most laser forming setups are run in a batch process with one sheet being bent at a time. A recent report demonstrated a way to transform laser forming into a continuous roll-to-roll process by combining laser cutting and bending [63]. Lasers are used to do much more, such as welding [120,160], marking [161,162], laser-induced chemistry [163–165], and are even used in analytical techniques [166,167]. Taken together, one could imagine a fully automated process wherein blank sheet metal is fed, then different lasers will cut, mark, chemically pattern, and then fold it into a desired 3D structure with inline quality control. Developing such a system will require developing further control schemes to know when and where to bend the structure in this complex process to yield the desired result.

Laser forming is a valuable technology that is poised to address two notable shortcomings of metal 3D printing—large structures and thin structures. Fully realizing this potential will require developing a detailed understanding of how the laser forming process impacts material properties to produce advanced planning and control schemes. With a completely automated process, laser forming will be available to make the rapid prototyping of metallic structures even lighter.

Author Contributions: A.L.B. performed the literature survey and wrote the initial draft of the paper. M.D.D. supervised the work and edited the paper. N.L. supervised the work and edited the paper. All authors have read and agreed to the published version of the manuscript.

Funding: The research was funded by the Army Research Laboratory and was accomplished under Cooperative Agreement Number W911NF-20-2-0243.

Acknowledgments: The views and conclusions contained in this document are those of the authors and should not be interpreted as representing the official policies, either expressed or implied, of the Army Research Laboratory or the U.S. Government. The U.S. Government is authorized to reproduce and distribute reprints for Government purposes notwithstanding any copyright notation herein.

Conflicts of Interest: The authors declare no conflict of interest.

References

1. Turner, N.; Goodwine, B.; Sen, M. A review of origami applications in mechanical engineering. *Proc. Inst. Mech. Eng. Part C J. Mech. Eng. Sci.* **2016**, *230*, 2345–2362. [CrossRef]
2. Hernandez, E.A.P.; Hartl, D.J.; Lagoudas, D.C. Introduction to Active Origami Structures. In *Active Origami*; Springer: Cham, Switzerland, 2019; pp. 1–53, ISBN 978-3-319-91865-5.

3. Felton, S.; Tolley, M.; Demain, E.; Rus, D.; Wood, R. A method for building self-folding machines. *Science* **2014**, *345*, 644–646. [CrossRef]
4. Taylor, A.; Miller, M.; Fok, M.; Nilsson, K.; Tsz Ho Tse, Z. Intracardiac Magnetic Resonance Imaging Catheter With Origami Deployable Mech. *Med. Devices* **2016**, *10*, 020957. [CrossRef]
5. Takano, T.; Miura, K.; Natori, M.; Hanayama, E.; Inoue, T.; Noguchi, T.; Miyahara, N.; Nakaguro, H. Deployable antenna with 10-m maximum diameter for space use. *IEEE Trans. Antennas Propag.* **2004**, *52*, 2–11. [CrossRef]
6. Tachi, T. Origamizing Polyhedral Surfaces. *IEEE Trans. Vis. Comput. Graph.* **2010**, *16*, 298–311. [CrossRef] [PubMed]
7. Zirbel, S.A.; Lang, R.J.; Thomson, M.W.; Sigel, D.A.; Walkemeyer, P.E.; Trease, B.P.; Magleby, S.P.; Howell, L.L. Accommodating Thickness in Origami-Based Deployable Arrays. *J. Mech. Des.* **2013**, 135. [CrossRef]
8. Lang, R.J.; Tolman, K.A.; Crampton, E.B.; Magleby, S.P.; Howell, L.L. A Review of Thickness-Accommodation Techniques in Origami-Inspired Engineering. *Appl. Mech. Rev.* **2018**, *70*, 010805. [CrossRef]
9. Tachi, T.; Hull, T.C. Self-Foldability of Rigid Origami. *J. Mech. Robot.* **2017**, *9*. [CrossRef]
10. Lang, R.J.; Howell, L. Rigidly Foldable Quadrilateral Meshes From Angle Arrays. *J. Mech. Robot.* **2018**, *10*, 021004. [CrossRef]
11. Zirbel, S.A.; Trease, B.P.; Magleby, S.P.; Howell, L.L. Deployment Methods for an Origami-Inspired Rigid-Foldable Array. In Proceedings of the 40th Aerospace Mechanisms Symposium, Baltimore, MD, USA, 14–16 May 2014; NASA Goddard Space Flight Center: Greenbelt, MD, USA, 2014.
12. Morgan, J.; Magleby, S.P.; Howell, L.L. An Approach to Designing Origami-Adapted Aerospace Mechanisms. *J. Mech. Des.* **2016**, *138*. [CrossRef]
13. Whitney, J.P.; Sreetharan, P.S.; Ma, K.Y.; Wood, R.J. Pop-up book MEMS. *J. Micromech. Microeng.* **2011**, *21*, 115021. [CrossRef]
14. Ahmed, S.; McGough, K.; Ounaies, Z.; Frecker, M. Origami-Inspired Folding and Unfolding of Structures: Fundamental Investigations of Dielectric Elastomer-Based Active Materials. In *Smart Materials, Adaptive Structures and Intelligent Systems*; American Society of Mechanical Engineers: Houston, TX, USA, 2013; p. V001T01A029/1-6.
15. Hayes, G.J.; Liu, Y.; Genzer, J.; Lazzi, G.; Dickey, M.D. Self-Folding Origami Microstrip Antennas. *IEEE Trans. Antennas Propag.* **2014**, *62*, 5416–5419. [CrossRef]
16. Tolley, M.T.; Felton, S.M.; Miyashita, S.; Aukes, D.; Rus, D.; Wood, R.J. Self-folding origami: Shape memory composites activated by uniform heating. *Smart Mater. Struct.* **2014**, *23*, 094006/1–9. [CrossRef]
17. Wang, D.H.; Tan, L.-S. Origami-Inspired Fabrication: Self-Folding or Self-Unfolding of Cross-Linked-Polyimide Objects in Extremely Hot Ambience. *ACS Macro Lett.* **2019**, *8*, 546–552. [CrossRef]
18. Upcraft, S.; Fletcher, R. The rapid prototyping technologies. *Assem. Autom.* **2003**, *23*, 318–330. [CrossRef]
19. Ligon, S.C.; Liska, R.; Stampfl, J.; Gurr, M.; Mülhaupt, R. Polymers for 3D Printing and Customized Additive Manufacturing. *Chem. Rev.* **2017**, *117*, 10212–10290. [CrossRef] [PubMed]
20. Das, S.; Bourell, D.L.; Babu, S.S. Metallic materials for 3D printing. *Mrs Bull.* **2016**, *41*, 729–741. [CrossRef]
21. Bak, D. Rapid prototyping or rapid production? 3D printing processes move industry towards the latter. *Assem. Autom.* **2003**, *23*, 340–345. [CrossRef]
22. Agarwala, M.; Bourell, D.; Beaman, J.; Marcus, H.; Barlow, J. Direct selective laser sintering of metals. *Rapid Prototyp. J.* **1995**, *1*, 26–36. [CrossRef]
23. Duda, T.; Raghavan, L.V. 3D Metal Printing Technology. *IFAC Pap.* **2016**, *49*, 103–110. [CrossRef]
24. Panchagnula, J.S.; Simhambhatla, S. Manufacture of complex thin-walled metallic objects using weld-deposition based additive manufacturing. *Robot. Comput. Integr. Manuf.* **2018**, *49*, 194–203. [CrossRef]
25. Hu, J.; Marciniak, Z.; Duncan, J. *Mechanics of Sheet Metal Forming*; Elsevier: Amsterdam, The Netherlands, 2002; ISBN 978-0-08-049651-1.
26. Qattawi, A.; Abdelhamid, M.; Mayyas, A.; Omar, M. Design Analysis for Origami-Based Folded Sheet Metal Parts. *SAE Int. J. Mater. Manf.* **2014**, *7*, 488–498. [CrossRef]
27. Walczyk, D.F.; Vittal, S. Bending of Titanium Sheet Using Laser Forming. *J. Manuf. Process.* **2000**, *2*, 258–269. [CrossRef]
28. Cleveland, R.M.; Ghosh, A.K. Inelastic effects on springback in metals. *Int. J. Plast.* **2002**, *18*, 769–785. [CrossRef]

29. Tseng, A.A.; Jen, K.P.; Chen, T.C.; Kondetimmamhalli, R.; Murty, Y.V. Forming properties and springback evaluation of copper beryllium sheets. *Met. Mater. Trans. A* **1995**, *26*, 2111–2121. [CrossRef]
30. Wagoner, R.H.; Lim, H.; Lee, M.-G. Advanced Issues in springback. *Int. J. Plast.* **2013**, *45*, 3–20. [CrossRef]
31. Abvabi, A.; Rolfe, B.; Hodgson, P.D.; Weiss, M. The influence of residual stress on a roll forming process. *Int. J. Mech. Sci.* **2015**, *101*, 124–136. [CrossRef]
32. Martin, J.H.; Yahata, B.D.; Hundley, J.M.; Mayer, J.A.; Schaedler, T.A.; Pollock, T.M. 3D printing of high-strength aluminium alloys. *Nature* **2017**, *549*, 365–369. [CrossRef]
33. Thomson, G.; Pridham, M.S. Controlled laser forming for rapid prototyping. *Rapid Prototyp. J.* **1997**, *3*, 137–143. [CrossRef]
34. Clausen, H.B. *DTU Plate Forming by Line Heating*; Department of Naval Architecture and Offshore Engineering, Technical University of Denmark: Lyngby, Denmark, 2000.
35. Scully, K. Laser Line Heating. *J. Ship Prod.* **1987**, *3*, 237–246.
36. Magee, J.; Watkins, K.G.; Steen, W.M. Advances in laser forming. *J. Laser Appl.* **1998**, *10*, 235–246. [CrossRef]
37. Geiger, M.; Vollertsen, F. The Mechanisms of Laser Forming. *Cirp Ann.* **1993**, *42*, 301–304. [CrossRef]
38. Shen, H.; Vollertsen, F. Modelling of laser forming—An review. *Comput. Mater. Sci.* **2009**, *46*, 834–840. [CrossRef]
39. Cheng, P.; Fan, Y.; Zhang, J.; Yao, Y.L.; Mika, D.P.; Zhang, W.; Graham, M.; Marte, J.; Jones, M. Laser Forming of Varying Thickness Plate—Part I: Process Analysis. *J. Manuf. Sci. Eng.* **2006**, *128*, 634–641. [CrossRef]
40. Li, W.; Yao, Y.L. Laser Bending of Tubes: Mechanism, Analysis, and Prediction. *J. Manuf. Sci. Eng.* **2001**, *123*, 674–681. [CrossRef]
41. Tam, A.C.; Poon, C.C.; Crawforth, L. Laser Bending of Ceramics and Application to Manufacture Magnetic Head Sliders in Disk Drives. *Anal. Sci. Suppl.* **2002**, *17*, s419–s421. [CrossRef]
42. Folkersma, G.; Römer, G.-W.; Brouwer, D.; in ’t Veld, B.H. In-plane laser forming for high precision alignment. *Opt. Eng.* **2014**, *53*, 126105. [CrossRef]
43. Hu, Y.; Xu, X.; Yao, Z.; Hu, J. Laser peen forming induced two way bending of thin sheet metals and its mechanisms. *J. Appl. Phys.* **2010**, *108*, 073117. [CrossRef]
44. Yocom, C.J.; Zhang, X.; Liao, Y. Research and development status of laser peen forming: A review. *Opt. Laser Technol.* **2018**, *108*, 32–45. [CrossRef]
45. Arcella, F.G.; Froes, F.H. Producing titanium aerospace components from powder using laser forming. *JOM* **2000**, *52*, 28–30. [CrossRef]
46. Laeng, J.; Stewart, J.G.; Liou, F.W. Laser metal forming processes for rapid prototyping - A review. *Int. J. Prod. Res.* **2000**, *38*, 3973–3996. [CrossRef]
47. Kant, R.; Joshi, S.N.; Dixit, U.S. 4—Research issues in the laser sheet bending process. In *Materials Forming and Machining*; Woodhead Publishing Reviews: Mechanical Engineering Series; Davim, J.P., Ed.; Woodhead Publishing: Cambridge, UK, 2016; pp. 73–97, ISBN 978-0-85709-483-4.
48. Omidvar, M.; Fard, R.K.; Sohrabpoor, H.; Teimouri, R. Selection of laser bending process parameters for maximal deformation angle through neural network and teaching–learning-based optimization algorithm. *Soft Comput.* **2015**, *19*, 609–620. [CrossRef]
49. Lambiase, F. An Analytical Model for Evaluation of Bending Angle in Laser Forming of Metal Sheets. *J. Mater. Eng. Perform.* **2012**, *21*, 2044–2052. [CrossRef]
50. Dearden, G.; Edwardson, S.P. Some recent developments in two-and three-dimensional laser forming for macro and micro applications. *J. Opt. A Pure Appl. Opt.* **2003**, *5*, S8–S15. [CrossRef]
51. Shi, Y.; Yao, Z.; Shen, H.; Hu, J. Research on the mechanisms of laser forming for the metal plate. *Int. J. Mach. Tools Manuf.* **2006**, *46*, 1689–1697. [CrossRef]
52. Arnet, H.; Vollertsen, F. Extending Laser Bending for the Generation of Convex Shapes. *Proc. Inst. Mech. Eng. Part B J. Eng. Manuf.* **1995**, *209*, 433–442. [CrossRef]
53. Liu, C.; Yao, Y.L.; Srinivasan, V. Optimal Process Planning for Laser Forming of Doubly Curved Shapes. *J. Manuf. Sci. Eng.* **2004**, *126*, 1–9. [CrossRef]
54. Edwardson, S.P.; Dearden, G. *Laser Assisted Forming for Ship Building*; Sail: Williamsburg, VA, USA, 2003.
55. Steen, W.M.; Mazumder, J. Laser Bending or Forming. In *Laser Material Processing*; Steen, W.M., Mazumder, J., Eds.; Springer: London, UK, 2010; pp. 389–416, ISBN 978-1-84996-062-5.
56. Che Jamil, M.S.; Sheikh, M.A.; Li, L. A study of the effect of laser beam geometries on laser bending of sheet metal by buckling mechanism. *Opt. Laser Technol.* **2011**, *43*, 183–193. [CrossRef]

57. Vollertsen, F.; Komel, I.; Kals, R. The laser bending of steel foils for microparts by the buckling mechanism-a model. *Model. Simul. Mater. Sci. Eng.* **1995**, *3*, 107–119. [CrossRef]
58. Experimental and numerical modeling of buckling instability of laser sheet forming. *Int. J. Mach. Tools Manuf.* **2002**, *42*, 1427–1439. [CrossRef]
59. Lazarus, N.; Smith, G.L. Laser Forming for Complex 3D Folding. *Adv. Mater. Technol.* **2017**, *2*, 1700109. [CrossRef]
60. Shi, Y.; Liu, Y.; Yao, Z.; Shen, H. A study on bending direction of sheet metal in laser forming. *J. Appl. Phys.* **2008**, *103*, 053101. [CrossRef]
61. Li, W.; Yao, Y.L. Buckling based laser forming process: Concave or convex. In *International Congress on Applications of Lasers & Electro-Optics*; Laser Institute of America: Orlando, FL, USA, 2000; pp. D220–D229. [CrossRef]
62. Hao, Y.; Lien, J.-M. Computational laser forming origami of convex surfaces. In Proceedings of the ACM Symposium on Computational Fabrication—SCF '1, Pittsburgh, PA, USA, 16–18 June 2019; pp. 1–11.
63. Lazarus, N.; Smith, G.L. Laser Folding in a Roll-to-Roll Manufacturing Process. *Lasers Manuf. Mater. Process.* **2018**, *5*, 237–247. [CrossRef]
64. Shen, H. Mechanism of laser micro-adjustment. *J. Phys. D Appl. Phys.* **2008**, *41*, 245106. [CrossRef]
65. Lawrence, S. Developable Surfaces: Their History and Application. *Nexus Netw. J.* **2011**, *13*, 701–714. [CrossRef]
66. Maji, K.; Pratihar, D.K.; Nath, A.K. Forward and inverse predictions of deformations in laser forming of shaped surfaces under coupling mechanism. *J. Laser Appl.* **2018**, *30*, 032011. [CrossRef]
67. Chen, G.; Xu, X. Experimental and 3D Finite Element Studies of CW Laser Forming of Thin Stainless Steel Sheets. *J. Manuf. Sci. Eng.* **2000**, *123*, 66–73. [CrossRef]
68. Vásquez-Ojeda, C.; Ramos-Grez, J. Bending of stainless steel thin sheets by a raster scanned low power CO2 laser. *J. Mater. Process. Technol.* **2009**, *209*, 2641–2647. [CrossRef]
69. Paunoiu, V.; Squeo, E.A.; Quadrini, F.; Gheorghies, C.; Nicoara, D. Laser Bending of Stainless Steel Sheet Metals. *Int J. Mater.* **2008**, *1*, 1371–1374. [CrossRef]
70. Zaeh, M.F.; Hornfeck, T. Development of a robust laser beam bending process for aluminum fuselage structures. *Prod. Eng. Res. Devel.* **2008**, *2*, 149–155. [CrossRef]
71. Geiger, M.; Merklein, M.; Pitz, M. Laser and forming technology—An idea and the way of implementation. *J. Mater. Process. Technol.* **2004**, *151*, 3–11. [CrossRef]
72. Lubiano, G.; Ramos, J.A.; Magee, J. Laser Bending of Thin Metal Sheets by Means of a Low Power CO_2 Laser 537. In Proceedings of the 2000 International Solid Freeform Fabrication Symposium, Austin, TX, USA; 2000.
73. Magee, J.; Watkins, K.G.; Steen, W.M.; Calder, N.J.; Sidhu, J.; Kirby, J. Laser forming of aerospace alloys. In *International Congress on Applications of Lasers & Electro-Optics*; Laser Institute of America: Orlando, FL, USA, 1997; pp. E156–E165. [CrossRef]
74. Kitada, K.; Asahi, N. Laser adjustment of beryllium copper sheet using temperature gradient mechanism. In Proceedings of the Third International Symposium on Laser Precision Microfabrication; International Society for Optics and Photonics: Bellingham, WA, USA, 2003; Volume 4830, pp. 30–35.
75. Jiang, S.Q.; Liu, A.H.; Wang, X.X.; Chen, Z. The Bending Forming Mechanism of Copper Alloy by Different Lasers. *Adv. Mater. Res.* **2014**, *968*, 142–145. [CrossRef]
76. Gärtner, E.; Frühauf, J.; Löschner, U.; Exner, H. Laser bending of etched silicon microstructures. *Microsyst. Technol.* **2001**, *7*, 23–26. [CrossRef]
77. Xu, W.; Zhang, L.C.; Wang, X. Laser Bending of Silicon Sheet: Absorption Factor and Mechanisms. *J. Manuf. Sci. Eng.* **2013**, *135*. [CrossRef]
78. Wu, D.-J.; Ma, G.-Y.; Liu, S.; Wang, X.-Y.; Guo, D.-M. Experiments and simulation on laser bending of silicon sheet with different thicknesses. *Appl. Phys. A* **2010**, *101*, 517–521. [CrossRef]
79. Wu, D.; Zhang, Q.; Ma, G.; Guo, Y.; Guo, D. Laser bending of brittle materials. *Opt. Lasers Eng.* **2010**, *48*, 405–410. [CrossRef]
80. Wu, D.; Ma, G.; Niu, F.; Guo, D. Temperature Gradient Mechanism on Laser Bending of Borosilicate Glass Sheet. *J. Manuf. Sci. Eng.* **2010**, *132*. [CrossRef]
81. Bucher, T.; Cardenas, S.; Verma, R.; Li, W.; Lawrence Yao, Y. Laser Forming of Sandwich Panels With Metal Foam Cores. *J. Manuf. Sci. Eng.* **2018**, *140*, 111015. [CrossRef]

82. Guglielmotti, A.; Quadrini, F.; Squeo, E.A.; Tagliaferri, V. Laser Bending of Aluminum Foam Sandwich Panels. *Adv. Eng. Mater.* **2009**, *11*, 902–906. [CrossRef]
83. Gisario, A.; Barletta, M. Laser forming of glass laminate aluminium reinforced epoxy (GLARE): On the role of mechanical, physical and chemical interactions in the multi-layers material. *Opt. Lasers Eng.* **2018**, *110*, 364–376. [CrossRef]
84. Seong, W.-J.; Jeon, Y.-C.; Na, S.-J. Ship-hull plate forming of saddle shape by geometrical approach. *J. Mater. Process. Technol.* **2013**, *213*, 1885–1893. [CrossRef]
85. Okamoto, Y.; Uno, Y.; Ohta, K.; Shibata, T.; Kubota, S.; Namba, Y. Study on Precision Laser Forming of Plastic with YAG Laser. *J. Jpn. Soc. Precis. Eng.* **2000**, *66*, 891–895. [CrossRef]
86. Okamoto, Y.; Miyamoto, I.; Uno, Y.; Takenaka, T. Deformation characteristics of plastics in YAG laser forming. In Proceedings of the Fifth International Symposium on Laser Precision Microfabrication, Bellingham, WA, USA, 8 October 2004; International Society for Optics and Photonics: Bellingham, WA, USA, 2004; Volume 5662, pp. 576–581.
87. Cheng, P.; Fan, Y.; Zhang, J.; Yao, Y.L.; Mika, D.P.; Zhang, W.; Graham, M.; Marte, J.; Jones, M. Laser Forming of Varying Thickness Plate—Part II: Process Synthesis. *J. Manuf. Sci. Eng.* **2006**, *128*, 642–650. [CrossRef]
88. Lazarus, N.; Bedair, S.S.; Smith, G.L. Origami Inductors: Rapid Folding of 3-D Coils on a Laser Cutter. *IEEE Electron. Device Lett.* **2018**, *39*, 1046–1049. [CrossRef]
89. Gautam, S.S.; Singh, S.K.; Dixit, U.S. Laser Forming of Mild Steel Sheets Using Different Surface Coatings. In *Lasers Based Manufacturing: 5th International and 26th All India Manufacturing Technology, Design and Research Conference, AIMTDR 2014*; Joshi, S.N., Dixit, U.S., Eds.; Topics in Mining, Metallurgy and Materials Engineering; Springer: New Delhi, India, 2015; pp. 17–39, ISBN 978-81-322-2352-8.
90. Axelevitch, A.; Gorenstein, B.; Golan, G. Investigation of Optical Transmission in Thin Metal Films. *Phys. Procedia* **2012**, *32*, 1–13. [CrossRef]
91. Rumble, J. *CRC Handbook of Chemistry and Physics*, 101st ed.; CRC Press: Boca Raton, FL, USA, 2020; ISBN 978-0-367-41724-6.
92. Shidid, D.P.; Gollo, M.H.; Brandt, M.; Mahdavian, M. Study of effect of process parameters on titanium sheet metal bending using Nd: YAG laser. *Opt. Laser Technol.* **2013**, *47*, 242–247. [CrossRef]
93. Yau, C.L.; Chan, K.C.; Lee, W.B. Laser bending of leadframe materials. *J. Mater. Process. Technol.* **1998**, *82*, 117–121. [CrossRef]
94. Hennige, T.; Holzer, S.; Vollertsen, F.; Geiger, M. On the working accuracy of laser bending. *J. Mater. Process. Technol.* **1997**, *71*, 422–432. [CrossRef]
95. Fidder, H.; Ocelík, V.; Botes, A.; De Hosson, J.T.M. Response of Ti microstructure in mechanical and laser forming processes. *J. Mater. Sci.* **2018**, *53*, 14713–14728. [CrossRef]
96. Walczak, M.; Ramos-Grez, J.; Celentano, D.; Lima, E.B.F. Sensitization of AISI 302 stainless steel during low-power laser forming. *Opt. Lasers Eng.* **2010**, *48*, 906–914. [CrossRef]
97. Patel, C.K.N. Continuous-Wave Laser Action on Vibrational-Rotational Transitions of CO_2. *Phys. Rev.* **1964**, *136*, A1187–A1193. [CrossRef]
98. Lawrence, J. A comparative investigation of the efficacy of CO $_2$ and high-power diode lasers for the forming of EN3 mild steel sheets. *Proc. Inst. Mech. Eng. Part. B J. Eng. Manuf.* **2002**, *216*, 1481–1491. [CrossRef]
99. Kim, J.; Na, S.J. Development of irradiation strategies for free curve laser forming. *Opt. Laser Technol.* **2003**, *35*, 605–611. [CrossRef]
100. Silve, S.; Podschies, B.; Steen, W.M.; Watkins, K.G. Laser Forming —A New Vocabulary for Objects. In Proceedings of the ICALEO 1999, San Diego, FL, USA, 15–18 November 1999; Volume F, pp. 87–96.
101. Shi, Y.; Shen, H.; Yao, Z.; Hu, J. Temperature gradient mechanism in laser forming of thin plates. *Opt. Laser Technol.* **2007**, *39*, 858–863. [CrossRef]
102. Magee, J.; Sidhu, J.; Cooke, R.L. A Prototype laser forming system. *Opt. Lasers Eng.* **2000**, *34*, 339–353. [CrossRef]
103. Namba, Y. Laser Forming in Space. In Proceedings of the International Conference on Lasers '85, Las Vegas, NV, USA; 1985; pp. 403–407.
104. Liu, J.; Sun, S.; Guan, Y.; Ji, Z. Experimental study on negative laser bending process of steel foils. *Opt. Lasers Eng.* **2010**, *48*, 83–88. [CrossRef]
105. Yoshioka, S.; Miyazaki, T.; Misu, T.; Oba, R.; Saito, M. Laser forming of thin foil by a newly developed sample holding method. *J. Laser Appl.* **2003**, *15*, 6. [CrossRef]

106. Shen, H.; Peng, L.; Hu, J.; Yao, Z. Study on the mechanical behavior of laser micro-adjustment of two-bridge actuators. *J. Micromech. Microeng.* **2010**, *20*, 115010. [CrossRef]
107. Tetzel, H.; Grden, M.; Vollertsen, F. Stress analysis based on strain measurement in sheet metal laser bending. *Prod. Eng. Res. Devel.* **2013**, *7*, 647–655. [CrossRef]
108. Cheng, J.; Yao, Y.L. Cooling effects in multiscan laser forming. *J. Manuf. Process.* **2001**, *3*, 60–72. [CrossRef]
109. Lambiase, F.; Di Ilio, A.; Paoletti, A. An experimental investigation on passive water cooling in laser forming process. *Int. J. Adv. Manuf. Technol.* **2013**, *64*, 829–840. [CrossRef]
110. Seyedkashi, S.M.H.; Cho, J.R.; Lee, S.H.; Moon, Y.H. Feasibility of underwater laser forming of laminated metal composites. *Mater. Manuf. Process.* **2018**, *33*, 546–551. [CrossRef]
111. Shen, H.; Ran, M.; Hu, J.; Yao, Z. An experimental investigation of underwater pulsed laser forming. *Opt. Lasers Eng.* **2014**, *62*, 1–8. [CrossRef]
112. Paramasivan, K.; Das, S.; Marimuthu, S.; Misra, D. Increment in laser bending angle by forced bottom cooling. *Int. J. Adv. Manuf. Technol.* **2018**, *94*, 2137–2147. [CrossRef]
113. Shen, H.; Hu, J.; Yao, Z.Q. Cooling Effects in Laser Forming. *Mater. Sci. Forum* **2010**, *663–665*, 58–63. [CrossRef]
114. Lambiase, F.; Di Ilio, A.; Paoletti, A. Productivity in multi-pass laser forming of thin AISI 304 stainless steel sheets. *Int. J. Adv. Manuf. Technol.* **2016**, *86*, 259–268. [CrossRef]
115. Chinizadeh, M.; Kiahosseini, S.R. Deformation, microstructure, hardness, and pitting corrosion of 316 stainless steel after laser forming: A comparison between natural and forced cooling. *J. Mater. Res.* **2017**, *32*, 3046–3054. [CrossRef]
116. Arora, H.; Singh, R.; Brar, G.S. Thermal and structural modelling of arc welding processes: A literature review. *Meas. Control.* **2019**, *52*, 955–969. [CrossRef]
117. Geiger, M.; Vollertsen, F.; Deinzer, G. *Flexible Straightening of Car Body Shells by Laser Forming*; SAE: Warrendale, PA, USA, 1993; p. 930279.
118. Dearden, G.; Edwardson, S.P.; Abed, E.; Watkins, K.G. Laser forming for the correction of distortion and design shape in aluminium structures using laser forming. In *International Congress on Applications of Lasers & Electro-Optics*; Laser Institute of America: Orlando, FL, USA, 2006.
119. Gurova, T.; Estefen, S.F.; Leontiev, A.; de Oliveira, F.A.L. Welding residual stresses: A daily history. *Sci. Technol. Weld. Join.* **2015**, *20*, 616–621. [CrossRef]
120. Stavridis, J.; Papacharalampopoulos, A.; Stavropoulos, P. Quality assessment in laser welding: A critical review. *Int. J. Adv. Manuf. Technol.* **2018**, *94*, 1825–1847. [CrossRef]
121. Shi, Y.J.; Chen, J.; Qi, Y.G.; Yao, Z.Q. Processing strategy for laser forming of complicated singly curved shapes. *Mater. Sci. Technol.* **2009**, *25*, 925–930. [CrossRef]
122. Mehrpouya, M.; Huang, H.; Venettacci, S.; Gisario, A. LaserOrigami (LO) of three-dimensional (3D) components: Experimental analysis and numerical modeling-part II. *J. Manuf. Process.* **2019**, *39*. [CrossRef]
123. Castle, T.; Cho, Y.; Gong, X.; Jung, E.; Sussman, D.M.; Yang, S.; Kamien, R.D. Making the Cut: Lattice Kirigami Rules. *Phys. Rev. Lett.* **2014**, *113*, 245502. [CrossRef]
124. Cheng, J.; Yao, Y.L. Process Design of Laser Forming for Three-Dimensional Thin Plates. *J. Manuf. Sci. Eng.* **2004**, *126*, 217–225. [CrossRef]
125. Ibraheem Imhan, K.; Btht, B.; Zakaria, A.; Shah B Ismail, M.I.; Hadi Alsabti, N.M.; Ahmad, A.K. Features of Laser Tube Bending processing based on Laser Forming: A Review. *J. Laser Opt. Photonics* **2018**, *5*. [CrossRef]
126. Wang, X.Y.; Wang, J.; Xu, W.J.; Guo, D.M. Scanning path planning for laser bending of straight tube into curve tube. *Opt. Laser Technol.* **2014**, *56*, 43–51. [CrossRef]
127. Guglielmotti, A.; Quadrini, F.; Squeo, E.A.; Tagliaferri, V. Diode laser bending of tongues from slotted steel tubes. *Int. J. Mater.* **2009**, *2*, 107–111. [CrossRef]
128. Che Jamil, M.S.; Imam Fauzi, E.R.; Juinn, C.S.; Sheikh, M.A. Laser bending of pre-stressed thin-walled nickel micro-tubes. *Opt. Laser Technol.* **2015**, *73*, 105–117. [CrossRef]
129. Campbell, R.C.; Campbell, B.R.; Lehecka, T.M.; Palmer, J.A.; Knorovsky, G.A. Precision laser bending of thin precious metal alloys. In Proceedings of the Laser-Based Micro- and Nanopackaging and Assembly, Bellingham, WA, USA, 20 March 2007; Volume 6459, p. 64590U.
130. Frühauf, J.; Gärtner, E.; Jänsch, E. Silicon as a plastic material. *J. Micromech. Microeng.* **1999**, *9*, 305–312. [CrossRef]

131. Schmidt, M.; Dirscherl, M.; Rank, M.; Zimmermann, M. Laser micro adjustment—From new basic process knowledge to the application. *J. Laser Appl.* **2007**, *19*, 10. [CrossRef]
132. Widlaszewski, J. Applications of laser forming in micro technologies. In *Selected Problems of Modeling and Control in Mechanics*; Wydawnictwo: Kielce, Poland, 2011.
133. Hoving, W. *Accurate Manipulation Using Laser Technology*; Beckmann, L.H.J.F., Ed.; Proc. SPIE 3097: Munich, Germany, 1997; pp. 284–295.
134. Zhuang, Z.; Lu, Z.; Huang, Z.; Liu, C.; Qin, W. School of Mechanical Engineering, Shanghai Jiao Tong University, 200240, Shanghai, China Experimental study on edge effects in laser bending. *Math. Biosci. Eng.* **2019**, *16*, 4491–4505. [CrossRef] [PubMed]
135. Shen, H.; Wang, H.; Hu, J.; Yao, Z. Processing Optimization in Multiheating Positions for Laser Thermal Adjustment of Actuators. *J. Manuf. Sci. Eng.* **2016**, *138*. [CrossRef]
136. Zhang, X.R.; Xu, X. Laser bending for high-precision curvature adjustment of microcantilevers. *Appl. Phys. Lett.* **2005**, *86*, 021114. [CrossRef]
137. Inoue, M.; Kawamata, H.; Tanaka, H. Thin Plate Formation Method, Thin Plate and Suspension Correction Apparatus, and Correction Method. U.S. Patent 7,624,610, 1 December 2009.
138. Murata, A.; Mukae, H.; Maegawa, T.; Higashionji, M.; Okada, T. Rotary Head Adjuster. U.S. Patent 5,341,256, 1994.
139. Murata, A.; Mukae, H.; Maegawa, T.; Higashionji, M.; Okada, T. Rotary Magnetic Head Having Head Base Which is Bent Along Thermal Plastic Deformation Line. U.S. Patent 6,185,073, 2001.
140. Birnbaum, A.J.; Yao, Y.L. The Effects of Laser Forming on NiTi Superelastic Shape Memory Alloys. *J. Manuf. Sci. Eng.* **2010**, *132*, 41002. [CrossRef]
141. Folkersma, K.G.P.; Römer, G.R.B.E.; Brouwer, D.M.; Herder, J.L. High precision optical fiber alignment using tube laser bending. *Int. J. Adv. Manuf. Technol.* **2016**, *86*, 953–961. [CrossRef]
142. Folkersma, G.; Brouwer, D.; Römer, G.-W. Microtube Laser Forming for Precision Component Alignment. *J. Manuf. Sci. Eng.* **2016**, *138*. [CrossRef]
143. Thompson, Y.; Gonzalez-Gutierrez, J.; Kukla, C.; Felfer, P. Fused filament fabrication, debinding and sintering as a low cost additive manufacturing method of 316L stainless steel. *Addit. Manuf.* **2019**, *30*, 100861. [CrossRef]
144. Lathers, S.; Mousa, M.; La Belle, J. Additive Manufacturing Fused Filament Fabrication Three-Dimensional Printed Pressure Sensor for Prosthetics with Low Elastic Modulus and High Filler Ratio Filament Composites. *3D Print. Addit. Manuf.* **2017**, *4*, 30–40. [CrossRef]
145. Hegde, M.; Meenakshisundaram, V.; Chartrain, N.; Sekhar, S.; Tafti, D.; Williams, C.B.; Long, T.E. 3D Printing All-Aromatic Polyimides using Mask-Projection Stereolithography: Processing the Nonprocessable. *Adv. Mater.* **2017**, *29*, 1701240. [CrossRef]
146. Hull, C.W. Apparatus for Production of Three-Dimensional Objects by Stereolithography. U.S. Patent 6,027,324, 22 February 2000.
147. Negi, S.; Dhiman, S.; Sharma, R.K. Basics, Applications and Future of Additive Manufacturing Technologies: A review. *J. Manuf. Technol. Res.* **2013**, *5*, 75.
148. Gao, H.; Sheikholeslami, G.; Dearden, G.; Edwardson, S.P. Development of Scan Strategies for Controlled 3D Laser Forming of Sheet Metal Components. *Phys. Procedia* **2016**, *83*, 286–295. [CrossRef]
149. Gao, H.; Sheikholeslami, G.; Dearden, G.; Edwardson, S.P. Reverse Analysis of Scan Strategies for Controlled 3D Laser Forming of Sheet Metal. *Procedia Eng.* **2017**, *183*, 369–374. [CrossRef]
150. Kim, J.; Na, S.J. 3D laser-forming strategies for sheet metal by geometrical information. *Opt. Laser Technol.* **2009**, *41*, 843–852. [CrossRef]
151. Kim, J.; Na, S.J. Feedback control for 2D free curve laser forming. *Opt. Laser Technol.* **2005**, *37*, 139–146. [CrossRef]
152. Edwardson, S.P.; Abed, E.; Bartkowiak, K.; Dearden, G.; Watkins, K.G. Geometrical influences on multi-pass laser forming. *J. Phys. D Appl. Phys.* **2006**, *39*, 382–389. [CrossRef]
153. Smith, G.L.; Lazarus, N.; McCormick, S. Laser Folded Antenna. In Proceedings of the 2018 IEEE MTT-S International Microwave Workshop Series on Advanced Materials and Processes for RF and THz Applications (IMWS-AMP), Ann Arbor, MI, USA, 16–18 July 2018; pp. 1–3.
154. Morgan, S.P. Effect of Surface Roughness on Eddy Current Losses at Microwave Frequencies. *J. Appl. Phys.* **1949**, *20*, 352–362. [CrossRef]

155. Kügler, H.; Vollertsen, F. Determining Absorptivity Variations of Multiple Laser Beam Treatments of Stainless Steel Sheets. *J. Manuf. Mater. Process.* **2018**, *2*, 84. [CrossRef]
156. Chua, C.L.; Fork, D.K.; Schuylenbergh, K.V.; Lu, J.P. Out-of-plane high-Q inductors on low-resistance silicon. *J. Microelectromech. Syst.* **2003**, *12*, 989–995. [CrossRef]
157. Fidder, H.; Els-Botes, A.; Woudberg, S.; McGrath, P.J.; Ocelik, V.; de Hosson, J.T.M. A Study of Microstructural Fatigue and Residual Stress Evolution in Titanium Plates Deformed by Mechanical and Laser Bending. *WIT Trans. Eng. Sci. Southampt.* **2015**, *91*, 23–34.
158. Sami Yilbas, B.; Khaled, M.; Akhtar, S.; Karatas, C. Laser bending of steel sheets: Corrosion testing of bended sections. *Ind. Lubr. Tribol.* **2011**, *63*, 367–372. [CrossRef]
159. Liu, Z.; Guzmán, C.; Liu, H.; Anacleto, A.; Francisco, T.; Abdoalshafie, M.; Ma, L.; Abodunrin, O.; Skeldon, P. Corrosion performance and restoration of laser-formed metallic alloy sheets. *J. Laser Appl.* **2009**, *21*, 76–81. [CrossRef]
160. Olsen, F.O.; Alting, L. Pulsed Laser Materials Processing, ND-YAG versus CO_2 Lasers. *Cirp Ann.* **1995**, *44*, 141–145. [CrossRef]
161. Lazarus, N.; Wilson, A.A.; Smith, G.L. Contactless laser fabrication and propulsion of freely moving structures. *Extrem. Mech. Lett.* **2018**, *20*, 46–50. [CrossRef]
162. Noor, Y.M.D.; Tam, S.C.; Lim, L.E.N.; Jana, S. A review of the Nd: YAG laser marking of plastic and ceramic IC packages. *J. Mater. Process. Technol.* **1994**, *42*, 95–133. [CrossRef]
163. Ehrlich, D.J.; Tsao, J.Y. A review of laser–microchemical processing. *J. Vac. Sci. Technol. B: Microelectron. Process. Phenom.* **1983**, *1*, 969–984. [CrossRef]
164. Osgood, R.M.; Deutsch, T.F. Laser-Induced Chemistry for Microelectronics. *Science* **1985**, *227*, 709–714. [CrossRef]
165. Kindle, C.; Castonguay, A.; McGee, S.; Tomko, J.A.; Hopkins, P.E.; Zarzar, L.D. Direct Laser Writing from Aqueous Precursors for Nano to Microscale Topographical Control, Integration, and Synthesis of Nanocrystalline Mixed Metal Oxides. *ACS Appl. Nano Mater.* **2019**, *2*, 2581–2586. [CrossRef]
166. Wachs, I.E. Raman and IR studies of surface metal oxide species on oxide supports: Supported metal oxide catalysts. *Catal. Today* **1996**, *27*, 437–455. [CrossRef]
167. Kalinushkin, V.P.; Uvarov, O.V.; Gladilin, A.A. Photoluminescent Tomography of Semiconductors by Two-Photon Confocal Microscopy Technique. *J. Electron. Mater.* **2018**, *47*, 5087–5091. [CrossRef]

Publisher's Note: MDPI stays neutral with regard to jurisdictional claims in published maps and institutional affiliations.

© 2020 by the authors. Licensee MDPI, Basel, Switzerland. This article is an open access article distributed under the terms and conditions of the Creative Commons Attribution (CC BY) license (http://creativecommons.org/licenses/by/4.0/).

MDPI AG
Grosspeteranlage 5
4052 Basel
Switzerland
Tel.: +41 61 683 77 34

Quantum Beam Science Editorial Office
E-mail: qubs@mdpi.com
www.mdpi.com/journal/qubs

Disclaimer/Publisher's Note: The title and front matter of this reprint are at the discretion of the Guest Editors. The publisher is not responsible for their content or any associated concerns. The statements, opinions and data contained in all individual articles are solely those of the individual Editors and contributors and not of MDPI. MDPI disclaims responsibility for any injury to people or property resulting from any ideas, methods, instructions or products referred to in the content.

MDPI

Academic Open
Access Publishing

mdpi.com

ISBN 978-3-7258-4268-1